TECHNICAL UNIVERSITY OF MUNICH

PHYSICS DEPARTMENT

HELMHOLTZ ZENTRUM MÜNCHEN

INSTITUTE OF RADIATION MEDICINE

Dissertation

Microbeam radiotherapy on the path to clinical application: A powerful compact x-ray source and microbeam treatment planning

Johanna Winter

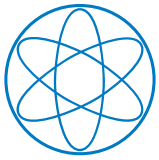

TECHNISCHE UNIVERSITÄT MÜNCHEN

TUM SCHOOL OF NATURAL SCIENCES

Microbeam radiotherapy on the path to clinical application: A powerful compact x-ray source and microbeam treatment planning

Johanna Winter

Vollständiger Abdruck der von der TUM School of Natural Sciences der Technischen Universität München zur Erlangung des akademischen Grades einer

Doktorin der Naturwissenschaften (Dr. rer. nat.)

genehmigten Dissertation.

Vorsitz:	Prof. Dr. Martin Zacharias
Prüfer der Dissertation:	1. Prof. Dr. Jan J. Wilkens
	2. Prof. Dr. Franz Pfeiffer

Die Dissertation wurde am 28.09.2022 bei der Technischen Universität München eingereicht und durch die TUM School of Natural Sciences am 12.04.2023 angenommen.

Acknowledgments

This work strongly benefited from the support of a number of people who contributed in different ways to this project and all of whom I thank sincerely. They made this work not only possible but greatly enjoyable.

I am grateful to Prof. Dr. Jan J. Wilkens, head of medical physics at the Department of Radiation Oncology at the Klinikum rechts der Isar (MRI), for sharing his broad expertise by providing valuable insights into medical physics in radiation oncology, for his motivating support, and for supervising my thesis.

Very special thanks go to Dr. Stefan Bartzsch, group leader of the Experimental Medical Physics team at the Institute of Radiation Medicine (IRM) at Helmholtz Munich, for his continuous and inspiring support, for the precious guiding throughout my thesis, for leaving me freedom to work independently, for taking time for every question and discussion, for digging deep into problems if necessary, and for giving valuable feedback to ideas, methods, scientific practice, presentations, and written texts. I really appreciate our discussions on equal terms about new and ongoing projects and his trust in my work.

I extend my gratitude to the entire µFlash collaboration team for pulling together to bring the prototype of the line-focus x-ray tube into being. Specifically, I would like to thank Prof. Dr. Kurt Aulenbacher from the Johannes Gutenberg University Mainz for taking the time to join my thesis committee meetings and for the opportunity of giving a lecture at the University Mainz. Many thanks go to Christian Petrich, Anton Dimroth, and Dr. Christoph Matejcek for the close and dedicated collaboration. Further thanks go to Prof. Dr. Marek Galek, Prof. Dr. Michael Butzek, Prof. Dr. Stephanie E. Combs, Sebastian Rötzer, Yunzhe Zhang, Mahadevan Ravichandran, Karl-Ludwig Krämer, and Prof. Dr. Markus Zimmermann. I am very much looking forward to the first x-rays emerging from our source.

Moreover, I greatly thank Dr. Dr. Kim M. Kraus from the MRI for the fruitful collaboration in starting the project of microbeam treatment planning. Thanks to Yating Zhang and Suzana Spasova for their contributions to this topic. Many thanks go to Prof. Dr. Julia Herzen and Neam Halat from the TUM as well as Dr. Emmanuel Brun from the University of Grenoble for contributing and sharing their experience in order to assess possibilities of phase contrast imaging using our novel x-ray source.

I thank the working teams Experimental Medical Physics and Radiobiology at the IRM for providing a very enjoyable working atmosphere. Particular thanks go to Mabroor Ahmed, Alexander Baikalov, Franziska Arweiler (nee Treibel), Sandra Bicher, and Jessica Stolz for our scientific discussions about the physical and radiobiological mechanisms of microbeam radiotherapy and FLASH therapy. I further thank Prof. Dr. Thomas Schmid and his working team for the insights into radiobiological studies. Thanks to Stefan, Mabroor, Sandra, and Rainer Lindner from the IRM as well as Dr. Paolo Pellicioli from the European Synchrotron Radiation Facility (ESRF) in Grenoble for teaching me how to perform preclinical microbeam experiments at our laboratory x-ray source and at the

biomedical beamline of the ESRF. Furthermore, I thank Daniel Lang for being a very pleasant office colleague and for managing the much needed server.

Further thanks go to Rainer for his always prompt support with any technical equipment as well as to Dr. Susanne Raulefs and Dr. Daniela Schilling from the MRI for their administrative support. Many thanks are sent to Stefan, Alex, Dominik Waibel, Christoph, and Christian for proof-reading my thesis.

Last but definitely not least, huge thanks go to Dominik and my family and friends for their never-ending loving support.

Abstract

Sparing healthy tissue while ensuring tumor control is a daily challenge for clinical radiation oncology because radiosensitive organs at risk often limit the effectiveness of radiotherapy against aggressive cancer types. Preclinical studies of microbeam radiotherapy (MRT) have demonstrated superior normal tissue sparing at similar tumor control rates compared to conventional radiotherapy. In contrast to homogeneous clinical dose distributions, the MRT dose distribution is characterized by a spatial fractionation on the micrometer scale, comprising peaks with a dose of several hundred Gray and valleys with a dose below the tissue tolerance. The requirements for MRT, including kilovolt (kV) x-rays from a micrometer-wide focal spot, are fulfilled at some third-generation synchrotrons. A wide clinical application, however, demands a compact MRT source that fits into conventional treatment rooms. The line-focus x-ray tube (LFxT) is a promising compact radiation source that produces an x-ray field capable of MRT by focusing an electron beam onto an extremely eccentric focal spot on a very fast rotating target.

In the first part of this work, the LFxT concept was refined and the feasibility of relevant technologies were proven for the development of an LFxT prototype for preclinical research and a more powerful LFxT for clinical MRT. Thereby, the main challenges were identified as a high heat production at the focal spot and heating of the vacuum chamber housing due to scattered electrons at the target surface. Monte Carlo simulations demonstrated that the preclinical LFxT can achieve microbeam dose distributions with a sharp, divergent peak-valley profile and markedly higher peak dose rates than present compact MRT sources. The simulated ultra-high dose rates promised the suitability of the clinical LFxT for x-ray FLASH irradiations, which might further spare healthy tissue than conventional radiotherapy with low dose rates. The high dose rates were facilitated by heat generation at the focal spot that was mainly determined by the heat capacity of the target material, allowing considerably higher electron beam powers than conventional x-ray tubes, for which heat conduction limits the beam power. Due to high electron beam intensities, scattered electrons yielded a strong heating of the vacuum chamber housing, which thus required active cooling. The heat load of the vacuum chamber housing as well as the temperature increase at the focal spot were simulated with finite element methods. Moreover, the electron beam focusing was assessed, and suitable x-ray exit windows were chosen.

To advance MRT a step further towards clinical application, the second part of this work extended microbeam treatment planning to multidirectional MRT on patient data, which enabled more realistic clinical MRT plans than with currently applied unidirectional MRT. For different patient cases, the kV MRT plans demonstrated sufficient target

coverage and sparing of organs at risk similar to conventional treatment plans with megavolt photons. The comparison of micrometer-scaled MRT dose distributions to conventional doses was facilitated by the implementation of the equivalent uniform dose (EUD). To decrease the entrance dose while conserving the target dose, clinical MRT might be applied by means of the novel microbeam arc therapy, which, however, yields EUD hotspots in regions of overlaying divergent microbeams. Cardiac gating and breathing motion mitigation will be necessary for clinical MRT as organ motion deteriorates the MRT dose distribution.

In conclusion, this work advances MRT towards clinical application by facilitating the realization of the LFxT as a compact source and by introducing novel technologies into microbeam treatment planning.

Kurzfassung

Die Krebsbehandlung verlangt eine Abwägung zwischen ausreichender Tumorkontrolle einerseits und Schonung gesunden Gewebes andererseits. Die Wirksamkeit der Strahlentherapie ist bei aggressiven Krebsarten limitiert durch nahegelegene strahlensensitive Risikoorgane. Präklinische Studien haben gezeigt, dass die neuartige Mikrostrahltherapie (MST) gesundes Gewebe besser schont als konventionelle Strahlentherapie, ohne an Tumorkontrolle einzubüßen. Im Gegensatz zu homogenen klinischen Dosisverteilungen ist die Dosisverteilung der MST charakterisiert durch eine mikrometerbreite räumliche Fraktionierung, die die Dosis in planar angeordnete Peaks mit einigen Hundert Gray und Valleys unter der Gewebetoleranz aufteilt. Die Anforderungen an das Strahlenfeld der MST, wie zum Beispiel eine mikrometerbreite Quelle der Röntgenstrahlen im Kilovolt (kV)-Bereich, werden bisher nur an wenigen Synchrotrons der dritten Generation erfüllt. Eine breite klinische Anwendung erfordert jedoch eine kompakte MST-Strahlenquelle, die in gewöhnliche Behandlungsräume passt. Eine vielversprechende MST-Quelle ist die Linienfokus-Röntgenröhre (englisch *line-focus x-ray tube*, LFxT), die den Elektronenstrahl für die Röntgenstrahl-Erzeugung zu einem extrem exzentrischen Brennfleck auf ein sehr schnell rotierendes Target fokussiert.

Der erste Teil dieser Arbeit verfeinerte das Konzept der LFxT und belegte die Funktionalität wichtiger Technologien für die Entwicklung eines Prototypen der LFxT für die präklinische Forschung sowie einer leistungsstärkeren LFxT für die klinische MST. Die größten Herausforderungen waren dabei eine hohe Wärmeentwicklung am Brennfleck und eine Aufheizung der Vakuumkammer durch gestreute Elektronen. Monte Carlo Simulationen zeigten, dass die präklinische LFxT Dosisverteilungen für die MST erzeugen kann, die ein scharfes, divergentes Peak-Valley-Profil aufweisen und eine deutlich höhere Dosisrate als bisher verfügbare kompakte MST-Quellen erlauben. Die simulierten ultrahohen Dosisraten der klinischen LFxT ermöglichten zudem eine FLASH Röntgenbestrahlung, die gesundes Gewebe besser schonen kann als konventionelle Strahlentherapie mit niedrigen Dosisraten. Die ultrahohen Dosisraten wurden dadurch ermöglicht, dass die Wärmeentwicklung am Brennfleck hauptsächlich durch die Wärmekapazität des Targetmaterials bestimmt wurde. Diese Art der Wärmeentwicklung ermöglichte eine wesentlich höhere Leistung des Elektronenstrahls der LFxT als bei konventionellen Röntgenröhren, bei denen die Wärmeleitfähigkeit des Materials die Elektronenstrahlleistung limitiert. Um der hohen Intensität des Elektronenstrahls standzuhalten, benötigte die Vakuumkammer eine aktive Kühlung, um der Wärmebelastung durch gestreute Elektronen entgegenzuwirken. Diese Wärmebelastung der Vakuumkammer sowie die Temperaturerhöhung am Brennfleck wurden mit Finite-Elemente-Methoden simuliert.

Zudem wurde die Fokussierung der Elektronen auf den Brennfleck untersucht und passende Röntgenaustrittsfenster ausgesucht.

Der zweite Teil dieser Arbeit zeigt einen weiteren Ansatzpunkt auf dem Weg zur klinischen Anwendung der MST: Die Bestrahlungsplanung wurde um multidirektionale MST auf Patientendaten erweitert, womit die MST-Pläne klinisch realistischer wurden als mit der derzeitigen unidirektionalen MST. Für verschiedene Bestrahlungsszenarien erreichten die MST-Pläne mit kV-Photonen eine ausreichende Dosisabdeckung der Zielvolumina und eine Schonung von Risikoorganen, die vergleichbar war mit konventionellen Bestrahlungsplänen mit Megavolt-Photonen. Der Vergleich von MST-Dosisverteilungen in Mikrometer-Auflösung zu konventionellen Dosisverteilungen wurde durch die Implementierung der homogenen Äquivalenzdosis (englisch *equivalent uniform dose*, EUD) ermöglicht. Für eine verringerte Eintrittsdosis bei gleichbleibender Dosis im Zielvolumen könnte die klinische MST mit der neuartigen Mikrostrahl-Arc-Therapie appliziert werden, wobei allerdings die Überlagerung von divergenten Mikrostrahlen zu EUD-Hotspots führt. Für die klinische MST verwaschen innere Organbewegungen die MST-Dosisverteilung, sodass Herz-Gating und Maßnahmen zur Einschränkung der Atembewegungen nötig werden.

Zusammenfassend bringt diese Arbeit die MST zwei Schritte weiter in Richtung klinische Anwendung: zum einen durch die Weiterentwicklung der LFxT als kompakte MST-Quelle, zum andern durch die Einführung neuer Techniken in die MST-Bestrahlungsplanung.

Contents

Part I.

Introduction

1. Introduction

1.1. Radiotherapy

Cancer is one of the leading causes of death worldwide [1]. Treatment measures and attempts are built on the three pillars of surgical resection, radiotherapy, and systemic therapies such as chemotherapy or immunotherapy, applied exclusively or combined. Approximately half of all cancer patients receive radiotherapy in a curative or palliative treatment, utilizing the advantages of targeted treatments and a possible preservation of the organ functionality [2]. While modern treatment strategies achieve cure rates of 50–90 % for some cancer types, e.g., breast cancer or Hodgkin's lymphoma, the five-year survival rate for other cancer types, such as locally advanced lung cancer or glioblastoma multiforme, is below 5 % [2, 3]. New treatment strategies for these cancerous tumors with poor prognosis are therefore urgently needed.

For effective tumor control, the ability of tumor cells to proliferate must be inhibited and all tumor stem cells must be destroyed according to the conventional concept of radiation oncology [2]. For that purpose, radiotherapy utilizes ionizing radiation that induces DNA damage directly or indirectly via free radicals formed in close-by water [2]. The ability of cells to proliferate after being irradiated can be measured by colony formation assays. Thereby, the clonogenic survival fraction S is assessed in-vitro after a radiation dose D of 1–10 Gy and described according to the linear quadratic model (LQM) as

$$S = \exp\left(-\alpha D - \beta D^2\right). \tag{1.1}$$

The radiobiological factors α and β describe the sensitivity of the cells to the applied radiation and characterize the linear and the quadratic part of the damage, respectively, where α can be interpreted as a lethal damage induced by a single radiation particle and β by multiple particles [4–6]. Favored for therapy, the differential effect says that tumor cells are more sensitive to radiation with a lower survival fraction than normal cells at the same dose.

For in-vivo studies, tumor control or normal tissue side effects are more useful endpoints than the survival fraction. Based on Poisson statistics, the dose response curves follow a sigmoidal shape for both the tumor control probability and the normal tissue complication probability [4]. For successful treatments, a trade-off must be found that provides ablation of the tumor on the one hand and sparing of healthy tissue, especially of radiosensitive organs at risk, on the other hand. The so-called therapeutic window designates the dose range where this differential effect is fulfilled.

Innovations in radiotherapy have often been associated with a widening of the therapeutic window by physical, biological, or biophysical measures. Physical measures include the dose conformity to the tumor shape, multidirectional irradiations, and more advanced intensity-modulated radiotherapy or volumetric-modulated arc therapy. Biologically, the therapeutic window was widened by the introduction of temporal fractionation and the combination of radiotherapy with systemic therapies. A biophysical widening has been achieved by proton and heavy ion therapy with an increased radiobiological effectiveness and a finite particle range. A spatial fractionation of the radiation field, in other words a spatially highly modulated dose distribution, can also lead to a biophysical widening of the therapeutic window, as described hereafter.

1.2. Microbeam radiotherapy

The historical origin of spatially fractionated radiotherapy lies in the grid therapy that was developed and applied by Alban Köhler in the first decade of the 20th century [7, 8]. He installed a millimeter-thick iron grid on the skin of radiotherapy patients and observed less necrotic skin burns and a faster cure of the skin than after treatments without the grid. Grid therapy has been clinically applied for treatments and palliative irradiations of large malignant tumors with kilovoltage and megavoltage x-rays [8–11]. The observed skin protection originated from the dose-volume effect: Healthy tissue tolerates a higher radiation dose if the irradiated volume is smaller [12]. In the 1950s and 1960s, the dose-volume effect was rediscovered, when an extremely high dose of 4000 Gy delivered by a 25 µm-wide deuteron beam was well tolerated by a mouse brain, while a dose of 160 Gy delivered by a 1 mm-wide beam induced severe brain necrosis [13]. Thirty years later with the development of powerful synchrotron and cyclotron radiation facilities, research of spatially fractionated radiotherapy was resumed. Nowadays, main development fields of spatially fractionated radiotherapy comprise grid and lattice radiotherapy with a dose modulation on the centimeter scale using x-rays or protons [11, 14, 15]; x-ray, proton, and light-ion minibeam radiotherapy with a dose modulation on the (sub-)millimeter scale [16–19]; and x-ray microbeam radiotherapy (MRT) with a dose modulation on the micrometer scale [20–22], which is the focus of this work.

The dose distribution of MRT is divided into a linear, periodic array of narrow high-dose beamlets, called peaks, and wider low-dose regions, called valleys, as depicted in figure 1.1. While the peak dose amounts to several hundred Grays, the valley dose stays below the tissue tolerance. Accordingly, the peak-to-valley dose ratio (PVDR) is commonly in the range of 20–50 for preclinical experiments [22–24]. Although there have been preclinical studies with peak widths of 25–100 µm and center-to-center spacings between neighboring peaks in the range of 200–800 µm, the biologically most effective geometrical setup has not been comprehensively evaluated [22, 25, 26]. For this work, a peak width of 50 µm and a center-to-center spacing of 400 µm were chosen in accordance with several effective preclinical MRT experiments [27–30]. Very high dose rates allow for preclinical or prospective clinical irradiations without blurring of the micrometer-

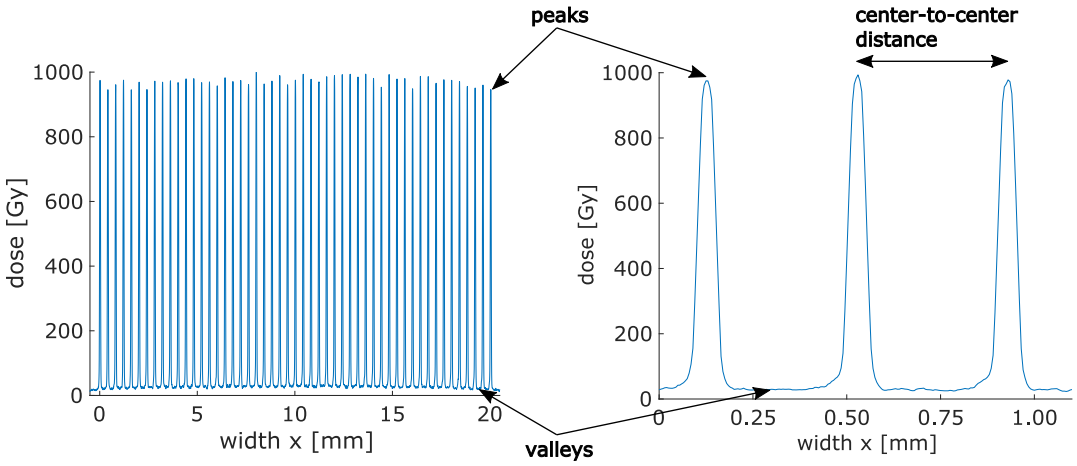

Figure 1.1.: Microbeam dose profile of high-dose peaks and low-dose valleys with a center-to-center distance of 400 µm. The profile is extended into the image plane to form a linear array perpendicular to the beam direction.

scaled dose distribution due to organ motion, such as breathing or cardio-synchronous pulsation of blood vessels.

In-vitro MRT studies demonstrated a higher dose resistance of normal cells compared to conventional homogeneous irradiations; for tumor cells in contrast, similar effects were observed for MRT and conventional irradiations [31–34]. Likewise, less severe side effects were observed in normal tissue after preclinical MRT compared to conventional radiotherapy, whereas tumor response was similar or even stronger following MRT [35–37]. Translational studies have mainly focused on phantom dosimetry [38–40], while veterinary trials have started [41], and first treatment planning studies on clinical patient data have been published [42, 43]. Most MRT studies compared the valley dose to the dose of conventional irradiations due to an observed correlation regarding the biological effects. However, there is evidence that the valley dose is not equivalent to a homogeneous dose but the peak dose and the spatial dose distribution also need to be considered [23, 24, 44, 45].

Possible candidates for human clinical trials include locally advanced lung cancer or highly malignant tumors of the central nervous system, such as glioblastoma multiforme, or pediatric diffuse intrinsic pontine glioma, which are all associated with a poor prognosis and no reliable curative treatment [37, 44, 46]. Prior to clinical trials, there are several challenges to be met: A more thorough understanding of the radiobiological effects of MRT (see section 1.3) can improve clinical treatments by prescribing an optimal dose distribution as a compromise between tumor toxicity and normal tissue sparing [26, 44]. The treatment geometry of multiport irradiations, a combined spatio-temporal fractionation, and concurrent systemic therapies need to be investigated [28, 29, 47, 48]. Moreover, widely available and affordable MRT sources are required not only for clinical trials but also for preclinical MRT research (see section 1.4) together with an

appropriate treatment planning system (see section 1.5) and with a precise and reliable patient positioning system [22, 48].

1.3. Radiobiological effects of microbeam radiotherapy

Even though the radiobiological mechanisms of MRT have not been fully understood, many studies have shown a better tolerance of normal tissue following MRT compared to conventional radiotherapy at similar tumor control rates. It has been suggested that the therapeutic window is widened after MRT by differences in the cellular architecture and the vascular structure of healthy and tumorous cells as well as by a tailored immune response, by intercellular communication, and by dose rate effects.

Crosbie et al. [31] observed a better repair of MRT-induced damage by normal cells with a more regular architecture than by tumor cells that have a stronger migration. Tumor blood vessels are faster growing, immature, and lower in density; furthermore, they have larger diameters and a more tortuous structure than vessels in healthy tissue. Following MRT, the blood supply and the oxygen saturation in tumors are reduced, leading to hypoxia, as the damage to the immature vessels cannot be effectively repaired [49, 50]. Conversely, lesions in normal blood vessels are rapidly repaired from adjacent unirradiated tissue and neither the capillary density, the vascular permeability, the perfusion, nor the blood volume decreases after MRT [49, 50]. Unimpaired blood vessels allow the transportation of vital nutrients but also of immune cells.

The immune system is pivotal for an effective cancer therapy, but tumor cells develop strategies to escape the immune response. Both MRT and conventional radiotherapy can recruit immune cells to the tumor; they, however, induce different molecular pathways related to inflammation and immunity [32, 51]. While conventional radiotherapy destroys most immune cells in the irradiated tissue, MRT leads to immunogenic cell death only in the peaks and spares the immune cells in the valley region. Thereby, the immune system has a larger surface to react after MRT. Different inflammation and immune response pathways after MRT and conventional radiotherapy have demonstrated their importance regarding the widened therapeutic window of MRT but still need further investigation [51–54].

The response of non-targeted tumor cells relies not only on immune effects but also on intercellular communication through gap junctions and a release of inflammatory factors [55]. For both normal and tumor cells, radiation-induced stress has been observed as micronuclei formation or cell killing in non-irradiated bystander cells close to directly irradiated cells [56–58]. Surprisingly, these out-of-field effects can also occur without direct cell-cell contact but by transferring the medium from irradiated to non-irradiated cells in-vitro [58]. Abscopal or long-range radiation effects have likewise been observed in-vivo and clinically [55]. Even though it is not yet clarified if the intercellular communication has a positive or negative effect on tumor killing and healthy tissue sparing, Steel et al. [34] assumed a lower sensitivity to bystander signaling by their investigated normal cells than by the tumor cells.

Most MRT research has been performed at ultra-high dose rates at third-generation synchrotrons. Ultra-high dose rates can induce the FLASH effect, which, similarly to MRT, decreases normal tissue damage without compromising tumor control (details on the FLASH effect can be found in chapter 8). For this reason, a widening of the therapeutic window following ultra-high dose rate MRT can be associated with the spatial fractionation, dose rate effects, or a combination thereof. However, beneficial MRT effects compared to conventional radiotherapy have also been observed in absence of the FLASH effect [34, 59, 60]. In this work, the focus lies on MRT, disregarding but not dismissing the FLASH effect.

1.4. Radiation sources for microbeam radiotherapy

The characteristic peak-valley dose profile of MRT is typically shaped by a multislit collimator that blocks the radiation in the region of the valleys and lets the radiation pass through in the region of the peaks. For a minimal valley dose, the collimator must be sufficiently thick to absorb basically all x-ray energy. At the same time, the collimator slits must be aligned to the radiation source for a high peak dose and steep penumbras, i.e., steep lateral dose falloffs from the peaks to the neighboring valleys. Both parallel and divergent collimators have been developed for parallel and divergent microbeam radiation fields [59, 61].

A sharp microbeam dose profile with a high PVDR and steep penumbras put high requirements on the radiation source. The ideal x-ray energy is at approximately 100 keV, hence considerably lower than for conventional radiotherapy in the megaelectronvolt range [38, 62]. A higher energy increases the range of the secondary electrons, which would blur the peak-valley profile and increase the valley dose. A lower energy yields a steeper depth dose curve, which impedes reaching deep-seated tumors and also increases the range of secondary electrons by a higher portion of photoelectrons compared to Compton electrons. The radiation field should have a low divergence and originate from a small focal spot to achieve steep penumbras and preserve a sharp microbeam dose profile in several centimeters depths, which is especially important for deep-seated tumors in preclinical and clinical MRT [63]. Lastly, high dose rates, ideally in the range of kGy/s, can avoid blurring of the micrometer-scaled dose distribution due to organ motion.

These physical requirements are well fulfilled at certain large third-generation synchrotrons worldwide, such as the European Synchrotron Radiation Facility (ESRF) in Grenoble, France, or the Australian Synchrotron in Melbourne, Australia. Originating from high-energy electrons in the synchrotron storage ring, the most appropriate x-ray source for MRT is a wiggler, which produces synchrotron radiation with a continuously high photon flux in a centimeter-wide fan beam [22]. The biomedical beamline ID17 at the ESRF delivers a quasi-parallel radiation field with a median x-ray energy of 107 keV and dose rates of up to 16 000 Gy/s [52, 64]. Located at 40 m from the source, the beam size is $40 \times 1\,\mathrm{mm}^2$ at the maximum [65], while larger field sizes can be achieved by a

vertical scanning of the sample through the beam, leading to effective dose rates of a few hundred Grays per second [66]. Besides the rather small field size, the main disadvantage of MRT at these specialized synchrotron beamlines is the scarce availability and the associated limited and expensive beam time. Furthermore, these synchrotrons are pure research facilities, not allowing an adequate patient care that is comparable to radiotherapy clinics. For this reason, compact MRT sources that fit into a research laboratory or a typical treatment room are urgently required for widely available MRT research, for prospective clinical trials, and definitely for clinical routine of MRT.

Widely discussed alternatives to synchrotrons are inverse Compton scattering sources with a diameter of a few meters, in contrast to third-generation synchrotrons with diameters of a few hundred meters. In inverse Compton scattering sources, high-energy electrons scatter at low-energy photons in the infrared range and transfer a portion of their energy to the photons, the energy of which gets thereby elevated to the x-ray regime [67, 68]. Advantages of inverse Compton scattering sources for MRT are a small source size and a low divergence. However, the photon energy has only reached 35 keV, which limits MRT to superficial irradiations, and the dose rate is in the range of Grays per minute [22, 67]. Preclinical MRT studies have been performed at the Munich compact light source (built by Lyncean Technologies Inc., Fremont, USA) with a peak dose rate of 4 Gy/min [27]. Despite further developments of inverse Compton scattering sources with increased x-ray energies up to 90 keV, e.g., at the ThomX project [69], dose rates remain too low for clinical MRT with centimeter-large field sizes [22].

A different type of x-ray source that has been suggested for MRT is the carbon nanotube field emission x-ray technology. Thereby, the cathode consists of carbon nanotubes, which are cylindrical carbon compounds with a thickness of 1–50 nm and a length of up to 20 cm [70]. In the cathode, heat raises the energy level of the electrons, and an extraction grid induces a strong electric field at the nanotube surface. Thereby, electrons tunnel out of the cathode and are accelerated towards the anode, where x-rays are produced. Hadsell et al. [71] presented a carbon nanotube prototype for MRT research, which provided a 160 kVp x-ray spectrum, a peak dose rate of 2 Gy/s, and a microbeam dose profile with a peak width of 300 µm and a PVDR of 17 at a depth of 13 mm. The peak width classifies the presented setup rather as minibeam instead of microbeam radiotherapy.

Additionally, several types of x-ray tubes with classic thermionic cathodes have been investigated for their applicability for MRT. At thermionic cathodes, the electron energy is lifted above the binding energy by a very high heat induction so that the electrons leave the cathode and are accelerated to the anode by an electric field. As for carbon nanotube field emission x-ray tubes, x-rays are produced by bremsstrahlung and characteristic x-rays at the focal spot at the anode. For a high x-ray energy output, the atomic number Z of the anode must be high as the electron-to-photon conversion efficiency η can be estimated by

$$\eta = 10^{-3} \cdot Z \cdot U\,, \tag{1.2}$$

where U is the electron acceleration voltage in megavolts. Only approximately 1 % of the electron energy is transferred into x-radiation, while the remaining energy is converted into heat. Accordingly, tungsten is a typical anode material having a high atomic number ($Z = 74$) and a high melting temperature. In clinical routine, x-ray tubes are mainly used for imaging. High-power x-ray tubes, which are integrated in computed tomography (CT) systems, have a rotating anode to distribute the heat at the focal spot over a large focal track area. These conventional x-ray tubes have the advantages of a large radiation field and a broad energy range. Disadvantages regarding MRT include a low flux and a large focal spot size of typically 1 mm^2. Several preclinical x-ray tubes have been modified to perform MRT research [59, 72, 73]; however, the dose rate does not exceed a few Grays per minute. Microfocus x-ray tubes operate in a similar way as conventional x-ray tubes, although focal spot dimensions below 5 µm have been achieved with thermionic cathodes and carbon nanotube cathodes [74, 75]. A low output power below 10 W prevents the anode of microfocus x-ray tubes from overheating, which, however, yields a low photon flux. An x-ray tube with a different anode type is the liquid-metal jet x-ray tube. The accelerated electrons produce photons in a jet of liquid tin or gallium, resulting in a bremsstrahlung spectrum of typically below 50 kVp with characteristic x-rays of a lower energy compared to tungsten anodes [76, 77]. Although the focal spot is small and the flux is high, the x-ray energy is too low for preclinical or clinical MRT.

A few years ago, Bartzsch and Oelfke [63] published the idea of the line-focus x-ray tube (LFxT), which is based on conventional x-ray tube technology with a thermionic cathode. The unique features of the LFxT are an extremely eccentric focal spot and a very fast rotating target, enabling very high dose rates from a very narrow x-ray source as well as a broad energy range. The LFxT has not been built so far but has great potential for preclinical and clinical MRT. The elaboration and further development of the LFxT technology are the focus of this work in chapters 3 to 8.

1.5. Microbeam treatment planning

Clinical planning of radiotherapy with megaelectronvolt photons relies on three-dimensional CT images that typically have a resolution of 0.1–1 mm in the transversal plane and a slice thickness of 0.5–5 mm [78]. The resolution of clinical treatment plans is often even down-sampled to 2.5 mm in each spatial direction for a faster dose calculation [79]. Conversely, a fully resolved dose distribution of MRT would require a resolution of few micrometers, at least in the direction of the peak-valley profile. For that purpose, clinical CT data cannot provide sufficient details and the treatment planning process would require much higher computational power than currently used. Consequently, alternative approaches are needed for microbeam treatment planning.

Most MRT dose calculation has been performed by using Monte Carlo simulations [22, 40, 80], which approximate physical processes by statistical methods, e.g., interaction probabilities of radiation with matter. On the one hand, millions or billions of primary

particles are needed for low uncertainties according to the law of large numbers so that Monte Carlo-based treatment planning takes longer than analytical treatment planning even with high-performance computers. On the other hand, Monte Carlo-based treatment plans provide a more precise dose distribution, especially at strong density heterogeneities in the phantom or patient, compared to fast pencil beam algorithms [79]. Moreover, Monte Carlo algorithms provide an accurate dose calculation over a large dose range, which is required for MRT fields with a high PVDR, and, furthermore, a flexible choice of physics models, which needs to be carefully made for the kiloelectronvolt-radiation of MRT [22]. Kiloelectronvolt x-rays are often multiply scattered before they deposit their energy via secondary electrons, in contrast to megaelectronvolt x-rays. A main drawback of MRT planning with Monte Carlo algorithms is the small voxel size in the micrometer range, which requires an extremely high number of primary particles and very high computational power. Analytical dose calculation based on convolution kernels has been applied by few authors for MRT planning [81, 82]; however, uncertainties were higher than with Monte Carlo-based algorithms, especially in the valley regions.

Combining the advantages of both Monte Carlo-based and kernel-based dose calculation was implemented by Donzelli et al. [62], who developed a hybrid dose calculation approach: The photon interactions are simulated by a Monte Carlo algorithm, yielding primary and scatter dose distributions of not spatially modulated radiation fields on the CT resolution. The kernel-based algorithm introduces the dose modulation on the micrometer scale as peaks and valleys. The hybrid dose calculation is described in more detail in chapter 9, and modifications for a clinical MRT planning can be found in chapter 10.

The few existing MRT planning studies for veterinary trials or on patient data reported the peak and valley dose distribution as well as the PVDR at specific locations [41, 42, 83], similar to preclinical and phantom studies. However, a standard to report these doses has not been established, e.g., whether to use the maximum peak dose or the mean peak dose within a certain width. For multidirectional MRT, peak and valley regions are not even clearly defined as beams are crossing and form complex dose distributions on the micrometer scale. As a starting point, the equivalent uniform dose (EUD) [84] has been suggested to interpret spatially fractionated dose distributions of MRT [85], in analogy to dose modulations on larger scales, e.g., for intensity-modulated radiotherapy plans [86]. Based on the LQM, the EUD concept says that two dose distributions are equivalent if they have the same clonogenic survival. The implementation of the EUD into microbeam treatment planning is described in chapter 10. Nevertheless, the applicability of the EUD for MRT still needs to be verified experimentally.

2. Aims of the thesis

The long-term vision of this project is the translation of microbeam radiotherapy (MRT) to clinical application. Prior to clinical trials, several research fields need to progress the knowledge and the technology of radiobiology, radiation sources, and treatment planning for MRT. This work focuses on answering two physics-based challenges thereof: The advancement of the line-focus x-ray tube (LFxT) as a compact MRT source is described in chapters 3 to 8 in part II, while chapters 9 to 12 in part III deal with the ongoing development of microbeam treatment planning.

The basic idea of the LFxT had been previously published and is based on a strongly eccentric focal spot and a very fast rotating target. Thereby, the heat capacity of the target material dominates the heat dissipation at the focal spot, allowing considerably higher electron beam power densities than conventional x-ray tubes, for which heat conduction dominates the heat dissipation and thus determines the focal spot temperature. The concept of the so-called heat capacity limit had been demonstrated with one-dimensional calculations, and the required power supply of the LFxT had been estimated to facilitate ultra-high dose rates.

My aim of part II is to elaborate the LFxT technology as an MRT source and to ascertain the technical prerequisites for its construction. The development is focused on a prototype for preclinical research as a proof of the LFxT concept, but throughout this work, required technology adjustments are investigated for a prospective, more powerful LFxT for clinical application of MRT. Part II is structured according to the functionality of the x-ray tube, starting from the desired microbeam radiation field and moving backwards to the electron source.

In chapter 4, I validate the suitability of the dose distribution and dose rate emerging from the LFxT for preclinical and clinical MRT by using numerical simulations. The micrometer-scaled spatially fractionated dose distribution puts high demands on the x-ray source. I investigate these demands regarding the x-ray spectrum, the size of the focal spot, and the distance from the focal spot to the multislit collimator that shapes the homogeneous radiation field into microbeams. Furthermore, I compare the simulated microbeam radiation field from the LFxT to that originating from a third-generation synchrotron, the most advanced state-of-the-art MRT source. Besides the spatial dose fractionation, I assess achievable dose rates considering the designed power supplies for both the preclinical and the clinical LFxT. Complementarily, I suggest materials for the x-ray exit window regarding their x-ray absorption and mechanical properties in chapter 7.3.

Due to the low electron-to-photon conversion efficiency, the location of the focal spot is exposed to a very high heat load even for conventional x-ray tubes and thus all the

more for the high-power, strongly focused electron beam of the LFxT. To cope with the extremely high heat load, the LFxT utilizes the heat capacity limit by means of the combination of a very fast rotating target and a strongly eccentric focal spot. In chapter 5, I analytically assess the heat capacity limit and substantiate this concept with three-dimensional numerical simulations for the preclinical and the clinical LFxT. I determine the temperature increase at the focal spot for the heat conduction limit, the heat capacity limit, and the transition between these limits.

At the focal spot, the electron energy is not completely transferred into x-radiation and heat, but a substantial part is transported to the vacuum chamber housing by electrons that are backscattered from the target surface. In chapter 6, I investigate the energy of the backscattered electrons that is absorbed at the vacuum chamber housing of the preclinical LFxT as well as its resulting temperature increase. Thereby, I verify the adequacy of the cooling system of the LFxT.

The development and realization of a novel x-ray source is only possible with a team of scientists with different areas of expertise. My collaboration projects in this work include the cooling concept of the preclinical LFxT prototype in chapter 6, the development of the electron accelerator and beam optics of the preclinical LFxT in chapter 7.1, the investigation of a magnetic deflection system of the electron beam to protect heat-sensitive components in the vacuum chamber in chapter 7.2, and concepts of the power supply for the clinical LFxT in chapter 8.

Chapter 8 discusses aspects that are still required for getting the LFxT prototype into operation and for the experimental validation of the LFxT technology. After successfully validating the proof of concept, the technology needs to be upscaled for a clinically applicable MRT, for which I outline major redevelopments and possible solutions. Moreover, the LFxT might enable x-ray FLASH irradiations, where ultra-high dose rates can widen the therapeutic window compared to conventional radiotherapy with lower dose rates, with a compact source. An additional application of the LFxT might be simultaneous phase contrast imaging of high- and low-density objects, which I discuss at the end of chapter 8.

The aim of part III is the advancement of microbeam treatment planning by creating more realistic clinical MRT plans than the unidirectional MRT plans typically applied on preclinical targets. In chapter 10, I develop an algorithm framework that enables the investigation of dose distributions resulting from different microbeam treatment geometries, including multiport MRT, on clinical patient data as well as the comparison to clinically planned dose distributions. Applying irradiations from several directions is standard for conventional radiotherapy to spread the entrance dose over a larger volume. However, multiport MRT raises the question of how to align microbeams from different directions. I implement interlaced MRT, which intends a homogeneous target dose, as well as peak-on-peak and cross-firing MRT, which maintain a strong dose modulation in the target volume. Furthermore, I demonstrate microbeam arc therapy in chapter 11 as a novel approach to spread the entrance dose. Independent of the geometry, multiport MRT forms a dose distribution on the micrometer scale even more

complex than a regular peak-valley profile that follows from typical unidirectional MRT. For clinical application, the equivalence of a spatially fractionated dose distribution to a conventional homogeneous dose remains to be specified. The equivalent uniform dose (EUD) is a concept of assigning a highly modulated dose to a homogeneous dose distribution yielding the same radiobiological effect. In chapter 10, I implement the EUD into a dose calculation algorithm to allow the evaluation of multiport MRT plans and the comparison to conventional radiotherapy plans. A further challenge for clinical MRT is organ motion due to breathing or cardio-synchronous pulsation of blood vessels, which can deteriorate the micrometer-scaled dose distribution. Chapter 12 presents analyses of the effects of motion on the MRT dose distribution and possible countermeasures.

Finally, part IV summarizes the main achievements of this work and gives a short outlook on the LFxT as a compact MRT source and on microbeam treatment planning.

Part II.

The line-focus x-ray tube (LFxT) as a compact microbeam source

3. Introduction to the LFxT

A promising compact radiation source for clinical application of microbeam radiotherapy (MRT) is the line-focus x-ray tube (LFxT) [63]. The LFxT is based on conventional x-ray tube technology for medical imaging with an electron beam of high acceleration voltage and high power hitting a target, where x-rays are produced by bremsstrahlung and characteristic x-rays. As for other microbeam sources, a multislit collimator shapes the homogeneous x-ray field into microbeams, where the slits have the same divergence as the radiation field, as described by Bartzsch et al. [59] or Treibel et al. [73]. For MRT, the electrons have an energy of several hundred kiloelectronvolts as a good tradeoff between a shallow slope of the depth-dose curve in the patient and a short range of secondary electrons for a sharp peak-valley microbeam dose profile [22, 87]. Similar to conventional, high-energy x-ray tubes, the target surface is made of a tungsten-rhenium alloy due to a high electron-to-photon conversion efficiency, a ductile material behavior, a high specific heat capacity, and a high melting temperature. The focal spot must be as narrow as the slits of the multislit collimator, i.e., in the micrometer range, to ensure a sharp peak-valley dose profile, small penumbras, and a low divergence of the beam core behind each collimator slit (see chapter 4, Bartzsch and Oelfke [63], and Winter et al. [87]). Contrary to conventional x-ray tubes, the vacuum chamber housing is not on electrical ground potential but on the same potential as the target. In this way, the whole vacuum chamber acts as the anode and backscattering electrons from the target travel on straight paths to the chamber housing instead of returning to the target surface off the focal spot (see chapter 6 and Winter et al. [88]).

Even conventional x-ray tubes need to cope with high heat loads due to an electron-to-photon conversion efficiency at the target of approximately 1 %. High-power x-ray tubes, e.g., for computed tomography, typically have a rectangular electronic focal spot with its short dimension in the rotation direction of an angled, rotating target to spread the heat load at the focal spot to a larger area, the so-called focal track [89, 90]. Additionally, cooling is applied at the target or the vacuum chamber housing [78].

The LFxT should deliver dose rates markedly higher than conventional x-ray tubes so that rotating the target does not sufficiently distribute and dissipate the very high heat load. For this reason, the LFxT has two unique characteristics: a very high target surface velocity (200 m/s) and an extremely eccentric focal spot, from which the name of the line-focus x-ray tube deduces. The eccentric focal spot has two advantages. First, incorporating the requirement of a focal width in the micrometer range, the heat load at an eccentric focal spot is distributed over a larger area compared to a squared focal spot, similar to but more pronounced than conventional rectangular focal spots. Thereby, the electron beam power can be considerably increased, assuming a constant maximum

surface power density defined by the melting temperature of the focal track material. Second, the combination of a very narrow focal spot in the micrometer range and a very fast rotating target shifts the physical characteristics of the heat dissipation from mainly heat conduction to mainly heat capacity. This heat capacity limit allows considerably higher electron beam power densities than the heat conduction limit that holds for conventional x-ray tubes (see chapter 5, Bartzsch and Oelfke [63], and Winter et al. [88]).

The LFxT development that is presented in this work comprises planning studies for a high-power clinical LFxT (1.5 MW) and a prototype (90 kW) for preclinical MRT studies. Figure 3.1 displays the computer aided design (CAD) model of the prototype, which is currently under construction at the Technical University of Munich. The LFxT prototype has been developed together with several collaboration partners from the Technical University of Munich, the Forschungszentrum Jülich, the Johannes Gutenberg University Mainz, and the University of Applied Sciences Munich. The investigations of the clinical and the preclinical LFxT included ideal and achievable microbeam radiation fields by varying x-ray beam parameters (chapter 4), the heat dissipation at the focal spot in the heat conduction limit and the heat capacity limit (chapter 5), as well as the consequences of backscattering electrons that hit the vacuum chamber housing (chapter 6). Chapter 7 presents the development of a suitable electron accelerator, investigations of a magnetic electron deflection system between the accelerator and the target, as well as possible x-ray window materials. Further development projects for both the preclinical and the clinical LFxT, and additional applications of the LFxT as a source for x-ray FLASH treatments and phase contrast imaging are discussed at the end of this part.

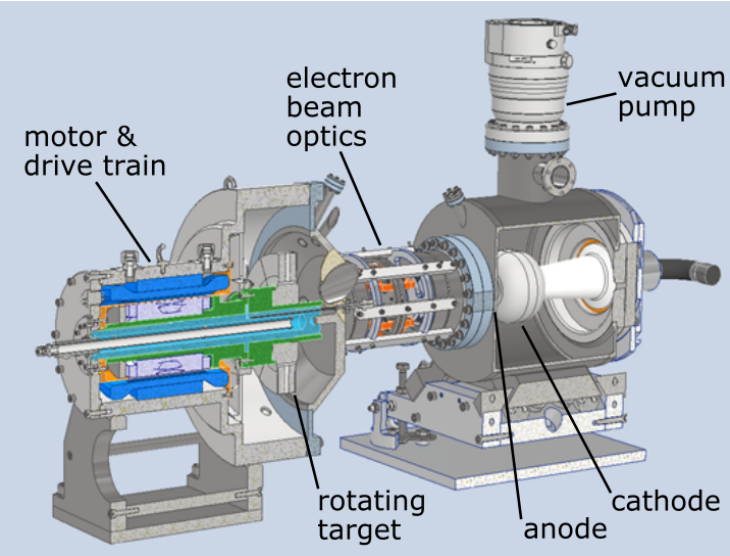

Figure 3.1.: Construction model of the line-focus x-ray tube. The electron beam is accelerated from the cathode through the anode and electron beam optics onto the target. The left part of the tube contains the motor for the target rotation.

4. Microbeam radiation field

4.1. Introduction

Microbeam radiotherapy (MRT) has proven a sparing of healthy tissue without compromising tumor response compared to conventional radiotherapy. To achieve this benefit of MRT, the spatially fractionated dose distribution requires a low valley dose, a high peak-to-valley dose ratio (PVDR), and steep lateral penumbras from the peaks to the neighboring valleys [22, 44]. Considering ray optics only, a multislit collimator subdivides a homogeneous radiation field from a point source into a microbeam field with rectangular peaks and zero valley dose at any distance from the collimator. Small-angle photon scattering at the inner surfaces of the collimator as well as photon and electron scattering in the sample increase the valley dose and smear the dose distribution to a peak-valley profile as seen in figure 1.1.

Simulation studies of monoenergetic x-ray beams revealed an optimal energy for preclinical MRT of approximately 100 keV to obtain short ranges of secondary electrons for steep penumbras [38, 62]. For this energy, Compton scattering dominates, which transfers only a portion of the photon energy to the secondary electrons. On one side, Compton electrons from photons of higher energy have longer ranges. On the other side, photons of lower energy have a higher interaction probability of photoelectric absorption, which transfers a higher portion of the photon energy to the secondary electrons, also leading to longer electron ranges and thus less steep lateral penumbras and lower PVDRs. The line-focus x-ray tube (LFxT), which might be a suitable compact radiation source for preclinical and clinical MRT, produces a continuous bremsstrahlung spectrum with characteristic x-rays from a target made of tungsten. Therefore, the optimal electron acceleration voltage and a suitable filtering, which reduces the portion of low-energy photons, need to be found.

For preclinical and clinical MRT, the sharp peak-valley dose profile needs to be preserved throughout the irradiated volume. For geometric reasons, this can be achieved by a parallel radiation field and by a focal spot as narrow as the slit width of the multislit collimator, which determines the peak width [63]. Most MRT experiments have been performed with quasi-parallel x-ray beams from certain third-generation synchrotrons, e.g., at a distance of approximately 40 m from the photon source at the biomedical beamline ID17 at the European Synchrotron Radiation Facility (ESRF) in Grenoble, France [52]. In contrast, the short beam path of the compact LFxT yields a divergent radiation field, the consequences of which on the microbeam dose distribution need to be investigated. For simulations, the most simple shape of a focal spot is a rectangle with homogeneous x-ray intensity, while realistic focal spots can have different

shapes and intensity distributions, such as Gaussian distributions. For this reason, the realistic focal spot of the LFxT needs to be simulated and the resulting microbeam dose distribution assessed.

Besides the spatial fractionation, MRT requires high peak dose rates to avoid blurring of the micrometer-scaled dose distribution due to organ motion (see chapter 12, Duncan et al. [91], and Manchado de Sola et al. [92]). Consequently, the dose rate is relevant for the performance of the LFxT and needs to be optimized in accordance with the technical feasibility.

This chapter investigates the microbeam radiation field of the LFxT. The microbeam dose distribution was optimized for a high PVDR and a sharp peak-valley dose profile with regard to the x-ray spectrum, the focal spot size, and the distance from the focal spot to the sample, which was placed contiguously behind the multislit collimator. Furthermore, the absolute dose rate of the LFxT was estimated, and the relative dose rate was simulated for different incident angles of the electron beam impinging onto the target and for different x-ray emission angles. Finally, the microbeam dose distribution was assessed for a realistic electron beam of the LFxT and compared to a microbeam dose distribution measured at the ID17 at the ESRF.

4.2. Methods

The microbeam radiation field was investigated with Monte Carlo simulations in Geant4 [93] and TOPAS [94], and the resulting dose-to-medium distributions and dose rates were analyzed using Matlab (version R2018b, The MathWorks Inc., USA). The dose distributions were scored in a water phantom located contiguously behind a multislit collimator with a slit width of 50 µm and a center-to-center distance between neighboring slits of 400 µm. The collimator slit width, termed also the theoretical peak width at the phantom surface, and the center-to-center distance were specified at the rear side of the collimator seen from the electron source, i.e., at the interface between the collimator and the phantom.

The definitions of the peak width, the valley width, the center-to-center distance, the penumbras, and the full widths at half maximum (FWHM) are depicted in figure 4.1. The center-to-center distance stated the distance between the respective center positions of two neighboring peaks, which was constant across the radiation field at a specific depth and widened with increasing depth in the phantom according to the field divergence. The dose of a single peak was defined as the mean dose within the central 60 % of the theoretical peak width, i.e., 30 µm at the phantom surface, whereby the theoretical peak width widened in the phantom according to the field divergence. The dose of a single valley was defined as the mean dose within the central part of the valley with a width 40 % of the center-to-center distance, i.e., 160 µm at the phantom surface, and also widening according to the field divergence. The lateral penumbra denoted the dose falloff from 80 % to 20 % of the mean dose of the individual peak in the x-direction, i.e., in the direction of the strong dose modulation. The longitudinal

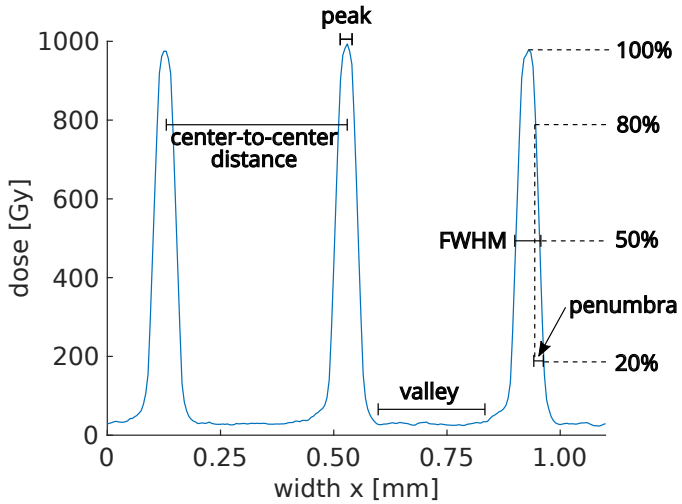

Figure 4.1.: Definitions of the peak, the valley, the center-to-center distance, the full width at half maximum (FWHM), and the lateral penumbra from 80 % to 20 % of the peak dose.

penumbra denoted the 80 %-to-20 % dose falloff in the y-direction. Similarly, the FWHM took the mean dose of the individual peak as reference for the 50 % level. The PVDR denoted the mean peak dose divided by the mean valley dose for each peak position. Peak doses, valley doses, penumbras, FWHM, and PVDR values at a specific depth were given as the respective mean value across the field except of the outer most values, e.g., the mean over peak position 2–50 in case of 51 peaks. Uncertainties represented the standard error of the respective mean by calculating the standard deviation of the respective value at a specific depth (except of the outer most values) divided by the square root of the number of values taken for the calculation of the mean and standard deviation.

4.2.1. Microbeam dose distribution

To obtain microbeam dose distributions, Monte Carlo simulations were performed in two steps using Geant4 (version 10.4.p02). The *G4EmPenelopePhysics* list, which was particularly developed for the simulation of low-energy electromagnetic interactions, was applied with a range cut of 1 µm for photons, electrons, and positrons; default step sizes for electrons and positrons (step function parameters $dRoverRange = 0.2$, $finalRange = 0.1$ mm); and fluorescence electrons and particle-induced x-ray emission activated [95, 96].

In a first step, unfiltered x-ray spectra were obtained by simulating an electron beam hitting a target. A point source of electrons with the energy of interest and $8 \cdot 10^8$ primary particles perpendicularly hit a target made of tungsten. The energy of the produced photons was scored with a hemispherical phase space detector placed contiguously on the target. Using Matlab, the phase space was converted into an energy spectrum by

creating a histogram with a bin size of 1 keV. Proceeding from this unfiltered spectrum, several filtered spectra were analytically calculated with different thicknesses, the mass density, and the energy-dependent mass attenuation coefficients of the respective filtering material. The material data were taken from the U.S. National Institute of Standards and Technology (NIST) [97].

In a second step, the dose deposition in water was simulated with 10^9 primary photons randomly sampled from the filtered energy spectrum of interest, which was obtained in the first step. The photons originated from a strongly eccentric focal spot with Gaussian intensity distributions in the x- and y-directions. The x-ray beam hit a multislit collimator made of tungsten, which formed the homogeneous radiation into a microbeam field size of $20 \times 20\,\mathrm{mm}^2$. The divergence of the photon beam was selected in a way that ensured full coverage of the collimator slits. The collimator consisted of three plates, with the center plate having twice the thickness of the outer plates. Each plate had 51 slits of $100\,\mu\mathrm{m} \times 20\,\mathrm{mm}$ ($x \times y$) so that a shift of the center plate by 50 µm in the x-direction effectively produced a slit width of 50 µm (following the realized collimator described by Treibel et al. [73]). The divergence of the slits in the x-direction corresponded to the divergence of the beam, which depended on the source-to-collimator distance. Directly behind the collimator, the dose was scored in a water phantom, which had a size of $(100\,\mathrm{mm})^3$ and scoring voxels of $0.005 \times 1 \times 1\,\mathrm{mm}^3$ ($x \times y \times z$).

Parameter optimization

To find optimal parameters of the radiation field for MRT with the LFxT, the x-ray spectrum, the focal spot size, and the source-to-phantom distance were varied as described in the following. For each parameter variation, the microbeam dose distribution was analyzed regarding the peak dose, the valley dose, the PVDR, the FWHM, and the penumbras.

The x-ray spectrum was varied between 200 kVp and 800 kVp by scoring the phase space of unfiltered x-rays produced by an electron beam of 200 keV to 800 keV hitting the tungsten target. For the analytically calculated filtration of the spectra, a beryllium thickness of 0.8 mm was kept for all simulations, representing a typical x-ray vacuum window. Different thicknesses of copper and aluminum were investigated for additional filtering.

The collimator thickness was adjusted to the respective unfiltered spectrum in a way that the collimator was thinnest possible while ensuring a leakage radiation below 0.25 % through the center plate (or both outer plates). As for the filtering of the x-ray spectra, the amount of leakage radiation through the plates of the multislit collimator was calculated with energy-dependent mass attenuation coefficients of tungsten from NIST [97]. The resulting total thickness of the collimator was 7–35 mm for the 200–800 kVp spectra. In auxiliary simulations, the density was set to 100 times the density of tungsten to validate a sufficient absorbance of the collimator for each spectrum separately. The dose distributions with enhanced density and with regular density of tungsten did

not differ perceptibly. For this reason, remaining effects of the collimator on the dose distribution resulted from its geometry but not from missing absorber material.

The Gaussian standard deviation of the focal spot size was varied between 10–500 µm in the x-direction and between 5–40 mm in the y-direction. Additional investigations included rectangular focal spots of homogeneous intensity with edge lengths in the same range as the standard deviations of the Gaussian-shaped focal spots.

The distance from the photon source to the phantom surface, i.e., the x-ray beam path length, was varied in the range of 10–80 cm. The collimator remained contiguously placed in front of the phantom, and the divergence of the collimator slits was adapted according to the source-to-phantom distance.

Comparison to synchrotron radiation

The microbeam dose distribution from a parallel x-ray beam with the spectrum of the biomedical beamline ID17 at the ESRF served as a comparison to state-of-the-art MRT. The spectrum of the ID17 had a maximum energy of 250 keV (higher energies were cut due to their low contribution of less than 1.5 %) and a mean energy of 104 keV (similar to the preclinical beam in the publication by Crosbie et al. [98]). Two simulations with 10^9 primary photons were performed, one with a divergent x-ray beam and one with a parallel x-ray beam, to differentiate the effects of the spectrum from the effects of the divergence. For the divergent beam, the simulation geometry remained unchanged as against the simulations of the LFxT with a Gaussian-shaped focal spot with standard deviations of 50 µm × 30 mm ($x \times y$). The parallel beam had the size of the microbeam field ($20 \times 20\,\mathrm{mm}^2$) with homogeneous intensity, and the collimator slits were set to parallel. For both simulation configurations, the collimator thickness was 7 mm in total, meaning the plates had thicknesses of 1.75 mm, 3.5 mm, and 1.75 mm, respectively. The surface of the water phantom, i.e., also the rear side of the collimator, was located at a distance of 50 cm from the photon source.

4.2.2. Dose rate

For high peak dose rates, the energy deposit in the phantom per primary electron needs to be maximized. The peak dose rate corresponds to the dose rate in an open field under ideal conditions, including a focal spot that is smaller than the collimator slits, because the multislit collimator lets the x-rays pass through the slits without disturbance. Here, the dose rate was evaluated for an open field to estimate the maximum possible peak dose rate and to find the most suitable incident and emission angles for highest dose rates. The valley dose rate can be calculated by the peak dose rate and the peak-to-valley dose ratio but will not be addressed here.

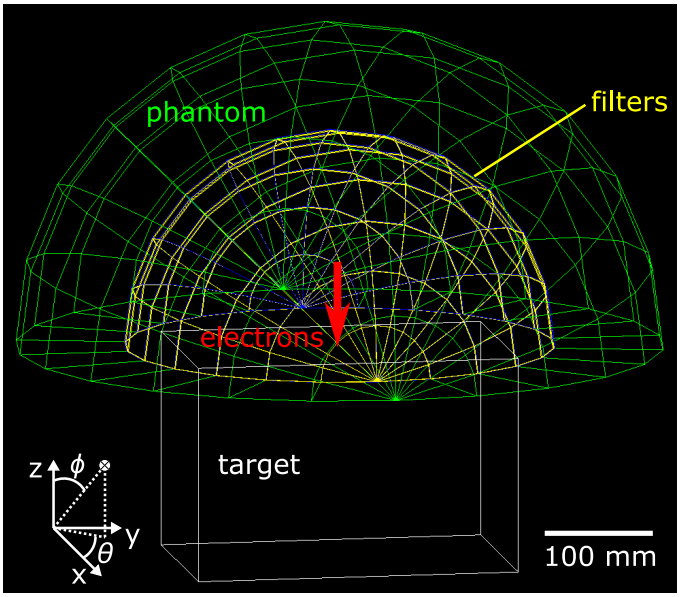

Figure 4.2.: Setup of the Monte Carlo simulations to investigate the dependence of the relative dose rate on the electron incidence and the photon emission angles. Electrons hit a tungsten target, the produced photons were filtered and detected in a 100 mm-thick water phantom. ϕ denotes the polar angle and θ the azimuthal angle.

Incident and emission angles

The energy deposit in the phantom depends on the incident angle of the electron beam onto the target and on the emission angle of the investigated x-radiation. The setup of the Monte Carlo simulations in Geant4 [93] (version 10.4.p02, with the same physics settings as in chapter 4.2.1) is depicted in figure 4.2. The electron beam of $2 \cdot 10^9$ primary particles had polar incident angles ϕ of 0–40° to the normal to the target surface, an energy of 300 keV, and a Gaussian-shaped focal spot of 50 µm × 30 mm ($x \times y$) (widths at 10 % of the maximum intensity, resulting from Gaussian standard deviations of 11.7 µm × 7 mm). The target was made of tungsten and had a cuboid shape with edge lengths of 200 mm × 300 mm × 200 mm ($x \times y \times z$). The produced x-rays were filtered by 0.8 mm beryllium and 1.0 mm aluminum, implemented in the simulations as hemispherical shells, which were contiguously placed on the target. The position in spherical coordinates and the energy of the produced photons were scored as a phase space in a hemispherical, 100 mm-thick water phantom, encompassing the target and the filters. The remaining space was set to vacuum. Using Matlab (version R2018b, The MathWorks Inc., USA), the scored energy was normalized by $1/\sin\phi$ and, thereafter, binned by the polar emission angle ϕ and the azimuthal emission angle θ.

Dose rate in an open field

Absolute dose rates were investigated with Monte Carlo simulations in Geant4 [93] (version 10.4.p02, with the same physics settings as in chapter 4.2.1) and in TOPAS [94] (version 3.2.2, based on Geant4 version 10.5.p01). For the simulations in TOPAS, the *G4EmPenelopePhysics* list was employed with default electromagnetic range limits (*EMRangeMin* = 100 eV, *EMRangeMax* = 500 MeV); default step sizes for electrons and positrons (step function parameters *dRoverRange* = 0.2, *finalRange* = 0.01 mm); and fluorescence electrons, Auger electrons, and particle-induced x-ray emission activated [95, 99]. For both simulation tools, a rectangular electron beam with a size of 50 µm × 30 mm, 10^8 or 10^9 primary particles, homogeneous intensity, and an energy of 300 keV, 400 keV, or 600 keV hit a target made of tungsten perpendicularly to the target surface. Layers of beryllium, aluminum, or copper of different thicknesses filtered the x-rays at a polar emission angle of 0° to the normal to the target surface in front of a water phantom. The phantom had a size of $(200\,\text{mm})^3$ with scoring voxels of $(1\,\text{mm})^3$, and the surface of the phantom was located at a distance of 50 cm from the focal spot. The energy deposit was scored in the Geant4 simulations, whereas the dose was scored in the TOPAS simulations. The remaining space was set to vacuum.

Using Matlab (version R2018b, The MathWorks Inc., USA), the scored energy was converted into dose by considering the voxel size and the density of water. The converted dose from the Geant4 simulations and the scored dose from the TOPAS simulations were further converted into dose rate by the number of primary particles in the simulations and the intended primary electron beam current, which was 0.3 A and 2.5 A for the LFxT prototype and the clinical LFxT, respectively. Subsequently, the dose rates were averaged at each depth in the phantom. The standard error of the mean was calculated as $\sigma_{\overline{x}} = \frac{\sigma}{\sqrt{N}}$ with the standard deviation σ of the dose rate and the number of voxels N at a specific depth. For the Geant4 simulations, the squared energy was scored in each voxel additionally to the energy, converted to the squared dose rate, and an alternative error of the mean was deduced by error propagation: $\sigma'_{\overline{x}} = \frac{1}{N}\sqrt{\sum_{v=1}^{N} \sigma_v^2}$ with the uncertainty of the dose in a voxel $\sigma_v = \sqrt{DS - D^2}$, where D denotes the dose and DS the squared dose scored in that voxel. Dose rates at different distances between the focal spot and the phantom were calculated according to the inverse square law as photon scattering in vacuum could be neglected.

4.2.3. Realistic electron beam

As a final analysis of the radiation field, the microbeam dose distribution and the peak dose rate were investigated for x-rays emerging from the phase space of an electron beam hitting a tungsten target. The phase space resulted from the development of the electron accelerator for the preclinical LFxT prototype (details of the development and the electron distribution at the focal spot can be found in chapter 7.1). The electrons had an energy of approximately 300 keV and were focused to a spot size of 50 µm × 20 mm as FWHM. The Monte Carlo simulations of the radiation field were performed in TOPAS

[94] (version 3.2.2) with the same physics settings as used for the TOPAS simulations in the second part of section 4.2.2.

The simulations of the microbeam dose distribution were performed in two steps: First, 10^9 electrons, which were sampled from the electron beam phase space, hit a target made of tungsten at an incident angle ϕ of 0°. The phase space of the produced x-rays was scored behind a filter of 1 mm aluminum at a polar emission angle ϕ of 0°. Second, this recorded phase space served as an x-ray source by reusing the scored photons 10^4 times. In an additional simulation, a point source of photons with the same spectrum as the recorded phase space served as a comparison. For both simulation configurations, the photons traveled through a multislit collimator, which had the setup described in section 4.2.1 with three plates made of tungsten and an effective slit size of $50\,\mu m \times 20\,mm$ ($x \times y$). The collimator was imported as a computer aided design (CAD) model into TOPAS, and its back surface was located at a distance of 21 cm from the focal spot. Contiguously behind the collimator, the dose was scored in a water phantom with a size of $30 \times 30 \times 100\,mm^3$ and scoring voxels of $0.01 \times 1 \times 1\,mm^3$ ($x \times y \times z$).

The absolute dose rate in an open field was estimated without a multislit collimator by performing Monte Carlo simulations in TOPAS in the same way as described in the previous section 4.2.2.

4.3. Results

4.3.1. Microbeam dose distribution

The simulated microbeam dose distribution of the LFxT exhibited a clear peak-valley profile with the same divergence of the radiation field and the collimator slits, exemplarily depicted in figure 4.3. The peak dose decreased with depth as shown in figure 4.4a for different x-ray spectra. The valley dose increased up to a water depth of 15 mm before decreasing similarly to the peak dose (see figure 4.4b), while the first voxel below the phantom surface ($z = 1\,mm$) detected an elevated valley dose. The statistical Monte Carlo simulations yielded uncertainties of the mean peak doses and the mean valley doses. For the doses presented in figure 4.4, the relative standard errors of the mean peak dose were in the range of 0.4–1.6 % and the relative standard errors of the mean valley dose in the range of 1.1–3.6 %. Due to a smaller number of particle interactions, the uncertainties were higher for the valley dose than for the peak dose and higher for regions deeper in the phantom than close to the surface.

The PVDR decreased up to a water depth of approximately 40 mm because of a faster decrease in the peak dose than in the valley dose (refer to figures 4.4a, 4.4b, and 4.5a). The PVDR in the surface voxel layer of the phantom ($z = 1\,mm$) was lower than in following voxel layers due to the elevated valley dose in the surface layer, as described above. At a water depth of 50–90 mm, the peak dose and valley dose decreased at similar rates, leading to a plateau region of the PVDR. At the rear 10 mm of the phantom, the PVDR increase resulted from a lower valley dose due to the absence of material behind

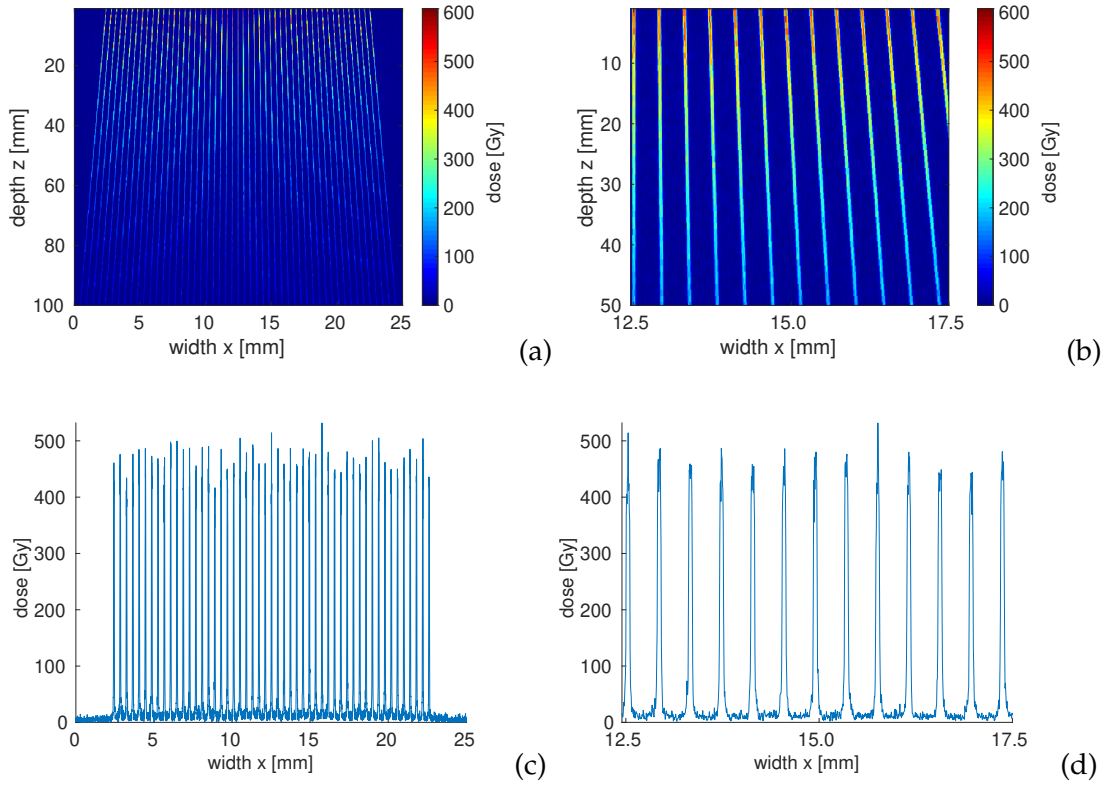

Figure 4.3.: Divergent microbeam dose distribution from the line-focus x-ray tube as a two-dimensional overview (a) and as a zoom thereof (b), summed over the central 10 mm along the y-direction. The focal spot had Gaussian standard deviations of 50 µm × 30 mm ($x \times y$). The x-ray beam with a 300 kVp spectrum, filtered by 0.8 mm beryllium and 0.4 mm copper, was oriented in the positive z-direction. The center of the field was located at $x = 12.5$ mm. The water phantom was placed at 50 cm from the focal spot, directly behind the multislit collimator. Panels (c) and (d) show the lateral dose profile at 5 mm water depth.

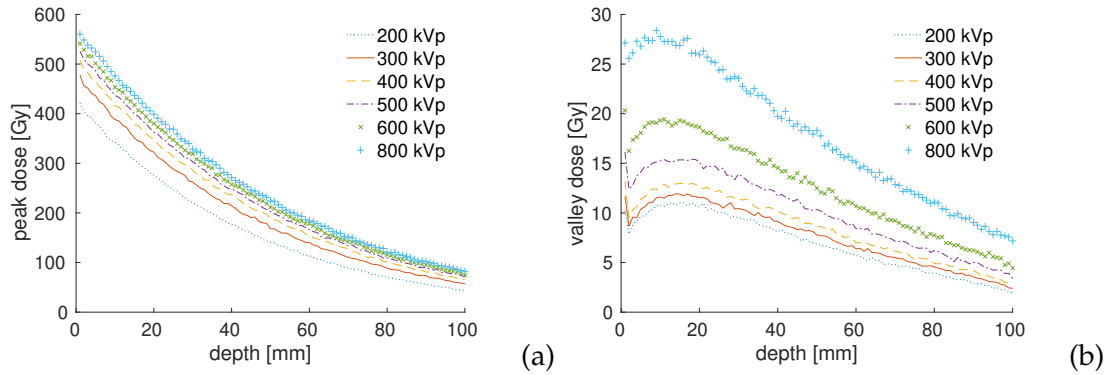

Figure 4.4.: Peak dose (a) and valley dose (b) behavior over depth for different x-ray spectra, all filtered by 0.8 mm beryllium and 0.4 mm copper. The focal spot size was 50 µm × 30 mm as Gaussian standard deviations, and the source-to-phantom distance was 50 cm. The ratio of the peak dose in panel (a) to the valley dose in panel (b) is displayed to scale. The relative standard errors of the mean were below 1.6 % of the peak dose and below 3.6 % of the valley dose and are not shown for clarity.

the phantom and thus less photon backscattering. Enlarging the phantom over the end of the detection volume removed the increase in PVDR at the rear end of the detection volume.

The microbeam dose distribution was optimized with regard to highest PVDRs and steepest lateral penumbras from the peaks to the neighboring valleys. Optimal parameters were a 300 kVp or a 400 kVp spectrum with a filtering of 0.8 mm beryllium and 0.4 mm copper, a focal spot width up to 50 µm, and a source-to-phantom distance of at least 50 cm. With these optimized beam parameters, the PVDR reached values above 40 up to a water depth of 6 mm, approximately 34 at 10 mm water depth, and stayed above 20 throughout 100 mm of water (confer the highest PVDR curves in figure 4.5). The following subsections expand on the different optimization parameters.

Optimization — x-ray spectrum

The highest PVDRs and steepest penumbras resulted from 300 kVp and 400 kVp x-ray spectra. On one side, higher maximum energies yielded longer ranges of the secondary electrons and thus less steep penumbras, wider FWHM, higher valley doses, and consequently lower PVDRs. On the other side, the 200 kVp spectrum resulted in a lower PVDR than the 300 kVp spectrum, see figure 4.5a. For all investigated spectra, the relative standard error of the mean PVDR at a specific depth was in the range of 1.2–4.2 %, with an increasing trend for lower energetic spectra and for larger depths in water due to a lower peak dose and thus a smaller number of particle interactions.

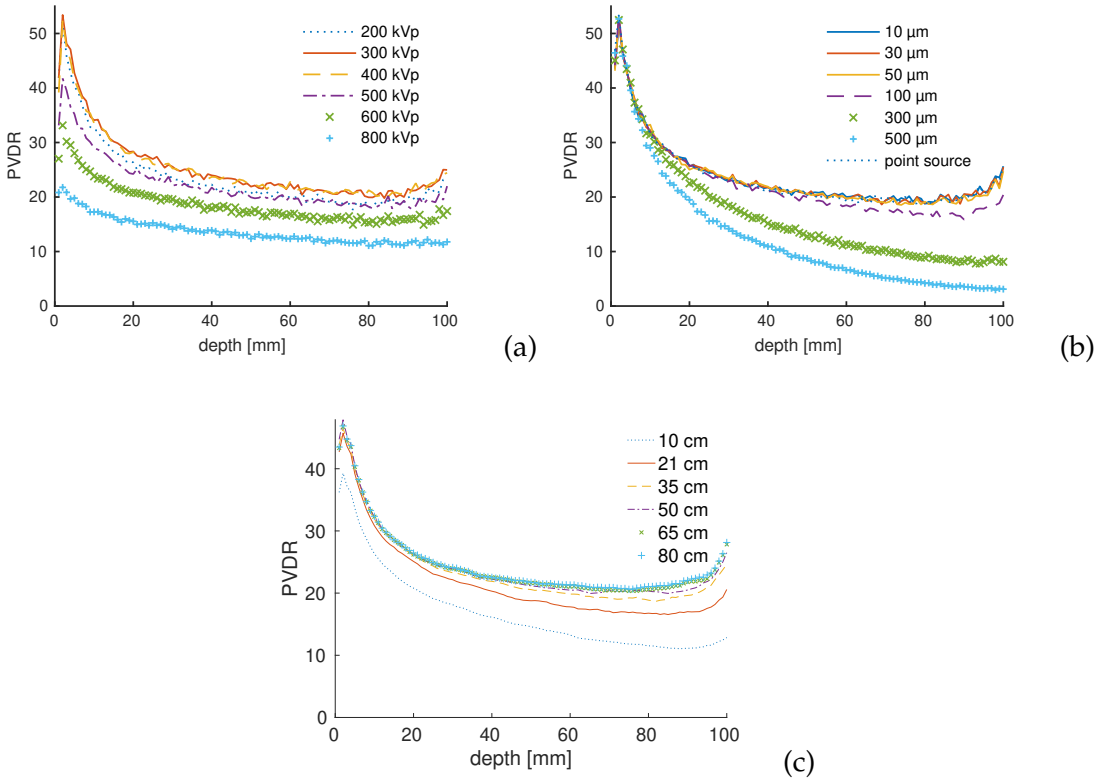

Figure 4.5.: Mean peak-to-valley dose ratio (PVDR) of the microbeam dose distribution in water in dependence of the x-ray spectrum (a, Winter et al. [87]), the focal spot width (b, Winter et al. [87]), and the source-to-phantom distance (c). The spectra were filtered by 0.8 mm beryllium and 0.4 mm copper. If not otherwise stated, the spot size was 50 µm × 30 mm as Gaussian standard deviations, the spectrum was 225 kVp, and the source distance was 50 cm. The standard error of the mean was below 5 % for all data points and is not shown for clarity.

A filtration of 0.8 mm beryllium and 0.4 mm copper of the 300 kVp and 400 kVp spectra were a good compromise between a high PVDR and high power output factors. With this filtration, the 300 kVp and 400 kVp spectra had mean energies of 97 keV and 109 keV, respectively. Using a focal spot size of 50 µm × 30 mm and a source-to-phantom distance of 50 cm, the 300 kVp spectrum resulted in PVDR values (± standard errors of the mean) of 53.5 ± 1.1 at 2 mm, 42.7 ± 0.7 at 5 mm, 30.7 ± 0.8 at 15 mm, and 20.4 ± 0.9 at 50 mm water depth. The 400 kVp spectrum yielded similar PVDR values of 52.3 ± 1.1 at 2 mm, 41.7 ± 0.8 at 5 mm, 30.4 ± 0.7 at 15 mm, and 20.9 ± 1.0 at 50 mm depth. Exchanging the copper filter by an aluminum filter of 1.0 mm thickness, the mean x-ray energy decreased to 76 keV for the 300 kVp spectrum, exemplarily; the output factor increased at the same time from 64 % to 87 % of the power of the unfiltered spectrum, while the

PVDR decreased slightly to 53.8 ± 1.1 at 2 mm, 39.3 ± 0.7 at 5 mm, 28.4 ± 0.7 at 15 mm, and 18.9 ± 0.9 at 50 mm water depth.

Optimization — focal spot size

The size of the focal spot was vital for a sharp peak-valley profile. Ideally, the x-rays originated from a focal spot that was as narrow as the collimator slits, i.e., 50 µm in this work. The region of the beam core behind each collimator slit shrank for wider spots. Furthermore, the wider the spot, the closer behind the collimator slit the beam core ended, which is illustrated in figure 4.6. Both the penumbras and the FWHM increased for wider focal spot widths.

With a source-to-phantom distance of 50 cm and a collimator slit width of 50 µm, the full width of a homogeneous rectangular focal spot intensity should not be larger than twice the collimator slit width, i.e., 100 µm, and the standard deviation of a Gaussian-shaped spot intensity should not be larger than 50 µm. Varying the spot width in the range of 0–50 µm (as Gaussian standard deviations) did not influence the PVDR, as seen in figure 4.5b. For wider spots, the PVDR decreased more steeply with depth. Reasons were a fast narrowing of the beam core and a broadening of the penumbra regions, hence a fast decrease in peak dose. The valley dose was not affected by a variation of the spot width for the simulated geometry. An exemplary widening of the Gaussian standard deviation of the focal spot from 50 µm to 300 µm led to a decrease in PVDR ($\pm$ standard error of the mean) from 33.3 ± 0.6 to 31.4 ± 0.5 at 10 mm water depth and from 20.6 ± 0.5 to 12.8 ± 0.3 at 50 mm water depth, respectively, using a 225 kVp spectrum with a filtering of 0.8 mm beryllium and 0.4 mm copper and a source-to-phantom distance of 50 cm. The relative standard error of the mean PVDR at a specific depth was in the range of 1.5–4.9 % for all investigated spot widths.

By decreasing the distance from the focal spot to the phantom, the beam core decreased and the penumbra region increased, especially for focal spots larger than the collimator slits, see also the following subsection. For this reason, the maximum acceptable spot width for a specific PVDR decreases with decreasing source-to-phantom distance.

The length of the focal spot (y-direction) did not affect the microbeam dose profile along the x-direction, hence neither the PVDR nor the lateral penumbras from the peaks to the valleys. A longer spot, however, increased the longitudinal penumbras (y-direction) at the edges of the radiation field.

Optimization — source-to-phantom distance

A decreased source-to-phantom distance led to a more divergent beam in the phantom. As the collimator remained contiguously in front of the phantom, the penumbra region behind each collimator slit increased with decreasing source-to-phantom distance and, if the focal spot was wider than the collimator slit, the region of the beam core decreased. Consequently, a shorter distance led to a faster peak dose decrease with depth. Additionally, the peak dose in the periphery of the radiation field (e.g., at $x = 22$ mm) was lower

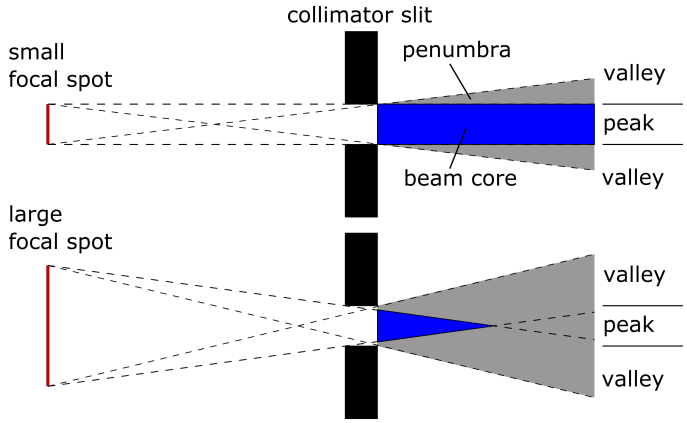

Figure 4.6.: A focal spot width wider than the collimator slits shrinks the beam core and increases the penumbra region.

than the peak dose at the center ($x = 12\,\text{mm}$) for shorter source-to-phantom distances. At the phantom surface, this difference was most pronounced with the farthermost peak receiving 54 % less dose than the maximum peak at the center of the radiation field, assuming a source-to-phantom distance of 10 cm, a Gaussian-shaped focal spot size of 50 µm × 30 mm, and a 225 kVp spectrum, filtered by 0.8 mm beryllium and 0.4 mm copper. This difference decreased with increasing depth in the phantom as well as with increasing source-to-phantom distance: At a water depth of 100 mm, the peak dose in the periphery was only 24 % lower than at the center for a source-to-phantom distance of 10 cm. At a water depth of 20 mm, the farthermost peak received 42 % less dose than the central peak for a distance of 10 cm, 18 % less for a distance of 21 cm, 8 % less for a distance of 35 cm, and 6 % less for a distance of 50 cm. For distances larger than 50 cm, the peak dose in the periphery of the radiation field converged to the peak dose at the center of the field.

The PVDR decreased faster with depth for shorter distances, and for a distance of 10 cm, also the PVDR at the surface was lower than for larger distances, as shown in figure 4.5c. Exemplarily, shortening the distance from 50 cm to 21 cm reduced the PVDR ($\pm$ standard error of the mean) from 32.1 ± 0.5 to 30.6 ± 0.5 at 10 mm water depth and from 21.4 ± 0.4 to 18.8 ± 0.3 at 50 mm water depth, respectively, assuming a Gaussian-shaped focal spot size of 50 µm × 30 mm and a 225 kVp spectrum with a filtering of 0.8 mm beryllium and 0.4 mm copper. For distances larger than 50 cm, a variation of the distance did not alter the PVDR. For all investigated distances, the relative standard error of the mean PVDR at a specific depth was in the range of 1.1–3.5 %.

A shorter distance yielded broader FWHM and less steep penumbras from the peaks to the valleys at all depths. Exemplarily, the FWHM increased from 53 µm to 57 µm at 10 mm and from 58 µm to 69 µm at 50 mm water depth, respectively, by shortening the source-to-phantom distance from 50 cm to 21 cm, assuming a Gaussian-shaped focal spot size of 50 µm × 30 mm and a 225 kVp spectrum, filtered by 0.8 mm beryllium and 0.4 mm

copper. This simulated FWHM increase equaled the geometrical increase according to the divergence of the beam, based on the FWHM at the surface of the phantom. For the same decrease in distance from 50 cm to 21 cm, the penumbras increased from 12 µm to 18 µm at 10 mm and from 17 µm to 28 µm at 50 mm water depth, respectively. Moreover, the longitudinal penumbra increased for a shorter source-to-phantom distance due to a stronger divergence. For distances larger than 50 cm, variation of the distance had minor impact on the FWHM and penumbras.

Comparison to synchrotron radiation

The comparison of the divergent 300 kVp x-ray field of the LFxT to the divergent and the parallel fields with the spectrum of the MRT beamline ID17 at the synchrotron ESRF exhibited slight differences in the microbeam dose distributions, which depended on the depth in the water phantom. The peak depth dose curve did not differ between the LFxT and the divergent ESRF configuration, while this curve was less steep for the parallel ESRF configuration than for both divergent configurations. Close to the surface of the phantom, the valley dose was lower for both configurations with the ESRF spectrum than for the LFxT spectrum. At depths larger than the maximum valley dose at 15 mm, the valley depth dose curve of both divergent beams decreased at the same rate, while the valley depth dose curve of the parallel beam was less steep due to the less steep peak depth dose curve.

Consequently, the PVDR of the ESRF beams were higher than of the LFxT beam at shallow water depths, while the PVDR of the divergent ESRF beam approached the PVDR of the LFxT with increasing depth (see figure 4.7). The PVDR of the parallel ESRF beam was 37.1 ± 0.6 ($\pm$ standard error of the mean) at a water depth of 10 mm and greater than 24 throughout the 100 mm-thick water phantom with a standard error of the mean in the range of 1.2–1.8 %. At shallow depths, the main reason for the higher PVDR (by up to 5) of the parallel ESRF beam than of the LFxT was the different spectrum, whereas, at larger depths, the main reason was the parallelism of the ESRF beam.

For the parallel ESRF beam, the FWHM was 51 µm for all depths. Both the lateral and the longitudinal penumbras did barely increase with depth (by < 1.5 µm laterally, by < 0.2 mm longitudinally), and the lateral penumbras from the peaks to the valleys were smaller than 9 µm for all investigated depths. On the contrary, the FWHM as well as the lateral and longitudinal penumbras increased with depth for the divergent beams, as described above for the LFxT.

4.3.2. Dose rate

Incident and emission angles

The highest output as dose per incident electron resulted from small electron beam incident angles and small x-ray emission angles to the normal to the target surface. Figure 4.8a depicts the energy output relative to the maximum intensity. The output exhibited a shoulder region for small angles for both the electron incident angle and the

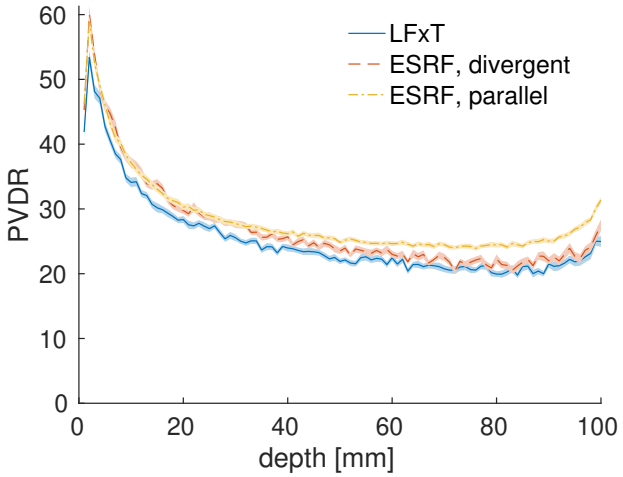

Figure 4.7.: Peak-to-valley dose ratio (PVDR) of the 300 kVp spectrum, filtered by 0.8 mm beryllium and 0.4 mm copper, of the line-focus x-ray tube (LFxT) compared to a divergent and a parallel x-ray beam of the spectrum of the beamline ID17 of the European Synchrotron Radiation Facility (ESRF) with a mean energy of 104 keV. Both divergent configurations had a Gaussian-shaped focal spot size of 50 µm × 30 mm and a source-to-phantom distance of 50 cm. The PVDR was averaged at each depth in water, and the shaded areas indicate the respective standard error of the mean.

x-ray polar emission angle ϕ due to a stronger intrinsic filtration (heel effect) for larger angles. In contrast, the emittance was uniform regarding the azimuthal emission angle θ. For an incident angle below 10°, the loss in intensity with respect to the maximum intensity was below 5 % for $\phi < 50°$.

The spectrum of the x-ray field depended on the emission angle. A larger emission angle to the normal to the target surface led to a stronger intrinsic filtration of low-energy photons due to the heel effect and thus to a higher mean energy, as seen in figure 4.8b. An electron beam with an energy of 300 keV and an incidence angle of 0°, combined with x-ray filters of 0.8 mm beryllium and 1.0 mm aluminum, produced a mean x-ray energy of 55 keV, 64 keV, and 100 keV for emission angles of 0°, 45°, and 85°, respectively.

Dose rate in an open field

Highest dose rates were achieved by a higher electron energy due to a higher electron-to-photon conversion efficiency (see equation (1.2)), by less filtration, and by a shorter distance from the focal spot to the phantom surface due to the inverse square law. The shape of the focal spot had no influence on the dose rate. The maximum energy deposit was found in the first millimeter at the phantom surface, there was no build-up effect. Relative to the entrance dose, the dose in an open field decreased more slowly with

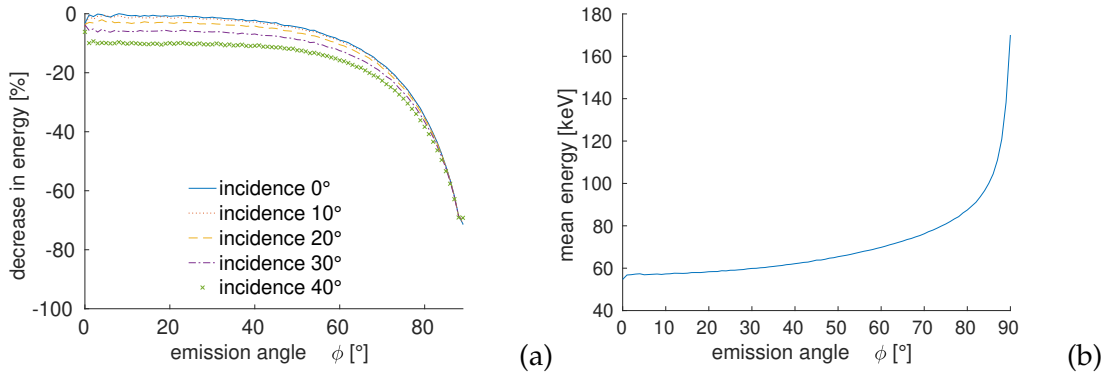

Figure 4.8.: (a) Dependence of the energy output on the electron incidence angle and the polar x-ray emission angle. (b) Emission angle-dependent mean x-ray energy from a 300 keV electron beam with an incidence angle of 0°, the x-rays were filtered by 0.8 mm beryllium and 1.0 mm aluminum.

increasing water depth than the peak dose. At a water depth of 100 mm, the relative peak dose was approximately 50 % and 39 % lower than the relative dose in an open field for a 300 kVp and a 600 kVp spectrum, respectively, both simulated with a source-to-phantom distance of 50 cm.

Absolute dose rates for different filtrations of the 300 kVp x-ray beam of the preclinical LFxT prototype with an electron beam power of 90 kW are listed in table 4.1. Absolute dose rates for the 600 kVp x-ray beam of the clinical LFxT with an electron beam power of 1.5 MW are listed in table 4.2. The range of the standard errors of the mean varied depending on the number of primary particles in the simulations: The TOPAS simulations for the preclinical LFxT with the phase space source and the 400 kVp spectrum as well as the TOPAS simulations for the clinical LFxT with a filtering of 1 mm aluminum were performed with 10^8 primary particles, which yielded relative standard errors of the mean between 5 % and 11 %. In contrast, the simulations of the remaining presented dose rates were performed with 10^9 primary particles and resulted in relative standard errors of the mean between 1 % and 7 %. Furthermore, there was a trend of higher standard errors for larger depths and more filtration due to a smaller number of particle interactions.

4.3.3. Realistic electron beam

The microbeam dose distribution resulting from the electron beam phase space exhibited a sharp peak-valley profile, as shown in figure 4.9a. The dose distribution and the behavior of the PVDR over depth was similar to the results described in section 4.3.1 with the same source-to-phantom distance of 21 cm, the Gaussian-shaped focal spot size of 50 µm × 30 mm, and the 300 kVp spectrum, filtered by 0.8 mm beryllium and 1 mm aluminum, which led to a mean x-ray energy of 72 keV independent of the focal

Table 4.1.: Absolute dose rates in water of the preclinical LFxT prototype with an electron energy of 300 keV (if not otherwise stated) and a beam current of 0.3 A. The distance from the focal spot to the phantom surface was 20 cm, and the rectangular focal spots had dimensions of 50 µm × 30 mm. The uncertainty intervals (±) indicate the standard error of the mean.

Simulation tool	Focal spot	X-ray filter material [mm]	Dose rate [Gy/s] at a depth of 2 mm	15 mm	50 mm
Geant4	Rectangle	0.8 Be + 1.0 Al	13.8 ± 0.3	$10.6 \pm 0.2^*$	5.9 ± 0.2
	Rectangle	0.8 Be + 0.4 Cu	$7.1 \pm 0.2^*$	5.9 ± 0.2	4.1 ± 0.2
	Rectangle	0.8 Be + 1.0 Cu	$5.3 \pm 0.2^*$	4.1 ± 0.2	3.0 ± 0.2
TOPAS	Rectangle	1.8 Be	14.8 ± 0.3	10.3 ± 0.3	5.1 ± 0.2
	Rectangle	0.8 Be + 1.0 Al	10.5 ± 0.3	9.2 ± 0.2	4.7 ± 0.2
	Phase space	0.8 Be + 1.0 Al	11.9 ± 0.9	10.1 ± 0.8	4.6 ± 0.5
	400 keV rectangle	1.0 Al	19.1 ± 0.9	14.4 ± 0.8	not scored

* The error of the mean deduced from the scored squared energy and error propagation was 0.3 Gy/s. For the unmarked values of the Geant4 simulations, the difference to the standard deviation of the mean was less than one decimal place.

spot shape. The PVDR resulting from the electron beam phase space was 42.8 ± 1.0 at 2 mm, 33.7 ± 0.8 at 5 mm, 23.2 ± 0.5 at 15 mm, and 16.3 ± 0.5 at 50 mm water depth, respectively, where the uncertainty intervals indicate the standard error of the mean.

The comparison to a point source of the same spectrum as the phase space did not show a difference up to a water depth of 20 mm, as depicted for the PVDR in figure 4.9b. At depths greater than 20 mm, the PVDR of the point source was higher than the PVDR of the phase space by less than 15 % throughout 100 mm of water. The standard error of the mean was in the range of 2–5 % of the PVDR for both the phase space source and the point source. Measurements by Martínez-Rovira et al. [40] at the ESRF ID17 with the same field size of $(20\,\text{mm})^2$ yielded a PVDR that was higher by 4 to 9.

The dose rate in an open field from the electron beam phase space resembled the dose rate of a rectangular, 300 keV electron beam with homogeneous intensity and the same x-ray filtering, as seen in table 4.1.

4.4. Discussion

The Monte Carlo simulations showed that the LFxT can produce a sharp microbeam dose distribution with a divergent peak-valley profile. As expected for photons in the kilovolt range, both the peak dose and the dose in an open field did not show a build-up effect in the first millimeters of the phantom, which stands in contrast to photons in the megavolt range that are typically used for radiotherapy [79]. The behavior of the peak dose over depth bore resemblance to depth-dose curves of homogeneous x-ray

Table 4.2.: Absolute dose rates in water of the clinical LFxT with an electron energy of 600 keV and a beam current of 2.5 A. The distance from the focal spot to the phantom surface was 30 cm, and the rectangular focal spots had dimensions of 50 µm × 30 mm. The uncertainty intervals (±) indicate the standard error of the mean. (The values in parentheses indicate the error of the mean deduced from the scored squared energy and error propagation.)

Simulation tool	X-ray filter material [mm]	Dose rate [Gy/s] at a depth of 2 mm	15 mm	50 mm
Geant4	0.8 Be + 1.0 Al	152.5 ± 3.0 (4.2)	111.4 ± 1.7 (2.1)	64.3 ± 1.4 (1.7)
	0.8 Be + 0.4 Cu	110.0 ± 2.9 (4.1)	79.6 ± 1.5 (1.9)	51.6 ± 1.3 (1.6)
	0.8 Be + 1.0 Cu	91.9 ± 2.8 (4.0)	65.3 ± 1.5 (1.8)	40.4 ± 1.3 (1.5)
TOPAS	1.8 Be	143.2 ± 2.1	102.1 ± 1.9	58.3 ± 1.5
	1.0 Al	134.0 ± 6.6	122.0 ± 6.8	57.4 ± 4.3
	0.8 Be + 1.0 Al	113.8 ± 1.0	98.5 ± 1.9	56.3 ± 1.4
	0.4 Cu	102.3 ± 1.0	93.0 ± 0.9	67.9 ± 0.8

fields in the kilovolt range according to the Beer-Lambert law. However, the peak dose decreased steeper with increasing depth than the dose in an open field in section 4.3.2. Reasons for the faster peak dose decrease were the divergence of the beam, leading to a peak widening and thus to a peak dose decrease due to energy conservation, and an unbalanced scattering: More photons scattered from the peak regions to the valley regions than vice versa.

The valley dose arose from photons that were Compton scattered from the peak regions to the valley regions and hence increased in the first millimeters of water before decreasing similarly to the peak dose. The lower valley dose close to the surface of the phantom yielded a higher PVDR, which can be utilized for superficial microbeam irradiations. The elevated valley dose at the surface (first voxel layer) of the phantom presumably originated from photon scattering and the production of secondary electrons at the inner surfaces of the collimator slits. Consistently, a separate simulation showed that the elevated valley dose at the surface disappeared by adding a 125 µm-thin layer of polymethylmethacrylate (PMMA) between the collimator and the phantom. Similar to this simulated PMMA layer, radiochromic films for MRT dosimetry contain a protective layer of polyester with a thickness of 125 µm [100].

The behavior of the PVDR over depth, including the plateau region from a depth of 40 mm on and the increase at the rear end of the phantom due to reduced scattering, was in agreement with observations by other authors, who used parallel microbeam fields at synchrotron beamlines [40, 101]. For a translation of MRT towards clinical application, it is important that divergent fields from a compact x-ray source can produce sharp microbeam dose profiles with similar characteristics to microbeam dose profiles from parallel fields at synchrotrons that were used for successful preclincial studies.

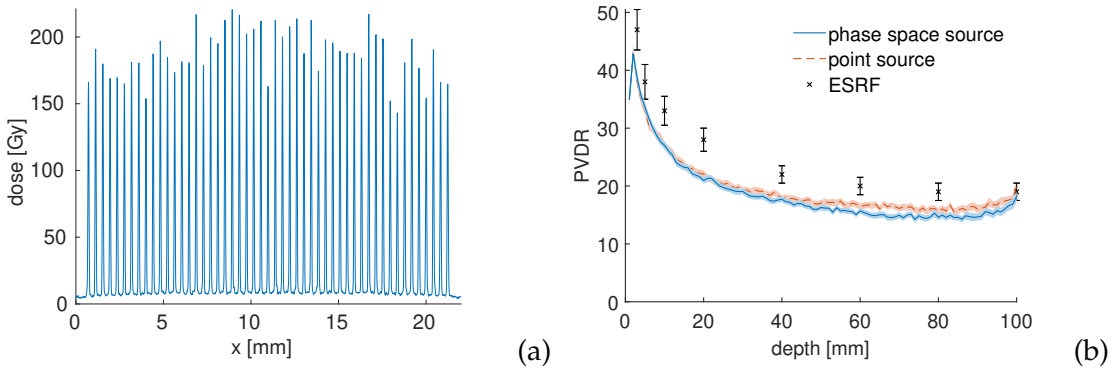

Figure 4.9.: Microbeam dose profile at 15 mm water depth (a) and peak-to-valley dose ratio (PVDR) (b) resulting from the electron beam phase space. The dose distribution was compared to a point source of the same spectrum as the phase space and to measurement values at the ESRF ID17 [40]. The shaded areas and error bars indicate the respective uncertainty intervals as standard errors of the mean.

The gold standard for preclinical MRT are quasi-parallel x-ray beams from third-generation synchrotrons. In contrast, a compact x-ray tube can only have a divergent beam due to a much shorter source-to-phantom distance. The divergence of the x-ray field entailed a reduction of the PVDR with increasing depth as well as a widening of the center-to-center distance, the penumbras, and FWHM with depth. These consequences of divergent fields were demonstrated in the last part of section 4.3.1 with the comparison of parallel and divergent beams using the same spectrum of the ID17 at the ESRF. Further increasing the source-to-phantom distance would bring the divergent microbeams from the LFxT closer to parallel but would also decrease the dose rate with one over the square of the distance. At the same time, a shorter source-to-phantom distance r leads to a steeper relative depth dose curve because the dose D decreases according to the Beer-Lambert law of attenuation as well as the inverse square law: $D \propto \exp(-\mu d)/(r+d)^2$, where μ is the attenuation and d is the phantom depth. An explanation for the lower dose in the periphery than at the center of the divergent field was the cuboid shape of the phantom, which resulted in a larger distance between the focal spot and the peripheral phantom surface than between the focal spot and the phantom surface at the center of the radiation field. A smaller distance yielded a more divergent field hitting the phantom than a larger distance. This effect was stronger in the surface layers of the phantom than in deeper layers, where the attenuation in water dominated the dose rate decrease. Consequently, the source-to-phantom distance of the LFxT needs to be a balanced compromise between more parallel beams and a high dose rate. Especially for the application of FLASH radiotherapy but also for MRT, a high dose rate is essential and

the divergence of the beam needs to be accepted but the consequences of the divergence can be mitigated by the choice of a sufficiently small focal spot.

The width of the focal spot is vital for a sharp microbeam dose profile, especially for a divergent beam, as illustrated in figures 4.5b and 4.6. For this reason, the majority of the focal spot intensity should be confined to a region not wider than the collimator slits, i.e., 50 µm in the x-direction for the presented MRT setup, whereas the y-dimension of the focal spot is less relevant than the x-direction, as stated above. A further reduction in focal spot width (x-direction) did not influence the PVDR or the FWHM but slightly steepened the lateral penumbras. However, a smaller focal spot leads to a higher heat load density at the target surface and might damage the target material, details can be found in chapter 5. For this reason, a focal spot of the same size as the collimator slits is desirable. As expected, the shape of the focal spot did not influence the dose rate in section 4.3.2 because the spot dimensions were much smaller than the target dimensions and the source-to-phantom distance.

For effective MRT, the lateral penumbras (x-direction in this work) should be steep to achieve a broad valley region of low dose. The longitudinal penumbras (y-direction) are not specifically important for MRT because they do not influence the peak-valley profile; however, they should not be too much elongated in order to spare tissue surrounding the target volume, as for conventional radiotherapy. The FWHM and the center-to-center distance should stay approximately constant with depth and all peaks at a specific depth should have the same height for similar characteristics of the microbeam dose distribution throughout the irradiated target volume.

The ideal x-ray spectrum for a high PVDR of 300–400 kVp with a filtration of 0.8 mm beryllium as an x-ray exit window and additionally 0.4 mm copper corresponded to the recommendation of a mean energy of approximately 100 keV by other authors [62, 101]. The aforementioned filtering led, however, to a more than 30 % decrease in beam power compared to a non-filtered beam, which decreased the peak dose rate accordingly. To obtain high peak dose rates, the filtration of 1.0 mm aluminum would be the better choice with a beam power decrease of less than 15 % compared to a non-filtered beam, even though the mean energy and thus the PVDR slightly decreased. A comparison of the dose rates in an open field with the aforementioned filtrations can be found in tables 4.1 and 4.2.

The zigzag behavior of the PVDR over depth resulted from the valley dose due to a small number of particle interactions in the valley region. The relative uncertainties $\sigma_{\bar{x}}$ as standard errors of the mean PVDR were overall below 5 %. An additional analysis showed that the $3\sigma_{\bar{x}}$ interval comprised the zigzag behavior of the PVDR, which suggested that the stated uncertainties had the correct order of magnitude. The simulations of the electron beam phase space might have had a systematic error from the multiple usage of the scored x-ray phase space.

The standard errors of the mean absolute dose rates in an open field amounted to 1–7 % for most presented values, whereas to 8–11 % for the phase space simulations with a lower number of simulated primary particles. As expected, the uncertainties were higher

for simulations with a smaller number of primary particles as well as for larger depths and more x-ray filtration due to a lower number of particle interactions. Nevertheless, the stated standard errors $\sigma_{\bar{x}}$ of the mean dose rates seemed too small because even the $3\sigma_{\bar{x}}$ intervals did not comprise the differences between values simulated using Geant4 and TOPAS with the same filtering of 0.8 mm beryllium and 1.0 mm aluminum. Notably, the TOPAS simulations consistently resulted in lower dose rates than the Geant4 simulations. A reason for the discrepancies between the simulation tools might have been the different versions of Geant4 as the TOPAS simulations were based on the more up to date Geant4 version 10.5.p01, while the direct Geant4 simulations were performed in version 10.4.p02. Between Geant4 versions 10.4 and 10.5, the default step function parameter $finalRange$ for electrons in the *G4EmPenelopePhysics* list was changed from 0.1 mm to 0.01 mm [96, 99]. Furthermore, Auger electrons were only activated for the TOPAS simulations but not for the Geant4 simulations.

One additional deficiency of the estimate of the absolute dose rates was the negligence of differences in the relative depth dose curves for different source-to-phantom distances. The inverse square law was only considered for the distance from the source to the phantom surface, however, not including the phantom depth, r (see above). Additional simulations of the clinical LFxT with a filtering of 1.0 mm aluminum demonstrated steeper depth dose curves for shorter source-to-phantom distances. However, this deficiency cannot explain the differences between the simulations using Geant4 and TOPAS with the filtering of 0.8 mm beryllium and 1.0 mm aluminum in tables 4.1 and 4.2 because the dose was scored at equal source-to-phantom distances of 50 cm.

For a more confident estimation of the expected dose rate in an open field, the simulations should be repeated with a considerably higher number of primary particles (trillions rather than billions of primary electrons, not extensively expanded by a multiple usage of a scored phase space but different random seeds for the electron source). A very high number of primary electrons is needed due to the low electron-to-photon conversion efficiency. Moreover, the simulation setup should resemble the geometry of the LFxT as closely as possible. For an estimate of the absolute peak and valley dose rates, the simulations with an increased number of primary particles should be performed with a multislit collimator. As the ratio of the peak dose to the open-field dose depends on the scattering characteristics, the simulations need to be repeated for all spectra of interest.

The simulations of the realistic electron beam with an energy of 300 keV demonstrated the feasibility of the electron accelerator and the LFxT setup for MRT in section 4.3.3. A filtration of 0.8 mm beryllium and 1.0 mm aluminum and a source-to-phantom distance of 21 cm achieved a PVDR above 30 up to a water depth of 7 mm and above 15 throughout a 100 mm-thick water phantom as well as a dose rate above 10 Gy/s in the first 15 mm of water. The PVDR was up to 33 % lower than the presented values measured by Martínez-Rovira et al. [40] with the same field size of a parallel beam at the ID17 at the ESRF. The lower PVDR could be mainly attributed to the field divergence and the lower mean energy of the LFxT radiation. Nonetheless, preclinical MRT experiments have

been successfully performed with a PVDR at the same level with the simulated PVDR of the LFxT: In a study by Bouchet et al. [35], the PVDR was 23 at a depth of 7 mm in the rat head. The PVDR was in the range of 18–48 at a PMMA depth of 10 mm in a study by Serduc et al. [23] and in the range of 5–19 at a water depth of 13 mm behind 0.6 mm of skull in a study by Dilmanian et al. [102].

During the development of the preclinical LFxT prototype, technical aspects needed to be considered besides the requirements for a sharp microbeam dose distribution. For example, the electron accelerator and beam optics need to be capable to form the electron beam to the desired focal spot dimensions, which is investigated in chapter 7.1. Thereby, the strongly eccentric electron distribution cannot be a homogeneous rectangle or an ideal Gaussian normal distribution. For this reason, the simulations with the realistic phase space from the electron accelerator development were important for the assessment of the radiation field of the LFxT. As mentioned above, the size of the focal spot correlates with the heat load on the target surface, which is investigated in detail in chapter 5. Furthermore, the construction of the x-ray source revealed space restrictions so that the minimum distance of the focal spot to the collimator was 20 cm for the preclinical LFxT prototype that is currently under construction. A smaller overall dimension would not allow to place all relevant components and would further increase the heat load on the vacuum chamber walls, which is analyzed in chapter 6.

The development of a clinical LFxT will demand different parameters of the radiation field and will therefore lead to a different setup than the preclinical prototype. The mean x-ray energy and hence the electron acceleration voltage should be higher to reach deeper-seated tumors with a less steep depth-dose curve than for preclinical experiments. Admittedly, photons with higher energy worsen the PVDR, as shown in section 4.3.1. The electron-to-photon conversion efficiency goes linearly with the electron energy, though, which results in considerably higher dose rates with a higher electron acceleration voltage. Altogether, a promising spectrum for clinical MRT could be achieved by a high electron acceleration voltage in the kilovolt range, e.g., 600 kV, for a high power output factor and a low surface dose together with a stronger filtration, e.g., 0.4 mm of copper, than for the preclinical LFxT to increase the mean energy and, thus, further decrease the surface dose at constant target dose. The electron accelerator and optics need to be redeveloped for the higher electron energy and higher beam power, details can be found in chapter 7.1. Thereby, the width of the focal spot will be likewise of utmost importance to obtain a sharp microbeam dose distribution. For a spectrum of higher energy, the multislit collimator also needs a rebuilding as the currently available collimator with a thickness of 7 mm would yield considerable radiation leakage. A 600 kVp spectrum requires a tungsten collimator with a total thickness of 24 mm for a leakage radiation below 0.25 % through the center plate if the three-plate design is maintained. Presumably, the manufacturing technique of the multislit collimator needs to be revised as the current technique of wire cutting of centimeter-thick tungsten is challenging in micrometer precision.

An open field from the clinical LFxT seems applicable to deliver dose rates sufficiently high for x-ray FLASH treatments, especially for superficial irradiations. For these treatments at ultra-high dose rates at a depth of several centimeters, the filtration should be reduced to obtain the highest possible dose rate. More importantly, the electron beam power needs to be drastically increased compared to the preclinical LFxT prototype. A suitable power supply is currently not commercially available but under development based on the high voltage direct current transmission technology* [87].

Ultra-high dose rates are not only necessary for FLASH radiotherapy but also beneficial for MRT as they allow treatment times of only few seconds for peak dose rates of a few hundred Grays. In a clinical setting of the treatment of tumors in the lung or abdomen, patients can thereby hold their breath during the full treatment time, which obviates effortful or uncomfortable motion-management techniques such as live image guidance or abdominal compression [103]. A full breathing motion would deteriorate the MRT dose delivery even more than a conventional radiotherapy dose delivery because of a strong smearing of the micrometer-scaled dose distribution. Details of the effect of breathing motion as well as of cardiosynchronous pulsation on the MRT dose distribution can be found in chapter 12.

*The power supply for a clinical LFxT is under development by my collaboration partner Prof. Dr. Marek Galek from the University of Applied Sciences, Munich.

5. Heat dissipation at the focal spot

5.1. Introduction

The very high power of the preclinical LFxT prototype of 90 kW puts particular demands on the heat management of the x-ray source. The focal spot is the location of the highest heat load. At all times, the temperature at the target surface must stay below the melting temperature of the material and the material must not deform or crack due to thermal stress. Consequently, the maximum temperature at the focal spot, its course over time, and the underlying heat dissipation processes need to be investigated for the LFxT development.

There are two main heat dissipation mechanisms from the target surface to deeper regions: heat conduction and electron penetration, which carries the energy of the electrons further into the target. Heat conduction is characterized by the heat diffusion length, which depends on the surface velocity of the rotating target, the width of the electron beam (in the direction of the velocity), and material parameters. The relevant material parameters include the mass density, the thermal conductivity, and the specific heat capacity. The heat dissipation due to electron penetration depends on the energy of the incoming electrons as well as the atomic number, the mass density, and the specific heat capacity of the material.

A focal spot of a conventional x-ray tube is characterized by a typical width w of 0.5–1 mm and a relatively slow target velocity v of, e.g., 50 m/s [78, 89, 104, 105]. Consequently, a long heating time $t = w/v$ results in a heat diffusion length l that is much longer than the electron penetration depth d. In other words, heat conduction plays a more important role than heat capacity. In this heat conduction limit, the temperature increase at the focal spot is higher for a narrower spot and a slower target velocity (see section 5.2.1 and Oosterkamp [106]).

In contrast, the objective of the LFxT is the operation in the heat capacity limit: A very narrow focal spot and a very fast rotating target lead to a very short heating time t and thus a short heat diffusion length l. Moreover, the electron penetration depth d is longer due to a higher electron energy compared to imaging x-ray tubes. Consequently, d is much longer than l and heat capacity plays a more important role than heat conduction. In this heat capacity limit, the temperature increase at the focal spot is again higher for a slower target velocity but independent of the spot width (see section 5.2.1, Bartzsch and Oelfke [63], and Winter et al. [88]).

This chapter describes the maximum temperature increase at the focal spot during one passing of the electron beam. First, the temperature increase in both the heat conduction and the heat capacity limit were derived numerically. Second, the temperature increase

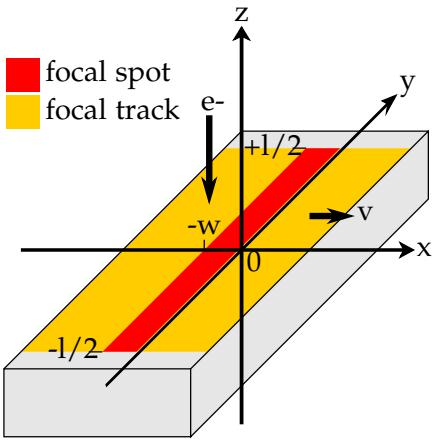

Figure 5.1.: The electron beam impinges onto the target in the negative z-direction. The focal spot has a width w and length l and passes along the x-direction with velocity v. Winter et al. [88].

was simulated with Monte Carlo and finite element methods with varying focal spot widths and target velocities. The simulations were then refined by using temperature-dependent material parameters and by including a realistic distribution of the electron beam. Finally, the temperature increase at the focal spot was investigated for a clinical LFxT with a power of 1.5 MW. The relationship between the temperature increase during one passing of the electron beam and the heat management of the whole x-ray tube is discussed at the end of this chapter.

5.2. Methods

The temperature increase at the focal spot after one passing of the electron beam was derived for the heat conduction and the heat capacity limit from basic energy equations. These limits were validated and the transition in between was investigated with numerical simulations. This chapter considered the two main heat dissipation mechanisms at the focal spot: heat conduction and electron transport; all other heat dissipation mechanism, such as thermal radiation, were neglected.

5.2.1. Derivation of the heat conduction limit and the heat capacity limit

Heat conduction limit

If heat conduction is the only considered heat dissipation mechanism, the temperature increase T at the focal spot can be derived from the heat equation,

$$\frac{\partial T_{\text{cond}}}{\partial t} - \alpha \Delta T_{\text{cond}} = f(\vec{x}, t)\,, \tag{5.1}$$

where $\frac{\partial}{\partial t}$ denotes the partial derivative with respect to time; $\alpha = \frac{\lambda}{\rho c}$ the thermal diffusivity with the thermal conductivity λ, the mass density ρ, and the specific heat capacity c; Δ the Laplacian operator; and f$(\vec{x}, t)$ an external heat source at position $\vec{x} = (x, y, z)$ and time t. The fundamental solution of the three-dimensional heat equation, the so-called heat kernel, is given by

$$H(\vec{x}, t) = \frac{1}{(4\pi\alpha t)^{3/2}} \exp\left(-\frac{\vec{x}}{4\alpha t}\right), \tag{5.2}$$

the integral over the full real space $\mathbb{R}^3$ of which is 1. The solution of the heat equation can be found by convolving the heat kernel with the external heat source as

$$T_{\text{cond}}(\vec{x}, t) = (H * f)(\vec{x}, t) = \int_0^t \mathrm{d}t' \int_{\mathbb{R}^3} \mathrm{d}\vec{x}' H(\vec{x} - \vec{x}', t - t') f(\vec{x}', t'). \tag{5.3}$$

For the focal spot of an x-ray tube, the external heat source is realized by the electron beam that deposits its power P_{cond} at the target surface of the half space ($z < 0$), see figure 5.1. The beam of width w (x-direction) and length l (y-direction) passes over the target with velocity v along its short dimension w. The maximum temperature will be reached after the full passage of the beam in the x-direction, at the center of the beam in the y-direction, and at the surface of the target at $z = 0$. The point of interest is at the location of the maximum temperature so that the extent of the heat source in the x-direction is confined by $(vt' - w, vt')$ and in the y-direction by $(-l/2, l/2)$. The external surface heat source is therefore given by

$$f(\vec{x}, t) = \frac{2P_{\text{cond}}}{wl\rho c} \cdot \Theta(x - (vt - w)) \cdot \Theta(vt - x) \cdot \Theta(y + l/2) \cdot \Theta(l/2 - y) \cdot \delta(z), \tag{5.4}$$

with the Heaviside step function

$$\begin{aligned} &\Theta : \mathbb{R} \to \{0, 1\} \\ &x \mapsto \begin{cases} 0: & x < 0 \\ 1: & x \geq 0 \end{cases}, \end{aligned} \tag{5.5}$$

and the Dirac delta function

$$\delta = \begin{cases} +\infty: & x = 0 \\ 0: & x \neq 0 \end{cases} \quad \text{with} \int_{-\infty}^{\infty} \delta(x)\mathrm{d}x = 1. \tag{5.6}$$

The factor 2 in the numerator of equation (5.4) results from the target filling the half space only (method of image charges). Inserting equations (5.2) and (5.4) into equation (5.3) leads to

$$
\begin{aligned}
T_{\text{cond}}(x,y,z,t) &= \frac{2P_{\text{cond}}}{wl\rho c}\int_0^t \mathrm{d}t' \int_{vt'-w}^{vt'} \mathrm{d}x' \int_{-l/2}^{l/2} \mathrm{d}y' \int_{-\infty}^{\infty} \mathrm{d}z' \delta\left(z'\right) \\
&\quad \cdot \frac{1}{\left(4\pi\alpha(t-t')\right)^{3/2}} \exp\left(-\frac{(x-x')^2+(y-y')^2+(z-z')^2}{4\alpha(t-t')}\right) \\
&= \frac{2P_{\text{cond}}}{wl\rho c}\frac{1}{(4\pi\alpha)^{3/2}}\int_0^t \mathrm{d}t' \int_{vt'-w}^{vt'} \mathrm{d}x' \int_{-l/2}^{l/2} \mathrm{d}y' \\
&\quad \cdot \frac{1}{(t-t')^{3/2}} \exp\left(-\frac{(x-x')^2+(y-y')^2+z^2}{4\alpha(t-t')}\right).
\end{aligned}
\tag{5.7}
$$

Evaluation at $\vec{x} = (vt, 0, 0)$ yields

$$
\begin{aligned}
T_{\text{cond}}(vt,0,0,t) &= \frac{2P_{\text{cond}}}{wl\rho c}\frac{1}{(4\pi\alpha)^{3/2}}\int_0^t \mathrm{d}t' \int_{vt'-w}^{vt'} \mathrm{d}x' \int_{-l/2}^{l/2} \mathrm{d}y' \\
&\quad \cdot \frac{1}{(t-t')^{3/2}} \exp\left(-\frac{(vt-x')^2+y'^2}{4\alpha(t-t')}\right).
\end{aligned}
\tag{5.8}
$$

Integration over y' follows as

$$
\int_{-l/2}^{l/2} \mathrm{d}y' \exp\left(-\frac{y'^2}{4\alpha(t-t')}\right) = 2\sqrt{\pi\alpha(t-t')}\,\mathrm{erf}\left(\frac{l/2}{\sqrt{4\alpha(t-t')}}\right),
\tag{5.9}
$$

where $\mathrm{erf}\left(\cdot\right)$ is the error function. Integration over x' follows as

$$
\begin{aligned}
&\int_{vt'-w}^{vt'} \mathrm{d}x' \exp\left(-\frac{(vt-x')^2}{4\alpha(t-t')}\right) = \\
&\qquad \sqrt{\pi\alpha(t-t')}\left[\mathrm{erf}\left(\frac{v(t-t')}{\sqrt{4\alpha(t-t')}}\right) - \mathrm{erf}\left(\frac{v(t-t')-w}{\sqrt{4\alpha(t-t')}}\right)\right],
\end{aligned}
\tag{5.10}
$$

yielding

$$
\begin{aligned}
T_{\text{cond}}(vt,0,0,t) &= \frac{P_{\text{cond}}}{2wl\rho c\sqrt{\pi\alpha}}\int_0^t \mathrm{d}t' \frac{1}{\sqrt{t-t'}}\,\mathrm{erf}\left(\frac{l/2}{\sqrt{4\alpha(t-t')}}\right) \\
&\quad \cdot \left[\mathrm{erf}\left(\frac{v(t-t')}{\sqrt{4\alpha(t-t')}}\right) - \mathrm{erf}\left(\frac{v(t-t')-w}{\sqrt{4\alpha(t-t')}}\right)\right] \\
&= \frac{P_{\text{cond}}}{2wl\sqrt{\pi\lambda\rho c}}\int_0^t \mathrm{d}t' \frac{1}{\sqrt{t-t'}}\,\mathrm{erf}\left(\frac{l/2}{\sqrt{4\alpha(t-t')}}\right) \\
&\quad \cdot \left[\mathrm{erf}\left(\frac{v(t-t')}{\sqrt{4\alpha(t-t')}}\right) - \mathrm{erf}\left(\frac{v(t-t')-w}{\sqrt{4\alpha(t-t')}}\right)\right].
\end{aligned}
\tag{5.11}
$$

The integration over time was performed numerically in Python (version 3.7.2).

The maximum temperature increase in the heat conduction limit was verified with the theoretically expected values from Oosterkamp [106, 107]. For short exposure times, the heat diffusion length $\sqrt{\alpha t}$ is shorter than the focal spot width w. Oosterkamp [106] defined the prerequisite for short exposure times for the smallest dimension of the focal spot f, here corresponding to w, as

$$1.5 < \frac{f}{4\sqrt{\alpha t}} = \frac{w}{4\sqrt{\frac{\lambda}{\rho c}\frac{w}{v}}} = \sqrt{\frac{w\rho c v}{16\lambda}}\,, \tag{5.12}$$

where lateral heat conduction in the x- and y-direction can be neglected. In that case, the temperature increase is given by

$$T_{\mathrm{cond}} = \frac{2P_{\mathrm{cond}}}{l\sqrt{\pi\lambda\rho c w v}}\,. \tag{5.13}$$

Heat capacity limit

At the limit of very short exposure times, heat conduction is negligible and the temperature increase is determined by the energy transport of the electrons into the target material. The maximum temperature increase T_{cap} after an exposure time $t = w/v$ was derived from energy conservation as

$$\begin{aligned} \delta P_{\mathrm{cap}} t &= \delta V \rho c T_{\mathrm{cap}} \\ \Rightarrow T_{\mathrm{cap}} &= \left\langle \frac{\delta P_{\mathrm{cap}}}{\delta V} \right\rangle_{\mathrm{max}} \frac{w}{\rho c v}\,, \end{aligned} \tag{5.14}$$

where $\left\langle \frac{\delta P_{\mathrm{cap}}}{\delta V} \right\rangle_{\mathrm{max}}$ denotes the maximum heat power density per volume. The power of a monoenergetic electron beam is the product of the number of incoming electrons per time $\dot{N}_{\mathrm{el}}$ and their primary energy E_{el}, $P_{\mathrm{cap}} = \dot{N}_{\mathrm{el}} E_{\mathrm{el}}$. For a homogeneous electron beam of width w and length l, the conversion $\delta V = \delta z \cdot w \cdot l$ applies. It follows

$$T_{\mathrm{cap}} = \left\langle \frac{\delta E_{\mathrm{el}}}{\delta z} \right\rangle_{\mathrm{max}} \frac{\dot{N}_{\mathrm{el}}}{wl} \frac{w}{\rho c v} = \left\langle \frac{\delta E_{\mathrm{el}}}{\delta z} \right\rangle_{\mathrm{max}} \frac{P_{\mathrm{cap}}}{E_{\mathrm{el}}} \frac{1}{l\rho c v} = \frac{P_{\mathrm{cap}}}{l\rho c v d}\,, \tag{5.15}$$

with the electron penetration depth

$$d = E_{\mathrm{el}} \Big/ \left\langle \frac{\delta E_{\mathrm{el}}}{\delta z} \right\rangle_{\mathrm{max}}\,, \tag{5.16}$$

where $\left\langle \frac{\delta E_{\mathrm{el}}}{\delta z} \right\rangle_{\mathrm{max}}$ denotes the maximum energy absorption per depth interval per electron, as defined by Bartzsch and Oelfke [63].

Transition

At the transition between the heat conduction and the heat capacity limit, both heat dissipation mechanisms contribute equally. For a constant target velocity, the transition is determined by the focal spot width

$$w_{\text{trans}} = \frac{4P_{\text{cond}}^2}{P_{\text{cap}}^2} \frac{\rho c v d^2}{\pi \lambda}, \tag{5.17}$$

while for a constant focal spot width the transition velocity of the target is given by

$$v_{\text{trans}} = \frac{P_{\text{cap}}^2}{4P_{\text{cond}}^2} \frac{\pi \lambda w}{\rho c d^2}. \tag{5.18}$$

The electron beam power P_{cond} in the heat conduction limit represents the portion of the primary power that is absorbed by the target, meaning that the power of electrons that are backscattered at the target surface is not included. In contrast, P_{cap} corresponds to the full primary electron beam power. In the heat capacity limit, the power loss due to backscattering is incorporated in the electron penetration depth d or more specifically in the factor $\left\langle \frac{\delta E_{\text{el}}}{\delta z} \right\rangle_{\text{max}}$.

5.2.2. Simulations

The temperature increase at the focal spot was numerically investigated with a combination of Monte Carlo simulations and finite element methods (FEM). The Monte Carlo simulation platform TOPAS [94] (version 3.6.1), which is based on Geant4 (version 10.6.p03), was used for the simulation of the electron transport into the target material tungsten. The *G4EmPenelopePhysics* list, which was particularly developed for the simulation of low-energy electromagnetic interactions, was applied with default electromagnetic range limits (*EMRangeMin* = 100 eV, *EMRangeMax* = 500 MeV), default step sizes for electrons and positrons (step function parameters *dRoverRange* = 0.2, *finalRange* = 0.01 mm), and the following options: fluorescence electrons activated, Auger electrons activated, particle induced x-ray emission activated, and ignoring of deexcitation cuts deactivated [95, 108]. The distribution of the energy deposit was scored in voxels of $1 \times 400 \times 1\,\mu\text{m}^3$ ($x \times y \times z$).

Using Matlab (version R2018b, The MathWorks Inc., USA), the electron penetration depth as per equation (5.16) was calculated from the maximum energy deposit per depth per primary electron. Moreover, the energy deposit per voxel was transformed into power density and normalized to the primary electron beam current of 0.3 A with the known number of primary electrons in the Monte Carlo simulations. This normalized power density distribution acted as a heat source in the FEM simulations with Comsol Multiphysics (version 5.6, Comsol Multiphysics GmbH, Göttingen, Germany) [109]. The Comsol module *Heat Transfer in Solids* activated heat conduction within the simulation volume, which had infinite element domains at all borders except the surface ($z = 0$)

where the Neumann boundary condition $\partial T/\partial z = 0$ applied. The target material was again tungsten ($\rho = 19\,300\,\mathrm{kg/m^3}$, $c = 138\,\mathrm{J/kg/K}$, $\lambda = 170\,\mathrm{W/m/K}$), and the initial temperature was 20 °C. While the heat source was passing along the x-direction, the temperature distribution was calculated with a time-dependent study.

Rectangular focal spot

The first simulations were performed with a rectangular focal spot of 50 µm × 30 mm ($x \times y$) of parallel electrons with a primary energy of 300 keV passing along its short dimension (positive x-direction) with a velocity of $v = 200\,\mathrm{m/s}$. The orientation of the electron beam was consistent to section 5.2.1 and is depicted in figure 5.1. Here, a two-dimensional model was sufficient for the FEM as there was thermal equilibrium in the y-direction at the center of the focal spot and thus no heat transport along the y-direction. The normalized heat power density was imported into the Comsol simulations as a cut through the center of the focal spot at $y = 0$ with zero extrapolation. The size of the simulation surface was $(1\,\mathrm{mm})^2$ ($x \times z$) divided into a *Mapped Mesh* of $(1\,\mu\mathrm{m})^2$.

Different setups were used to simulate the heat conduction limit, the heat capacity limit, and a full simulation. For heat conduction only, a boundary heat source deposited all its energy on the surface of the volume. For heat capacity only, the energy density distribution of the penetrating electrons acted as a volume heat source while heat conduction was deactivated (thermal conductivity $\lambda = 0$). For the full simulation, both heat conduction and heat capacity contributed to the heat dissipation. For all three setups, the focal spot width was varied between 10 µm and 20 mm while holding the velocity constant ($v = 200\,\mathrm{m/s}$) to investigate the dependence of the temperature increase on the spot width. Subsequently, the velocity was varied between 0.1–1000 m/s while holding the spot width constant at 1 mm. This study was not performed with a constant spot width of 50 µm because the heat conduction limit for short exposures cannot be reached (confer section 5.3.1). According to the respective spot width and velocity, the simulation surface in the x-direction and the simulation time were adjusted so that the maximum temperature reached a plateau.

Temperature-dependent material parameters

Secondly, the simulations were brought a step closer to reality by performing the FEM with temperature-dependent parameters of tungsten, deduced from a publication by Plansee [110]. Using Python (version 3.7.2), a linear fit of the temperature dependent specific heat capacity resulted in

$$c = 0.0139\,\frac{\mathrm{J}}{\mathrm{kg\,K^2}} \cdot T + 128\,\frac{\mathrm{J\,K}}{\mathrm{kg}}\,, \tag{5.19}$$

and the thermal conductivity was fitted with a second order polynomial to

$$\lambda = 2.65 \cdot 10^{-5}\,\frac{\mathrm{W}}{\mathrm{m\,K^3}} \cdot T^2 - 0.0886\,\frac{\mathrm{W}}{\mathrm{m\,K^2}} \cdot T + 184\,\frac{\mathrm{W}}{\mathrm{m\,K}}\,. \tag{5.20}$$

These relations were put into the Comsol simulations as temperature-dependent material parameters. The temperature increase was simulated with a rectangular focal spot size of 50 µm × 30 mm, a target velocity of 200 m/s, and an initial temperature of 20 °C and 860 °C, respectively. The latter value represented the maximum base temperature of the target and resulted from FEM simulations of the whole target wheel during cycles of 20 s irradiation time and 20 min cooldown time. With active cooling at the target shaft, a steady-state of a maximum temperature of the focal track of 860 °C was reached after four irradiation-cooldown cycles* [88].

Electron beam phase space

Thirdly, an electron beam phase space was used as a radiation source in the Monte Carlo simulations. This phase space represented the electron beam hitting the target of the preclinical LFxT prototype that my working team is currently constructing together with collaboration partners. Details of the electron accelerator and the phase space at the beam waist can be found in chapter 7.1.3. The electron beam had full widths at half maximum of 50 µm × 20 mm. Due to the use of tracking simulations to record the phase space, the z-position of the electrons varied by up to 3 mm before the x- and y-positions were projected onto one z-layer with the intercept theorem. The electron energy varied between 297–298 keV. Here, a three-dimensional model was necessary for the FEM simulations. The simulation volume had a size of $0.5 \times 30 \times 0.5\,\mathrm{mm}^3$ ($x \times y \times z$) with a larger *Mapped* mesh than before of $(7\,\mu\mathrm{m})^3$ due to random access memory limits of the in-house server. The material parameters were set back to temperature-independent.

Clinical LFxT

Lastly, the expected temperature increase at the focal spot was investigated for a clinical LFxT with an electron energy of 600 keV and an electron current of 2.5 A. Here, the first simulation setup, as described above, was used with a rectangular focal spot with a size of 50 µm × 30 mm, a target velocity of 200 m/s, and temperature-independent material parameters as the temperature dependence only had minor effects on the maximum temperature (see section 5.3.2).

5.2.3. Comparison to a commercial x-ray tube

Furthermore, the temperature increase at the focal spot was estimated for the rotating-envelope Straton x-ray tube (Siemens Healthcare GmbH, Erlangen, Germany) [105] for comparison of the thermal characteristics at the focal spot between the LFxT and a commercial, high-power x-ray tube. With Monte Carlo simulations as described in

*These FEM simulations were performed in Ansys Mechanical (version 19 R3, Ansys, Inc., Pennsylvania, USA) by my collaboration partner Anton Dimroth from the Forschungszentrum Jülich and the RWTH Aachen University.

section 5.2.2, the electron penetration depth, as per equation (5.16), and the absorbed fraction of a 150 keV electron beam hitting a tungsten target were estimated.

Then, the expected temperature increase was calculated in the heat conduction limit (5.13) and the heat capacity limit (5.15). The target material was a tungsten-rhenium alloy (WRe5[†]) with a mass density of $\rho = 19\,400\,\mathrm{kg/m^3}$, a specific heat capacity of $c = 133\,\mathrm{J/kg/K}$, and a thermal conductivity of $\lambda = 78\,\mathrm{W/m/K}$ [111, 112]. The focal track radius of 48 mm and the rotation frequency of 150 Hz resulted in a surface velocity of 45.2 m/s [105]. The anode angle of x-ray targets is typically in the range of 7–9° [113], whereof 9° were chosen for the calculations for the maximum temperature increase. According to Schardt et al. [105], the focal spot F1 features the highest surface power density of $(P/A)_{\mathrm{Straton}} = 1.56 \cdot 10^{10}\,\mathrm{W/m^2}$, resulting from a focal spot size of $0.6 \times 0.7\,\mathrm{mm^2}$ and a power of $P_{\mathrm{Straton}} = 42\,\mathrm{kW}$ that F1 can withstand for 20 s.

5.3. Results

5.3.1. Validation of the heat conduction limit and applicability of both limits

The theoretical temperature increase in the heat conduction limit according to equation (5.13) was verified with the numerical integration over time of equation (5.11). For a constant focal spot width, the theoretical and numerically calculated temperature increase coincided if the velocity was far beyond the limit for short exposures according to equation (5.12). Figure 5.2 shows the temperature increase from the start of exposure until the steady state for a focal spot width of 1 mm and 50 µm, for which the minimum velocities for short exposures were 2.30 m/s and 46.0 m/s, respectively. For a constant velocity of 200 m/s, the spot width must be wider than 11.5 µm to fulfill condition (5.12) for short exposure times. Therefore, the spot must be considerably wider than 11.5 µm for a temperature increase that is theoretically predicted by the heat conduction limit.

The condition for short exposure times was then set in relation to the transition width or transition velocity between the heat conduction and the heat capacity limit according to equations (5.17) and (5.18). As seen in table 5.1, there exists no velocity for a focal spot width of 50 µm for that the heat conduction limit is valid for short exposure times because the transition velocity to the heat capacity limit is slower than the minimum velocity for short exposure times in the heat conduction limit. For a spot width of 1 mm and a velocity of 200 m/s, there are valid ranges for both the heat conduction limit with short exposures and the heat capacity limit.

5.3.2. Simulations

According to the Monte Carlo simulations, the target absorbed 54.6 kW, i.e., 60.7 % of the primary electron beam power of 90 kW. The remaining energy that was backscattered at the target surface is addressed in chapter 6. The power density distribution widened by

[†]Tungsten 95 % mass fraction, rhenium 5 % mass fraction.

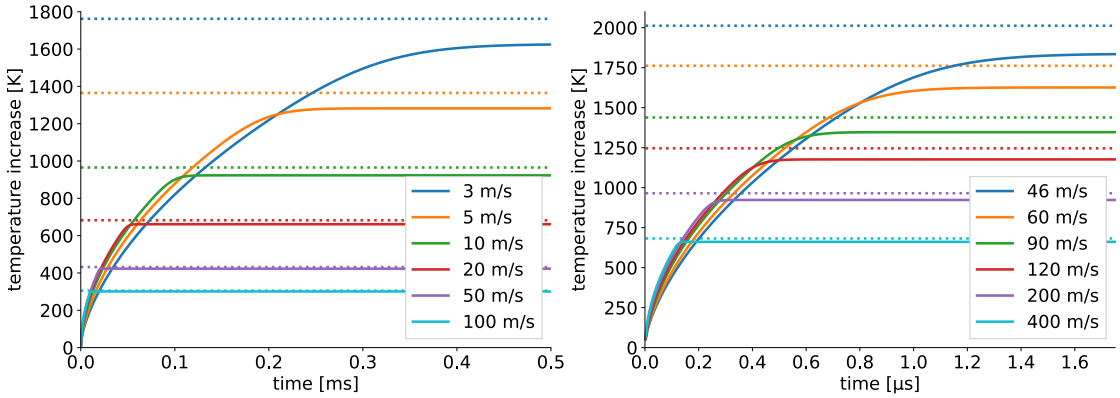

Figure 5.2.: Temperature increase from the start of exposure at 0 s until the steady state according to the heat conduction limit for a 1 mm wide (left) and a 50 µm wide (right) focal spot with a power of $P_{\text{cond}} = 54.6\,\text{kW}$. Horizontal dotted lines correspond to the theoretical temperature increase according to the heat conduction limit (equation (5.13)), solid lines to the respective values according to the heat equation.

a few micrometers with depth due to electron scattering. The maximum power density was found in a depth of 5 µm in tungsten and amounted to $2.0 \cdot 10^{15}\,\text{W/m}^3$ for the rectangular focal spot of 50 µm × 30 mm and to $7.5 \cdot 10^{15}\,\text{W/m}^3$ for the focal spot based on the electron beam phase space, respectively. In the same depth, the maximum energy absorption per depth interval was 10.1 keV/µm, yielding an electron penetration depth of $d = 29.7\,\mu\text{m}$ according to equation (5.16). Here, d specifies the depth at which the electrons would stop if they had the maximum stopping power (found at 5 µm depth) over their entire stopping path.

Rectangular focal spot — temperature dependence on focal spot width

For the rectangular focal spot, the FEM simulations of the boundary heat source matched the theoretical prediction of the heat conduction limit, which can be seen in figure 5.3 for

Table 5.1.: Focal spot width w_{se} and velocity v_{se} to fulfill the condition for short exposures in the heat conduction limit alongside the transition width w_{t} and transition velocity v_{t} between the heat conduction and heat capacity limit.

	Condition for short exposure (heat conduction)	Condition for heat conduction limit
Focal spot width 50 µm	$v_{\text{se}} > 46.0\,\text{m/s}$	$v_{\text{t}} < 7.64\,\text{m/s}$
Focal spot width 1 mm	$v_{\text{se}} > 2.30\,\text{m/s}$	$v_{\text{t}} < 152\,\text{m/s}$
Target velocity 200 m/s	$w_{\text{se}} > 11.5\,\mu\text{m}$	$w_{\text{t}} > 1.3\,\text{mm}$

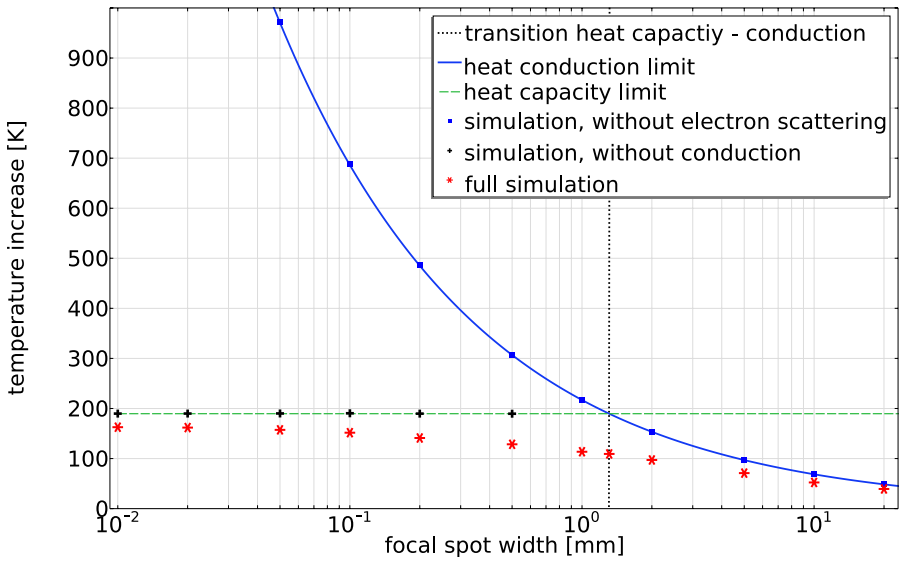

Figure 5.3.: Temperature increase at a rectangular focal spot in dependence of the spot width. The primary electron beam power was 90 kW, the target velocity was 200 m/s, and the spot length was 30 mm. Winter et al. [88]

a constant target velocity, varying focal spot width, and constant material parameters. If mainly heat conduction contributed to the heat dissipation, the temperature steeply increased for decreasing focal spot widths. The FEM simulations of the volume source with disabled thermal conduction matched the theoretical prediction of the heat capacity limit and confirmed the independence of the temperature increase of the focal spot width. Especially for very narrow spot widths, the temperature increase in the heat capacity limit was far lower than in the heat conduction limit.

The full simulations yielded a lower temperature increase than predicted by either limit because both heat dissipation mechanisms contributed, although by a different amount depending on the spot width. At the transition width of 1.3 mm between the heat conduction and the heat capacity limit, the full simulation resulted in a temperature increase of 109 K, while both limits predicted 190 K. For broad focal spots, the temperature increase approached the heat conduction limit, as seen in figure 5.3. A spot width of 20 mm resulted in a temperature increase that was less than 20 % below the prediction by the heat conduction limit. In contrast, the temperature increase approached the heat capacity limit for narrow focal spot widths. The LFxT with a spot width of 50 µm operates clearly in the heat capacity limit, where the full simulation resulted in a temperature increase of 157 K, which was 17 % below the prediction by the heat capacity limit.

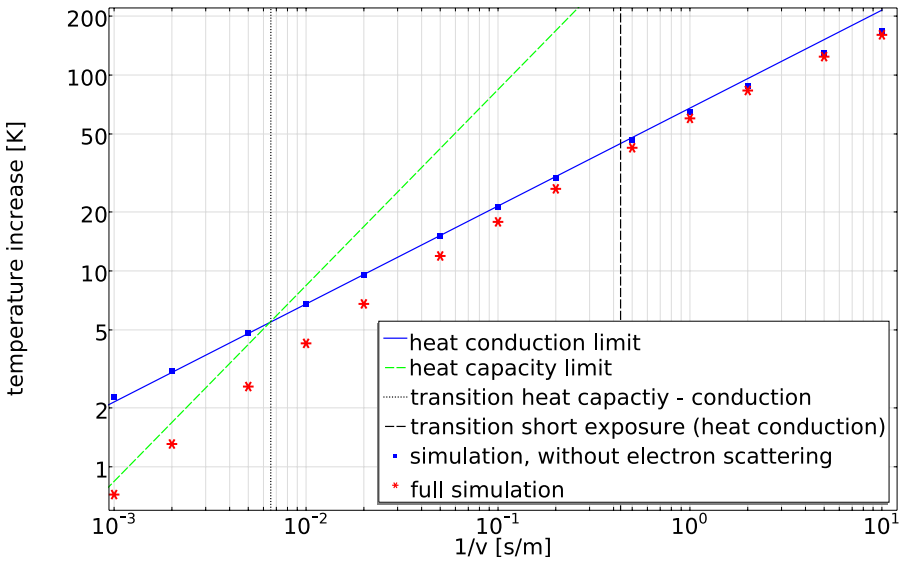

Figure 5.4.: Temperature increase at a rectangular focal spot in dependence of the target velocity v. The spot size was $1 \times 30\,\mathrm{mm}^2$, and the primary electron beam power was $P = 2\,\mathrm{kW}$.

Rectangular focal spot — temperature dependence on target velocity

Similar results to the previous subsection were found for the dependence of the temperature increase on the target velocity while holding the focal spot width constant at 1 mm. For high velocities, the full FEM simulations converged to the heat capacity limit, for low velocities, to the simulation of the boundary heat source (electron scattering disabled), as seen in figure 5.4. The simulations of the boundary heat source matched the prediction by the heat conduction limit for velocities fulfilling the condition for short exposure times (5.12). For velocities slower than 2.3 m/s, the temperature increase was, however, below the prediction of the heat conduction limit as lateral heat conduction could not be ignored. Here, the power density was normalized to a primary electron beam power of 2 kW for a resulting temperature increase in a reasonable range, which did not affect the qualitative analysis as the temperature increase scales linearly with the electron beam power if constant material parameters are given.

Rectangular focal spot — temperature-dependent material parameters

The FEM simulations with temperature-dependent material parameters of tungsten led to a similar temperature increase as the simulations with temperature-constant material parameters. For an initial temperature of 20 °C, the maximum temperature increase was 162 K, which was 5 K higher than for the simulations with constant material parameters. The reason for the difference was the slightly lower specific heat capacity according to equation (5.19) than for the temperature-independent parameters extracted from reference [63]. For an initial temperature of 860 °C, the temperature increased by a

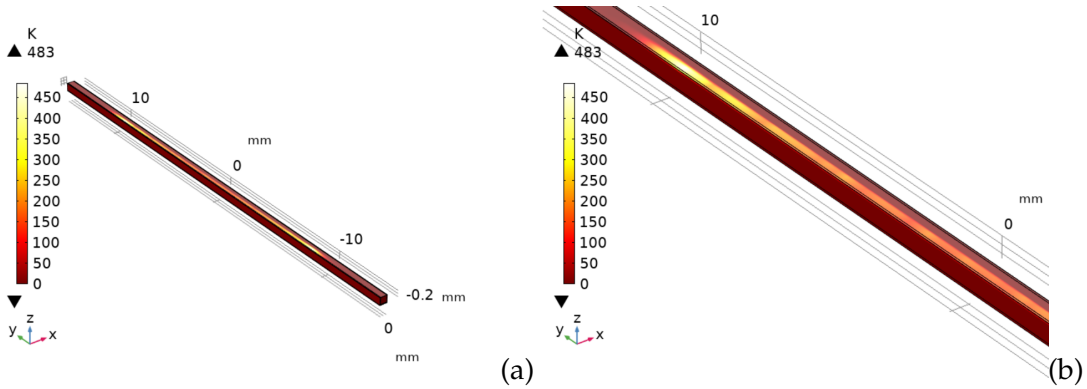

Figure 5.5.: Distribution of the temperature increase at the focal spot based on the electron beam phase space as an overview of the entire simulation volume (a) and as a zoom thereof (b). In this illustration, the electron beam with a primary power of 90 kW has passed along the positive x-direction up to the center of the simulation volume.

maximum of 150 K, which was lower than for the simulations with an initial temperature of 20 °C. This lower temperature increase resulted from the increasing specific heat capacity of tungsten with increasing temperature because these simulations with a focal spot width of 50 µm and a target velocity of 200 m/s were in the heat capacity limit.

Focal spot based on the electron beam phase space

The focal spot based on the phase space of the realistic electron beam led to an inhomogeneous temperature distribution according to the inhomogeneous electron distribution in the beam. The maximum temperature increase was 483 K at the periphery of the spot, as seen in figure 5.5, due to a higher electron density than at the center of the focal spot. The higher temperature increase compared to the homogeneous, rectangular focal spot resulted from the inhomogeneity and from the shorter spot length.

Clinical LFxT

In the Monte Carlo simulations of the clinical LFxT, a slightly higher fraction of 62.5 % of the primary electron beam power of 1.5 MW remained in the tungsten target due to the higher electron energy of 600 keV compared to the preclinical LFxT. The maximum energy deposit per depth interval was 8.17 keV/µm in a depth of 13 µm, which resulted in an electron penetration depth of $d = 73.4\,\mu\text{m}$ according to equation (5.16). The FEM simulations with a focal spot width of 50 µm resulted in a maximum temperature increase of 1180 K, while the heat capacity limit predicted 1280 K and the heat conduction limit predicted 16 600 K. The target velocity of 200 m/s was considerably higher than

the transition velocity of 1.2 m/s. Consequently, the clinical LFxT operates in the heat capacity limit.

5.3.3. Comparison to a commercial x-ray tube

For a 150 keV electron beam, the tungsten target absorbed 60.3 % of the primary beam power, and the penetration depth was 10.8 µm according to equation (5.16). The resultant transition focal spot width of 0.08 mm was considerably smaller than the focal spot width of the Straton x-ray tube of 0.6 mm. The Straton x-ray tube thus operates in the heat conduction limit, as do other typical commercial x-ray tubes.

With 60 % of the primary electron beam power of 42 kW being transformed into heat, the temperature at the focal spot increased by 2734 K in the heat conduction limit.[‡] Consequently, the temperature increase at the focal spot of the LFxT is expected to be lower than for the Straton x-ray tube, not only for the preclinical LFxT prototype but also for the clinical LFxT.

5.4. Discussion

In this chapter, the temperature increase after one passing of the electron beam on the target was investigated numerically. The assumption that the LFxT operates in the heat capacity limit was verified in dependence of both the focal spot width and the target velocity. The heat capacity limit brings high potential due to the independence of the temperature increase of the focal spot width. Hence, the focal spot width can be further decreased without bringing higher thermal load onto the target. Limits of the focal spot width remain lateral electron scattering in the target [63] and the electron beam optics, including space charge effects and a finite emittance of the electron beam [87].

For the realistic electron beam of the preclinical prototype, the temperature increase of less than 500 K appears uncritical for a target made of a tungsten-rhenium alloy. However, this temperature increase must be integrated into the heat management of the entire target wheel, the base temperature of which increases considerably during operation. As described in section 5.2.2 and reference [88], the maximum temperature at the focal track is expected to increase during the first four cycles of irradiation and cooldown phases up to a maximum of 860 °C. The maximum absolute temperature at the focal spot follows from the sum of the temperature increase after one passing and the maximum focal track temperature as approximately 1340 °C. With a melting point of the tungsten-rhenium alloy WRe5 above 3180 °C [110], this maximum temperature still appears uncritical. Moreover, the FEM simulations with an initial temperature of 860 °C exhibited another advantage of the heat capacity limit: The temperature increase after one passing of the electron beam decreased with increasing focal track base temperature because the specific heat capacity of tungsten rhenium increased. In contrast, the thermal

[‡]The temperature increase would be 7446 K according to the heat capacity limit, which, however, does not apply.

conductivity that determines the temperature increase in the heat conduction limit for conventional x-ray tubes decreases with increasing temperature [110]. Furthermore, the estimated temperature increase at the focal spot of the commercial Straton x-ray tube was even higher than that of the LFxT, which strengthens the confidence in the stability of the focal track of the LFxT.

Pronounced thermal gradients at the focal spot as well as different thermal expansion coefficients of the thin focal track material and the target base material lead to high thermal stresses that could damage the target. These thermal stresses, especially at the material interface and surface, are impracticable to simulate with solid state FEM models, which usually rely on bulk material and do not comprise microscopic effects such as recrystallization or phase changes. Furthermore, the material parameters are not fully known as they also depend on the conditioning of the target wheel after production. However, the thermal stresses at the focal spot of the LFxT are considered uncritical as the temperature increase after one passing of the electron beam is expected to be lower than that of the Straton x-ray tube that is commercially available and must therefore be robust. Despite the uncritical thermal stresses of the LFxT, the higher rotation speeds compared to conventional x-ray tubes induce additional stresses on the target, which need to be investigated during the target designing.

The theoretical estimates of the temperature increase in the heat conduction limit and the heat capacity limit as well as the FEM simulations were not fully independent but depended on provisional results of the Monte Carlo simulations. The Monte Carlo simulations provided the power fraction absorbed by the target P_{cond} for the calculation of the temperature increase in the heat conduction limit as well as the electron penetration depth d for the temperature increase in the heat capacity limit. Furthermore, the heat power density distribution resulting from Monte Carlo simulations was put in the FEM simulations as a heat source. These provisional results depended on the version of Geant4 underlying TOPAS and on the applied physics list. For a 500 keV electron beam, Geant4 version 10.4.p02 (from May 2018) yielded a 15 % lower d than Geant4 10.5.p01 (from April 2019, underlying TOPAS version 3.2.2) and Geant4 10.6.p03 (from November 2020, underlying TOPAS version 3.6.1) using the *G4EmPenelopePhysics* list. The *G4EmLivermorePhysics* list, also designed for low-energy interactions but drawing on different data libraries than than the *G4EmPenelopePhysics* list [95], yielded similar results as the *G4EmPenelopePhysics* list with differences in P_{cond} and d below 1 %. By using the *G4EmLivermorePolarizedPhysics* list in TOPAS version 3.6.1, the fraction of absorbed energy was up to 40 % higher and the electron penetration depth was up to 40 % lower than that of the *G4EmPenelopePhysics* list, respectively. Whether activating or deactivating the physics list option of ignoring deexcitation cuts, differences in P_{cond} and d amounted to 3 % and 5 %, respectively. Consequently, the choice of the physics list needs to be carefully considered. In this work, the simulations were performed with the most current version of TOPAS and the *G4EmPenelopePhysics* list particularly developed for low-energy interactions of non-polarized particles [95] (with default electromagnetic range limits; default step sizes for electrons and positrons; and the options fluorescence

electrons, Auger electrons, and particle induced x-ray emission activated; ignoring of deexcitation cuts deactivated). Furthermore, the results of the Monte Carlo simulations were used consistently for the estimation of the temperature increase in both limits and with FEM. Even though changes in P_{cond} and d relate directly to changes in the temperature increase at the focal spot, these uncertainties in the Monte Carlo simulations did not disparage the verification of the heat capacity limit.

A clinical LFxT, as presented, is assumed to operate in the heat capacity limit, too. The expected temperature increase at the focal spot after one passing of the electron beam might be too high for a conventional rotating target, though. The estimated temperature increase for the Straton x-ray tube is even higher, but the Straton x-ray tube employs a more elaborated cooling by its rotating-envelope design. Thereby, the anode backwall gets directly cooled by convection, which leads to higher cooling rates and a lower target base temperature compared to convective cooling through the target shaft [105]. Nevertheless, the cooling design of the LFxT prototype can be retained for the development of a higher-power clinical LFxT by replacing the conventional target materials by, e.g., carbon fiber reinforced carbon [88].

In conclusion, the numerical simulations demonstrated that the LFxT operates in the heat capacity limit. The heat capacity limit allows higher electron beam power densities with a lower focal spot temperature than the heat conduction limit of conventional x-ray tubes. The focal spot material of the LFxT seems robust against the occurring heat as the maximum temperature is lower than for the investigated commercial x-ray tube. For the development of a clinical LFxT, new target materials or a more elaborated cooling system seem necessary to withstand the thermal load from an electron beam power of 1.5 MW.

6. Backscatter electrons in the LFxT

6.1. Introduction

Less than one percent of the primary electron beam power produces the desired x-radiation at the focal spot. A large portion of the electrons scatters back from the target surface due to large-angle scattering at the high-Z material [114]. As described in chapter 3, there is no electric field inside the main vacuum chamber of the preclinical LFxT prototype. Hence, the backscattered electrons travel without external force to the vacuum chamber walls and deposit their energy as heat. As the electric field-free vacuum chamber is a particularity of the LFxT and not present in conventional x-ray tubes, its consequences on the heat load and on the focal spot width needed to be examined during the LFxT development.

A simplified version of the computer aided design (CAD) model of the LFxT prototype* used for the investigations in this chapter is depicted in figure 6.1. The vacuum chamber housing is made of stainless steel due to its high melting temperature, ductile behavior, and affordability as a base material. The main heat deposit is expected opposite the focal spot. Hence, there were cooling channels designated around the electron beamline entry port and around the x-ray exit window made of diamond (details to the window material can be found in chapter 7.3). A water cooling system was chosen because of a more efficient heat transfer of water compared to oil. During both the irradiation phase of 20 s and the cooldown phase of 20 min, the water will be pumped through several channels with cooling ribs close to the locations of the highest heat load. One cooling channel surrounds the electron beamline entry port; one channel is located beside the first one towards the rotation axis; one channel is placed in the slanted vacuum chamber wall close to the x-ray exit window; and one channel is incorporated into the flange of the x-ray exit window (all except the channel in the window flange can be seen in figure 6.1). The thermal energy from this cooling system as well as from the cooling system through the drive shaft and the motor is stored in a water tank and dissipated to the ambient air by a heat exchanger during the idle time of 20 min between subsequent irradiations.

The temperature of the vacuum chamber housing must not only stay below the melting temperature of the used stainless steel but as low as possible since the vacuum quality worsens at high temperatures as discussed in section 6.4. The maximum operating temperature of the x-ray exit window is limited by its flange gasket to 250 °C [115].

*The CAD model of the LFxT was developed and refined in the course of the LFxT development by the whole µFlash collaboration team. Main contributions came from Anton Dimroth, Christian Petrich, Dr. Christoph Matejcek, and Dan Ungureanu.

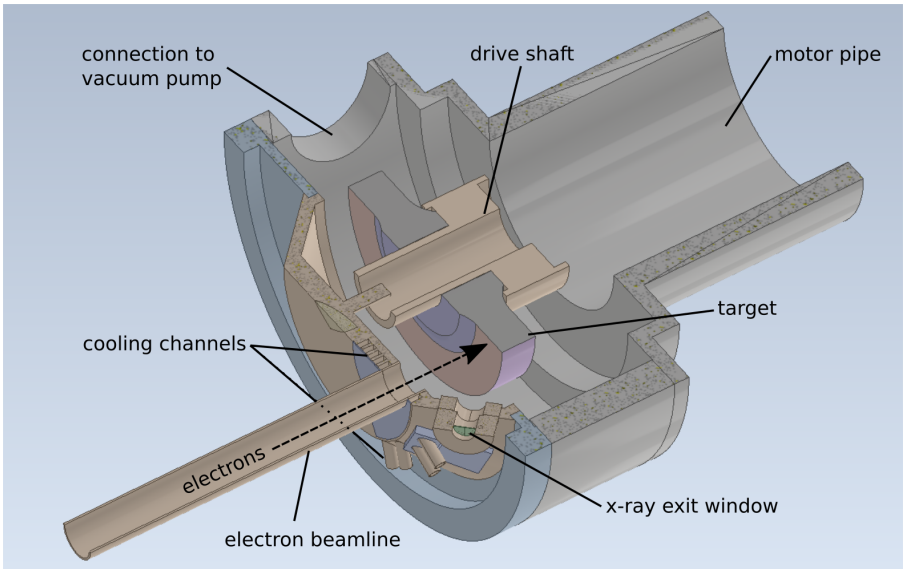

Figure 6.1.: The simplified model of the line-focus x-ray tube that was used for the simulations in this chapter.

In conventional x-ray tubes, only the target acts as the anode, while the vacuum chamber housing is on electric ground potential. The arising electric field in the vicinity of the focal spot makes the backscattered electrons returning to the target off the focal spot, which might widen the focal spot area [114]. A focal spot widening would be critical for the LFxT that relies on the very narrow focal spot for a sharp microbeam dose profile (see chapter 4 and Winter et al. [87]).

First, the distribution of backscattered electrons and the resulting heat load onto the vacuum chamber housing are investigated in section 6.2.1. In section 6.2.2, the focal spot width is analyzed in dependence of different electric field strengths for the development of a subsequent LFxT version that could have the vacuum chamber housing on ground potential.

6.2. Methods

6.2.1. Vacuum chamber heating

The electron scattering in the vacuum chamber was investigated with Monte Carlo simulations in TOPAS [94] (version 3.6.1, based on Geant4 version 10.6.p03). The physics list *G4EmPenelopePhysics* was used with default electromagnetic range limits (*EMRangeMin* = 100 eV, *EMRangeMax* = 500 MeV); default step sizes for electrons and positrons (step function parameters *dRoverRange* = 0.2, *finalRange* = 0.01 mm); and fluorescence electrons, Auger electrons, and particle induced x-ray emission activated, while ignoring of deexcitation cuts remained deactivated [95, 108].

The CAD model of the LFxT, as seen in figure 6.1, served as the geometry for the electron scattering simulations. The interest was mainly directed towards the x-ray exit window, the region around the electron beamline entry port, the cooling channels, and the remaining vacuum chamber in general. The target was set to tungsten, the remaining parts of the geometry to iron, representing stainless steel in the Monte Carlo simulations. The free space was set to vacuum with a mass density of $1.2 \cdot 10^{-10}\,\mathrm{mg/cm^3}$ corresponding to a vacuum quality of 10^{-7} mbar. Two different electron beams were simulated with 10^6 primary particles. One parallel, 300 keV beam with a homogeneous, rectangular focal spot of 50 µm × 30 mm and one realistic electron beam based on the phase space, as described in chapters 7.1.3, 4.2.3, and 5.2.2.

The backscattered electrons and produced photons were investigated with a hemispherical phase space detector with an inner radius of 16 mm on the target surface, surrounding the focal spot area and detecting all particles leaving the target underneath. Additionally, the energy deposit was scored in a parallel, material-free geometry encompassing the complete LFxT model in voxels of $2 \times 2 \times 2\,\mathrm{mm^3}$. Using Python (version 3.7.2), the energy deposit per voxel was transformed to the absolute absorbed power density by the voxel volume and by normalizing the number of primary particles in the Monte Carlo simulations per second to a primary electron beam current of 0.3 A.

To analyze the temperature increase at the vacuum chamber, these provisional results of the absolute power density were put into FEM simulations using Ansys Mechanical (version 19 R3, Ansys Inc., Pennsylvania, USA) as a heat source for an irradiation time of 20 s[†]. The target material was set to tungsten and the remaining material, including the x-ray window component, to stainless steel (AISI 316L). The rationale behind the material simplification of the x-ray window was the fact that the largest part of the window component is the flange that is made of stainless steel and limits the operating temperature of the window component, while the diamond itself can withstand higher temperatures. Furthermore, the heat capacity of diamond is in the same order of magnitude as that of stainless steel, whereas the thermal conductivity is markedly higher for diamond (see table 7.2). The initial and ambient temperatures were assumed to be 60 °C.

Two types of simulations were performed, with and without cooling of the vacuum chamber housing. For the cooling, there was one water channel surrounding the electron beamline entry port (heat transfer coefficient of $h_1 = 9.7 \cdot 10^4\,\mathrm{W/m^2/K}$ with a cooling area of $A_1 = 2.2 \cdot 10^{-3}\,\mathrm{m^2}$), one channel beside the first one towards the drive shaft ($h_2 = 3.5 \cdot 10^4\,\mathrm{W/m^2/K}$, $A_2 = 2.5 \cdot 10^{-3}\,\mathrm{m^2}$), one channel in the slanted wall between the electron beamline and the x-ray exit window ($h_3 = 2.0 \cdot 10^4\,\mathrm{W/m^2/K}$, $A_3 = 8.9 \cdot 10^{-4}\,\mathrm{m^2}$), and one channel inside the mounting flange of the x-ray exit window ($h_4 = 3.0 \cdot 10^4\,\mathrm{W/m^2/K}$, $A_4 = 1.9 \cdot 10^{-3}\,\mathrm{m^2}$). The different heat transfer coefficients

[†]The simulations using Ansys Mechanical were performed by my collaboration partner Anton Dimroth from the Forschungszentrum Jülich and the RWTH Aachen University.

resulted from the design of the cooling system and depended mainly on the coolant volume flow[‡].

6.2.2. Focal spot widening due to returning electrons

A subsequent LFxT version could have the vacuum chamber housing on ground potential and thus an electric field in the vicinity of the target. A preclinical LFxT with a 300 kVp x-ray spectrum could have an electric potential difference between the target and the vacuum chamber walls of 150 kV (with the cathode on −150 kV) or of 300 kV (with the cathode on ground potential). A clinical LFxT with a 600 kVp x-ray spectrum could have an electric potential difference in the vacuum chamber of 300 kV or of 600 kV accordingly.

The consequences of such an electric field in the vicinity of the focal spot on the spot width were investigated using Monte Carlo simulations in TOPAS with the same version and physics settings as mentioned in section 6.2.1. A parallel electron beam (10^7 primary particles) with an energy of 300 keV and a homogeneous, rectangular focal spot of 50 µm × 30 mm ($x \times y$) hit a tungsten target with a simulation volume of $0.1 \times 40 \times 0.05\,\mathrm{mm}^3$ ($x \times y \times z$). The remaining space was set to vacuum (mass density of $1.2 \cdot 10^{-6}\,\mathrm{mg/cm}^3$). The simulations were performed in absence and in presence of simplified iron walls representing the vacuum chamber housing. The walls are depicted in figure 6.2, and their distances to the focal spot matched the respective minimum distance in the CAD model in figure 6.1. An electric field pointed perpendicularly away from the target surface (positive z-direction, compare figure 6.2) so that backscattered electrons were accelerated to return to the target. The paths of the electrons were investigated for field strengths of 0 kV, 150 kV, 300 kV, and 600 kV across 7.9 cm, which was the distance of the parallel wall to the target surface. The energy deposit was scored in the target in voxels of $1 \times 1000 \times 1\,\mu\mathrm{m}^3$ ($x \times y \times z$).

6.3. Results

6.3.1. Vacuum chamber heating

Independent of the shape of the electron beam, the power of backscattered electrons was 34.8 kW, i.e., 38.2 % of the primary electron beam power. The number of backscattered electrons was 49.4 % of the primaries. The power of produced photons was only 0.56 % of the primary electron beam power, which matches the estimate by equation (1.2) that quantifies the electron-to-photon conversion efficiency, considering the atomic number $Z = 74$ of tungsten, the acceleration voltage of $U = 0.3\,\mathrm{MV}$, the number fraction 50.6 % of electrons penetrating into the target (not backscattered), and the phase space detector covering the half space $z > 0$ only[§].

[‡]The cooling system of the LFxT prototype was designed and estimated by my colleagues Christian Petrich and Sebastian Rötzer from the Technical University of Munich.

[§]$\eta = 10^{-3} \cdot 74 \cdot 0.3 \cdot 0.506/2 = 0.0056$.

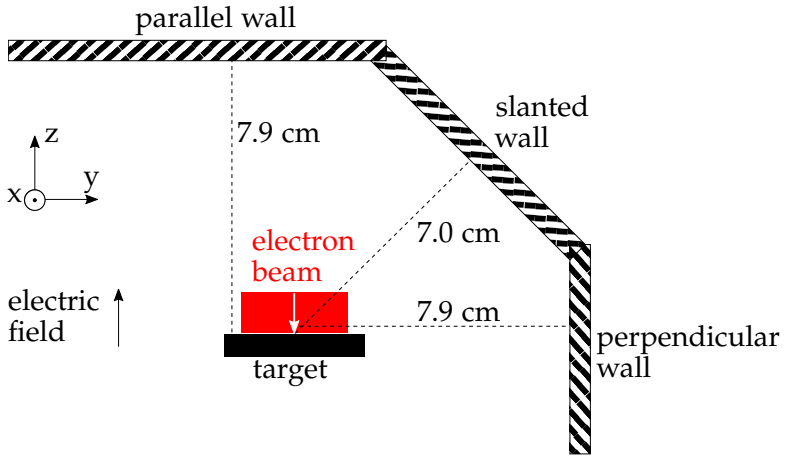

Figure 6.2.: Sketch of the simulation setup for the investigation of the focal spot widening due to backscattered electrons. The simulations were performed with different electric field strengths in presence and in absence of the simplified vacuum chamber walls, the naming of which refers to their orientation of the target surface. The point of origin was located at the center of the electron beam at the target surface.

The detected energy deposit in the CAD geometry amounted to 99.0 % of the primary electron beam energy, whereof 61.2 % remained at the focal spot and 38.8 % was distributed in the vacuum chamber housing. The maximum surface power density (outside of the focal spot) of 1.5 $\mathrm{MW/m^2}$ was reached in the vicinity of the x-ray exit window. The highest surface power density at the wall opposing the focal spot close to the beamline port was 1.3 $\mathrm{MW/m^2}$. The power density distributions can be seen in figure 6.3 for different cuts through the geometry. The speckles at low power densities originated from the randomness in Monte Carlo simulations.

Without any cooling, the heating resulted in a temperature up to 694 °C at the end of the irradiation time of 20 s, as seen in figure 6.4a. Cooling of the walls around the beamline and the x-ray exit window reduced the maximum temperature to 250 °C, as seen in figure 6.4b.

6.3.2. Focal spot widening due to returning electrons

The implementation of an electric field in the vicinity of the focal spot deflected the backscattered electrons from their straight paths, which they followed in absence of an electric field. The higher the electric field strength, the less electrons hit the wall parallel to the target surface, while the more electrons hit the slanted wall and the perpendicular wall at lower z-values. For an electric field strength of at least 300 kV across the distance of 7.9 cm between the target surface and the parallel wall, the scattered electrons did not reach the opposite wall but instead hit the slanted or perpendicular wall or passed the target to negative z-values due to their energy of below 300 keV. For the same reason,

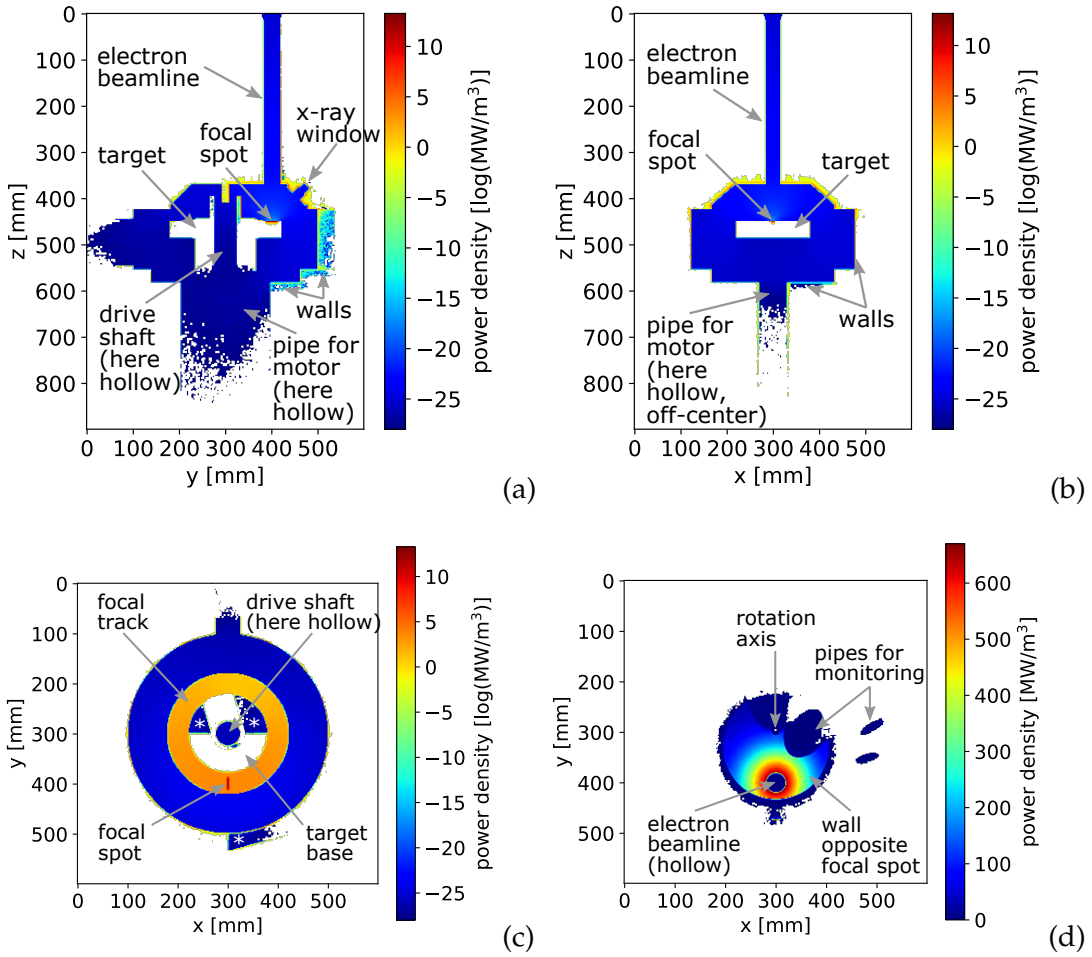

Figure 6.3.: Heat power density at the vacuum chamber housing due to backscattered electrons and produced x-rays. Cuts through the geometry at the focal spot at $x = 300\,\text{mm}$ (a), at $y = 390\,\text{mm}$ (b), at $z = 450\,\text{mm}$ that shows the focal track (c), and through the wall opposing the focal spot at $z = 368\,\text{mm}$ (d). The power density in panels (a)-(c) is displayed on a logarithmic scale; values below $10^{-28}\,\text{MW}/\text{m}^3$ are not displayed. Regions marked with a white asterisk * in panel (c) were artifacts from the geometry import in TOPAS but had no impact on the regions of interest.

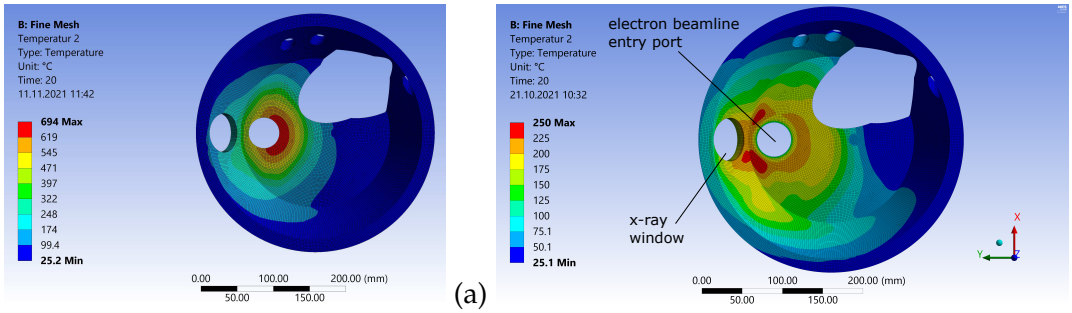

Figure 6.4.: Temperature at the interior of the vacuum chamber housing after an irradiation time of 20 s with a 90 kW electron beam without cooling (a, image by Anton Dimroth) and with cooling (b, Winter et al. [88]). The x-ray window, the electron beamline, the target, and other parts are not shown for a clear illustration.

an electric field strength of 600 kV across 7.9 cm caused all electrons to travel to negative z-values by passing the target (surface at $z = 0$) because the perpendicular wall had the same distance to the focal spot as the parallel wall, which defined the field strength.

Nevertheless, the size of the focal spot was independent of the applied electric fields. There was no increase in spot width or in spot length discernible. This result was observed in absence as well as in presence of the iron walls, which mainly absorbed incoming electrons and did not lead to considerable second-generation backscattering. Figure 6.5 displays the energy deposit profile along the short dimension of the focal spot (x-direction) at the target surface as well as in a depth of 5 µm, where the energy deposit was maximum, averaged over the central 30 mm in the direction of the long focal spot dimension (y-direction). The rounded edges of the energy deposit profile originated from electron scattering in the target.

6.4. Discussion

The backscattering electrons entail a trade-off between a low thermal load at the vacuum chamber housing (if the walls have a large distance to the focal spot) and a high dose rate that requires a short distance between the focal spot and the sample and accordingly a short distance between the focal spot and the x-ray exit window. For the LFxT prototype, measures were taken to shift this trade-off towards a higher dose rate without damaging the chamber housing: The chamber walls have a rather large thickness of 35 mm, and a water cooling system was applied with cooling ribs in the vicinity of highest heat loads. The water tank stores the heat during the short exposure time of 20 s and dissipates the energy to the ambient air during the cooldown time of 20 min between two irradiations.

The main heat load at the vacuum chamber housing was generated by backscattered electrons, the produced photons contributed only marginally. The number of

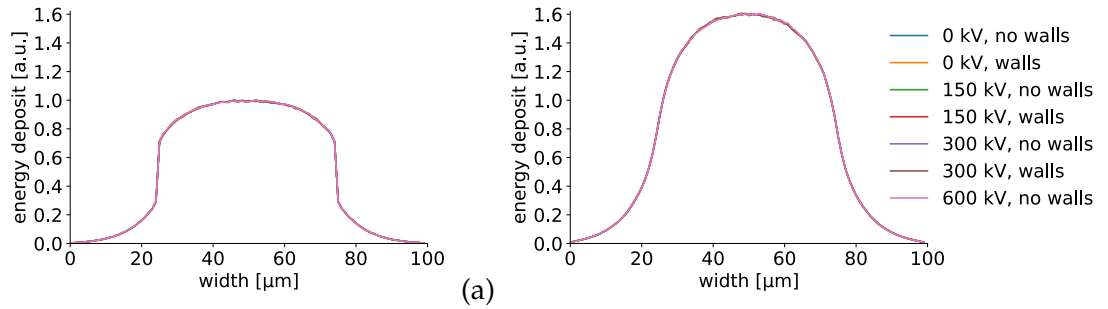

Figure 6.5.: Energy deposit at the focal spot along the x-direction at the surface (a) and at a depth of 5 µm in the tungsten target (b). No difference in focal spot width was detected for electric fields between 0–600 kV across 7.9 cm, independent of the presence of surrounding walls. All profiles were normalized to the maximum energy deposit at the target surface of the simulation with no electric field and no walls.

backscattered electrons in the simulations corresponded to the respective first generation backscatter coefficient for 300 keV electrons hitting a tungsten target simulated by Ali and Rogers [114] by a difference of 1.2 percentage points. The missing 1 % of the primary electron beam power that was not detected in the CAD geometry might have left the geometry as photons through the windows and vacuum chamber walls and mainly as backscattered electrons through the electron beamline and the openings of the vacuum chamber that connect to the vacuum pump and the motor (confer figure 6.1). The missing energy was so small though that it was neglected for the results in this chapter; it will especially not influence the locations of highest temperatures.

Without cooling, the vacuum chamber reached temperatures above the tolerances of the x-ray exit window made of diamond. Even though diamond transforms to graphite only at 1700 °C, the maximum temperature of the x-ray window should be below 250 °C due to the flange gasket [115]. This constraint could be satisfied by the simulations with cooling of the outer wall around the electron beamline and the x-ray window. For a safety margin, cooling channels are built into the window mounting for an effective cooling by means of a short distance between the cooling water and the location of highest temperature.

Despite the melting point of stainless steel being well above the maximum expected chamber wall temperature without cooling [111], the vacuum quality worsens at high temperatures due to a stronger gas permeation through the vacuum chamber walls. The diffusion is expected to be strongest for hydrogen, the smallest molecule in air. For a chamber temperature of 604 °C, the vacuum quality worsens from $3 \cdot 10^{-8}$ mbar to $2 \cdot 10^{-6}$ mbar in a conservatively analyzed timeframe of 1 min, while already for a chamber temperature of 402 °C, the vacuum can be kept at a pressure of 10^{-7} mbar in

the same timeframe[¶]. A vacuum pressure of 10^{-7} mbar is necessary in the vicinity of the cathode to not damage the thermionic barium-tungsten dispenser cathode (conservatively applying an order of magnitude safety margin) [116]. For additional safety, a vacuum pump close to the cathode can retain a differential vacuum that facilitates a vacuum quality at the cathode one order of magnitude better than in the target chamber. Accordingly, the temperature of the chamber walls should be kept as low as possible, and active cooling opposite the focal spot is vital.

The cooling system will be crucial for the functionality of the LFxT. The cooling parameters applied in the FEM simulations were estimated from the design of the cooling channels and the delivery rate of the pumps of the LFxT prototype. Film boiling must be avoided to ensure an effective water cooling and is not expected for the designed cooling system[||]. In case the cooling of the vacuum chamber walls is not sufficiently powerful for the heat produced during irradiation, the LFxT prototype might only be able to run for irradiation times shorter than 20 s or with less power than 90 kW. However even in that case, the functional principle of the LFxT should not be affected. Alternatively, further measures can be taken, e.g., a higher coolant volume flow, a thicker chamber wall, or a thermal storage at the locations of highest heat load that stores the heat during the irradiation time of 20 s and emits the heat during the cooldown time of 20 min. Possible materials of a thermal storage might be graphite or tungsten, which both have a higher melting point and a higher heat capacity than stainless steel [111, 117].

For the development of a more powerful clinical LFxT, the cooling system needs to be adapted to the respective vacuum chamber geometry and considered as a functionally critical component. On the one hand, the total heat load will not differ drastically from the preclinical prototype as the delivered dose will be similar. On the other hand, a higher dose rate will lead to a higher heat rate. For this reason, there is a need for either a fast and efficient cooling or for a large heat capacity for storing the thermal energy until the cooldown phase after irradiation. A further idea of coping with the high heat load is a magnetic deflection of the electrons in the vicinity of the target, as discussed in chapter 7.2.

According to the Monte Carlo simulations, the focal spot width will not widen with the presence of an electric field that accelerates the backscattered electrons back onto the target plane. In contrast, Ali and Rogers [114] found a non-negligible impact of off-focal x-radiation from electrons that were backscattered and returned back onto the target in a region of 3 cm radius around the desired focal spot. This off-focal radiation increased the magnitude of the x-radiation at the patient plane, and its impact was stronger for a higher tube voltage, a shorter interelectrode distance, and less collimation of the x-ray beam, among others [114]. From their results, it could be expected that returning

[¶]The calculations of the gas permeation through the chamber walls were performed by my colleague Dr. Christoph Matejcek from the Johannes Gutenberg University Mainz and the Technical University of Munich, assuming the chamber geometry of the CAD model of the LFxT prototype and a wall thickness of 10 mm.

[||]Estimate by my colleague Prof. Dr. Michael Butzek from the Forschungszentrum Jülich.

electrons also affect the focal spot width of the LFxT as the maximum tube voltage investigated by Ali and Rogers [114] was 300 kV, equivalent to the LFxT. However, the interelectrode distance of the LFxT of 7.9 cm was much larger than in the simulations by Ali and Rogers [114] who used 1.5 cm, which resulted in a much higher electric field strength than for the LFxT. As the backscattered electrons hit the target in a region of several centimeters around the focal spot, the probability of electrons hitting exactly the few micrometers next to the desired focal spot of 50 µm width was presumably too low to increase the spot width. Further, and most importantly, electrons that produce photons far off the desired focal spot are not expected to contribute to the microbeam x-ray field of the LFxT due to the strict collimation of the precisely aligned multislit collimator.

For the development of a clinical LFxT with an electron acceleration voltage of 600 kV, the consequences of an electric potential difference inside the vacuum chamber housing should be further investigated. If a vacuum chamber housing on ground potential (instead of on the target potential) does not affect the electronic focal spot, the construction of the electric insulation would be easier and less expensive. X-rays produced far off the focal spot presumably do not disturb the microbeam dose distribution due to the strict collimation but should nevertheless be examined by Monte Carlo simulations. However, the target would receive an even higher heat load if the electrons are accelerated back onto its surface, which needs to be considered in the design of the target and the cooling through the drive shaft.

7. Additional aspects of the LFxT development

The preclinical prototype of the line-focus x-ray tube (LFxT) comprises various components, which would be too many to investigate in detail in this work. Besides the topics addressed in the previous chapters, I assessed further aspects of the LFxT development, whereof the electron accelerator and beam optics, a magnetic deflection system of the electron beam between the accelerator and the target, and possible materials of the x-ray exit windows are presented in this chapter.

7.1. Electron accelerator

7.1.1. Introduction and requirements

The electron accelerator and electron beam optics are vital components of an x-ray tube since they define the electronic focal spot and thus the x-ray spectrum and the radiation field. The acceleration voltage of typical x-ray tubes for imaging lies in the range of 30–150 kV [90], whereas the LFxT prototype requires a voltage of 300 kV. Furthermore, the electron beam current needs to reach 0.3 A to obtain peak dose rates of 10 Gy/s at a distance of 20 cm from the focal spot (see chapter 4.3.2). The resulting electron beam power of 90 kW lies at the upper edge of common x-ray tube beam powers [90, 105], whereas the clinical LFxT requires a considerably higher power of 1.5 MW at an acceleration voltage of 600 kV.

The specifications of the LFxT, namely a micrometer-wide, strongly eccentric focal spot combined with a high beam current, put high requirements on the electron accelerator and beam optics. Hence, a new development of the electron accelerator for the LFxT prototype was needed. For effective microbeam radiotherapy (MRT) with a sharp peak-valley profile, the focal spot requires a width not larger than 50 µm (see chapter 4.3.1). The exact focal spot length is less important for the microbeam dose profile but should be in the range of 20–30 mm to obtain very high dose rates and at the same time distribute the heat load onto a large surface to prevent damage of the target (see chapter 5). Furthermore, very high dose rates demand a possibility to switch off the electron beam very fast in the timeframe of milliseconds to ensure safe irradiations. Moreover, the complete accelerator setup should be smaller than approximately one meter to fit into the compact concept of the LFxT and specifically into the x-ray cabinet that provides radiation protection.

This section addresses necessary electron beam characteristics for the accelerator development and a solution for the preclinical LFxT prototype with an acceleration voltage of 300 kV and a beam power of 90 kW, which was found in close collaboration with my colleague Dr. Christoph Matejcek from the University of Mainz and the Technical University of Munich. Then, the requirements for the spatial precision is presented at the beam waist, where the electrons hit the target surface. The last section discusses relevant adjustments for the development of the electron accelerator for a clinical LFxT with an electron acceleration voltage of 600 kV and a beam power of 1.5 MW.

7.1.2. Electron beam characteristics

A high beam quality is necessary for focusing the electron beam to a focal spot width in the micrometer range. More precisely, the electron beam must originate at the cathode with the lowest emittance possible, since the emittance can only increase in the course of acceleration and focusing but must be low for a narrow focal spot width at the target. At the same time, the space charge increases the cross section of the beam as well as the emittance due to non-linear effects.

Emittance

The transverse emittance is a measure of the electron beam quality and quantifies the possibility of beam focusing. The emittance can be regarded independently in each spatial direction so that, here, the emittance is addressed in the x-direction only, in which the beam dimension is most critical for a sharp microbeam dose profile (see chapter 4.3.1). The root mean square (rms) emittance is defined as

$$\epsilon_{\mathrm{rms}} = \sqrt{\langle x^2 \rangle \langle x'^2 \rangle - \langle x x' \rangle^2}\,, \tag{7.1}$$

where $\sqrt{\langle x^2 \rangle}$ indicates the rms of the beam envelope in the x-direction and $\sqrt{\langle x'^2 \rangle}$ the angle of the rms envelope to the x-axis [118, 119]. For an emittance comparison at different positions of an accelerator, the rms emittance is normalized with the longitudinal electron momentum to

$$\epsilon^{\mathrm{n}}_{\mathrm{rms}} = \gamma\beta\sqrt{\langle x^2 \rangle \langle x'^2 \rangle - \langle x x' \rangle^2}\,, \tag{7.2}$$

where $\beta = v/c$ denotes the ratio of the electron velocity v to the speed of light c and $\gamma = 1/\sqrt{1-\beta^2}$ the relativistic Lorentz factor. The Lorentz factor can be calculated for a relativistic electron beam accelerated by the voltage U as

$$\gamma = \frac{E_{\mathrm{tot}}}{E_0} = \frac{E_{\mathrm{kin}} + E_0}{E_0} = \frac{e_0 U}{m_0 c^2} + 1\,, \tag{7.3}$$

where E_{tot} indicates the total energy, E_0 the rest energy, and E_{kin} the kinetic energy; e_0 and m_0 are the charge and the rest mass of an electron, respectively. The rms transverse direction $\sqrt{\langle x'^2 \rangle}$ of the electron beam can be simplified by the small-angle approximation

as $\sqrt{\langle x'^2 \rangle} = \sqrt{\overline{p_x^2}} \Big/ \langle p_z \rangle$. The non-relativistic transverse momentum p_x depends on the cathode temperature T_c, while the relativistic longitudinal momentum p_z depends on the relativistic velocity β after acceleration as [118, 120]

$$\begin{aligned} \sqrt{\overline{p_x^2}} &= \sqrt{m_0 k_B T_c}\,, \\ p_z &= \gamma\beta m_0 c\,, \end{aligned} \tag{7.4}$$

with the Boltzmann constant k_B, resulting in the rms transverse direction

$$\sqrt{\langle x'^2 \rangle} = \frac{\sqrt{\overline{p_x^2}}}{p_z} = \frac{1}{\gamma\beta}\sqrt{\frac{k_B T_c}{m_0 c^2}}\,. \tag{7.5}$$

At the cathode, the correlation term in equation (7.2) is assumed to vanish, and hence the normalized emittance follows as

$$\epsilon^{\mathrm{n}}_{\mathrm{rms}} = \sigma_x \sqrt{\frac{k_B T_c}{m_0 c^2}}\,, \tag{7.6}$$

where σ_x is the rms radius of the exit area of the electrons, with $\sigma_x = d_c/4$ for a circular cathode with a diameter d_c [121].

For the preclinical LFxT prototype, an acceleration voltage of 300 kV yields a Lorentz factor of $\gamma = 1.59$ and a relativistic electron velocity after acceleration of $\beta = 0.78$. Barium-tungsten dispenser cathodes (type 411M) as a potential cathode choice (see section 7.1.3) can deliver a maximum beam current density of $15\,\mathrm{A/cm^2}$ at their maximum operating temperature of 1470 K [122]. Consequently, the minimum emitter area is $2\,\mathrm{mm^2}$ and hence the minimum diameter of a circular cathode surface is $d_c = 1.6\,\mathrm{mm}$ for a beam current of 0.3 A. The rms emittance follows as $\epsilon^{\mathrm{n}}_{\mathrm{rms}} = 0.20\,\mathrm{mm \cdot mrad}$ according to equation (7.6). Under the assumption that the correlation term still vanishes and the emittance does not increase in the course of the accelerator, the divergence of the beam at the target surface can be approximated from equations (7.2) and (7.6) with the full beam width at the focal spot of $d_s = 0.05\,\mathrm{mm}$,

$$x' = \frac{\epsilon^{\mathrm{n}}_{\mathrm{rms}}}{\gamma\beta\sigma_x} = \frac{4\epsilon^{\mathrm{n}}_{\mathrm{rms}}}{\gamma\beta d_s}\,, \tag{7.7}$$

which leads to a divergence of $x' = 12.9\,\mathrm{mrad}$ or $0.74°$. A maximum beam diameter of $d_q = 10\,\mathrm{mm}$ at the quadrupoles (see section 7.1.3) yields a maximum focal distance of $f_{\max} = 0.5 \cdot d_q / \tan(x') = 39\,\mathrm{cm}$. Consequently, the focusing optics need to have a sufficiently strong power to achieve this focal distance.

The clinical LFxT will have an acceleration voltage of $U = 600\,\mathrm{kV}$ and an electron beam current of 2.5 A. Assuming the same types of cathode and quadrupole, it follows that $\gamma = 2.17$, $\beta = 0.89$, $d_c = 4.6\,\mathrm{mm}$, $\epsilon^{\mathrm{n}}_{\mathrm{rms}} = 0.57\,\mathrm{mm \cdot mrad}$, $x' = 23.6\,\mathrm{mrad}$, and $f_{\max} = 21\,\mathrm{cm}$. The clinical LFxT thus requires considerably stronger focusing optics than

the preclinical LFxT prototype due to both a higher beam current and a shorter focal distance. Alternative accelerator setups for the clinical LFxT are discussed in section 7.1.5.

In contrast to linear beam optics considered so far, the emittance increases in non-linear electromagnetic fields, which arise for example due to spherical aberration of quadrupoles, chromatic dispersion in deflection or focusing magnets, or non-homogeneous space charge fields [119]. A higher emittance then requires even stronger focusing powers to achieve the desired focal spot width of 50 µm. Stronger focusing powers enlarge the non-linear fringe fields of the magnets, which in turn further increases the emittance. Moreover, a stronger focusing decreases the focal distance so that the target needs to be closer to the focusing magnets, which brings additional challenges regarding the construction and the heat management of the LFxT. For this reason, comprehensive tracking simulations are needed for the development of the electron accelerator and beam optics of the preclinical and clinical LFxT.

Space charge

An electron within a high current density experiences a defocusing Coulomb force due to the electric repulsion off close-by electrons. For a cylindrical beam, the underlying space charge ρ can be derived from the beam current I as

$$\begin{aligned} I &= \frac{Ne_0}{\Delta t} = \frac{Ne_0 \cdot v_z}{\Delta t \cdot \Delta z/\Delta t} = \frac{Ne_0 v_z}{\Delta z} = \frac{Ne_0 v_z A}{V} = \frac{Ne_0 \beta c A}{V}\,, \\ \Rightarrow \rho &= \frac{Ne_0}{V} = \frac{I}{\beta c A} = \frac{I}{\beta c \pi R^2}\,. \end{aligned} \tag{7.8}$$

N denotes the number of electrons with charge e_0 per time interval Δt, $v_z = \Delta z/\Delta t = \beta c$ the longitudinal velocity, and $V = A \cdot \Delta z$ a volume element with a circular cross section $A = \pi R^2$ perpendicular to Δz. Assuming an electron beam that travels in the z-direction and has a radius R of the beam envelope in the y-direction, the electric field strength E is given by

$$\vec{E} = \frac{\rho}{2\varepsilon_0} R \vec{e_y} = \frac{I}{2\pi\varepsilon_0 \beta c R} \vec{e_y}\,, \tag{7.9}$$

where ε_0 is the electric constant.

At the same time, the electron beam self-induces a magnetic field, which is non-negligible for relativistic electron energies. For the electron beam of equation (7.9), the magnetic flux density $\vec{B}$ is given by

$$\begin{aligned} \vec{B} &= \frac{1}{c^2} \vec{v} \times \vec{E} \\ &= \frac{1}{c^2} (\beta c \vec{e_z}) \times \left(\frac{I}{2\pi\varepsilon_0 \beta c R} \vec{e_y} \right) \\ &= \frac{I}{2\pi\varepsilon_0 c^2 R} (-\vec{e_x})\,. \end{aligned} \tag{7.10}$$

Accordingly, the total radial electromagnetic force F_R to a relativistic electron at the beam envelope of a cylindrical beam is given by the sum of the Coulomb force F_C and the Lorentz force F_L as

$$\begin{aligned}\vec{F_R} &= \vec{F_C} + \vec{F_L} \\ &= e_0(\vec{E} + \vec{v} \times \vec{B}) \\ &= e_0 \left[\frac{I}{2\pi\varepsilon_0 \beta c R} \vec{e_y} + (\beta c \vec{e_z}) \times \frac{I}{2\pi\varepsilon_0 c^2 R} \left(-\vec{e_x}\right) \right] \\ &= \frac{e_0 I}{2\pi\varepsilon_0 R} \left[\frac{1}{\beta c} \vec{e_y} + \frac{\beta}{c} \left(-\vec{e_y}\right) \right] \\ &= \frac{e_0 I}{2\pi\varepsilon_0 \beta c R} \vec{e_y} \left(1 - \beta^2\right) \\ &= \frac{e_0 I}{2\pi\varepsilon_0 \beta c R \gamma^2} \vec{e_y} \,,\end{aligned} \tag{7.11}$$

utilizing the relation $\left(1 - \beta^2\right) = 1/\gamma^2$. The magnetic force has thus a focusing component and counteracts the Coulomb field by a factor of $1/\gamma^2$ (compare equations (7.9) and (7.11)) for any beam geometry [123]. Equation (7.11) demonstrates that the space charge has stronger effects for higher electron beam currents on the one hand and lower kinetic energies on the other hand.

For an estimate of the space charge effects of the LFxT, the space charge-induced envelope increase was calculated for a drifting, cylindrical electron beam based on the approach by Humphries [123]. Identifying the electromagnetic force in equation (7.11) with the relativistic electron mass multiplied by the acceleration $\left(\gamma m_0 \cdot \mathrm{d}^2 R/\mathrm{d}t^2\right)$ and converting the time derivative into a space derivative by $(\mathrm{d}/\mathrm{d}t = (\beta c)\mathrm{d}/\mathrm{d}z)$, the equation of motion can be simplified with the generalized beam perveance K as

$$\begin{aligned}\frac{\mathrm{d}^2 R}{\mathrm{d}z^2} &= \frac{K}{R} \,, \\ K &= \frac{e_0 I}{2\pi\varepsilon_0 m_0 \left(\beta\gamma c\right)^3} \,.\end{aligned} \tag{7.12}$$

To find the ratio of beam radius increase $\chi = R/r_w$ relative to the smallest radius r_w at the beam waist, Humphries [123] defined an auxiliary variable

$$F(\chi) = \sqrt{2K} \frac{z}{r_w} \,, \tag{7.13}$$

with the drift distance z from the beam waist and the relation

$$F(\chi) = \int_1^{\chi} \frac{\mathrm{d}y}{\sqrt{\ln y}} \,. \tag{7.14}$$

A derivation can be found in reference [123].

For 300 keV electrons, the arising magnetic field counteracts the space charge force by a factor of $1/\gamma^2 = 0.40$. The generalized beam perveance of $K = 1.85 \cdot 10^{-5}$ follows

from a beam current of $I = 0.3\,\mathrm{A}$. Assuming an electronic focal spot with a diameter of 50 µm, i.e., a waist radius of $r_w = 25\,\mu\mathrm{m}$ of a cylindrical beam, and an exemplary drift length of $z = 1\,\mathrm{cm}$, equations (7.13) and (7.14) provide $F(\chi) = 2.43$ and $\chi = 2.25$ (with the aid of table 5.1 in reference [123]). The beam radius therefore increases by a factor of 2.25 over a drift length of 1 cm. For a 600 keV, 2.5 A electron beam, the generalized beam perveance is $K = 4.07 \cdot 10^{-5}$, and the beam radius increases by a factor of 3.44 over a drift length of 1 cm. For both the preclinical and clinical LFxT, a drift distance of 1 mm leads to an envelope increase of considerably less than 10 %. These estimates indicate that although the space charge forces might need to be compensated by additional focusing, these forces do not presumably prevent a focal spot width in the micrometer range, even for a cylindrical electron beam.

Even more, the electron beam of the LFxT has a strongly eccentric cross section to distribute the thermal load at the target surface over a larger area (see chapter 5). For a paraxial sheet beam with a width x_0 that is much smaller than the other dimensions y_0, z_0 and a uniform current density per unit length $J = 2e_0 n_0 \beta c x_0$, the diverging force can be derived in a similar way as equation (7.11) and is given by

$$F_{x_0} = \frac{e_0 J}{2\varepsilon_0 \gamma^2 \beta c} = \frac{e_0^2 n_0 x_0}{\varepsilon_0 \gamma^2}\,, \tag{7.15}$$

with the volumetric particle density n_0 [123]. The beam current density per unit length of an electron beam with a rectangular cross section of 50 µm × 20 mm decreases by a factor of 509 compared to a cylindrical electron beam with a diameter of 50 µm. Consequently, the diverging force due to space charge decreases by a similar factor and thus plays only a marginal role for the strongly eccentric electron beam at the focal spot of the LFxT.

These estimates were performed for a homogeneous charge distribution within the electron beam. Non-homogeneous charge distributions, however, result in non-linear space charge fields and thus in an increase in the rms emittance [119]. The K-V equations (named after Kapchinskij and Vladimirskij) can be used for more sophisticated calculations of the influence of the space charge on the beam dimensions in linear approximation, while non-linear effects need to be investigated by tracking simulations [118, 119].

At the cathode, electrons have a considerably lower longitudinal velocity and are thus more influenced by space charge forces than after acceleration (see equations (7.11) and (7.15)). To counteract these forces, a focusing element at the cathode is advisable [121]. Tracking simulations of the electron beam have shown that a Pierce electrode at the cathode of the LFxT prototype can compensate the space charge forces.*

7.1.3. Realization for the LFxT prototype and focal spot distribution

The electron accelerator of the LFxT comprises the basic components of accelerators in conventional x-ray tubes, i.e., a cathode, an anode, and focusing elements. However,

*The tracking simulations were performed by my colleague Dr. Christoph Matejcek.

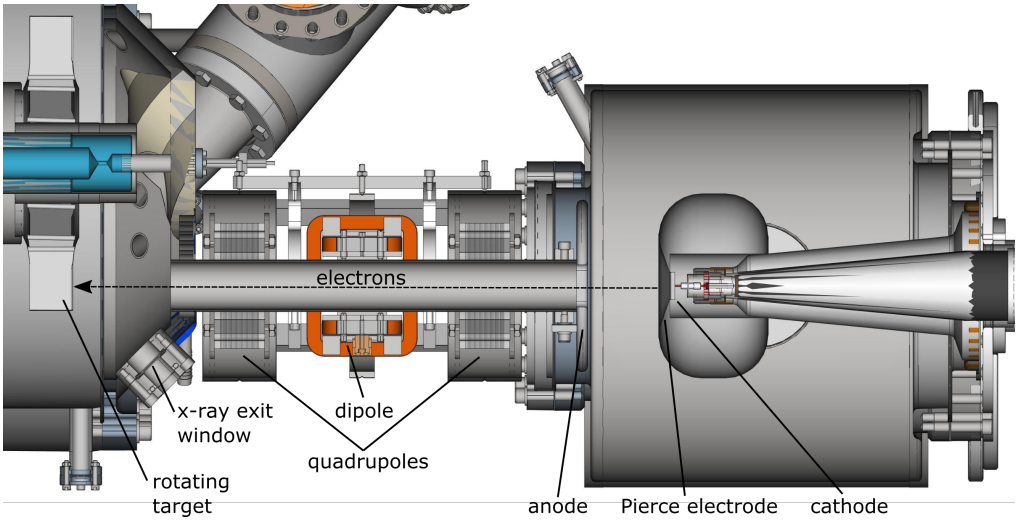

Figure 7.1.: Construction model of the electron accelerator of the LFxT. The distance from the cathode to the target surface is approximately 54 cm.

these components are constructed in a way to match the specific requirements of the strongly eccentric focal spot of the LFxT. Figure 7.1 shows the setup of the electron accelerator including the beam optics[†].

Thermionic cathodes, such as barium-tungsten dispenser cathodes, provide stable emission of high currents and promise a long lifetime [124]. An eccentric cathode shape was chosen to achieve a small emittance in the short dimension (x), while providing a high electron beam current from a large emitting area [87]. Tracking simulations revealed a suitable cathode width of 0.4 mm in the x-direction. Smaller cathodes are more challenging and thus less precise to manufacture and would further require higher operating temperatures, which entail a shorter lifetime. The cathode will be indirectly heated, which produces a more homogeneous beam profile along the long dimension of a rectangular cathode compared to a direct cathode heating inducing a magnetic field by the current inside the cathode [125].

The electron beam of the LFxT is prefocused mainly in the x-direction by a slanted Pierce electrode to balance the space charge forces, which are strongest at the cathode before the electrons are accelerated [121]. In this way, the electron beam is kept off the stray field at the periphery of the quadrupoles that would otherwise increase the emittance. The beam diameter should be smaller than 10 mm for the investigated quadrupoles. During standard operation, the Pierce electrode is on the same electric potential as the cathode for prefocusing the beam. Additionally, the Pierce electrode can be used for a very fast beam switch-off in the microsecond range by increasing the

[†]The construction model of the LFxT was developed and refined in the course of the LFxT development by the whole µFlash collaboration team. Main contributions came from Dr. Christoph Matejcek, Anton Dimroth, Christian Petrich, and Dan Ungureanu.

negative potential to approximately −600 V relative to the cathode, i.e., to −150.6 kV to electric ground, to suppress the electric field at the cathode.

In the space between the cathode and the anode, acceleration tubes can provide a homogeneously increasing electric potential for acceleration, an electric insulation between the negative and positive poles, and an additional focusing to keep the electron beam centered. For an eccentric beam, rectangular tubes are better suited than circular tubes because of a smaller required space for the rectangular cross section. Besides the high costs of rectangular acceleration tubes, a disadvantage is the long drift distance and therefore a rather low electric field strength. Conversely, with a stronger electric field, space charge effects decrease so that the beam diameter and the emittance remain smaller. For this reason, acceleration tubes were omitted, and simpler insulators were instead included between the cathode and the anode. In the LFxT construction, the acceleration voltage of 300 kV is built up across 12 cm.

Behind the anode, quadrupole magnets are ideal for creating a strongly eccentric focal spot since they naturally focus the electron beam in one direction and defocus in the perpendicular direction. One quadrupole allows the definition of the size of the electron beam in one dimension, within the limits of the electron beam characteristics and the quadrupole. It was ascertained that focusing the electron beam to a width of 50 µm (x-direction) would result in a beam length considerably larger than 30 mm (y-direction). Hence, two quadrupoles were included to facilitate two-dimensional focusing of the electron beam and for a higher flexibility to vary the spot size. A concurrent adjustment of the focal distance would require an additional focusing magnet, which is, however, not needed for the LFxT prototype. Figure 7.2 shows the evolution of the beam width (x-direction) along the beamline. The first quadrupole slightly focuses the beam in the y-direction and thus defocuses in the x-direction. A wide beam in the x-direction experiences then a stronger focusing by the second quadrupole, which facilitates a micrometer-wide focal spot. At the same time, the beam length is constrained to 20–30 mm in the y-direction.

Between the two quadrupoles, a dipole magnet was added as steerer that can recenter the electron beam. A central position of the electrons in the quadrupoles avoids the fringe fields, which would lead to an emittance growth, especially in the second quadrupole having a strong focusing field. Moreover, precise centering in the y-direction is important since the electron beam needs to completely hit the focal track material of the target. The focal track material has a safety margin of only few millimeters to the target base material that cannot withstand the electron beam power. Conversely, centering in the x-direction, i.e., along the focal track velocity, is less essential for the machine safety; nevertheless, the multislit collimator needs to be aligned with the focal spot for a sharp microbeam dose profile (see section 7.1.4).

In conventional x-ray tubes, the target is on anode potential, whereas the vacuum chamber housing is typically on ground potential. Consequently, electrons that are backscattered at the target surface are accelerated back onto the target and impinge next to the focal spot. The resulting off-focal radiation can amount to 10 % of the patient dose

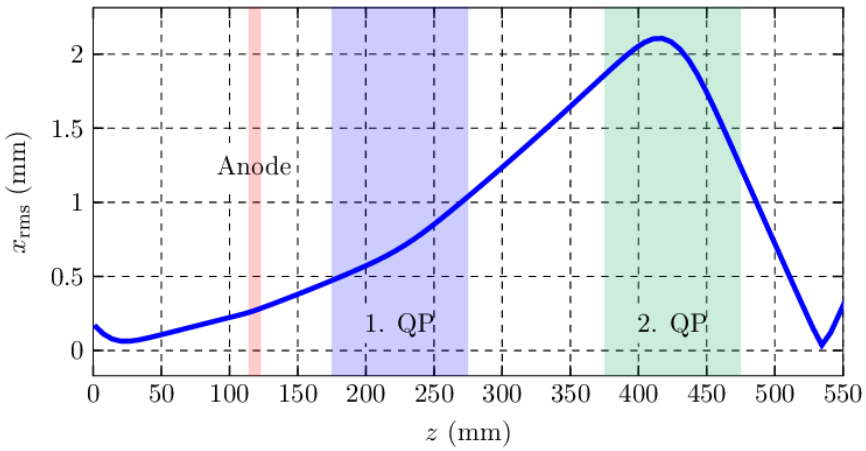

Figure 7.2.: Electron beam width in the direction of the short dimension of the focal spot as root mean square (rms) along the beamline. At the cathode (at $z = 0\,\mathrm{mm}$), the beam is prefocused by a Pierce electrode. Behind the anode, the beam width gets defocused by the first quadrupole (QP) before getting strongly focused by the second QP. The tracking simulations were performed and the figure was created by my colleague Dr. Christoph Matejcek.

[114]. In the LFxT construction, the target and the anode are separated. Thereby, the complete vacuum chamber including its housing and the drive train of the target are on anode potential, i.e., on $+150\,\mathrm{kV}$ relative to ground potential. Details and consequences of this setup are described in detail in chapter 6.

Tracking simulations demonstrated the feasibility of the presented accelerator and beam optics to achieve the required focal spot dimensions of $50\,\mu\mathrm{m} \times 20\,\mathrm{mm}$ as full width at half maximum (FWHM). Figure 7.3 presents the current density profile at the beam waist, where the electrons hit the target. The resulting phase space of the electron beam at its waist was used as a basis for the assessment of the microbeam dose distribution (see chapter 4), of the temperature increase of the vacuum chamber housing due to backscattering electrons (see chapter 6), and of the temperature increase at the focal spot (see chapter 5). The latter assessment revealed the importance of a rather homogeneous current density across the focal spot area for a lower maximum temperature of the focal track material. For this reason, the tracking simulations were finally optimized for a slightly smoother profile in the y-direction (not shown).

A high vacuum facilitates an undisturbed electron beam path from the cathode to the target. Moreover, the cathode requires a high vacuum with an air pressure below 10^{-6}–$10^{-7}\,\mathrm{mbar}$ for good durability [90, 116]. A higher pressure shortens the lifetime by poisoning the cathode with hydroxides and carbonates, which reduce emission and can cause blisters and cracks at the cathode surface [116, 126]. A separate vacuum pump will thus retain a high vacuum close to the cathode, which is the most sensitive component in terms of the vacuum quality. Moreover, the vacuum chamber needs to be baked out

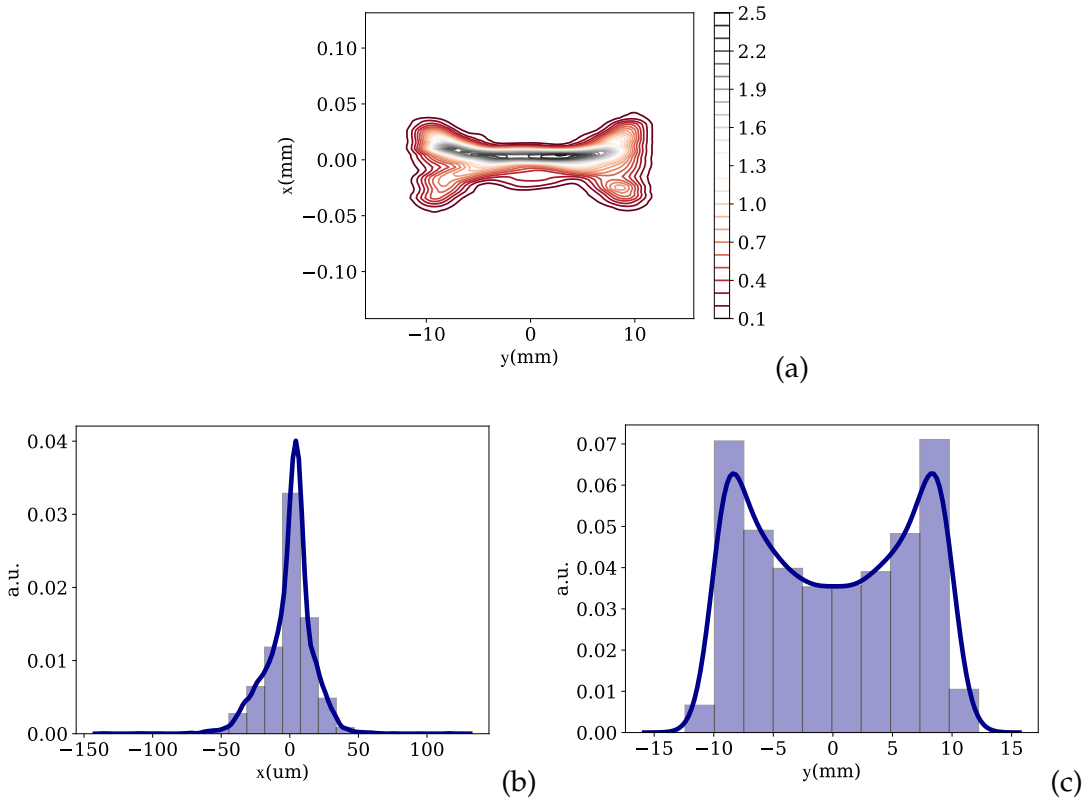

Figure 7.3.: Electron beam at the focal spot. (a) The color bar indicates the beam current density [a.u.]. (b, c) Current density profiles across the short and long focal spot dimension, respectively. Note the different dimensions of the axes. The results and figures were created by my colleague Dr. Christoph Matejcek.

before irradiations to reduce desorption from the high-temperature target material but also from the vacuum chamber housing.

7.1.4. Target precision requirements

The electron beam exhibits a waist, which should be at the target surface for the smallest focal spot possible. As soon as the target or the waist moves in the beam direction, the size of the focal spot increases, which needs to be corrected for by the quadrupole magnets. Reasons for a shift of the target surface can be thermal expansion, bending of the target due to the one-sided thermal load, target vibrations, or vacuum pump vibrations. The beam current intensity can vary due to output fluctuations of the thermionic cathode or power supply fluctuations of the quadrupoles and electrodes.

The impact of alignment shifts between the target surface and the beam waist was investigated in the direction of the peak-valley profile (x-direction, compare figures 4.3 and 5.1) and in the beam direction (z-direction). In TOPAS, Monte Carlo simulations

were performed in the same way as described in chapter 4.2.3 with the only variation being the shift of the electron beam phase space in either the x- or z-direction.

A stationary shift of the electron beam in the x-direction yielded a shift of the peaks and a slanted truncation of the peaks for shifts larger than 200 µm for geometrical reasons. For shifts up to 100 µm, the peak dose rate, the valley dose rate, the FWHM of the peaks, the peak-to-valley dose ratio (PVDR), and the lateral penumbras from the peaks to the neighboring valleys did not change. A shift of 200 µm resulted in a decrease of 4 % of the FWHM and a decrease of 2.5 % of the peak dose rate. The PVDR increased for shifts larger than 200 µm due to a stronger decrease in the valley dose than in the peak dose for truncated peaks. Even though a high PVDR is desirable for MRT, the multislit collimator should be aligned with the focal spot to achieve the highest peak dose rate and the desired FWHM that is defined by the collimator.

A temporal wobbling of the electron beam in the x-direction is equivalent to a smeared and thus broader focal spot. In chapter 4.2.1, the effect of the spot width on the microbeam dose profile was investigated in detail. For example, a wobbling by $\pm$125 µm of a beam with an original width of 50 µm corresponds to an effective focal spot width of 300 µm, which resulted in a PVDR decrease of 38 % in 50 mm water depth compared to the PVDR of the original beam width of 50 µm (see chapter 4.3.1). Hence, the microbeam dose profile is more prone to temporal instabilities than to time-stable changes in the relative position of the electron beam to the multislit collimator.

For an assessment of an alignment shift between the target surface and the beam waist in the beam direction (z-direction), the shape of a drifting electron beam close to its waist can be described by

$$r^2 = \varepsilon\beta_0 + \frac{\varepsilon}{\beta_0}\left(z - z_0\right)^2 , \tag{7.16}$$

with the parameters of the phase space ellipse ε and β_0 [127]. For the LFxT, the beam radius is $R = 0.025\,\mathrm{mm}$ at the waist z_0 corresponding to half the focal spot width. The quadrupole of interest has a focal length of $f = 100\,\mathrm{mm}$ and a maximum beam diameter of 10 mm. Applying these values to equation (7.16), i.e., $r\left(z = 100\,\mathrm{mm}\right) = 5\,\mathrm{mm}$, results in $\varepsilon\beta_0 = R^2 = (0.025\,\mathrm{mm})^2$, $\varepsilon/\beta_0 = 0.0025$, $\varepsilon = 0.001\,25\,\mathrm{mm}$, and $\beta_0 = 0.5\,\mathrm{mm}$. Table 7.1 lists relationships between the target shifts, the effective focal spot widths according to equation (7.16), and resulting PVDRs and FWHM at a water depth of 50 mm. Target shifts up to 200 µm were not perceptible in the PVDR or FWHM. For a shift of 400 µm, the PVDR decreased by 0.4 % and the FWHM increased by 3 %.

A rough estimate of the thermal expansion of the focal track material results in a shift of 4.5 µm, assuming a temperature increase of 1000 K, a thermal expansion coefficient of tungsten of 4.5 µm/m/K [111], and a focal track thickness of 1 mm. Even though the target base material of tungsten-zirconium-molybdenum has a higher thermal expansion coefficient, the temperature increase is much lower in the target base. For this reason, a thermal expansion in the micrometer range is irrelevant for the electron beam focusing. A larger displacement of the target surface arises from the one-sided heating of the target. The target thermally expands stronger on the side that faces the electron beam

Table 7.1.: Effects of a shift of the target surface in the electron beam direction on the focal spot width according to equation (7.16), and resulting from Monte Carlo simulations, the peak-to-valley dose ratio (PVDR) and the full width at half maximum (FWHM), both scored at a water depth of 50 mm.

Target shift [mm]	Focal spot width [µm]	Mean PVDR	Mean FWHM [µm]
0.0	50	22.9	63
0.2	54	22.9	63
0.4	64	22.8	65
0.6	78	22.3	66
0.8	94	21.8	69
1.0	112	21.2	73

than on the opposite site, which results in a bending of the target away from the electron source. As the bending is less severe for a thicker target, a target thickness of 50 mm was chosen, limited by state-of-the-art manufacturing techniques [88]. For the optimized target design, finite element analyses resulted in a shift of the target surface of less than 0.1 mm in the z-direction[‡]. This bending is not critical and a readjustment of the quadrupoles does not seem necessary (compare table 7.1).

In conclusion, the stationary x-position should be correct to 200 µm, the temporal shift in the x-direction should be below ± 25 µm, and the shift in the beam direction (z-direction) should be below 0.8 mm to prevent a PVDR decrease of more than 5 % at a water depth of 50 mm.

7.1.5. Clinical LFxT

To achieve peak dose rates above 100 Gy/s, the clinical LFxT will have a higher electron energy of 600 keV and a considerably higher beam current of 2.5 A, which involves a redevelopment of the electron accelerator and beam optics. The insulation between the cathode and the anode as well as to surrounding components needs to feature a higher blocking voltage. A higher beam current induces stronger space charge effects, while a higher electric field strength (assuming the same acceleration distance as for the preclinical LFxT prototype) slightly counteracts the more pronounced widening of the electron beam. Nevertheless, the quadrupoles must be more powerful than for the preclinical LFxT to compensate the beam widening due to space charge. Certainly, the focal spot width needs to be retained at 50 µm for a sharp microbeam dose profile (see chapter 4.3.1).

For the considerably higher current densities, a different cathode type seems necessary. In the field of thermionic cathodes, lanthanum hexaboride (LaB_6) cathodes might be a

[‡]These simulations were performed by my collaboration partners Yunzhe Zhang and Sebastian Rötzer from the Technical University of Munich as well as Anton Dimroth from the Forschungszentrum Jülich.

good choice because of their higher electron yield per area and thus a smaller emitting area [87, 123]. Even though LaB_6 cathodes need a higher operation temperature of approximately 1700 °C, they deliver an electron beam with a lower emittance, have lower demands on the vacuum quality (10^{-5} mbar), and a longer lifetime than barium tungsten dispenser cathodes [123, 126]. A main disadvantage is a low shock resistivity due to the brittleness of LaB_6 and thus a high fragility during production and operation [128]. A different approach can be photocathodes, which utilize the photoelectric effect for electron emission: A high-power laser hits a surface coating material with a low work function so that electrons are emitted and accelerated towards the anode. Photocathodes operate at room temperature, emit electrons with a small average transverse velocity, can deliver high current densities, and thus have a considerably lower emittance compared to thermionic cathodes [120, 123].

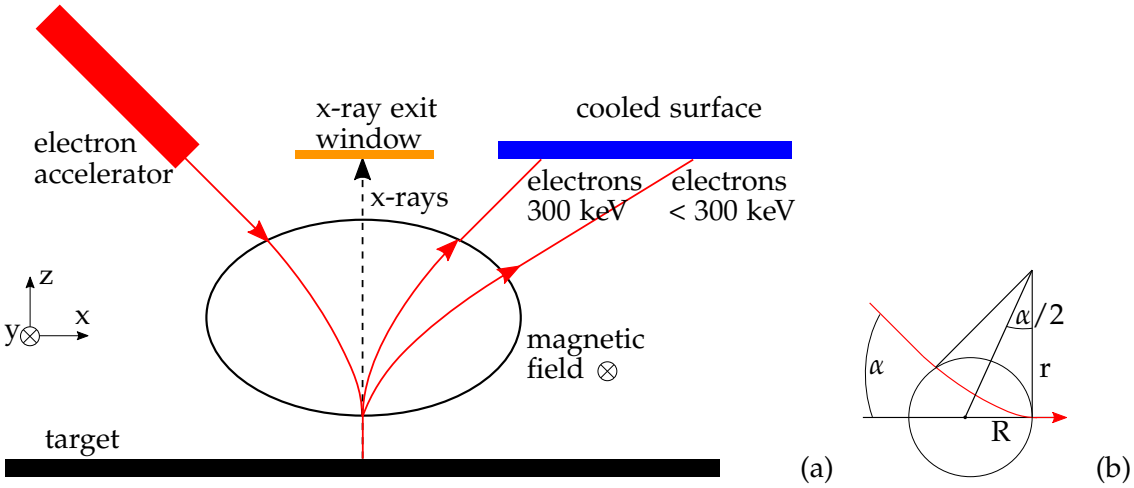

Figure 7.4.: (a) Idea of a magnetic deflection system at the target surface to protect the x-ray exit window and the electron accelerator from backscattered electrons. (b) Relationship between the radius of a cylindrical magnetic field R, the bending radius of the electron beam r, and the deflection angle α.

7.2. Magnetic deflection of the electron beam

7.2.1. Introduction

Backscattered electrons from the target surface travel to the vacuum chamber housing and deposit a high load onto the chamber walls and the x-ray exit window (see chapter 6). Based on that observation, the idea of a magnetic deflection system was developed to protect heat-sensitive components, mainly the quadrupoles in the electron beam optics and the x-ray exit window, from overheating. Figure 7.4a depicts this idea: A magnetic field between the accelerator and the target deflects the backscattered electrons so that they travel to a cooled surface of the vacuum chamber housing. Thereby, the electron accelerator and the x-ray exit window are protected. The produced x-rays are not affected by the magnetic field since they have no electric charge. In this section, consequences of a magnetic deflection system in the vicinity of the target surface was investigated.

7.2.2. Methods

The influence of a magnetic field was assessed with Monte Carlo simulations in TOPAS [94] (version 3.2.2, based on Geant4 version 10.5.p01). The *G4EmPenelopePhysics* list was used with default electromagnetic range limits (*EMRangeMin* = 100 eV, *EMRangeMax* = 500 MeV), default step sizes for electrons and positrons (step function parameters *dRoverRange* = 0.2, *finalRange* = 0.01 mm), and fluorescence electrons, Auger electrons, and particle-induced x-ray emission activated [95, 99]. Figure 7.5 illustrates the setup of the simulations for a deflection angle of the primary electrons of 90°. A rectangular

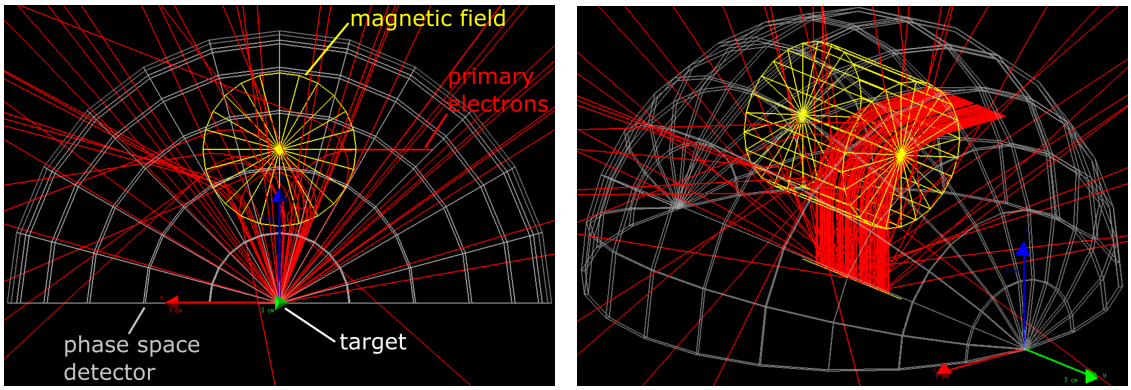

Figure 7.5.: Simulation setup at two viewing angles. A magnetic field from a dipole deflects the primary and backscattered electrons. The magnetic field points in the positive y-direction (green arrow) and deflects 300 keV electrons by 90°. Red arrow: x-direction, blue arrow: z-direction.

electron beam with a size of 50 µm × 30 mm and an energy of 300 keV was deflected by either 0°, 45°, or 90° by a dipole magnet and hit a target made of pure tungsten in the negative z-direction. The simplified magnetic field was oriented in the positive y-direction, located with its center 4 cm in the positive z-direction above the target surface, and had a cylindrical shape with a radius of 2 cm, a length of 4 cm, and the required magnetic flux density for the respective deflection angle.

The momentum p of an electron on a trajectory with a bending radius r caused by a magnetic flux density B, which is oriented perpendicular to the velocity of the electron, can be calculated as

$$p = e_0 B r \,. \tag{7.17}$$

The momentum of a relativistic electron is $p = \gamma m_0 \beta c$ so that the required magnetic flux density can be retrieved from

$$B = \frac{\gamma m_0 \beta c}{e_0 r} \,. \tag{7.18}$$

The relationship of the bending radius r of the electron beam trajectory and the radius of the cylindrical magnetic field R is depicted in figure 7.4b, i.e.,

$$r = \frac{R}{\tan(\alpha/2)} \,, \tag{7.19}$$

with the assumption of $R = 2$ cm in these simulations.

Electrons with an energy of 300 keV have a relative velocity of $\beta = 0.78$ and $\gamma = 1.59$. A deflection angle of 45° required a bending radius of $r_{45°} = 4.8$ cm and thus a magnetic flux density of $B_{45°} = 0.044$ T. For a deflection angle of 90°, the bending radius equaled $r_{90°} = 2.0$ cm and the required magnetic flux density was $B_{90°} = 0.106$ T.

Backscattered electrons and produced photons were scored by a hemispherical phase space detector with a radius of 7 cm, located centrally, contiguously on the target, as

depicted in figure 7.5. The phase space scorer saved the properties of the particles passing the inner surface of the detector with the position of the particles, the direction cosines U and V of their momentum with regard to the x-axis and the y-axis, respectively, their total energy, the particle type, and the algebraic sign of their direction cosine W with regard to the z-axis [129]. For the deflection angles of 0°, 45°, and 90°, the respective phase space was analyzed using Matlab (version R2018b, The MathWorks Inc., USA). The direction cosines U and V of all scored electrons were converted into direction angles u and v, which denoted the angles between the vector of momentum and the unit base vectors of the positive x- and the y-axis, respectively. The direction angles u and v were rounded to integers, and the electron energy was accumulated separately for each u and v, forming an angular energy histogram.

7.2.3. Results and Discussion

As expected, the magnetic field did not influence the distribution, intensity, or spectrum of produced photons, rather only the primary electron beam and the backscattered electrons. The energy of all scored photons amounted to only 1.4 % of the total scored energy of all particles. The backscattered electrons were deflected towards the positive x-direction (red arrow in figure 7.5), i.e., in the opposite direction of the electron accelerator, which was the goal of the magnetic deflection system. Electrons of lower energy were deflected with a smaller radius and hence by a larger angle than electrons of higher energy, which can also be derived from equations (7.18) and (7.19).

The magnetic field distorted the distribution of backscattered electrons that was otherwise symmetric to the x-axis without a magnetic field. Figure 7.6 shows the energy histogram of the direction angles of the momenta of backscattered electrons for the Monte Carlo simulations carried out with deflection angles of 0°, 45°, and 90°. The specific shape of the angular energy distribution depended on the specific geometry described above. Here, electrons that were backscattered at a small angle to the target surface did not travel through the spatially restricted magnetic field. Nevertheless, the qualitative effect of an exemplary magnetic field in the vicinity of the target can be investigated with these simulations.

Concerning the direction angle of the electron momentum with regard to the x-axis, the maximum of the angular energy was higher in the presence of a magnetic field than without a magnetic field. The maximum angular energy was farther shifted to lower x-angles, i.e., in the positive x-direction, the larger the deflection angle. At a direction angle perpendicular to the x-axis, the scored energy decreased in the presence of a magnetic field. This decrease was stronger for a higher magnetic flux density. Concerning the direction angle with regard to the y-axis, the energy distribution was symmetric and did not change between simulations without a magnetic field and a deflection angle of 45°. In contrast, the energy decreased at a direction angle perpendicular to the y-axis for a deflection of 90° due to a relevant portion of backscattered electrons that missed the hemispherical phase space detector and traveled to negative z-values (four electrons in figure 7.5). This decrease in scored energy did not happen for a deflection angle of

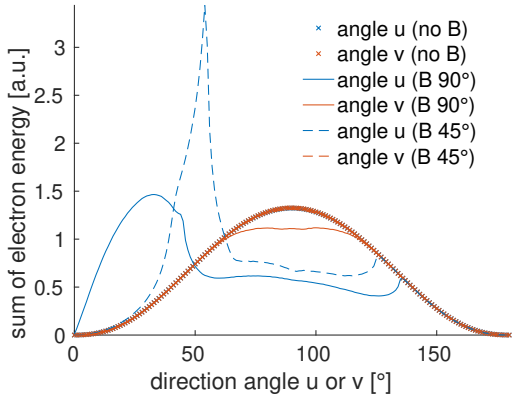

Figure 7.6.: Angular energy distribution of electrons backscattered from the target surface with three magnetic flux densities between the target and the detector. The summed energy of electrons detected at a specific direction angle u and v between the momentum direction and the unit base vectors of the x-axis or y-axis, respectively, is shown for the absence of a magnetic field (no B) as well as for deflection angles of the primary electron beam of 90° (B 90°) and 45° (B 45°).

45° because of the specific setup with a distance of 2 cm between the target surface and the magnetic field border, the magnetic field radius of 2 cm, and the radius of the phase space detector of 7 cm.

These results demonstrated that a magnetic deflection of the electron beam can partially protect the electron beamline from backscattered electrons without interfering with the produced photons, even though the simulation setup was largely simplified. The direction of the maximum angular energy of backscattered electrons was shifted towards smaller angles to the target surface. In that direction of the maximum energy, the distance from the focal spot to the vacuum chamber wall increases and thus the heat load density decreases according to the inverse square law if the wall is parallel to the target surface. However, the protection of the wall must be ensured for the increased maximum angular energy deposit. A deflection angle of the primary electron beam of less than 90° is advisable to spread the backscattered electrons to the vacuum chamber walls instead of to the target that already receives a high heat load from the primary electrons (see chapter 5 and Winter et al. [88]). Nevertheless, an implementation of a magnetic deflection system at the target surface needs further investigation with more detailed simulations including a model of the realistic vacuum chamber housing and a realistic shape and size of the magnetic field including the non-linear fringe fields, which depend on the component that generates the magnetic field.

Suitable magnetic fields could be generated by different electromagnetic components and could have different shapes, e.g., cylindrical, triangular, or quadrilateral. Electromagnetic coils have the advantage of allowing an adjustment of the magnetic field

strength, which is useful if different electron energies are used in the x-ray tube. If a dipole magnet is used instead, an iron yoke causes a lower emittance growth compared to air-cored coils. A further possibility is a Wien filter, which is typically used as an electron velocity filter, with an electric field, e.g., from a capacitor, and a magnetic field perpendicular to each other and perpendicular to the primary electron velocity [130, 131]. Correctly adjusted, the Wien filter does not influence the primary electron beam, if the electric force and the Lorentz force balance, but only deflects backscattered electrons. For an easy handling in case of adjustments or repairing, the electromagnetic component for deflection should be located outside of the vacuum chamber, which would, however, require a large magnet and a sophisticated electromagnetic shielding concept.

In conclusion, a magnetic field allows a deflection of the backscattered electrons away from the heat-sensitive electron beamline and the x-ray exit window. However, the resulting non-homogeneous electron distribution with a higher maximum intensity than without a magnetic field brings different problems and thus needs to be worth the effort of the more complicated electron beam optics. For these reasons, no magnetic deflection system will be implemented at the LFxT prototype but an efficient cooling system was instead developed close to the vacuum chamber locations that receive the highest heat loads (see chapter 6.1).

7.3. X-ray windows

7.3.1. Introduction

The x-ray tube is evacuated, while air surrounds the irradiated sample. X-ray windows realize the barrier between vacuum and air, where only low-energy x-rays should be filtered and higher-energy x-rays should leave the vacuum chamber unaffectedly. In contrast, backscattered electrons should be completely blocked for radiation protection safety. The window aperture defines the dimensions of the divergent radiation field at a certain distance.

In conventional x-ray tubes, the used portion of the x-radiation is tapped at a shallow angle from the inclined target surface to decrease the optical focal spot size compared to the thermal focal spot size [90, 104]. X-ray windows typically consist of a submillimeter-thick sheet of beryllium, titanium, or stainless steel [104, 105, 111].

The LFxT comprises two types of x-ray windows, namely one window for MRT and two windows for imaging, e.g., phase contrast x-ray imaging. For high dose rates, the MRT window is located at an angle of 45° to the normal to the target surface (see chapter 4.3.2). The imaging windows are located at 90° to the target surface normal, parallel to the short or long dimension of the focal spot, respectively, to minimize the optical focal spot size in one dimension in each case (see figure 8.2). The MRT window needs to withstand a very high heat load resulting from backscattered electrons in the electric field-free vacuum chamber, whereas the imaging windows receive a considerably lower heat load (see chapter 6.3). Furthermore, the windows need to fit into the construction of the LFxT. In this section, the mechanical, thermal, and radiation-absorbing requirements for the x-ray windows of the LFxT are discussed, and suitable solutions for the windows are suggested.

7.3.2. Requirements

The x-ray windows of the LFxT need to fulfill several essential requirements for the functionality of the LFxT. First, the MRT window needs to be highly heat-resistant to withstand a surface heat load of $1.5\,\mathrm{MW/m^2}$ for the irradiation time of 20 s (see chapter 6.3). The heat load mainly results from backscattered electrons of less than 300 keV, which, furthermore, need to be fully absorbed. The heat resistance includes resistance to melting, strong bending, bursting, rupture, or becoming dislodged from the holder. For that purpose, the window material should have a high melting temperature, a high specific heat capacity, and a high heat conductivity. Also, the attachment of the window to its holder and to the vacuum chamber housing should exhibit a good heat transfer. Second, all windows need a low x-ray absorption, especially for photons above 50 keV. Photons of lower energy are considered not useful for MRT due to their steep depth-dose curve [22]. For imaging, the most relevant x-ray energies are at the K-edges of tungsten at 58–69 keV (see chapter 8). For a low x-ray absorption, the window material should have a low mass attenuation coefficient, a low density, and a small thickness. Third, the

material of all windows should be chemically inert to avoid chemical reactions with the holder material or with air. Fourth, the windows and their attachments to the vacuum chamber housing must be high vacuum tight up to a pressure of 10^{-7} mbar, which prevents damage of the thermionic barium-tungsten dispenser cathode [116].

Additional requirements for the x-ray windows allow an easy mounting into the LFxT construction and ensure the largest possible field of view at the same time. The free aperture of the MRT window should shape an x-ray field of $20 \times 20\,\mathrm{mm}^2$ at a distance of 20 cm from the focal spot to allow an irradiation of a whole mouse brain in preclinical MRT experiments [132]. At the same time, the overall dimensions of all window holders and their attachments to the vacuum chamber housing should be as small as possible since the constructing space is limited. Furthermore, the windows should be linked to the vacuum chamber housing by a common flange to easily allow a contingent replacement. The material of the windows and their mountings should be electrically conductive as the backscattered electrons otherwise charge the window leading to an electric field inside the vacuum chamber. The electrical conductivity is more important for the MRT window than for the imaging windows due to the aforementioned distribution of backscattered electrons. For an easy handling, the windows with their mountings should be atoxic and, lastly, the costs should fit into the available budget.

7.3.3. Materials

To find suitable x-ray window materials fulfilling the listed requirements for the LFxT, beryllium, graphite, diamond, carbon fiber reinforced carbon (CFRC), titanium, and stainless steel were assessed. Table 7.2 displays relevant characteristics of these materials. The energy output was calculated for a 300 kVp x-ray spectrum from a tungsten target filtered by 1.0 mm of the respective material with energy-dependent mass attenuation coefficients from the U.S. National Institute of Standards and Technology (NIST) [97]. All investigated materials are brazeable or solderable.

Advantages of beryllium, the most common x-ray window material, are a low atomic number, a low density, and thus a high energy output. Furthermore, beryllium has a very high specific heat capacity, and a high melting temperature. Conversely, beryllium is rather expensive and a strategic material, meaning that any usage must be officially granted. Moreover, beryllium salts are highly poisonous, and inhalation of beryllium dusts can cause acute and chronic lung diseases [111]. Especially for self-built x-ray tubes, the risk of breaking the very brittle material and resulting health risks need to be considered. All other investigated materials are atoxic.

The atomic number of carbon is only two above that of beryllium, hence the three assessed materials consisting of carbon have an energy output almost as high as beryllium. Furthermore, they exhibit a very high melting temperature. However, graphite reacts to carbon dioxide (CO_2) at temperatures of 620–720 °C in an oxygen-containing atmosphere. Even though the expected temperatures are clearly lower (see chapter 6.3), a large safety margin is favored. In ambient pressure, also diamond does not reach its

Table 7.2.: Characteristics of potential materials of the LFxT x-ray windows. The energy output and the mean energy were calculated for a 300 kVp x-ray spectrum from a tungsten target (mean energy 57.9 keV without filtering) filtered by 1 mm of the respective material. CFRC denotes carbon fiber reinforced carbon, $\perp$ the direction perpendicular to the fibers, and $\parallel$ the direction along the fibers. λ indicates the thermal conductivity, c the specific heat capacity, a the thermal diffusivity, and T_{melt} the melting temperature. Parameters were taken from Cardarelli [111], GTD Graphit Technologie GmbH [133], and Stahlhandel Gröditz GmbH [117].

	Beryllium (Be)	Graphite (C)	Diamond (C) (Type IIa)	CFRC (C)	Titanium (Ti)	Stainless steel (AISI 316L)
Atomic number Z	4	6	6	6	22	26, 24, 28, 42*
Density [kg/m^3]	1848	1400–2266	3515	1550	4540	8000
Energy output	97.1 %	96.0 %	92.4 %	96.3 %	71.9 %	53.4 %
Mean energy [keV]	59.4	62.4	65.6	62.1	89.6	105.2
λ [W/m/K]	210	85–350	500–2500	5–12 ($\perp$), 20–52 ($\parallel$)	21.9	15
c [J/kg/K]	1824	709	502	750	538	500
a [mm^2/s]	62.3	53–353	283–1417	4–10 ($\perp$), 17–45 ($\parallel$)	9.0	3.75
T_{melt} [°C]	1283	3650#	3550†	> 2000	1668	1200

* 68 % iron (Z = 26), 18 % chromium (Z = 24), 12 % nickel (Z = 28), 2 % molybdenum (Z = 42). Other elements were neglected for the calculation of the energy output and the mean energy.

\# In oxygen-containing atmosphere, graphite reacts to carbon dioxide ($C0_2$) at temperatures of 620–720 °C.

† At ambient pressure, diamond transforms to graphite above approximately 1700 °C.

melting point but transforms to graphite above approximately 1700 °C, which will not be reached at the vacuum chamber housing though (see chapter 6.3). In contrast to all other assessed materials, diamond is an electrical insulator. An advantage of diamond is the broad-band optical transparency, also for infrared and visible light, so that diamond windows allow direct observation of the focal spot by spectrometers. Both graphite and diamond are very hard and have a very low thermal expansion coefficient. Typically, graphite is irregularly anisotropic leading to a range in density and thermal conductivity [111]. Diamond has the highest thermal conductivity near room temperature of all known materials [111], in clear difference to CFRC. The anisotropy of CFRC yields a thermal conductivity that is by a factor of four higher along the fibers than perpendicular to them. In contrast to all other assessed materials, CFRC is not vacuum-tight so that it needs to be combined with another material, e.g., a metal, as a coating or as an adjacent layer. The CFRC layer can thereby act as an electron capture and needs to be thermally connected to the cooled vacuum chamber housing, while the second material does not need to resist such a high thermal loads. This double-material design is, however, more complicated to manufacture than a single-material window.

Both titanium and stainless steel have a lower energy output than beryllium or carbon-based materials, so that an x-ray window must be considerably thinner than 1 mm. Titanium can have a thickness of up to 0.16 mm and stainless steel of up to 0.05 mm for an energy output above 90 %. Both materials are ductile and their thermal diffusivity is much lower than for the other assessed materials. Titanium is highly reactive with air or moisture but forms a protective oxide layer, which is not of concern [111]. The other assessed materials are chemically inert at the expected temperatures [111].

7.3.4. Realization

For the MRT window of the LFxT prototype, diamond was chosen mainly because of its very high thermal diffusivity that facilitates an efficient heat transport away from the window. The diamond foil will be brazed into a copper holder, which easily deforms and thus avoids stress to the thin foil that thermally expands and might break in a rigid holder [134]. The copper holder will be brazed into a CF flange made of stainless steel. The brazing enables a high thermal conductance from the diamond window via the flange to the cooling system [134]. Diamond can withstand temperatures up to 700 °C [135], the CF flange can, however, only be baked at 250 °C [134]. At higher temperatures, both the copper and the stainless steel corrode, which, however, does not impair their functionality[§]. Galvanic coatings, e.g., made of gold, can protect the copper and stainless steel from corroding but need an oxygen diffusion barrier to the flange, which makes this construction complex and expensive[§].

The diamond window has a thickness of (0.4 ± 0.1) mm, resulting in an energy output of 96.7 % (95.9–97.5 %) for a 300 kVp x-ray spectrum from a tungsten target. For the prevention of a pressure-induced fracture, the minimum thickness t_{min} of a flat window

[§]Personal communication with a manufacturer of diamond x-ray windows, November 2020.

should satisfy

$$t_{\min} = 0.554 \cdot d \sqrt{\frac{\Delta p \cdot S_{\mathrm{sf}}}{\sigma_f}}, \tag{7.20}$$

where d is the window diameter, Δp the pressure difference between the two sides of the window, S_{sf} a safety factor, and σ_f the mechanical strength [136]. Conservatively assuming $\sigma_f = 400\,\mathrm{MPa}$ and $S_{\mathrm{sf}} = 4$ [135], the MRT window with a diameter of $d = 16\,\mathrm{mm}$ should have a minimum thickness of $t_{\min} = 0.28\,\mathrm{mm}$, which the production uncertainty range of the window satisfies. Electrons with an energy of 300 keV have a CSDA (continuous slowing down approximation) range of $0.0946\,\mathrm{g/cm^2}$ in carbon [137], resulting in 0.27 mm considering the density of diamond from table 7.2. As all backscattered electrons have an energy below 300 keV, they are expected to be absorbed in the window. As diamond is an electrical insulator, there is a risk of electrical charging of the window, which might influence the electric field inside the vacuum chamber and thus possibly deflect the electron beam. The size of the diamond window is, however, small and the flange is electrically conductive, so that it is unlikely that the electric field gets altered and the electron beam deflected during the exposure time of 20 s.

The flange contains pipes for water cooling due to a higher cooling efficiency for a shorter distance between the heat input and the coolant. The CF25 flange is the smallest possible flange to hold a window with a diameter of 16 mm, which is important for a compact construction with the shortest possible distance from the focal spot to the irradiated sample for high dose rates on the one hand and the largest possible field size on the other hand. In the construction of the LFxT prototype, the inner surface of the vacuum chamber housing is located 7.5 cm from the focal spot. The welding flange has a thickness of 1.5 cm. A distance of 1.8 cm from the welding flange to the x-ray window results in a total distance of 10.8 cm from the focal spot to the x-ray window. A diameter of the circular window of 16 mm yields a diameter of the radiation field of 30 mm at a distance of 20 cm from the focal spot according to the intercept theorem, and thus an edge length of 21 mm of a quadratic radiation field usable for MRT.

The imaging windows receive a considerably lower heat load than the MRT window. The expected temperature of the stainless steel surrounding these windows is below 75 °C (compare figure 6.4, the imaging windows are located vertically below (negative x-direction) the electron beamline entry port and horizontally beside (positive y-direction) the x-ray window but are not shown). For this reason, commonly used x-ray windows made of beryllium were chosen due to a lower price compared to custom-made diamond windows. There will be no protective coating, which can prevent corrosion but decreases the maximum operating temperature [138]. The imaging windows will have a free aperture diameter of 13 mm and will be mounted into CF25 flanges by metal diffusion for a higher heat resistance compared to a less expensive epoxy bonding [138]. A thickness of 250 µm suffices for a safe mounting into the flanges, which are bakeable at 250 °C like the CF flange of the diamond window[¶].

[¶]Personal communication with a manufacturer of beryllium x-ray windows, November 2020.

8. Discussion and outlook regarding the LFxT

The overall objective of the development of the line-focus x-ray tube (LFxT) is the translation of microbeam radiotherapy (MRT) into clinical applications. Although clinical trials have been planned for several years [40, 46], a main challenge remains the absence of suitable radiation sources [46, 48]. Even though most MRT research has been performed at large third-generation synchrotrons, MRT in clinical routine requires a compact source that is readily available, easily accessible, and affordable for radiotherapy clinics. Even for phase I clinical trials, hospital-based MRT sources are favorable compared to pure research facilities such as third-generation synchrotrons for better patient monitoring and care. The LFxT technology is promising for the clinical translation of MRT but still needs to be verified experimentally.

The preclinical prototype will serve as a proof of concept of the LFxT technology and will facilitate easily accessible preclinical MRT research at the same time. Before human clinical trials can start, the radiobiological mechanisms of MRT must be better understood and veterinary trials with larger animals are necessary [46]. Currently available compact MRT sources are inverse Compton scattering sources with an x-ray energy below 35 keV and a peak dose rate of 4 Gy/min [27, 139], carbon nanotubes with an x-ray spectrum of 160 kVp and a peak dose rate of 1 Gy/min [71, 140], or modified preclinical x-ray tubes with an x-ray spectrum of 225 kVp and a peak dose rate up to 8 Gy/min [73]. In contrast, the LFxT prototype is expected to deliver dose rates that are a hundredfold higher compared to the cited values, and a higher x-ray energy allows the treatment of deeper-seated tumors. A higher dose rate diminishes blurring of the micrometer-scaled dose distribution due to organ motion and simplifies in-vivo experiments due to shorter anesthesia times compared to currently available preclinical MRT sources. Furthermore, for both in-vitro and in-vivo experiments, DNA repair effects need to be considered for irradiation times in the range of hours to achieve peak doses of several hundred Grays with currently available MRT sources [2, 6, 141]. The repair effects are of minor importance for irradiation times of a few seconds with the LFxT.

8.1. Further developments for the LFxT prototype and experimental validation

This work presents vital aspects for the functionality of the LFxT. Monte Carlo simulations demonstrated the feasibility to obtain a microbeam dose distribution and dose rates considerably higher than achievable with currently available compact MRT sources. With numerical simulations, the heat capacity limit was proven as the basis of the LFxT functionality. Furthermore, the consequences of backscattering electrons were assessed in the vacuum chamber, and a suitable electron accelerator and x-ray exit windows for the LFxT prototype were investigated.

Nevertheless, the construction of the LFxT prototype requires many more components, which need to be compatible with each other. For this reason, the collaboration team consisted of physicists, engineers, biologists, and medical doctors to develop and build up the prototype. Within this collaboration, a suitable target made of titanium-zirconium-molybdenum (TZM) was developed, designed to reduce mechanical and thermal stress by maximizing the thickness and diameter of the punched disk-shaped target and by adding relief wells (see Winter et al. [88]). Further developments included the motor and drive train of the target, an appropriate vacuum system, and a suitable cooling system. For operation, a software control as well as a monitoring and safety system are under development to ensure radiation protection and mechanical safety for both personal safety and machinery safety. For first physical and biological experiments with the LFxT, a multislit collimator is needed with the correctly adjusted divergence and a sufficient thickness as well as an experimental setup including a stage for cell containers and small animals.

To prove the concept of the LFxT, several aspects must be verified experimentally. The operation in the heat capacity limit needs to be validated by comparing the measured focal spot temperature to the value predicted by the presented numerical simulations and the analytical heat capacity limit, considering the respective focal spot width and the actual target velocity (compare chapter 5.3). The shape of the focal spot can thereby be quantified with an infrared camera or with radiological measurements. Ideally, the focal spot width is varied between 50 µm and 10 mm to obtain a graph similar to figure 5.3, which clearly demonstrates the deviation of the temperature increase for micrometer-wide focal spots from the heat conduction limit of conventional x-ray tubes. During the measurements, the focal spot length, the electron beam power, and the target velocity must be held constant. Alternatively, the target velocity can be varied, while maintaining the focal spot shape, similar to the results presented in figure 5.4. For this second validation technique, it should be ensured that the focal spot has a width that allows both the heat capacity limit and the heat conduction limit with short exposure times. If the focal spot is too narrow at low target velocities, the assumption of one-dimensional heat conduction and thus also the analytical estimate of the heat conduction in equation (5.13) are not valid (compare section 5.3.1 with table 5.1 and equation (5.12)). A suitable spot width would be 1 mm as demonstrated in table 5.1. Especially for the

second validation technique, it must be ensured that the focal spot temperature at low target velocities does not exceed the maximum recommended temperature given by the target manufacturer.

In addition to the verification of the heat capacity limit, physical dosimetry, e.g., with radiochromic films, needs to verify the expected dose rate in an open field (compare section 4.3.2), suitable peak and valley dose rates, and the sharp microbeam dose distribution. Biological dosimetry as described by Treibel et al. [73] can verify physical dosimetry and can additionally detect cellular effects evoked by MRT. Finally, cell culture experiments and in-vivo MRT studies are expected to result in similar observations as for other MRT sources.

8.2. Further developments for the clinical LFxT

Clinical microbeam treatments require a redevelopment of the LFxT. As mentioned throughout this work, the clinical LFxT was designed with an x-ray spectrum of 600 kVp and an electron beam power of 1.5 MW. Chapter 4.3 demonstrated that these parameters of the clinical LFxT allow to deliver both MRT and ultra-high dose rates for x-ray FLASH treatments. By obtaining dose rates above 100 Gy/s, the irradiation times then shorten to few seconds for a peak dose of several hundred Grays. As for the preclinical prototype, an interval between two irradiations of 20 min for patient positioning is assumed. Main development projects for the clinical LFxT are the high-voltage (HV) supply, the electron accelerator and beam optics (discussed in chapter 7.1), and the rotating target. Furthermore, the safety system needs to ensure radiation protection at higher dose rates, an insulation of higher electric voltages, and mechanical safety from a presumably higher rotational energy of the target with a larger diameter compared to the preclinical LFxT. With collaboration partners, finding solutions for these development projects has already started.

The clinical LFxT requires a megawatt power for several seconds, which is unfeasible for commercially available HV generators. In close collaboration with Prof. Dr. Marek Galek from the University of Applied Sciences in Munich, a novel HV supply is therefore developed based on modular multi-level converters (MMC) from the high-voltage direct-current transmission technology [87, 142, 143]. Figure 8.1 illustrates the designed MMC setup. The MMC consists of several identical submodules with a low blocking voltage and separate energy storages. The submodules are serially connected to produce a high output voltage. In contrast to commercial MMCs, the capacitor is exchanged with a DC/DC (direct current) converter to increase the voltage to the kilovolt range, and the submodules will be realized as planar transformers on a printed circuit board [87]. The submodules can be individually switched to adjust the level and slope of the output voltage during turning-on and operation, which is necessary as even small disturbances can cause severe interferences during high-voltage switches. A fast and automated switching is facilitated by an electronic interconnection of the submodules via fiber optics. Separate rechargeable batteries in each submodule allow a distributed energy

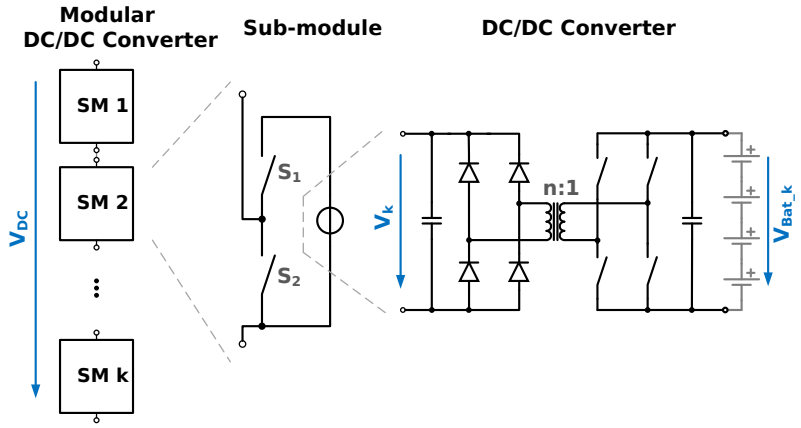

Figure 8.1.: Setup of the high-voltage supply for the clinical LFxT based on a modular multi-level converter, which consists of identical submodules (SM) with DC/DC (direct current) converters for a distributed energy storage. Winter et al. [87].

storage for easy handling in case of interruptions and for simpler constructional and structural safety measures compared to a single, much more powerful energy storage. Inverting the DC/DC converters allows a sequential charging of the batteries during the beam-off time so that a single low-voltage power supply suffices for a continuous input power below 10 kW. The sequential charging and buffering avoid drawing megawatt powers from the public electric grid, which would cause disturbances in the power supply. The energy within each submodule is buffered by twelve conventional lithium ion batteries, each with a charge of 5 Ah and a usable voltage of 3.7 V on average. During irradiation, each of the 300 serially connected submodules has an output voltage of 2 kV, an output power of 6.6 kW, and an output current of 3.3 A [87]. Consequently, the buffered energy of 67 kJ per submodule facilitates possible irradiation times of 2 min.

The focal track of the preclinical LFxT prototype is made of a tungsten-rhenium alloy, and the target base consists of TZM like typical x-ray tube targets, where the target thickness and diameter are limited by state-of-the-art manufacturing techniques [88]. Although the total dose delivered by the clinical LFxT will be similar to the dose delivered by the preclinical prototype, the sample is expected to have larger distance to the focal spot due to construction limitations. The same dose at a distance of 30 cm instead of 20 cm increases the required electron beam power by a factor of 2.25 due to the inverse square law, which increases the total heat load over the course of an irradiation accordingly. Moreover, the heat will evolve in a shorter timeframe due to higher dose rates, which leaves less time for heat dissipation and thus leads to higher thermal gradients and a higher thermal stress. For these reasons, a different target design seems necessary. First, a larger target diameter gains more time for heat dissipation between each revolution. Second, an alternative target material should be considered [88]. Carbon-fiber reinforced carbon might be a suitable substitute because of its high

specific strength, i.e., its high ratio between mechanical strength and density, and a lower thermal expansion coefficient than TZM, especially in the direction of the carbon fibers [133, 144].

For clinical application of the LFxT as an MRT source, there are additional aspects regarding MRT that need to be investigated. The treatment planning system needs to consider the characteristics of the microbeam radiation field, including the focal spot size, the divergence of the x-ray field, and the x-ray spectrum. There has been progress on the specific treatment planning for divergent microbeams in-house but it is still under development. Moreover, a measure of the comparability between the spatially fractionated MRT dose distribution and a conventional clinical dose distribution needs to be validated. The approach of the equivalent uniform dose is described in chapter 10. If MRT will be delivered in several fractions analogously to conventional radiotherapy, the application of several beam angles or a kind of arc therapy should be considered (see chapters 10 and 11) and the combination of spatial and temporal fractionation investigated [47]. Furthermore, the biological mechanisms should be understood to a large extent, suitable clinical cases need to be defined, and a precise and reliable patient positioning system, possibly with image guidance, needs to be developed.

8.3. X-ray FLASH radiotherapy

As the clinical LFxT is expected to deliver dose rates above 100 Gy/s, it might be a suitable compact source for x-ray FLASH treatments besides MRT. Subsecond treatments with ultra-high dose rates of more than 40 Gy/s can trigger the FLASH effect, which involves a reduced normal tissue toxicity at same tumor control rates compared to conventional dose rates [145–147]. Even though contradictory results have been published [24, 148, 149], the FLASH effect has been observed for numerous preclinical studies with different radiation modalities such as electrons [150], photons [151], protons [152], carbon ions [153, 154], and helium ions [155]. Although the radiobiological and radiochemical mechanisms have not been fully understood, authors suggest that the FLASH effect is caused by a consumption of oxygen that is higher than its supply, with the involvement of oxygen depletion, reactive oxygen species, and transient hypoxia [146, 156, 157]. Additionally, there might be a different immune response after ultra-high dose rate irradiations compared to conventional low dose rate irradiations [158, 159]. Electron FLASH radiotherapy was used for a first successful treatment of a patient with cutaneous lymphoma [158] and for a veterinary trial with cats bearing squamous cell carcinomas [150]. In addition, several treatment planning studies have been published for FLASH treatments with electrons [160, 161] and protons [162–164] for different human cancer sites.

Ultra-high dose rate experiments have mainly been performed using electrons with an energy below 10 MeV from modified clinical linear accelerators or proton beams, where an ultra-high dose rate is easier to achieve than with x-ray tubes that have a very low electron-to-photon conversion efficiency [146, 165, 166]. For this reason, x-ray

FLASH has been mainly investigated at large third-generation synchrotrons such as the European Synchrotron Radiation Facility in Grenoble, France [151], the Australian Synchrotron in Melbourne, Australia [24], and the Brookhaven National Laboratory in Upton, New York, USA [102]. For the same reasons as mentioned for MRT in chapter 1, synchrotrons are unsuitable for clinical routine so that a compact source for x-ray FLASH treatments is required and the LFxT might be a suitable solution. Beneficially, the LFxT can deliver concurrent MRT and x-ray FLASH treatments, which possibly widen the therapeutic window even more than either MRT or FLASH treatments [167, 168]. Typical electron beams in the low megavolt range as well as x-ray beams in the kilovolt range have the drawback of short penetration depths. For deep-seated human tumors, subsecond FLASH treatments require higher-energy beams such as very high energy electrons, protons, or photon beams in the megaelectronvolt range [46, 146, 147, 166, 169].

8.4. The LFxT as an x-ray imaging source

The LFxT appears to be a suitable compact radiation source not only for MRT and x-ray FLASH but also for phase contrast x-ray imaging (PCI) due to its unique x-radiation field from a strongly eccentric focal spot, a high flux, and an energy at the upper edge of the orthovoltage range. In contrast to conventional attenuation x-ray imaging, PCI detects the x-ray phase shift of a sample. Soft tissue exhibits a phase shift cross section of x-rays that is orders of magnitude higher than the absorption cross section. Consequently, slight changes in the phase can be detected with a higher contrast than slight changes in the x-ray absorption. First clinical studies with PCI include mammography at the synchrotron in Trieste, Italy [170]. A further application of PCI is virtual histology that allows a high resolution in three dimensions and renders a laborious and destructive sample preparation unnecessary, conversely to conventional histology that includes slicing and staining of the sample [171]. For both PCI of human organs and virtual histology, the x-ray energy is typically below 50 keV, especially at compact x-ray sources [170, 172–176].

The strongly eccentric focal spot of the LFxT with a width in the micrometer range leads to a high spatial coherence in the short focal spot direction [63]. With the designed electron optics of the LFxT prototype, the focal spot size can be reduced to 50 µm × 10 mm ($x \times y$) as full widths at half maximum (the electron power should then be reduced to not overheat the target or the vacuum chamber housing). As described in chapter 7.3, two windows are designated for x-ray imaging with the LFxT. These windows are located perpendicular to the target surface and parallel to the focal spot axes, respectively, as depicted in figure 8.2. With an aperture of 13 mm, the projected focal spot size can be obtained by the tangent of the viewing angle ($\tan\alpha = a/d$, see figure 8.2) and the focal spot dimension in the respective direction. Accordingly, the projected focal spot size is 50 µm × 0.65 mm ($x \times y$) as viewed through the horizontal window and 2.7 µm × 10 mm ($x \times y$) as viewed through the vertical window.

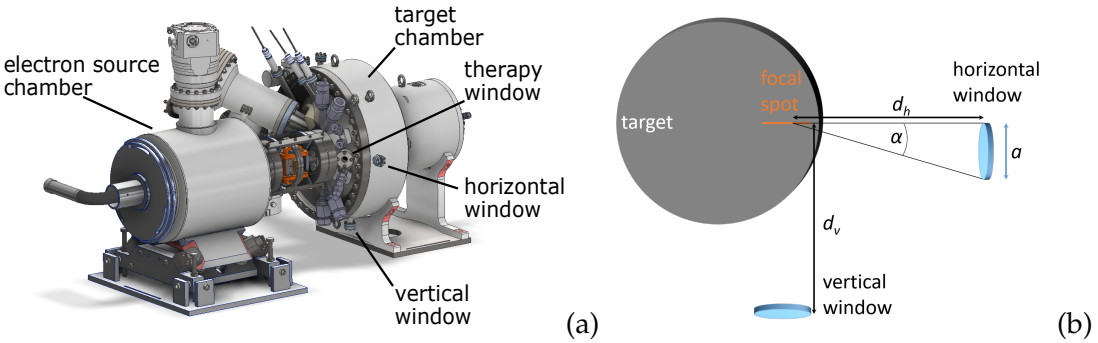

Figure 8.2.: Horizontal and vertical imaging windows of the LFxT prototype embedded in the CAD model (a) and as a sketch (b). The aperture size is $a = 13\,\text{mm}$ for both windows. The distance from the focal spot is $d_h = 200\,\text{mm}$ for the horizontal window and $d_v = 240\,\text{mm}$ for the vertical window, respectively.

The x-ray spectrum of the LFxT prototype was investigated at the angles of the imaging windows using Monte Carlo simulations in TOPAS with a phase space detector, similar to the TOPAS simulations described in chapter 4.2.2. Considering an emission angle of 86.5–90° to the normal to the target surface, the unfiltered x-ray spectrum had a mean energy of 93 keV with the highest intensities at 58 keV, 59 keV, 67 keV, and 69 keV, corresponding to the characteristic Kα- and Kβ-lines of tungsten [177], which can be used as a first estimate of the design energies for a PCI setup. The mean energy was higher compared to an emission angle of approximately 45° for MRT due to the heel effect (see figure 4.8b). For an electron beam current of 0.3 A, the photon flux was approximately $1.5 \cdot 10^9\,1/\text{s}/\text{mm}^2$ at a distance of 1 m from the focal spot and an angle between 86.5–90° to the target normal, which matches the estimate by Bartzsch and Oelfke [63]. The flux through the imaging windows of the LFxT are thus lower than at synchrotrons but at the same level as at inverse Compton scattering sources and higher than at microfocus x-ray tubes or metal jet x-ray tubes [63, 68, 178].

The coherence length l_c of an x-ray source with a random phase distribution can be calculated by the x-ray wavelength λ, the focal spot diameter w in the direction of interest, and the distance from the focal spot d as $l_c = \lambda \cdot d/w$. For the LFxT, l_c was estimated for the characteristic Kα_1 line of tungsten, which corresponded to the highest x-ray intensity, at an energy of 59 keV, i.e., $\lambda = 21\,\text{pm}$, and a distance from the focal spot of $d = 1\,\text{m}$. Accordingly, the coherence lengths in the x-direction are 0.42 µm and 7.8 µm for the horizontal and the vertical window, respectively. These values are markedly lower than estimates by Bartzsch and Oelfke [63], who considered a considerably smaller focal spot of 1.3 µm, only limited by electron scattering, leading to a coherence length of 16 µm. The specifications to obtain longer coherence lengths with the LFxT are not further specified by Bartzsch and Oelfke [63]. A high coherence in one dimension suffices for certain PCI techniques such as grating-based PCI, where possibly the source grating becomes unnecessary and two gratings are adequate [179].

Suitable PCI techniques for the polychromatic spectrum of the LFxT prototype might be propagation-based PCI for high-resolution applications or optic-based PCI, e.g., grating-based, edge-illumination, or speckled-based PCI. Thereby, several challenges will occur. Among others, the strongly eccentric focal spot smears the image in the long dimension of the spot, which may be counteracted by a tomography method using two-dimensional angular sampling of the source or, more easily, of the sample [180]. Additionally, the higher x-ray energies yield smaller phase shifts and thus a reduced sensitivity than lower x-ray energies; the reduction is, however, not as pronounced as for attenuation imaging. Furthermore, higher x-ray energies require technically more complicated optical elements, for example thicker absorption gratings, very sensitive detectors due to lower photon absorption cross sections, and a correction during phase retrieval for increased image noise due to increased Compton scattering in the detector. For these reasons, the preclinical LFxT prototype with an acceleration voltage of 300 kV might be better suited for PCI than the clinical LFxT with 600 kV.

Possible PCI applications with the LFxT include high-resolution imaging of bone and soft-tissue or lower-resolution imaging of large samples, for which the energy of currently available PCI x-ray sources is too low. Due to the higher x-ray energy of the LFxT, bones might not need to be invasively decalcified, which is typically done for PCI preparation, and even a simultaneous imaging of bone and soft tissue seems feasible, which has so far only been achieved at synchrotrons [172, 181]. A simultaneous imaging of bone and tissue would allow the investigation of their transition regions or of bone tumors. Large samples of interest can be laboratory animals, like rats or rabbits, or entire human organs like a vertebra or the heart, which have also only been imaged at synchrotrons [182].

8.5. Conclusion

This work confirms the great potential of the LFxT technology for clinical application of MRT with a sharp microbeam dose distribution and ultra-high dose rates and includes vital developments for both a clinical LFxT and the preclinical LFxT prototype. The Monte Carlo simulations in this work demonstrated the suitability of the radiation field from the LFxT for MRT. Using three-dimensional time-dependent numerical simulations, the heat capacity limit was validated for micrometer-wide focal spots, which allows considerably higher electron beam powers than the heat conduction limit of conventional x-ray tubes. Specifically for the preclinical LFxT prototype, the heat load distribution onto the vacuum chamber housing was assessed as a basis for the development of the relevant cooling system. By processing the discussed aspects of the experimental validation, the concept of the LFxT technology will be proven with the preclinical prototype, and the further development of a clinical LFxT as well as applications in x-ray FLASH radiotherapy and in PCI will follow.

Part III.

Microbeam treatment planning

9. Introduction to microbeam treatment planning

Preclinical studies of microbeam radiotherapy (MRT) have shown that the valley dose rather than the peak dose predominantly determines the radiobiological effects like normal tissue damage [23, 24, 35]. For this reason, recent preclinical experiments have mainly compared the MRT valley dose with a homogeneous broad-beam dose to assess tumor growth impairment and normal tissue toxicity [28, 35], although the valley dose has proven to not be equivalent to the broad-beam dose [24, 35, 44, 45]. Related to radiobiological tumor response, Bouchet et al. [35] found a similar efficacy for MRT valley doses that were approximately half of the broad-beam doses. Trappetti et al. [28] observed both a better tumor control and a stronger edema after MRT with a valley dose equivalent to the broad-beam dose. Both groups of authors concluded that several MRT parameters such as the valley dose, the peak dose, the peak width, and the center-to-center spacing need to be considered for predicting the biological effect. These parameters together with a temporal fractionation and several beam directions should further be optimized to widen the therapeutic window of MRT compared to conventional radiotherapy.

External beam radiotherapy with multiple beam directions is common clinical practice due to a lower beam entrance dose at a constant target dose and is applied as a step-and-shoot technique, as dynamic arc therapy with volumetric modulation or intensity modulation, or as helical tomotherapy. MRT involves an additional degree of freedom compared to radiotherapy with a homogeneous radiation field, that is the arrangement of the microbeams that can be a peak-on-peak geometry, an interlacing geometry [52, 183, 184], or a cross-firing geometry [29, 184, 185]. The peak-on-peak geometry has not been applied for MRT, but for proton minibeam radiotherapy by precisely realigning the minibeams to the same locations for several temporal fractions [47].

Microbeams can be interlaced by shifting the peaks in the direction of the peak-valley profile, which is parallel to the rotation axis for different beam ports. The interlaced geometry, also called interspersed MRT, has been realized with parallel microbeams at synchrotron facilities, where a homogeneous target dose can be created if the number of ports matches the ratio of center-to-center distance to peak width (details can be found in the publication by Serduc et al. [52]). A main drawback is the required alignment precision of few micrometers to avoid an overlapping of peaks, which seems achievable with heart-gated synchronized irradiations in preclinical experiments at specific synchrotron beamlines [52, 184]. In a clinical setting, an alignment accuracy of few micrometers is, however, not realistically achievable as state-of-the-art

stereotactic frames for brain or head and neck irradiations accomplish an accuracy in the submillimeter range [186]. The alignment accuracy for thoracic or abdominal targets is even lower due to less precise immobilization possibilities and stronger internal organ motion due to breathing and the cardiac activity.

Cross-firing microbeams involve a rotation of the multislit collimator around the beam direction so that the orientation of the peak-valley profile changes for different beam ports (details can be found in the publication by Fernandez-Palomo et al. [29]). The cross-firing geometry, also called multidirectional MRT, generates a micrometer-scaled dose modulation in the target volume as well as in the beam paths, which implies lower demands on the alignment precision. There have been two concepts published for a rotational delivery of MRT, namely spiralMRT presented by Donzelli et al. [187] and microbeam arc therapy (see chapter 11 and Winter et al. [87]).

For unidirectional MRT, the peak and valley doses are typically reported separately in millimeter resolution. The complex dose distribution of multidirectional MRT renders the definitions of peak and valley regions inapplicable, though, and a dose reporting in micrometer resolution impracticable due to an enormous computational memory required. Even more importantly, the interpretation of a strongly modulated dose distribution and their comparability to experiential clinical doses for tumor control and constraints for organs at risk are not established. The easiest translation to a macroscopic dose would be the mean dose, which, however, underestimates the cell survival [85].

The concept of the equivalent uniform dose (EUD) more sophisticatedly addresses the question how to compare a spatially fractionated dose distribution with a spatially non-fractionated dose applied in clinical routine. Thereby, the EUD assigns a single dose value to an inhomogeneous dose distribution that leads to the same radiobiological effect. The basis of the EUD is the same as of the biological effective dose (BED) stating the equivalence of two dose distributions if they yield the same clonogenic cell survival according to the linear-quadratic model (LQM), which was introduced in chapter 1.1 [4, 84]. The BED is clinically well established to compare different temporal fractionation schemes with a total physical dose D, a fraction dose d, and a number of fractions n. Thereby, the survival fraction S as per equation (1.1) is modified to

$$S(D) = \exp\left(-\alpha n d - \beta n d^2\right), \tag{9.1}$$

where α and β are the radiobiological parameters in the LQM [4]. The biological effect caused by a specific BED represents the natural logarithm of the survival fraction after that dose [5, 6]. As a typical fractionation scheme, the equivalent dose in 2 Gy fractions (EQD2) can be derived by identifying an effective dose of a fractionation scheme with $d_1 = 2\,\mathrm{Gy}$ and $n_1 d_1 = \mathrm{EQD2}$ to an arbitrary fractionation scheme with $D_2 = n_2 d_2$, resulting in

$$\begin{aligned} \alpha n_1 d_1 + \beta n_1 d_1^2 &= \alpha n_2 d_2 + \beta n_2 d_2^2 \\ \Rightarrow n_1 d_1 \left(d_1 + \alpha/\beta\right) &= n_2 d_2 \left(d_2 + \alpha/\beta\right) \\ \Rightarrow \qquad \mathrm{EQD2} &= D_2 \frac{d_2 + \alpha/\beta}{2\,\mathrm{Gy} + \alpha/\beta}. \end{aligned} \tag{9.2}$$

For microbeam dose distributions, the dose D thereby corresponds to the EUD. The EUD calculation is based on the clonogenic survival fraction in equation (1.1) according to the LQM of a single irradiation. A spatially modulated dose distribution with weights w_i of single dose values D_i is equivalent to an EUD if the mean survival fraction $\overline{S}$ of the modulated dose equals the survival fraction S_{EUD} of the uniform dose as

$$\begin{aligned} & \overline{S} = S_{\mathrm{EUD}} \\ \Rightarrow \quad & \overline{S} = \exp\left(-\alpha \cdot \mathrm{EUD} - \beta \cdot \mathrm{EUD}^2\right) \\ \Rightarrow & \ln\left(\overline{S}\right) = -\alpha \cdot \mathrm{EUD} - \beta \cdot \mathrm{EUD}^2 . \end{aligned} \tag{9.3}$$

It follows

$$\begin{aligned} \mathrm{EUD} = & -\frac{1}{2}\frac{\alpha}{\beta} + \sqrt{\frac{1}{4}\left(\frac{\alpha}{\beta}\right)^2 - \frac{1}{\beta}\ln\left(\overline{S}\right)} \text{ with} \\ & \overline{S} = \frac{1}{N}\sum_{i=1}^{n} w_i \exp\left(-\alpha D_i - \beta D_i^2\right) , \end{aligned} \tag{9.4}$$

where N is the sum of all weights, $N = \sum_{i=1}^{n} w_i$. Developed for considering inhomogeneities in dose distributions [84], the EUD has been successfully applied in clinical three-dimensional conformal radiotherapy or intensity modulated radiotherapy for dose distributions with moderate spatial modulation [86, 188]. Recently, the EUD has been proposed for evaluating doses with a spatial fractionation on the submillimeter and micrometer scale [85]. As a result, the EUD allows to transform a microscopic dose distribution to an equivalent macroscopic dose in millimeter resolution.

10. Microbeam treatment planning on clinical patient data

10.1. Introduction

Treatment planning studies of novel radiotherapy techniques can help to design first clinical trials by choosing suitable targets and predicting advantages over conventional radiotherapy as well as possible difficulties and complications. For microbeam radiotherapy (MRT), the dose to the tumor and to organs at risk (OAR) has been mainly investigated in phantoms with Monte Carlo simulations and radiochromic film dosimetry [38, 39, 189]. Besides, Smyth et al. [42] published a first planning study on patient data using a simple unidirectional MRT setup. The authors presented valley doses to OAR as well as peak doses and peak-to-valley dose ratios (PVDR) to target volumes. Even though they suggested potential candidates for first clinical trials based on their simulated PVDR values, a more flexible beam setup with several beams from different directions resembles clinical treatment plans more closely and might elucidate additional candidates.

In this work, first microbeam treatment plans with several beams were created on clinical patient data. For that purpose, parallel photon beams from a third-generation synchrotron were used because first clinical MRT trials might be carried out at synchrotrons, where the preparation has been lasting for years [40, 41, 46]. Furthermore, most veterinary MRT trials and preclinical experiments have been conducted at few specific third-generation synchrotrons worldwide, gathering experience in preparing, shaping, and adjusting the synchrotron radiation for MRT. Additionally, parallel beams yield a less complex microbeam geometry compared to divergent beams from compact MRT sources.

Several research groups have created preclinical microbeam treatment plans with the dose calculation algorithm called hybridDC [62], which combines the advantages of Monte Carlo and analytic simulations into a hybrid dose calculation algorithm. hybridDC has recently been implemented into an open-source and a commercial treatment planning platform [190, 191].

Here, hybridDC was adjusted for MRT planning on clinical patient data, which is described in sections 10.2.1 and 10.2.2, and subsequently applied to a clinical patient case (see sections 10.2.3 and 10.3.1). Furthermore, the functionality of hybridDC was extended to generate the equivalent uniform dose (EUD) in millimeter resolution from complex, micrometer-scaled dose distributions of overlapping peaks and valleys, as shown in sections 10.2.4 and 10.3.2. In section 10.2.5, the MRT planning framework was

utilized to create MRT plans on five relevant treatment scenarios and to compare them to clinical treatment plans in section 10.3.2. Section 10.4 discusses achievements and limitations of the presented approach and specifies further development aspects. The clinical radiotherapy data, including computed tomography (CT) images, contours of relevant structures, prescription doses, dose constraints, and clinical treatment plans, have been provided by the Department of Radiation Oncology at the Klinikum rechts der Isar of the Technical University of Munich.

10.2. Methods

The microbeam treatment planning was based on hybridDC [62]. Thereby, Monte Carlo simulations generated primary and scatter dose distributions of photons. Proceeding from the primary and scatter dose, the dose distribution of secondary electrons was calculated by an analytic convolution kernel that introduced the micrometer-scaled dose modulation of MRT and was therefore independent of the number of simulated primary particles. The Monte Carlo simulations in Geant4 (version 10.4.p02) [93] were performed with the custom *hyDLivermorePolarizedPhysics* list with electromagnetic range limits of $EMRangeMin = 100\,\text{eV}$ and $EMRangeMax = 1\,\text{GeV}$ and the photon interaction processes of the *G4LivermorePhotoElectricModel*, the *G4LivermorePolarizedComptonModel*, and the *G4LivermorePolarizedRayleighModel*. The production cuts were set to 1 mm for photons and 10 µm for electrons. As default for Monte Carlo dose calculation, the MRT dose is reported as dose-to-medium.

HybridDC was embedded as an additional module into the open-source treatment planning platform 3DSlicer [192, 193] for an easy usage with a graphical user interface* [190]. This implementation had been used for preclinical MRT planning of single-beam irradiations and displayed separate peak and valley dose distributions as well as one-dimensional peak-valley dose profiles in single voxels. 3DSlicer, combined with the open-source Radiotherapy module [194], allows, among many other functions, the loading of CT data and externally calculated dose distributions, the extraction of contours, and a treatment plan evaluation by means of dose-volume histograms (DVHs) and dose metrics.

The MRT dose calculation was applied to clinical radiotherapy data from the Department of Radiation Oncology at the university hospital Klinikum rechts der Isar of the Technical University of Munich. The radiotherapy data included planning CT images, conventional treatment plans, as well as the contours of OAR and of target volumes including the clinically applied margins. The clinical plans were created by experienced radiation oncologists with the treatment planning system Eclipse (Varian Medical Systems Inc., Palo Alto, California, USA) and reported dose-to-water. The CT data had a resolution of $0.8 \times 0.8 \times 1.0\,\text{mm}^3$, $1.0 \times 1.0 \times 2.0\,\text{mm}^3$, or $1.0 \times 1.0 \times 3.0\,\text{mm}^3$ ($x \times y \times z$), while the conventional treatment plans had a resolution of $1.0 \times 1.0 \times 1.0\,\text{mm}^3$,

*HybridDC was implemented into 3DSlicer by my colleague Mabroor Ahmed from the Helmholtz Zentrum München and the Technical University of Munich.

$2.5 \times 2.5 \times 2.0\,\mathrm{mm}^3$, or $2.5 \times 2.5 \times 3.0\,\mathrm{mm}^3$. For MRT dose calculation with hybridDC, the CT was rebinned by a factor of $2 \times 2 \times 1$, if not otherwise mentioned, for shorter calculation times and lower demands of computational resources, resulting in MRT dose voxels of $1.6 \times 1.6 \times 2.0\,\mathrm{mm}^3$, $2.0 \times 2.0 \times 2.0\,\mathrm{mm}^3$, or $2.0 \times 2.0 \times 3.0\,\mathrm{mm}^3$, respectively.

A comparison of different treatment plans requires equally effective doses to the target volume to ensure a similar tumor control for all plans. Until further clarification of the clinical effect of a spatial dose fractionation, the MRT dose in the target volume should either be homogeneous by means of an interlaced geometry (introduced in chapter 9), or the application of the EUD is necessary (see chapters 1.5 and 9). The irradiation geometry to achieve the same effective dose to the target volume does, however, not need to be the same for MRT and conventional radiotherapy. As secondary electrons from kV photons have shorter ranges than secondary electrons from clinically applied MV photons, clinical field sizes can be too small for an entire target coverage with MRT. For this reason, the field sizes as well as the number of beam ports, the gantry angles, and the isocenter location were guided by the clinical plans but were adjusted for the MRT plans if necessary.

10.2.1. MRT geometry

For the MRT planning studies presented in this work, parallel x-ray beams were used with the spectrum from the biomedical beamline ID17 at the European Synchrotron Radiation Facility (ESRF, Grenoble, France) with a mean energy of 104 keV. The microbeam peak width was 50 µm and the center-to-center distance between neighboring peaks was 400 µm.

In this work, the couch angle, defining the rotation around the y-axis, remained at 0°, so that the gantry angle set the beam direction as a rotation around the z-axis. Different microbeam treatment geometries were obtained by adjusting the angle of the multislit collimator, which rotated the orientation of the peak-valley profile around the beam direction. For a couch angle of 0° and independent of the gantry angle, both the peak-on-peak geometry and the interlaced geometry required a collimator angle of 90°, whereas a cross-firing geometry resulted from a collimator angle of 0°. To interlace the peaks for an intended homogeneous target dose, eight beams were necessary due to the ratio between the peak width and the center-to-center distance, and each beam was shifted by the peak width, i.e., by 50 µm, in the z-direction, which was realized by a separate isocenter shift for each beam.

All presented MRT plans were calculated with equal beam weighting, i.e., the same number of primary particles were used for each beam for the Monte Carlo simulations in hybridDC.

10.2.2. Adjustments of the dose calculation algorithm

The first MRT plans were calculated with rectangular fields with a varying gantry angle, a multislit collimator angle of 0° or 90°, and no additional field shaping. However, an

essential method for OAR dose sparing in modern radiotherapy is the dose conformality to the target volume so that MRT also required conformal fields for a reasonable comparison to clinical plans. On that account, the field contours of the MRT plans in section 10.2.5 were restricted by the shape of the respective planning target volume (PTV) projected onto the beam direction using a Python script (Python version 3.7.2). A dilatation of the beam contour by a convolution with a cross-shaped kernel with a size of 3×3, 5×5, or 7×7 CT voxels ensured sufficient target coverage[†]. For each plan, the size of the dilatation kernel was manually adjusted for a full target coverage at the smallest possible contour to best spare healthy tissue from direct irradiation. The possibility to read in irregularly shaped beam contours had been implemented already in the original version of hybridDC.

The dose calculation with hybridDC in lung tissue was activated for the planning of lung tumor treatments and other microbeam irradiations in the thorax region. In the original version of hybridDC, the dose calculation had been disabled for voxels with mass densities of $\rho \leq 0.2\,\mathrm{g/cm^3}$. In volumes with these low densities, there are only few interactions of photons with matter. In case of an interaction, secondary electrons have a markedly longer range than in soft tissue, and the microbeam dose profile is hence blurred compared to a profile in pure water. In pure air, the peak-valley profile completely vanishes; whereas the profile becomes sharper, the more water is contained in an air-water mixture. However, a disabled dose calculation in some parts of the lung renders an unrealistic DVH, and treatment plan evaluation is therefore impossible.

To allow plan evaluation with DVHs, the electron kernel of hybridDC was modified as described in the following, whereas the Monte Carlo simulation generating primary and scatter dose remained unchanged. First, dose calculation was activated in all voxels receiving primary dose, i.e., not only in voxels with $\rho > 0.2\,\mathrm{g/cm^3}$. Second, the material of all voxels with a density of $\rho < 0.90\,\mathrm{g/cm^3}$ were set to water. As adipose tissue has the lowest density of soft tissue with $\rho = 0.95\,\mathrm{g/cm^3}$ [195], all tissues with a lower density (including a margin of tolerance) were considered as an air-water mixture, i.e., lung tissue. Thereby, a microbeam dose profile was also calculated in lung tissue and DVHs became more realistic. The rationale behind this approach was that any interaction of photons in the lung happens in cells of, e.g., alveoli, bronchioles, or small blood vessels, even though the interactions are few in number. These structures of submillimeter size are not visible in CT images that have a coarser resolution. The part of the dose calculation voxel that contains air receives a homogeneous scatter dose, whereas the part of the voxel that contains cells receives a peak-valley profile similar to a profile in water. As energy deposition in air is negligible, the dose and the peak-valley profile in cells, which contain mostly water, is of interest.

[†]The Python script that obtains the beam contours from the PTV shape and includes the dilatation was written by my colleague Yating Zhang from the Helmholtz Zentrum München and the Technical University of Munich.

10.2.3. Comparison of a kV MRT plan to an MV clinical plan

The microbeam dose calculation in lung tissue was applied to a clinical lung cancer case for a first comparison of an MRT plan to a clinical treatment plan. The synchrotron radiation of MRT has two main differences to the MV radiation applied clinically for radiotherapy: First, the lower energy in the kV range and, second, the spatial dose fractionation. For a differentiation of the two effects, three treatment plans of the lung cancer case were compared: 1) a clinical plan with nine coplanar beams of different gantry angles with 6 MV and 15 MV photons, 2) a kV MRT plan with the eight of the nine beam directions from the clinical plan in an interlaced geometry and rectangular field sizes slightly larger than the clinical plans to fully cover the target with each beam, 3) a kV plan with the same irradiation geometry as the MRT plan but with broad beam fields, i.e., homogeneous fields without spatial fractionation. The broad beam fields were calculated by accumulating the primary and scatter doses of all beams. For the MRT plan, the valley doses of all beams were summed up, which resulted in the dose to OAR. Due to the interlaced geometry with an approximatively homogeneous target dose, the peak dose was specified as the dose to the target volumes by finding the maximum peak dose of the different beams in each voxel. Both the MRT plan and the kV broad beam plan were normalized so that the dose to 99.5 % of the PTV, $D_{99.5\,\%}$, matched the $D_{99.5\,\%} = 37.5\,\mathrm{Gy}$ of the PTV in the clinical plan for a full target coverage. For the MRT plan, the normalization factor was calculated for the peak dose and then also applied for the valley dose distribution.

The used patient case was a small peripheral non-small cell lung cancer, which was clinically treated with stereotactic body radiation therapy (SBRT) with a prescription dose of 37.5 Gy in fractions of 12.5 Gy to the 60 % isodose. Here, the CT was rebinned by a factor of $4 \times 4 \times 2$ for MRT dose calculation, resulting in a planning resolution of $4.0 \times 4.0 \times 6.0\,\mathrm{mm}^3$. Dose constraints for OAR were adopted from the Department of Radiation Oncology at the Klinikum rechts der Isar, Munich and from literature [196] as $V_{20\,\mathrm{Gy}} < 10\,\%$ and $D_{\mathrm{mean}} < 8\,\mathrm{Gy}$ to the lung, $D_{\mathrm{max}} < 25.2\,\mathrm{Gy}$ and $V_{17.7\,\mathrm{Gy}} < 5\,\mathrm{cm}^3$ to the esophagus, $D_{\mathrm{max}} < 24\,\mathrm{Gy}$ to the heart, $D_{\mathrm{max}} < 18\,\mathrm{Gy}$ to the spinal cord, and $D_{\mathrm{max}} < 30\,\mathrm{Gy}$ to the trachea. Additional to the clinically delineated contours, a 20 mm-thick shell around the PTV was created by expanding the PTV contour by 20 mm and subtracting the PTV using 3DSlicer to investigate the region of healthy tissue close to the target volume.

10.2.4. Implementation of the equivalent uniform dose

For the comparison of MRT plans with different microbeam treatment geometries and for the comparison to clinical plans, the EUD assigned in each voxel a spatially modulated dose distribution to a single dose value that leads to the same clonogenic survival according to the linear-quadratic model. As shown in figure 10.1, the EUD calculation was implemented in a two-step approach: In step 1, hybridDC generated a differential dose histogram of the physical dose for each dose calculation voxel. In step 2, the EUD

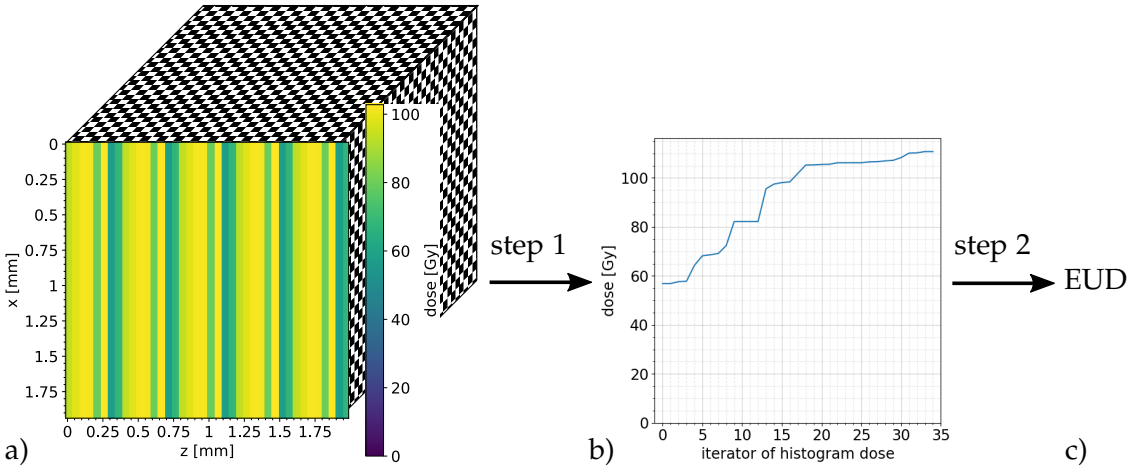

Figure 10.1.: Schematic of the EUD calculation for each dose voxel, visualized with an interlaced MRT geometry with $78 \times 78 \times 80$ subvoxels, each with a volume of $(25\,\mu\text{m})^3$. a) The three-dimensional dose distribution is analyzed in a micrometer-sized subvoxel resolution. The interlaced geometry is discernible as a dose modulation in the z-direction only, the dose distribution is constantly extended into the image plane (y-direction). b) The differential dose histogram specifies the dose of the 35 equally weighted bins. c) The EUD is calculated from the dose histogram for each dose calculation voxel.

was calculated based on the histogram and radiobiological parameters using a Python script (Python version 3.7.2). The reason for the separation was the non-linearity of the EUD (see equation (9.4)), which rendered a direct normalization of the EUD by linear scaling impossible. In hybridDC, the physical dose depended on the number of primary particles in the Monte Carlo simulations and was scaled linearly to the desired dose to the target volume. After scaling the physical dose, the EUD needed to be recalculated.

In step 1, the microscopic dose distribution, calculated by the electron convolution kernel, was analyzed in a subvoxel resolution of $(25\,\mu\text{m})^3$. Smaller subvoxels with a size of $(10\,\mu\text{m})^3$ did not discernibly alter the EUD distribution but led to considerably longer computation times and were therefore ceased. The dose values in each subvoxel were sorted in increasing order and arranged into 35 equally sized groups. Then, the mean dose of each group resulted in one dose value in the differential dose histogram. Accordingly, one histogram with 35 bins was obtained and saved for each dose calculation voxel. The bin number was reviewed with one MRT plan for the lung cancer case described in section 10.2.3. The EUD distribution using 70 instead of 35 histogram bins resulted in a voxelwise maximum EUD difference between $+0.004\,\text{Gy}$ and $-0.15\,\text{Gy}$. Due to the negligible difference and less required memory, 35 histogram bins were used in the following.

In step 2, the EUD was calculated according to equation (9.4), where D_i was the dose of a histogram bin and $n = 35$ the number of bins. The weights were unity for all

dose values ($w_i = 1$) because the mean dose of each bin was calculated from equally sized groups of subvoxel doses. In out-of-field regions with scatter dose only, the EUD was equivalent to the valley dose, which was saved from hybridDC for each beam and accumulated and added to the EUD distribution using Python.

Step 2 was validated for multiple single voxels within and close to the PTV by applying the peak-on-peak, the interlaced, and the cross-firing geometries to the lung cancer case described in section 10.2.3 and the case of the glioblastoma resection cavity introduced in section 10.2.5. The validation was performed by manual recalculation of the EUD based on the histograms and the radiobiological parameters α and β, which were introduced in chapters 1.1 and 9. The radiobiological parameters were set to $\alpha/\beta = 10\,\mathrm{Gy}$, $\alpha = 0.3\,\mathrm{Gy}^{-1}$, $\beta = 0.03\,\mathrm{Gy}^{-2}$ for the lung cancer and $\alpha/\beta = 2.096\,\mathrm{Gy}$, $\alpha = 0.035\,\mathrm{Gy}^{-1}$, $\beta = 0.0167\,\mathrm{Gy}^{-2}$ for the glioblastoma resection cavity [43].

10.2.5. Application to clinical patient data

The EUD implementation was applied to MRT plans with a cross-firing geometry. The plans were created for a variety of clinical cases regarding size and location of the tumor: a glioblastoma resection cavity, a non-small cell lung cancer treated with SBRT (as described in section 10.2.3), a palliatively irradiated sarcoma bone metastasis of the ribs, a sarcoma brain metastasis treated with radiosurgery in a single fraction, and a breast tumor[‡]. Reasons for the patient selection and the clinical dose prescriptions can be found in the publication by Kraus and Winter et al. [43]. The number of beam ports and the gantry angles of the MRT plans were adopted from the clinical treatment plans, while the size and shape of the beams were obtained by the PTV-conformality described in section 10.2.2.

For each voxel of the MRT dose calculation, hybridDC generated the differential dose histogram, from which the EUD was calculated, as described in section 10.2.4. The radiobiological parameters α and β were assigned to the volumes of interest for plan evaluation based on the delineated contours, which were extracted as labelmaps from 3DSlicer. Most values for α/β, α, and β were taken from the publications by Leeuwen et al. [197] or Klement et al. [198] for tumors and by Kehwar [199] for normal tissues. In cases of lack of evidence, the default values $\alpha/\beta = 2\,\mathrm{Gy}$, $\alpha = 0.1\,\mathrm{Gy}^{-1}$, and $\beta = 0.05\,\mathrm{Gy}^{-2}$ were assigned to normal tissue [200]. All used radiobiological parameters are listed in the publication by Kraus and Winter et al. [43]. The three-dimensional distributions of the radiobiological parameters were linearly interpolated for smoother EUD distributions, instead of discrete borders of the parameters from the labelmaps. Furthermore, the interpolation reduced rebinning errors in cases where the discrete

[‡]The MRT plans were created in collaboration with Dr. Dr. Kim M. Kraus from the Klinikum rechts der Isar at the Technical University of Munich.

borders of the (α, β) labelmaps in CT resolution did not exactly match the structure borders in the rebinned resolution for dose calculation.[§]

The MRT dose distributions were planned as single fractions, while the clinical plans had been applied in up to 30 fractions in case of the glioblastoma. For a comparison, all dose distributions were converted into the equivalent dose in 2 Gy fractions (EQD2) according to equation (9.2) with the same α/β values for the respective structure as used for the EUD calculation. Also, the prescribed doses and the dose constraints for OAR were converted to EQD2.

The normalization of the MRT dose distribution was based on a target coverage at least as good as for the clinical plan, using the dose to 98 % of the PTV, $D_{98\,\%}$. Accordingly, the MRT doses were normalized so that the $D_{98\,\%}$ of the EQD2 retrieved from the EUD matched the $D_{98\,\%}$ of the clinical EQD2 in the PTV for the cases of the glioblastoma resection cavity, the sarcoma bone metastasis, and the sarcoma brain metastasis. For the remaining two cases, the MRT dose normalization was slightly adapted manually for a sufficient target coverage and, at the same time, a minimum dose to OAR [43]. The normalization of the MRT EQD2 required an iterative process because only the physical dose could be scaled linearly. The non-linear EUD and EQD2 needed to be recalculated for the scaled physical dose distribution or rather the scaled physical dose histograms.

The evaluation of the MRT plans and the comparison to the clinical plans were based on visual assessment of the dose distributions, DVHs, and specific dose metrics that were clinically relevant to the treatment cases. For the OAR, the dosimetric constraints were adopted from the Department of Radiation Oncology at the Klinikum rechts der Isar, Munich and from literature [196, 201–204].

10.3. Results

The developed framework enabled microbeam treatment planning on clinical patient data and the evaluation of the peak dose, the valley dose, and the EUD distributions for different treatment geometries with several beam ports.

10.3.1. Comparison of a kV MRT plan to an MV clinical plan

To differentiate the effects of the lower x-ray energy and the spatial fractionation, figures 10.2(a-d) display the peak and the valley dose distribution of the kV MRT plan, the dose distribution of the kV broad beam plan, and the conventional dose distribution of the clinical MV plan for the lung cancer case. For the MRT plan, the dose to OAR is reported as the valley dose and the dose to the target volumes as the peak dose, which was combined from different beams as described in chapter 10.2.3.

[§]The contour extraction as labelmaps as well as the introduction of the contours, the radiobiological parameters for the EUD, and the EQD2 calculation were implemented into the Python script by my colleague Dr. Dr. Kim M. Kraus.

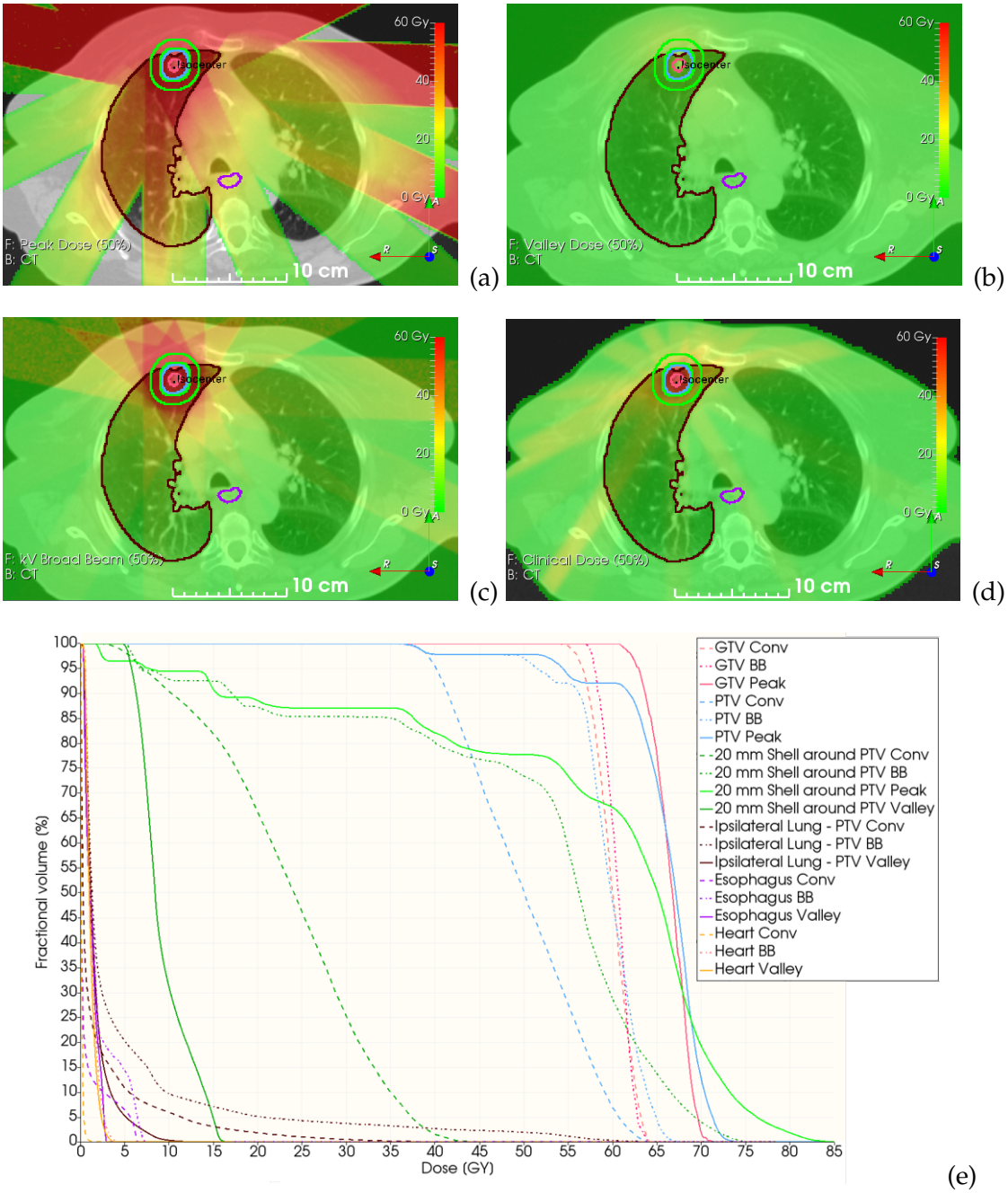

Figure 10.2.: Distributions of a peak (a) and valley dose (b) of an MRT plan, the corresponding kV broad beam (BB) plan (c), and a conventional (Conv) MV radiotherapy plan (d) of a lung cancer case overlaid on the CT slice. The color bars show the dose between 0–60 Gy and the coordinate axes the anterior (A), right (R), and superior (S, out of image plane) directions. In the dose-volume histogram (e), solid lines correspond to the MRT plan (peak for target volumes, valley for OAR), dotted lines to the BB plan, and dashed lines to the Conv plan. The MRT and BB plans were normalized to match the $D_{99.5\,\%}$ to the PTV of the Conv plan.

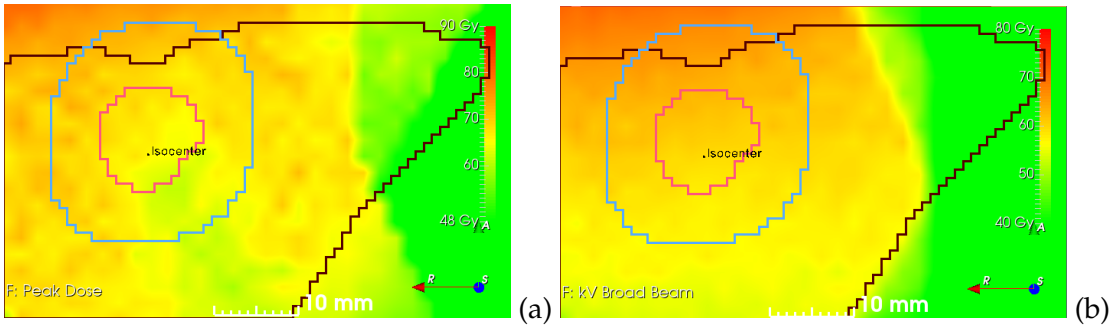

Figure 10.3.: Dose distribution in the PTV (blue), GTV (red), and the ipsilateral lung (brown) for the kV MRT plan (a) and the kV broad beam plan (b). The color bars have different limits for illustration purposes.

In figure 10.2e, the DVH curves of the gross tumor volume (GTV) of all three plans exhibited a similar steepness. Conversely, the DVH curves of the PTV were considerably steeper for both kV plans than for the clinical MV plan. Furthermore, the maximum dose, D_{max}, to the PTV was higher than D_{max} to the GTV for both kV plans even though the PTV fully encompassed the GTV; the highest dose to the PTV was found in the anterior direction outside of the GTV, as seen in figure 10.3. The reasons were the full target coverage with a constant radiation intensity across the fields for each kV beam and the alignment of the beams mainly from the anterior direction. In contrast, the clinical prescription to the 60 % isodose induced the maximum dose of the target volumes inside the GTV and a less steep PTV DVH curve for the small target volume. For the same reasons, the median dose to the PTV was notably higher for the kV plans than for the MV plans due to the dose normalization to $D_{99.5\,\%}$ to the PTV. The steps of the DVH curves of the PTV and the 20 mm-thick shell around the PTV arose from the coarse rebinning of the CT voxels for dose calculation and from beams that were not sufficiently large for an entire PTV coverage.

The MRT peak doses were higher than the kV broad beam doses to both target volumes, GTV and PTV, due to the approach of combining the dose of several beams: The broad beam doses were accumulated, resulting in an averaging effect of beams that have traveled through different path lengths in tissue. Whereas, the MRT peak doses were obtained as the voxelwise maximum dose of the different beams based on the assumption of an approximatively homogeneous dose in the voxels due to the interlaced geometry. Figure 10.3 displays the more spotted peak dose of the MRT plan compared to the smoother dose of the broad beam plan.

All treatment plans fulfilled the dose constraints for OAR for lung tumor radiotherapy specified in section 10.2.3. Even though the doses to OAR did not approach critical values, the median doses, $D_{50\,\%}$, to all investigated OAR were lowest for the clinical plan due to smaller beams than for the kV plans. The location of the OAR decided for the best plan regarding the maximum dose to the respective organ: For structures inside the

beam path, D_{max} was lowest for the MRT plan because only scatter dose contributed to the valley dose. These structures, e.g., the ipsilateral lung and the esophagus, received the highest D_{max} with the kV broad beam plan, because the steeper depth dose of kV photons demanded a higher entrance dose for the same target dose than a less steep depth dose of MV photons. Conversely, OAR that were located outside of the beam paths, such as the heart, received the lowest D_{max} for the clinical plan because of the position in the inferior direction to the beam paths for all plans. Thereby, the broader kV beams approached closer to the heart resulting in more scatter dose than the narrower MV beams. As only scatter radiation contributed to the dose to the heart, the DVH curves of the kV broad beam plan and the MRT valley dose corresponded with each other.

The 20 mm-thick shell around the PTV consisted of normal tissue but was not delineated as a specific OAR for clinical planning. The DVH curve of this shell was less steep (with a more uniform steepness) for the clinical plan than for the kV plans due to the clinical prescription to the 60 % isodose, similar to the less steep PTV curve of the clinical plan. The DVH in figure 10.2e shows both the valley and the peak dose for the shell because several but not all beams crossed in this region, which resulted in a complex dose distribution instead of a clear peak-valley profile from a single beam or an interlaced geometry from eight beams. The clinically effective dose was difficult to predict from the DVH but can be expected in the broad range between the valley and the peak dose. The curve of the kV broad beam plan approximately followed the curve of the MRT peak dose up to a dose of 47 Gy. The fractional volume of doses above 47 Gy and D_{max} were lower for the broad beam plan than for the MRT plan because of the averaging effect in the dose calculation of the broad beam plan and the voxelwise maximum dose of the MRT peak dose, as described for the target volumes.

10.3.2. Implementation of the equivalent uniform dose

The basis of the EUD calculation for each voxel was the differential dose histogram obtained from the micrometer-scaled dose distribution in subvoxel resolution. The different microbeam treatment geometries with several beams were discernible from the histograms and examined with MRT plans of several patient cases. The three-dimensional dose distributions and the corresponding dose histograms of specific voxels were investigated within and close to the target volume, where beams overlapped.

Figure 10.4 depicts two-dimensional dose distributions of the isocenter voxel resulting from a cross-firing geometry applied to the lung cancer case as well as a peak-on-peak geometry and an interlaced geometry applied to the case of the glioblastoma resection cavity (refer to figure 10.7(c-d) for the EUD distribution with cross-firing geometry). All dose distributions in figure 10.4 were generated with eight beams of equal weight. The peak-on-peak geometry entailed the largest low-dose region, while the cross-firing geometry also entailed a substantial portion of the subvoxels with low dose. In contrast, the minimum dose at the isocenter voxel was approximately half of the maximum dose for the interlaced geometry and thereby considerably higher than for the other

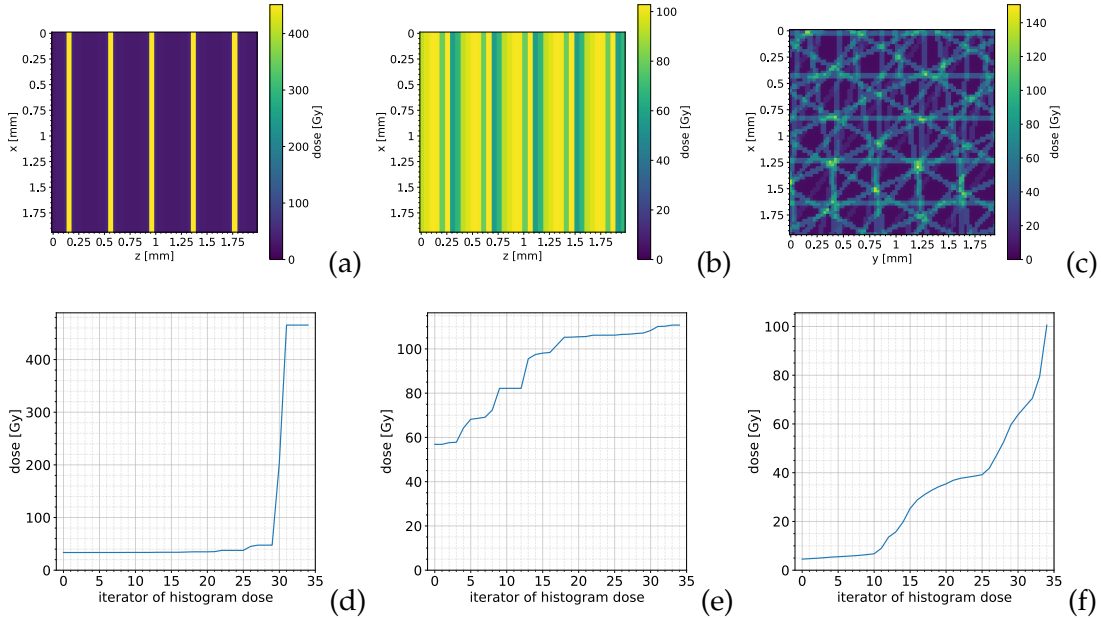

Figure 10.4.: Two-dimensional dose distributions (a-c) and differential dose histograms (d-f) of the isocenter voxel with different MRT geometries with eight beams. The dose distributions are constantly extended into the image plane as the third dimension. (a) and (d) show a peak-on-peak geometry, (b) and (e) an interlaced geometry, (c) and (f) a cross-firing geometry. The subvoxels have a resolution of $(25\,\mu m)^3$, and dose is not normalized between the geometries.

geometries. Notably, the interlaced geometry did not result in a homogeneous voxel dose either. Relative differences in the total dose to a specific voxel were below 1 % between the different treatment geometries.

The peak-on-peak geometry allowed the evaluation of a peak dose, a valley dose, and a derived PVDR. However, the EUD was needed for the interpretation of the dose distributions resulting from the interlaced or the cross-firing geometry. At the isocenter voxels shown in figure 10.4, the EUD amounted to 34.3 Gy for the peak-on-peak geometry, 58.2 Gy for the interlaced geometry, and 7.1 Gy for the cross-firing geometry. (Note that the EUD was not normalized between the geometries.) The EUD was thus mainly determined by the minimum dose in a voxel.

Besides the MRT geometry, the specific dose distribution depended on the primary and scatter dose delivered to the voxel of interest by the Monte Carlo simulations. This dependency becomes clearest for the interlaced geometry with eight beams, as demonstrated in figure 10.5 for the lung cancer case. If a voxel received the same primary and scatter dose of each of the eight beams, the dose within the voxel was homogeneous. Conversely, different primary and scatter doses induced a heterogeneous

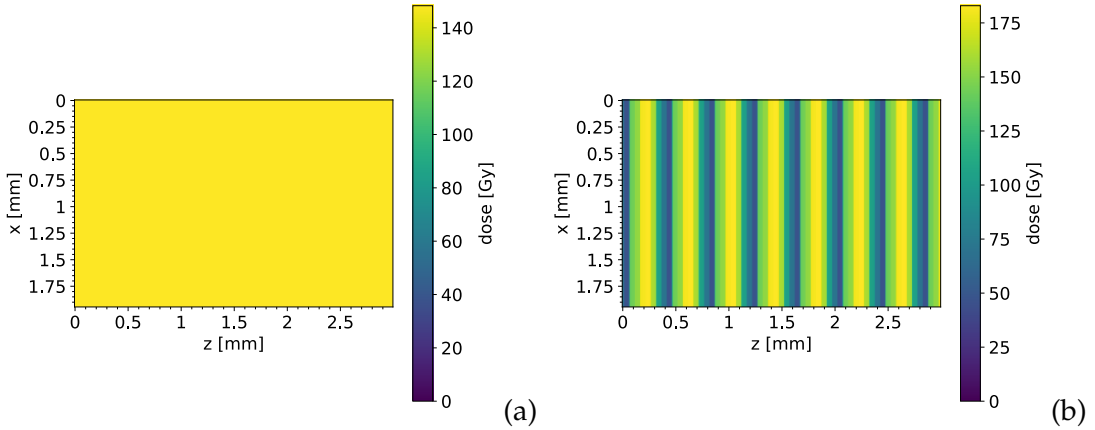

Figure 10.5.: Two-dimensional dose distributions of the isocenter voxel with an interlaced MRT geometry with eight beams. (a) All beams have the same primary and scatter doses. (b) Realistic distribution with different primary and scatter doses. Here, the subvoxel resolution was $(10\,\mu m)^3$.

dose distribution even for the interlaced geometry, which occurred due to different radiological depths for different beams.

10.3.3. Application to clinical patient data

With kV MRT, it was possible to create treatment plans comparable to clinical MV radiotherapy plans. First approaches of MRT plans with rectangular fields achieved sufficient target coverage. However, the fields extended largely into normal tissue, yielding high doses to the region around the target volume. This observation demonstrated the importance of tumor-conformal fields.

With PTV-conformal MRT fields, most dose constraints for OAR were fulfilled for the investigated patient cases, while some OAR were better spared with the clinical plan and some OAR were better spared with the MRT plan. Target coverage was ensured by the normalization of the MRT dose (EQD2 from the EUD) to $D_{98\,\%}$ to the PTV of the clinical plan, based on the assumption of a sufficient coverage with the clinical plan.

Figure 10.6 displays the DVH based on the EQD2 from the EUD with the MRT plan and from the dose distribution with the clinical plan for the five investigated patient cases. Interesting aspects for the further development of the MRT planning are explained hereafter, while more details on the dose metrics to the PTV and to OAR can be found in the publication by Kraus and Winter et al. [43].

For the cases of the glioblastoma resection cavity, the sarcoma bone metastasis, and the breast cancer, the DVH curves of the target volumes had a markedly less steep slope for the MRT plan than for the respective clinical plan, as seen in figure 10.6(a, c, e). A less steep slope implied a less homogeneous dose within the target volume, which possibly partly resulted from the steeper depth dose curve of kV radiation than

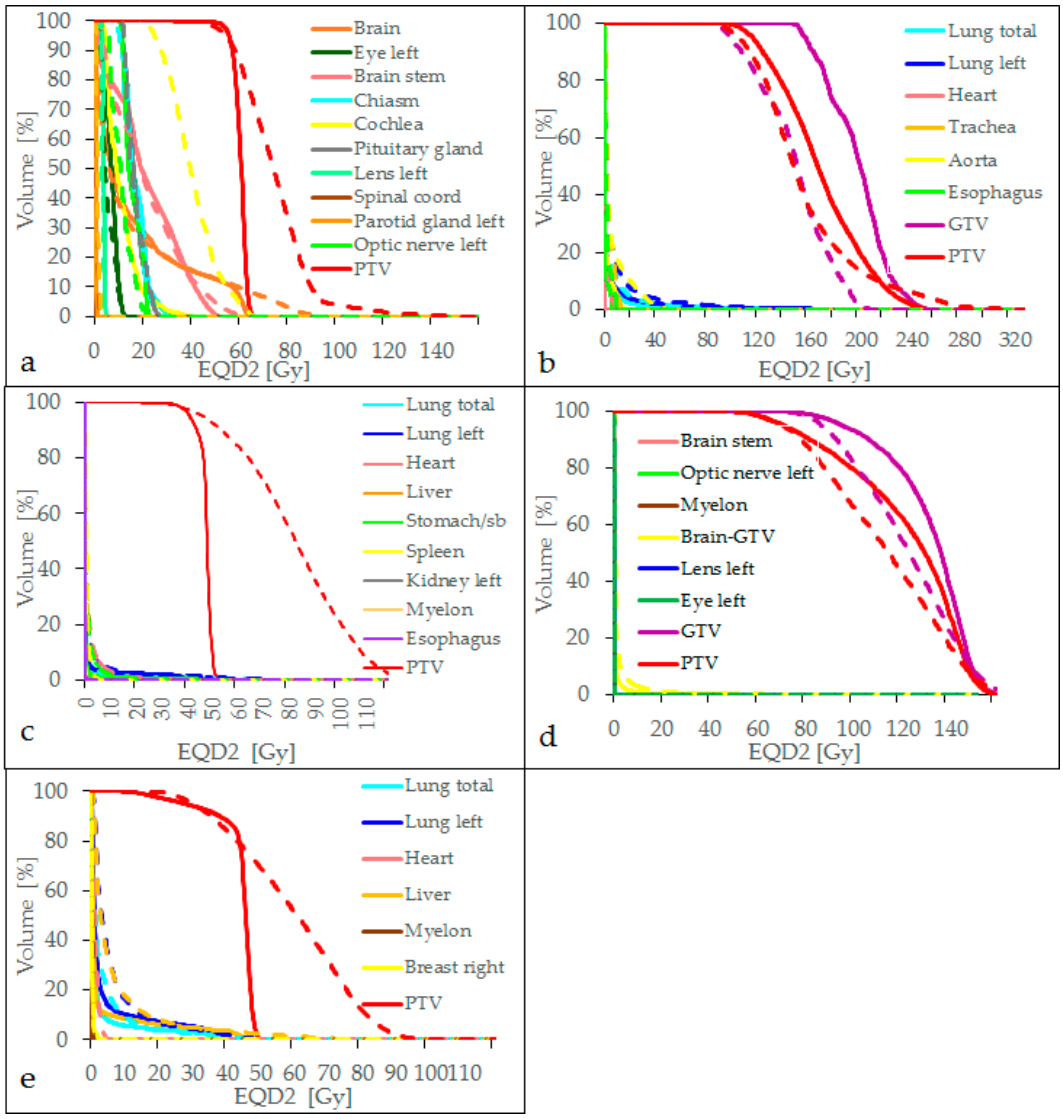

Figure 10.6.: Dose-volume histograms of the treatment plans for the glioblastoma resection cavity (a), the lung cancer (b), the sarcoma bone metastasis (c), the sarcoma brain metastasis (d), and the breast cancer (e). Solid lines represent the clinical plan and dashed lines the MRT plan. Kraus and Winter et al. [43].

of MV radiation in the large PTV but mainly from the missing possibility of dose optimization and of beam weighting. For most patient cases, a higher number of beam ports resulted in a more homogeneous target dose than a lower number of ports. For the comparison shown here, the MRT plans were created with the same number of beams as the respective clinical plan, where the plans of the sarcoma bone metastasis and the breast cancer had only two beams.

A general observation was a stronger dose fluctuation of the MRT dose in lung tissue compared to the clinical dose. The reason was the statistical Monte Carlo simulation method: The low density of air resulted in only few interactions, which, however, led to a high dose-to-medium due to the small denominator of the air density. The clinical treatment planning differed in two ways: First, the dose was calculated analytically, and second, the dose was reported as dose-to-water (see section 10.4 for a differentiation of dose-to-medium and dose-to-water).

For the case of the glioblastoma resection cavity in figure 10.6a, the cochlea received a considerably higher dose with the MRT plan than with the clinical plan; the constraint of $D_{\mathrm{max}} < 45\,\mathrm{Gy}$ was only fulfilled for the clinical plan. The reason was the contour overlap of the cochlea and the PTV, which can be seen in figure 10.7. During clinical planning, the cochlea was manually spared, which was not possible with the PTV-conformal MRT beams of equal weight.

For the lung cancer case in figure 10.6b, a very high maximum dose of $D_{\mathrm{max}} = 47\,\mathrm{Gy}$ to the trachea (constraint $D_{\mathrm{max}} < 32\,\mathrm{Gy}$) resulted from a single-voxel dose hotspot in the air volume within the trachea. The maximum dose to a volume of $0.1\,\mathrm{cm}^3$ was 19 Gy and thus fulfilled the specified constraint for the trachea. The hotspot arose from the statistical dose-to-medium calculation by Monte Carlo simulations, as described above for the strong dose fluctuation in lung tissue. High doses to the heart and the aorta followed from the PTV-conformal fields of homogeneous intensity, which all fully covered the PTV, in contrast to the clinical bell-shaped dose profile in the PTV due to the prescription to the 60 % isodose. Consequently, a larger volume behind the target received a higher dose for the MRT plan because of the broader fields.

For the bone metastasis case, the brain metastasis case, and the breast cancer case, both plans fulfilled all dose constraints for OAR, except of the D_{max} to the brain in the brain metastasis case and the D_{max} to the contralateral breast in the breast cancer case, which were, however, exceeded by both plans. The dose to OAR was generally higher for the MRT plan than for the clinical plan. For the bone metastasis case and the breast cancer case, the higher MRT dose could be partially explained by the dose normalization to $D_{98\,\%}$ and the less steep DVH curve of the PTV. Furthermore, the dose optimization, which was only applied for the clinical plans, was more relevant for small target volumes, which were found for the sarcoma metastases in the bone and brain. The MRT plan for the breast cancer case provided a better sparing of the total lung and the contralateral breast than the clinical plan.

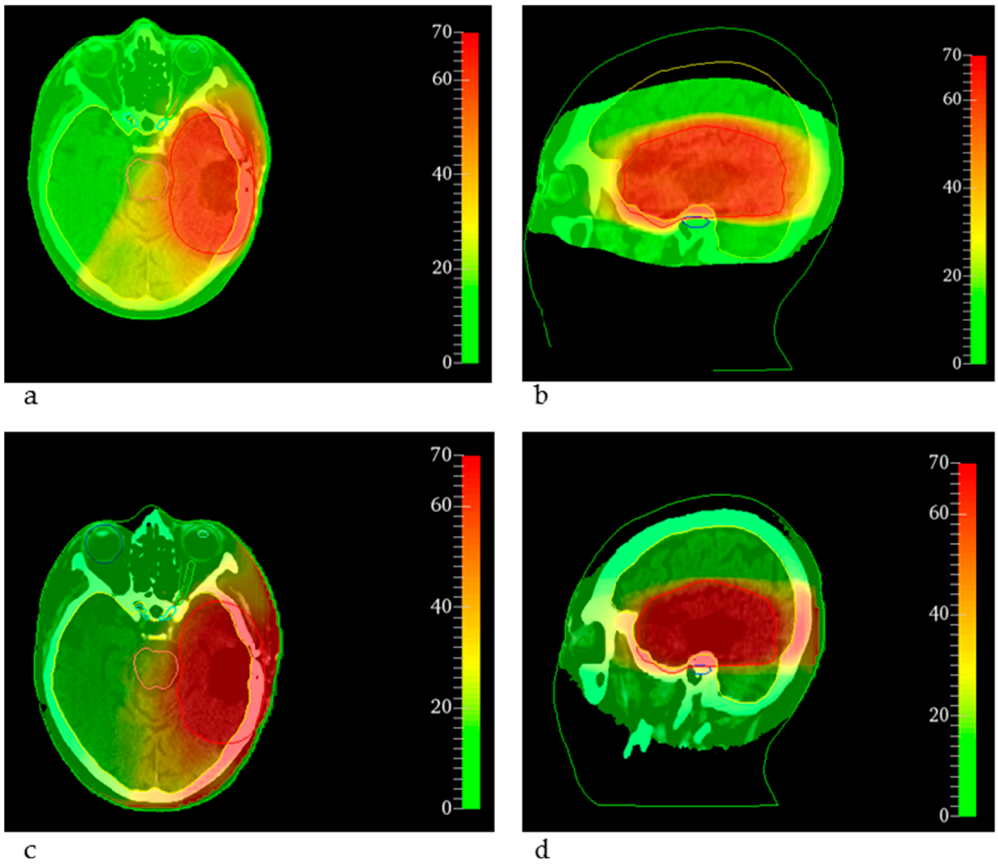

Figure 10.7.: Dose distributions of the clinical treatment plan (a,b) and MRT plan (c,d) of a glioblastoma resection cavity overlaid on the CT slice. The color bar indicates the EQD2 in Gy, the red contour the PTV, the yellow contour the brain, the light red contour the brain stem, and the blue contour in (b) and (d) the cochlea. Kraus and Winter et al. [43].

10.4. Discussion

MRT with kV photons generated comparable, however not generally better treatment plans to conventional clinical radiotherapy with MV photons with respect to target coverage and OAR sparing. The comparable plans were achieved even without any beam weighting or intensity modulation for MRT.

Conclusions from the comparison of a kV MRT plan to an MV clinical plan

The evaluation of the kV MRT plan for the lung cancer case, presented in section 10.3.1, and the comparison to the kV broad beam and the MV clinical plan revealed several difficulties for MRT planning and allowed an advancement of the treatment planning process.

First, the microbeam treatment plan based on the peak and valley dose distributions did not allow an appropriate comparison to the clinical plan, especially due to uncertainties of the biological effect in the region surrounding the PTV. In the PTV-surrounding region several but not all beams crossed, and thus, the clinical effect was expected to be in the large range between the peak and the valley dose. Additionally, the normalization of the MRT dose and the steps in the PTV DVH curve resulted in a $D_{50\,\%}$ to the PTV that was higher by 34 % than the clinical $D_{50\,\%}$. The $D_{50\,\%}$ to the GTV was higher by 11 % than the clinical $D_{50\,\%}$. The reason for the higher $D_{50\,\%}$ was the requirement of a full (or rather 99.8 %) PTV coverage for the MRT plan compared to the clinical plan, even though the PTV DVH curve of the clinical plan was intentionally less steep due to the prescription to the 60 % isodose to the small PTV. A lower dose to the target volumes, e.g., a normalization of the MRT dose to a full coverage of the GTV or to the $D_{50\,\%}$ to either target volume, would yield a lower dose to OAR for the presented MRT plan. An evaluation of an MRT plan with several fields demands the introduction of the EUD, especially in the region around the target volume of several crossing beams. The assumption of a homogeneous dose in the voxels of the target volume due to the interlaced geometry proved to be an oversimplification (see section 10.3.2 and figure 10.5). As the beams contribute different doses in realistic patient geometries, the dose determination as the voxelwise maximum peak dose turned out wrong, and a plan evaluation requires the EUD calculation also in the target volumes.

Second, the rebinning of the CT by the factors $4 \times 4 \times 2$ ($x \times y \times z$) for dose calculation shortened the computation time but was too coarse for a sophisticated evaluation of the MRT plan. Moreover, the applied beams were smaller than the PTV due to the coarse rebinning, resulting in steps of the DVH curve. The planning resolution was more important for small target volumes like the presented lung cancer than for large target volumes. Consequently, a rebinning of $2 \times 2 \times 1$ was applied for all subsequent MRT plans. An omission of the rebinning without exceeding computational limits, achievable, e.g., by only calculating the dose in volumes within the external body contour, would allow an evaluation of the rebinning effects and possibly more exact MRT plans.

Third, a reasonable normalization or scaling of the MRT dose distribution was essential for the evaluation of the treatment plan, especially of the dose to OAR. A different dose normalization can lead to different dose metrics to both target volumes and OAR and thus to different conclusions of treatment plan comparisons. Decisions to be taken mainly include the contour structure of a target volume for dose normalization and the fractional volume of the selected structure receiving a specific dose, which can typically be $D_{98\,\%}$ or $D_{50\,\%}$. The clinical SBRT plan for the lung cancer case caused challenges regarding the MRT dose normalization due to the clinical dose prescription to the 60 % isodose to the PTV, yielding to a shallow DVH curve and a bell-shaped dose profile through the target volume. The current MRT planning framework without beam or intensity weighting only allowed rectangular beam intensity profiles, which resulted in steeper DVH curves than the bell-shaped intensity profiles. Consequently, clinical treatment plans with a dose profile through the target volume that is more similar to a

rectangular MRT dose profile would be more practicable for first comparisons between MRT and clinical plans. The examination of the dose profile through the target volume for different MRT and clinical treatment plans might lead to a better understanding of the impact of a specific MRT dose normalization, ideally in consultation with radiation oncologists. For a further development, beam and intensity weightings can improve MRT planning and make MRT plans more competitive to clinical plans, which apply these techniques or even inverse dose optimization as standard.

Finally, the treatment plans with kV photons were expected to deliver steeper lateral dose falloffs due to a shorter range of secondary electrons than the clinical plan with MV photons. However, these differences in lateral dose falloffs were not observed, because the broader, rectangular beams of the kV plans, in contrast to the conformal and optimized beams of the MV plan, influenced the dose distributions more strongly than the lateral dose falloffs. This observation was seen in the DVH in figure 10.2e as smaller fractional volumes of low-dose to OAR for the clinical MV plan than for the kV plans. A more detailed analysis of the lateral dose falloffs can provide a deeper understanding of the differentiation between the effects resulting from the kV spectrum and from the spatial fractionation. This analysis requires a replanning of the clinical dose distribution with the same fields as the kV plans, the only difference to the kV broad beam plan being the energy spectrum. The replanning of the clinical dose distribution should ideally be performed with the same dose calculation algorithm as the kV plans, i.e., with hybridDC.

MRT geometry

Microbeam treatment planning with several beam ports offers additional degrees of freedom and, hence, further decisions to be taken than in conventional treatment planning. The MRT geometries presented in sections 10.2.1 and 10.3.2 include the interlaced, the peak-on-peak, and the cross-firing geometry, which can all be achieved with the identical conventional beam geometry. The implementation of the different microbeam treatment geometries into the dose calculation algorithm was analyzed and verified, while a comprehensive comparison of treatment plans based on a DVH and dose metrics remains missing. Nevertheless, only the cross-firing geometry can be suggested for pursuing treatment planning studies.

The interlaced geometry could theoretically allow a simple interpretation of the homogeneous dose in the voxels of the target volume. However, realistic planning scenarios exhibited a heterogeneous dose in the target voxels due to differences in the primary and scatter dose contribution from different beams, as demonstrated in figure 10.5. Even though beam weighting or dose optimization would allow the same primary dose contribution from all beams in a single voxel, e.g., the isocenter voxel, this approach is impracticable for a complete target volume. For this reason, a homogeneous dose in the target voxels cannot be assumed for plan evaluation, but the micrometer-scaled dose distribution must be considered similarly as for the other MRT geometries. Moreover, the application of interlaced MRT constrains the number of beam ports to the ratio of

the peak width to the center-to-center distance, i.e., eight beams in this work. Besides, the interlaced geometry is unfeasible for clinical application due to the requirement of a realignment of the patient and inner organs with an accuracy of few micrometers. State-of-the-art invasive or frameless fixation systems for a clinical stereotactic head immobilization reach an accuracy in the submillimeter range [186], which is not sufficient for interlaced MRT.

The peak-on-peak geometry seems biologically promising according to the publication by Sammer et al. [47], who observed less severe side effects in normal tissue after accurate realignment of proton minibeams to the same irradiation positions than after a shift of the irradiation positions. Nevertheless, the peak-on-peak MRT geometry requires a similar alignment accuracy as the interlaced geometry and is therefore not practicable for clinical application.

The main advantage of cross-firing MRT is a required alignment accuracy that is similar as for conventional radiotherapy. Furthermore, the number of beam ports can be flexibly chosen, likewise for the peak-on-peak geometry. Moreover, Eling et al. [36] found strong anti-tumor effects in rats bearing brain tumors after multiport cross-firing MRT at low normal tissue toxicities compared to unidirectional MRT or broad beam irradiation. For these reasons, cross-firing MRT appears the most promising geometry for clinical application and was therefore applied for the investigation of MRT plans on clinical patient data in section 10.3.3.

Independent of the number of beam ports, larger MRT fields induce more scattered radiation and thus a higher valley dose and a lower PVDR than smaller fields [205]. For this reason, it was expected that smaller target volumes would be advantageous for MRT. Furthermore, shallowly located target volumes seem promising for MRT due to the less steep depth-dose curve of kV photons compared to clinical radiotherapy with MV photons. Consistently, the PVDR analysis by Smyth et al. [42] suggested small or shallow tumors, e.g., brain tumors, head and neck tumors, or loco-regionally breast cancer, as potential targets for first clinical trials. The results in section 10.3.3 could not confirm this finding, though. A main difference between the studies was the treatment geometry: Smyth et al. [42] applied unidirectional MRT, whereas the MRT planning framework presented in this work facilitated various beam directions for more realistic clinical scenarios. For this reason, effects from different planning parameters overlapped, e.g., the number of beams, the beam directions with the resulting radiological depths of the target volume, field sizes, and the micrometer-scaled dose distribution within the dose calculation voxels. A differentiation of these effects requires a more comprehensive MRT planning study by only changing one parameter at the time. More comprehensive studies of that kind are necessary for a well-founded selection of a treatment case for a first clinical MRT trial.

Equivalent uniform dose

Previous phantom, in-vitro, or planning studies for MRT have mostly reported the peak and the valley dose distributions. For multidirectional cross-firing MRT, these values

are not defined due to the complex micrometer-scaled dose distribution. Furthermore, a clinical evaluation of MRT plans requires a single dose measure that corresponds to the MRT dose in the CT resolution. The EUD had been suggested for spatially fractionated radiotherapy and was introduced into the MRT planning algorithm in this work.

The EUD calculation based on differential dose histograms of single voxels in section 10.3.2 showed that the EUD was mainly determined by the minimum dose to a voxel. This observation is in agreement with previous findings of unidirectional MRT that the valley dose mainly determines the tissue toxicity and that the EUD tends towards the valley dose for distributions of mean doses higher than the radiobiological parameter α/β [44, 85].

On the one hand, the EUD facilitates the assessment of MRT plans. On the other hand, the concept has still several drawbacks and uncertainties. First, the linear-quadratic model (LQM) that underlies the EUD, was designed for treatment plans with several temporal fractions of doses in the range of 1–6 Gy [4]. In contrast, many MRT experiments have been conducted with single fractions of peak doses much higher than the stated range. The applicability of the LQM to higher doses per fraction has been discussed for years [206] and argued in favor of doses up to 18 Gy [207]. The EUD becomes therefore less accurate for a peak dose per fraction that is considerably larger than the value of the radiobiological parameter α/β [85, 206]. Second, the EUD calculation requires values for the α/β but also separate values for α and β. In clinical routine, the α/β ratio is used for the EQD2 calculation so that ratios have been published for tumors and OAR from in-vitro as well as clinical studies [4]. However, there is a lack of data for separate values of α and β, especially for normal tissue, such that the used parameters are assumed to have a higher uncertainty than α/β. At the same time, the EUD strongly increases for a constant α/β if α and β approach zero as the survival fraction then also approaches zero (refer to equation (9.4)). Third, the EUD and the radiobiological parameters α and β are based on clonogenic cell survival and only account for DNA repair; while reoxygenation, repopulation, and redistribution of cells are neglected. Moreover, the EUD does not predict radiobiological effects of, e.g., the immune system, which plays an important role in highly fractionated beams [51, 53]. Finally, in-house, unpublished data of colony formation assays after MRT and proton minibeam irradiations indicated that the EUD can predict the clonogenic cell survival of normal cell lines, however overestimates the survival of tumor cell lines. For this reason, the EUD needs further in-vitro and later in-vivo experimental verification for MRT before it can be used for planning patient irradiations. Possibly, the EUD calculation requires adjustments or even a substitute for tumor tissues.

The linear scaling of the MRT dose was only possible for the physical dose, whereas the EUD and EQD2 needed to be recalculated after the scaling due to their non-linearity. Notably, the PVDR did not stay constant during the conversion between different fractionation schemes. The conversion of a single fraction to EQD2 increased the weights on higher doses, i.e., on the peak doses more than on the valley doses, and thus increased

the PVDR (refer to equation (9.2)). For this reason, the applicability of the EQD2 to MRT should be further investigated.

In conclusion, the EUD has several limitations and uncertainties regarding the application to MRT. Nevertheless, it is up to now the best and only concept of reporting complex micrometer-scaled dose distributions in CT resolution to my knowledge because it is motivated by and based on radiobiological experiments.

Comparison of dose-to-medium to dose-to-water

This work reported the dose-to-medium for MRT plans and compared them to clinical plans reporting the dose-to-water despite the evident inconsistency. Clinical treatment planning, based on, e.g., pencil beam or collapsed cone algorithms, relies on density scaling of the tissue and on input data, such as depth-dose curves measured in water. These plans therefore naturally issue dose-to-water. Conversely, Monte Carlo algorithms calculate the dose as an energy deposit to a specific mass of a medium and consequently issue dose-to-medium. Controversial debates within the radiation oncology and medical physics communities about the best method for dose reporting have lasted for decades, although no general guideline has been established [208–211]. It remains unclear whether dose-to-medium or dose-to-water better predicts the clinical outcome. The best prediction method has particularly not been investigated for MRT.

The conversion from dose-to-medium to dose-to-water has been implemented in different ways. Siebers et al. [212] developed a conversion method based on the Bragg-Gray cavity theory [213]. The calculated stopping power ratios for energies of secondary electrons between 10 keV and 20 MeV were found to be independent of the depth in tissue and independent of the location whether it was in-field or out-of-field, which makes the method potentially transferable to peak and valley regions. For energies below 600 keV that are relevant for MRT, the authors found correction factors between dose-to-medium and dose-to-water of approximately 1 % for soft tissue and lung, of approximately 3 % for soft bone, and up to 14 % for cortical bone. Differences between soft tissue and lung only occurred due to different densities, which can be explained as the dose in lung tissue is deposited in cells that mainly consist of water. Accordingly, the energy absorption coefficient of lung tissue correlates with its mass density. This explanation follows a similar line of argument as the rationale for the adjustment of the MRT dose calculation in lung tissue in section 10.2.2 (see also the following subsection for further discussion). Dogan et al. [209] applied the method by Siebers et al. [212] and observed systematic differences in dose-volume metrics for head and neck cancer patients and prostate carcinoma patients between Monte Carlo-calculated treatment plans reporting dose-to-medium and converted plans reporting dose-to-water. However, the differences were below 6 % in all target volumes and OAR, except for the femoral head of the prostate carcinoma case, where the hard bone led to a difference of 8 %. Ma and Li [210] stated that Monte Carlo dose calculation algorithms should report dose-to-medium, which agreed better with conventionally analytically calculated dose than a converted dose-to-water. Conversely, Reynaert et al. [211] stated that the conversion

from dose-to-medium to dose-to-water should be performed by multiplying dose-to-medium with the ratio of the mass energy absorption coefficients between water and the respective medium, which is only valid in regions of electronic equilibrium and results in considerably larger differences than stated before.

Concluding from these previous works, dose-to-medium was reported for the MRT plans because of the higher reliability in Monte Carlo dose calculation than in any conversion method. A conversion would introduce additional uncertainties regarding the tissue type and the respective stopping power ratio or mass energy absorption coefficient ratio for each dose calculation voxel [208]. Furthermore, dose differences of markedly less than 14 % in most structures were not critical for the investigations in this work, which mainly presented the developed MRT planning framework and applied the framework to first clinical patient data. Especially in tissues other than bone, only minor differences between dose-to-medium and dose-to-water of less than 6 % were expected and none of the investigated treatment cases in section 10.3.3 specified a bony structure as OAR. For this reason, other uncertainties, such as the radiobiological parameters for the EUD calculation, were presumably higher than the differentiation between dose-to-medium and dose-to-water. Nevertheless, the cortical bone received a higher dose-to-medium with the MRT plan in figures 10.7(c-d) compared to the dose-to-water with the clinical plan in figures 10.7(a-b) in the patient case with the glioblastoma resection cavity. This observation resulted from the omitted conversion and corresponded to the reports of largest differences in hard bone. For the planning of clinical trials, a conversion of the MRT plan to dose-to-water should be considered, especially if bones are included in the treatment plan, due to the clinical experience and reporting of clinical trials using dose-to-water.

MRT dose calculation in the lung

The microbeam dose calculation in lung tissue demands attention for several reasons. The statistical Monte Carlo simulations yield strong dose fluctuations in the low density material as explained in section 10.3.3. Furthermore, the lung microstructure poses challenges on the dose calculation as the structure size is in the same order of magnitude as the microbeam dose modulation. Bronchi and larger blood vessels in the millimeter-range are discernible in clinical CT images, whereas smaller structures are not resolved but yield an averaged CT value. Nevertheless, small structures such as bronchioles with a typical diameter of 0.5 mm, alveoli of 200–500 µm, alveolar membranes of 0.2–0.6 µm [214, 215], as well as pulmonary blood vessels and nerves of different sizes interact with photons, which distorts the micrometer-scaled peak-valley profile and modifies the peak and valley doses [216].

To enable treatment plan evaluation in the thorax region at all, a method for microbeam dose calculation in lung tissue was implemented in this work, which has, however, not been validated experimentally. During the evaluation of an MRT plan, the uncertainty of the dose to the lung must therefore be borne in mind because of the long ranges of secondary electrons in air that smear out the microbeam dose distribution but are not

considered in the implemented dose calculation algorithm. In lung tissue, the actual peak doses were thus probably lower and the valley doses higher than assessed in this work. As the lowest value in a dose calculation voxel is relevant for the EUD, an increase in the valley dose directly impacts the EUD. Consequently, the presented doses to the lung are presumably lower than they would be measured in radiobiological experiments and need therefore further investigation.

There are two approaches conceivable for the MRT dose calculation in the lung: A model of the lung microstructure, e.g., artificial alveoli as randomly placed or grid-shaped arranged spheres, can be implemented into the microbeam treatment planning algorithm hybridDC in the structures delineated as lung tissue. Alternatively, the convolution kernel for the electron dose calculation in hybridDC is modified to directly distort the microbeam dose distribution for all voxels that are delineated as lung tissue. The second approach seems easier to implement as the electron convolution kernel is already calculated for each dose voxel and depends on the voxel material. On that account, even different distortion models depending on, e.g., the CT value, would be possible. The distortion models could be based on measurement data of a microbeam dose distribution in ex-vivo lung tissue. A further argument for the second approach is the direct modeling of the effect instead of a modeling of the cause of the microbeam dose distortion; the direct modeling decreases the number of parameters and thus presumably the uncertainties. Micro-CT data can be expedient to validate the implemented algorithm with phantoms, ex-vivo samples, or in preclinical experiments. However, micro-CTs are not applicable for clinical routine due to a high radiation dose, a small field-of-view, a limited availability, and high costs [78].

Further developments for MRT planning

The microbeam treatment planning can be improved and advanced in many ways regarding the treatment geometry, the dose calculation algorithm, the workflow, and the implementation of further extensions.

Most importantly, the treatment fields should be shaped more flexible. The implementation of PTV-conformal fields already drastically improved MRT plans on clinical patient data by reducing the dose to normal tissue surrounding the target volume compared to rectangular fields. Applying multileaf-collimators, as common for clinical radiotherapy, would allow the radiation oncologist to individually shape the treatment field separately for each beam. A flexible field shaping could homogenize the target dose and spare OAR close to the target volume, especially for donut-shaped or kidney-shaped target volumes, as seen in the clinical plan for the cochlea close to the glioblastoma resection cavity in figure 10.7. Furthermore, the currently applied method to create treatment fields conformal to a specific target volume required several manual adjustments that readily lead to mistakes, e.g., during exporting and rebinning the labelmap of the desired target volume from 3DSlicer into a Python script and during setting the size of the cross-shaped convolution kernel. For this reason, conformal fields should be created automatically to the correct size and shape so that manual adjustments would

be required only for unusual cases. Moreover, different weightings of complete beams are easy to implement and can be a first step towards intensity modulation. Intra-field intensity modulation would bring the MRT plans even closer to clinical treatment plans, but the clinical realization needs to be tested.

The dose calculation algorithm should be advanced by revising the EUD calculation and the dose calculation in lung tissue as described above. Furthermore, beam hardening effects are not considered in the current version of hybridDC but might play a larger role for MRT planning of patient cases due to longer beam paths compared to preclinical MRT planning.

The planning workflow can be optimized by reducing the manual steps and increasing automation. So far, the CT data needed to be centered to the origin of the coordinate system in 3DSlicer before MRT dose calculation, and related data needed to be manually shifted by the same vector, which was time-consuming and brought complications for plan evaluation. Instead, the displacement of the CT should be automated in the treatment planning process. Furthermore, the normalization of the MRT dose to the clinical dose was cumbersome due to the iterative process required by the non-linearity of the EUD and EQD2 equations. Ideally, hybridDC directly creates a normalized treatment plan, which requires the specified dose metric for the EUD or EQD2 normalization as an input from the user as well as the radiobiological parameters α and β for each structure of interest deposited as a lookup table in hybridDC. As a direct normalization of the EUD or EQD2 in hybridDC might be difficult, an interim step can be the extension of the MRT module in 3DSlicer that calculates the EUD, the EQD2, and the iterative normalization using an underlying Python script. For advanced MRT planning and certainly for the planning of clinical trials, the MRT dose needs to be normalized and optimized to the individual clinical case, including a consideration of the dose profile in target volume.

A long-term goal is an MRT-optimized treatment planning, which admittedly requires a better understanding of the planning parameters, their impact on MRT dose distributions, and finally a broader in-vivo MRT experience. Microbeam treatment planning might be further improved by introducing radiobiological effects such as the increased radiobiological effectiveness (RBE) of kV photons compared to MV photons [217, 218], even though the International Commission on Radiological Protection recommend an RBE weighting factor of 1 for all photon energies [219]. First models for the tumor control probability and the normal tissue complication probability have been investigated for spatially fractionated radiotherapy [220]. These models could deepen the understanding of the MRT mechanisms and simplify clinical MRT planning.

The microbeam treatment planning algorithm should be extended to fields from compact MRT sources, e.g., from the line-focus x-ray tube presented in part II. This extension includes divergent fields, a variation of the focal spot size, different energy spectra, and non-polarized x-radiation requiring a review of the Geant4 physics settings. Compact sources are crucial for clinical application of MRT due to a wider availability and lower costs. Treatment plans with a crossing of divergent microbeam fields involve

even more complex dose distributions than plans with parallel beams from synchrotrons. Hotspots and coldspots in the valley dose and EUD distribution occur from a partial overlap of peaks independent of the microbeam geometry, which is demonstrated in chapter 11 for microbeam arc therapy. Moreover, robust treatment planning should be investigated for multidirectional MRT.

Finally, the combination of temporal fractionation with spatial fractionation, which has started in preclinical experiments [29, 47, 54, 185], should be explored before clinical trials. Eventually, a combined administration of systemic drugs or immunotherapy with MRT might increase the tumor control.

11. Microbeam arc therapy

11.1. Introduction

With unidirectional microbeam radiotherapy (MRT), steeper depth-dose curves of orthovoltage photons lead to higher doses to superficial healthy tissue for the same target dose than typically applied clinical radiation fields with MV photons. Multidirectional MRT can decrease beam entrance doses to superficial organs at risk that are located in the beam path. Microbeam arc therapy is a strategy that is further developed from multidirectional MRT in imitation of clinical arc therapy but with a strong dose modulation in micrometer resolution. The spatial dose fractionation is retained in the target volume, in contrast to spiralMRT that is a different method of a rotational delivery of microbeams [187].

This chapter presents the concept of microbeam arc therapy and simulated dose distributions of divergent microbeam arc therapy in a head phantom study. The equivalent uniform dose (EUD) helps to interpret the micrometer-scaled physical dose distribution by transforming the dose in micrometer resolution to a macroscopic dose in millimeter resolution that leads to the same radiobiological effect, as introduced in chapter 9. In a future application of microbeam arc therapy, the practicability will decide on whether the radiation source rotates around the target or, vice versa, the target rotates in the static beam of an MRT source.

11.2. Methods

The concept of microbeam arc therapy is depicted in figure 11.1. A head phantom is irradiated with MRT during a rotation around the axis centrally through the target volume, parallel to the x-axis, which is the direction of strong modulation of the peak-valley profile. The rotation distributes the entrance dose over a large volume, while the highest dose is delivered to the center of the irradiated sample. The spatial dose fractionation is retained in x-direction.

11.2.1. Simulations

For a principle demonstration of microbeam arc therapy, Monte Carlo simulations of unidirectional MRT were performed in Geant4 (version 10.4.p02) [93], and the dose distribution in the phantom was rotated using Matlab (version R2018b, The MathWorks Inc., USA). In Geant4, the *G4EmPenelopePhysics* list was employed with fluorescence

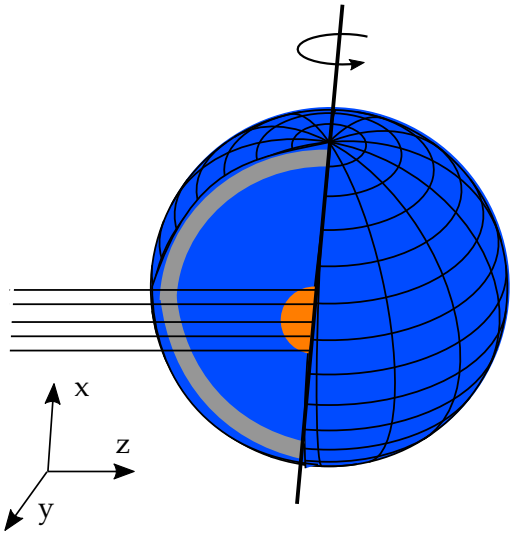

Figure 11.1.: The concept of microbeam arc therapy applied to a phantom study. In the microbeam field, the x-rays travel in positive z-direction and hit the head phantom, consisting (from the exterior to the center) of a water-equivalent skin (blue), a cortical bone (gray), water-equivalent brain (blue), and water-equivalent tumor (orange) (not to scale). The rotation axis is parallel to the x-direction and located centrally in the tumor.

electrons and particle-induced x-ray emission activated; default step sizes for electrons and positrons (step function parameters $dRoverRange = 0.2$, $finalRange = 0.1\,\mathrm{mm}$); and a range cut of 1 µm for photons, electrons, and positrons [95, 96].

A water sphere with a radius of 63 mm represented a water-equivalent brain including a centrally located water-equivalent tumor with a radius of 10 mm. The brain was surrounded by a 6 mm-thick cortical bone (material composition and the mass density of $\rho_{\mathrm{cort}} = 1.95\,\mathrm{g/cm^3}$ extracted from the ICRU report 44 [195]) and a 1 mm-thick water-equivalent skin. The remaining space was set to vacuum.

The radiation from the line-focus x-ray tube was simulated with varying electron acceleration voltages and a focal spot size of 50 µm × 20 mm ($x \times y$). The spectrum was obtained using Monte Carlo simulations as described in chapter 4.2.1: An electron beam of 400 keV, 600 keV, or 800 keV hit a tungsten target, the produced photons were scored in a phase space detector, and the spectra were filtered by 0.8 mm beryllium and 0.4 mm copper with energy-dependent mass attenuation coefficients from NIST [97]. In Geant4, a multislit collimator with divergent slits divided the homogeneous radiation field into microbeams with a peak size of 50 µm × 20 mm ($x \times y$) and a center-to-center distance of 400 µm (x-direction), defined at the rear end of the collimator, as described in section 4.2.1. The collimator had a total thickness of 13 mm, 24 mm, and 35 mm for the 400 kVp, 600 kVp, and 800 kVp spectrum, respectively. The distance from the focal spot to the rear end of the multislit collimator was 50 cm, and the head phantom was located

contiguously behind the collimator. The radiation field had a size of 20 mm × 20 mm ($x \times y$) at the phantom surface and diverged along the beam path in the z-direction. The energy deposit was scored in the head phantom in cuboid voxels of 5 µm × 1 mm × 1 mm ($x \times y \times z$).

Using Matlab, a full-arc rotation (360°) of the microbeams was simulated by rotating the dose deposition artificially. The rotation axis through the center of the phantom was parallel to the x-axis (confer figure 11.1). For each x-position, the energy deposit in the spherical head phantom was transformed from Cartesian to cylindrical coordinates (the x-axis being the longitudinal axis). Then, the energy deposit was integrated over the angular coordinate, and the dose-to-medium was calculated by dividing the integrated energy by the manually set mass of the radial segment. The dose was allocated to the cylindrical and subsequently to the Cartesian coordinates. Following, the dose distribution was normalized to a valley dose of 2 Gy at the center of the tumor as a typical radiotherapy fraction dose, also applied with 30 fractions for the clinical treatment plan of the glioblastoma resection cavity in chapter 10.3.3.

The peak-to-valley dose ratio (PVDR) and the target-to-entrance dose ratio in the target volume were calculated from the central peak ($x = 70.02$–70.05 mm) and central valley region ($x = 70.16$–70.36 mm). For this purpose, the target dose was averaged over the central 35 µm × 13 mm × 13 mm and 205 µm × 13 mm × 13 mm ($x \times y \times z$) for the peak and valley, respectively. The entrance dose in the cortical bone was averaged over the same dimensions as the target dose except the z-direction that extended over the bone thickness of 6 mm. The standard deviations were deduced from error propagation of the standard deviations of the central peak and valley doses for the PVDR and of the target and entrance dose values, respectively. In contrast to the PVDR of unidirectional MRT in chapter 4.3.1, only one PVDR is calculated so that the standard error of the mean corresponds to the standard deviation.

The microbeam arc dose distribution in micrometer resolution in the x-direction was converted into an EUD distribution in a resolution of $(1\,\text{mm})^3$. Here, generic radiobiological parameters were used for the EUD calculation according to equation (9.4). The parameters were set to $\alpha/\beta = 10\,\text{Gy}$, $\alpha = 0.3\,\text{Gy}^{-1}$, and $\beta = 0.03\,\text{Gy}^{-2}$ for the tumor region [2, 221] and to $\alpha/\beta = 2\,\text{Gy}$, $\alpha = 0.1\,\text{Gy}^{-1}$, and $\beta = 0.05\,\text{Gy}^{-2}$ for the remaining part as normal tissue [200, 222].

Additionally, the dose and EUD distributions were investigated for two varied microbeam fields with the 400 kVp spectrum. First, field size was reduced to 20 mm × 10 mm ($x \times y$). Second, parallel microbeams with a field size of 20 mm × 20 mm were applied. For both variations, all other simulation parameters remained unchanged.

11.3. Results

Microbeam arc therapy drastically reduced the peak entrance dose by spreading the dose over all polar angles perpendicular to the rotation axis, while the peak and valley doses at the tumor center were not noticeably affected. The dose distribution was rotationally

symmetric, which is depicted for the central peak in figure 11.2a. Along the rotation axis, the clear peak-valley profile, known from unidirectional MRT in chapter 4.3.1, was retained, as seen in figures 11.2b and 11.2c. At the center of the tumor ($x = 70\,\mathrm{mm}$), the highest peak dose extended over the full field size of $(20\,\mathrm{mm})^2$, covering the target volume in the y- and z-direction, visible in figure 11.2c for the y-direction. On the rotation axis, the volume of highest dose decreased with distance to the center of the tumor due to the divergence of the beams and a thus smaller overlay region of opposing peaks. The highest dose at, e.g., $x = 60\,\mathrm{mm}$, $z = 70\,\mathrm{mm}$ extended over only 2 mm in the y-direction. Off the rotation axis, opposing peaks did not overlap in the periphery of the tumor, which strongly decreased the maximum dose, exemplarily shown in figures 11.2(d-f). Due to the absence of an overlap region of opposing peaks, the dose was not accumulated but smeared to a double peak, where the higher peak resulted from the entry beam (shorter distance to the phantom surface) and the lower peak from the exit beam. Between the double peak, the valley region was elevated due to the smeared-out peak from beams of different directions. The specific dose distribution depended on the interplay between the phantom and irradiation geometries, including the peak width, the center-to-center distance of the peaks, the field size, and the beam divergence. For this complex dose distribution, the peak dose, the valley dose, and the PVDR cannot be defined, but the EUD provides an interpretation.

An x-ray spectrum of higher energy yielded a lower peak dose in the target volume due to a higher amount of scattered radiation to the valleys and the normalization to the valley dose. Only defined at the center of the target volume, the PVDR was analyzed for the central peak and the central valley. The PVDR at the tumor center amounted to 19.2 ± 2.3, 14.9 ± 2.0, and 11.1 ± 1.3 for the 400 kVp, 600 kVp, and 800 kVp spectrum, respectively. The uncertainties state the standard deviations deduced from error propagation. The PVDR values corresponded to the values for unidirectional MRT in chapter 4.3.1: At a water-equivalent depth of 76 mm, taking into account the higher density of cortical bone, the PVDR of unidirectional MRT were 20.6 ± 0.5, 14.9 ± 0.3, and 11.6 ± 0.2 for the 400 kVp, 600 kVp, and 800 kVp spectrum with the same filtering, respectively. Here, the uncertainty intervals state the standard error of the mean PVDR over all peak positions.

Moreover, a higher energy resulted in a lower peak entrance dose because of a less steep depth-dose curve and the normalization to the dose in the target volume. Table 11.1 lists the target-to-entrance dose ratios of the central peak and the central valley with corresponding standard deviations. The full-arc rotation increased the target-to-entrance dose ratio by a factor of approximately 38 in the central peak and by a factor of approximately 23 in the central valley, independent of the photon energy.

Figure 11.3 displays the EUD distribution in different cross sections through the head phantom. The EUD was considerably higher in the periphery of the tumor, e.g., at $x = y = 60\,\mathrm{mm}$, $z = 70\,\mathrm{mm}$, than at the center, which is shown in figures 11.3(b-d). The reason was the reduction or partial absence of a low-dose valley region due to a smearing of the peaks in the periphery of the tumor (see figures 11.2(d-f)). The overdosing could

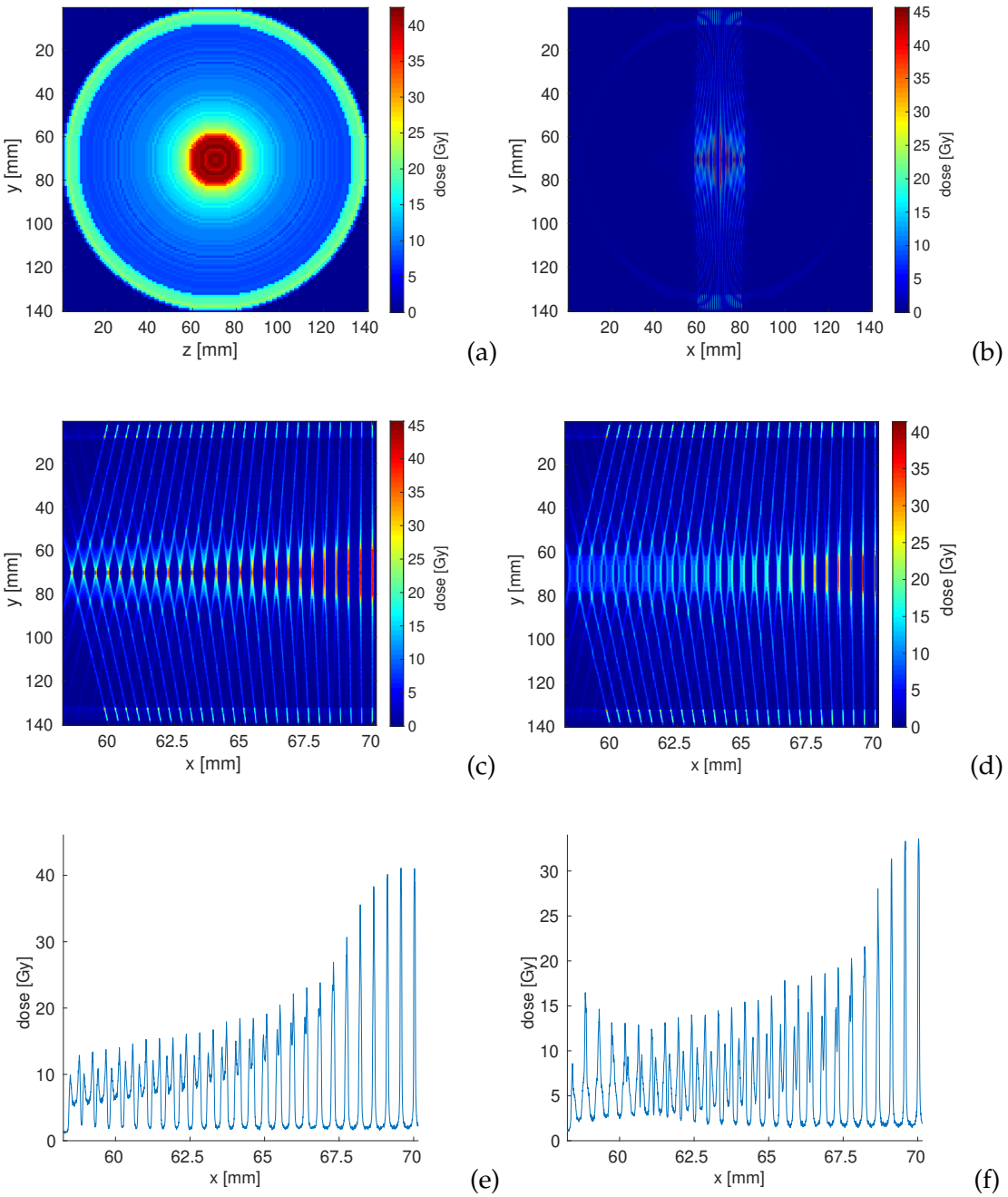

Figure 11.2.: Microbeam arc therapy with 400 kVp photons applied to a simple head phantom. Dose distribution in the central peak ($x = 70\,\text{mm}$) (a). Dose along the rotation axis centrally through the tumor ($z = 70\,\text{mm}$) as an overview (b) and as a zoom in the x-direction to half of the tumor region (c). Dose parallel to the rotation axis off the central tumor axis ($z = 62\,\text{mm}$) (d). Dose profiles parallel to the rotation axis ($y = 62\,\text{mm}$) at $z = 70\,\text{mm}$ (e) and at $z = 62\,\text{mm}$ (f). (a, c) from Winter et al. [87].

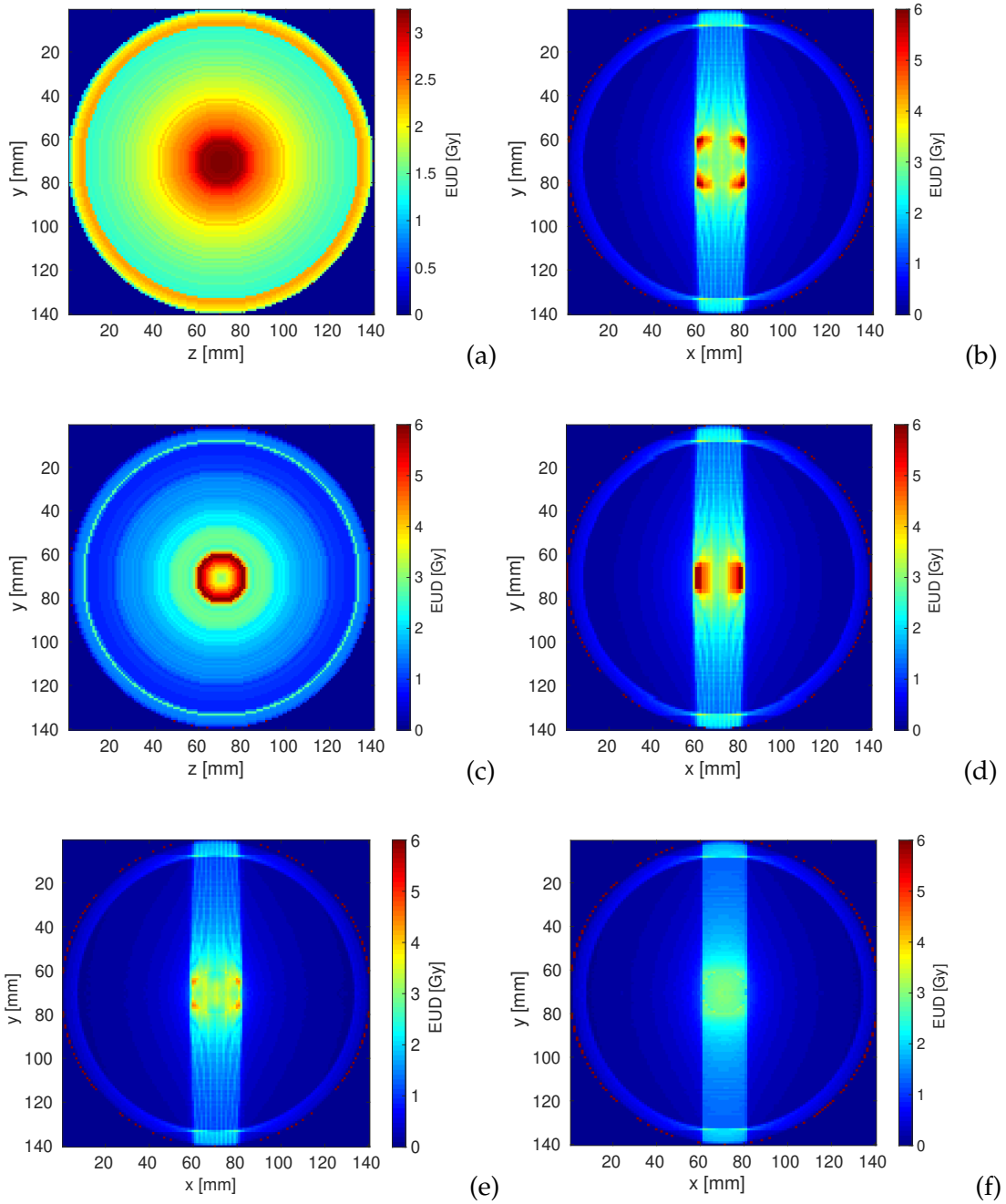

Figure 11.3.: Distributions of the equivalent uniform dose (EUD) in a head phantom with microbeam arc therapy with 400 kVp photons. Cross section through the tumor center at $x = 70$ mm (a) and $z = 70$ mm (b) and through the periphery of the tumor at $x = 60$ mm (c) and $z = 60$ mm (d). A smaller field size reduced the hotspots in the tumor (e); parallel beams removed the hotspots (f), (e-f) displayed centrally at $z = 70$ mm. Note the different color bar scaling in (a). (a) from Winter et al. [87].

Table 11.1.: Target-to-entrance dose ratios of the central peak and central valley in a head phantom with unidirectional MRT and microbeam arc therapy using 400 kVp, 600 kVp, and 800 kVp photons. Uncertainty intervals denote the standard deviations.

	Peak unidirectional	Peak arc	Valley unidirectional	Valley arc
400 kVp	0.059 ± 0.011	2.21 ± 0.26	0.075 ± 0.042	1.68 ± 0.40
600 kVp	0.075 ± 0.014	2.81 ± 0.35	0.116 ± 0.057	2.65 ± 0.61
800 kVp	0.083 ± 0.015	3.13 ± 0.39	0.156 ± 0.067	3.66 ± 0.79

be reduced by decreasing the size of the microbeam field as demonstrated in figure 11.3e. The ratio between the highest to the central dose in the tumor decreased from 2.0 to 1.2 by decreasing the field size from 20 mm × 20 mm to 20 mm × 10 mm ($x \times y$). Furthermore, the overdosing did not occur for parallel microbeams, where the center of the tumor received the highest EUD, confer figure 11.3f. Single voxels of exceptional high dose outside of the phantom resulted from rounding artifacts in the conversion between Cartesian and cylindrical coordinates during the EUD calculation.

In regions of a clear peak-valley profile, the EUD followed the trend of the valley dose with an offset for both divergent and parallel microbeams. As shown in figure 11.4a, the EUD was higher than the physical valley dose by a factor between 1.4 and 2.8 for a profile centrally through the head phantom. In regions of a more complex dose distribution due to the crossing of divergent beams, the valley dose was not defined (confer figures 11.2(d-f)), which resulted in an EUD that did not follow the trend of the physical dose. Exemplarily shown in figure 11.4b, the off-center EUD followed the physical dose only for the parallel field due to the clearly defined valley dose, but not for the divergent field that did not allow the definition of the valley dose in off-center regions.

As discernible in figures 11.3(b, d), the beam entry and exit paths received a non-homogeneous EUD perpendicular to the beam direction (e.g., at $x = 60$–80 mm, $y = 120$ mm, $z = 70$ mm). The reason was the varying microscopic dose profile across the beam or, more precisely, the varying low-dose regions within the 1 mm-wide voxels (x-direction) of the EUD calculation due to the overlap of the divergent microbeams from different directions.

11.4. Discussion

Microbeam arc therapy can be utilized to drastically reduce the peak entrance dose and by a lower factor also the valley entrance dose with respect to a constant target dose. As the valley dose is closer associated with healthy tissue toxicity than the peak dose, a low valley entrance dose is desirable. The specific improvement factor of the target-to-entrance dose ratio depends mainly on the geometry of the phantom and the radiation

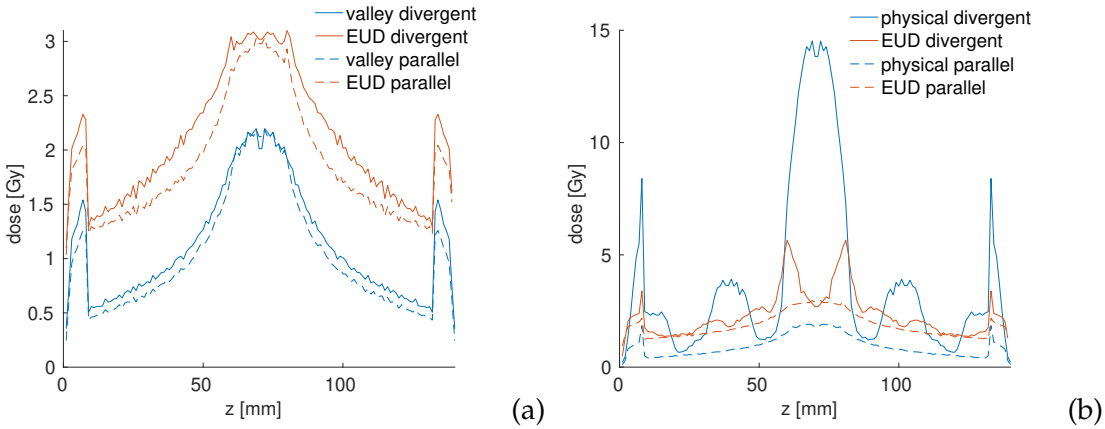

Figure 11.4.: Profiles of the physical dose and the equivalent uniform dose (EUD) in a head phantom at $y = 70\,\text{mm}$ with microbeam arc therapy using divergent and parallel fields. (a) The physical dose represents the central valley dose, averaged over x =70.16–70.36 mm, EUD at $x = 70\,\text{mm}$. (b) Off-center physical dose averaged over x =62.16–62.36 mm (valley dose for the parallel field), EUD at $x = 62\,\text{mm}$.

source as well as on the applied rotation angle. The simulated head phantom had a strongly simplified geometry with a centrally located target volume. In this work, a full-arc rotation demonstrated the microbeam arc concept. Conversely, certain irradiation directions may be omitted in a clinical application to spare sensitive organs at risk or long beam paths through healthy tissue in case of a peripheral target volume. Ideally, microbeam beam arc therapy should be combined with a conformal shaping of the radiation field to a typically aspherical tumor, similar to clinical volumetric-modulated arc therapy with dynamic multi-leaf collimation.

The divergent radiation field caused a complex dose distribution of crossing microbeams and thus a smeared-out dose profile in the periphery of the target volume. In this region, the commonly reported peak and valley doses were not defined so that the EUD enabled dose reporting and treatment plan evaluation. In this work, the method of EUD calculation was simplified by default radiobiological parameters for the tumor and the normal tissue but, nevertheless, demonstrated the applicability of the EUD for microbeam arc therapy. The EUD followed the trend of the valley dose in regions of a clear peak-valley dose profile, i.e., on the rotation axis and at the center of the tumor for a divergent microbeam field and in the complete phantom for a parallel field. This result corresponded to the observation in preclinical experiments of unidirectional MRT that the valley dose mainly determines the normal tissue toxicity, while the maximum dose to a micrometer-scaled volume does not seem to be relevant for the biological effect [35, 44, 60]. The EUD approaches the valley dose for distributions of mean doses much higher than the α/β ratio [85]. The maximum of the mean dose (average calculated

over 1 mm in the z-direction) was 9.5 Gy and the coarsely estimated mean dose at the tumor center was 7.4 Gy* and hence lower than $\alpha/\beta = 10$ Gy, resulting in the offset that the EUD was higher than the valley dose. Even though the EUD seems promising to predict radiobiological effects of spatially fractionated radiotherapy, the EUD needs to be validated in-vitro with colony formation assays, especially in regions of complex dose distributions due to crossing beams. Furthermore, the clinical effect of a spatially fractionated target dose and of EUD hotspots need to be explored as it is still unclear if these hotspots should be avoided or could even be beneficial.

The presented microbeam arc therapy with divergent fields requires several adjustments of the MRT planning system hybridDC, which was utilized in chapter 10. First, the divergence of the radiation field needs to be incorporated into the dose calculation algorithm, which is rather straightforward to implement and has been applied for preclinical MRT with a compact small-animal irradiator [190]. As depicted by the dose distribution in figure 11.2, the primary radiation field extended to regions outside of the central tumor volume that had a radius of 10 mm because the dose calculation here was not adjusted to the divergent field. Second, the observed overlapping and smearing of the peaks, the elevated valley dose, and the EUD hotspots in peripheral tumor regions need to be considered. The consideration demands the calculation of the micrometer-scaled dose distribution during the rotation of the sample. The hybridDC algorithm facilitates a micrometer-precise dose calculation as a basis for the EUD calculation, as presented in chapter 10.2.4. Third, the rotation of the sample needs to be implemented into the treatment planning system, either with time-dependent Monte Carlo simulations or with a stepwise artificial rotation.

Different concepts of multiport MRT involve a homogeneous target dose, e.g., interlaced MRT [183] with static beams or spiralMRT [187] with a single microbeam rotating helically around the phantom. The advantage of a homogeneous target dose is the applicability of clinical experience and prescription doses. In contrast, the concept of microbeam arc therapy presented here yields a spatial dose fractionation not only in normal tissue but also in the target region, like cross-firing MRT, which might widen the therapeutic window compared to a homogeneous target dose [35, 36]. The application of a spatially fractionated target dose demands, however, a reconsidered dose prescription, e.g., based on the EUD.

On the one hand, the positioning accuracy for microbeam arc therapy is similar to unidirectional MRT and thus considerably lower compared to MRT with an interlaced or peak-on-peak geometry, which require a micrometer-precise realignment for the different treatment fields. On the other hand, the rotational motion must be accurate to few micrometers in the direction parallel to the rotation axis to avoid blurring of the peak-valley profile at the center of the target volume. Additionally, microbeam arc therapy is prone to a deterioration of the dose profile due to exterior or interior organ motion. The reason is a presumably longer irradiation time because of the

*The valley dose of 2 Gy occupied 7/8 of the volume and the peak dose of 45 Gy occupied 1/8 of the volume, resulting in an approximate mean dose of $7/8 \cdot 2\,\text{Gy} + 1/8 \cdot 45\,\text{Gy} = 7.4\,\text{Gy}$.

sample rotation than unidirectional MRT with possibly ultra-high dose rates. Exterior motion can be best avoided for radiotherapy treatments of the head due to existing immobilization devices for stereotactic radiotherapy. Chapter 12 gives details of interior organ motion during MRT, which includes for example the pulsation of blood vessels in the brain. In case the organ motion can be handled, longer irradiation times of microbeam arc therapy can bring the advantage of lower dose-rate requirements for the MRT source. During the technical realization of microbeam arc therapy, close attention must be payed to the accuracy and stability of the radiation field and sample setup as well as to the investigation whether the target rotates on a stage or the radiation source rotates around the static target.

In conclusion, the concept of microbeam arc therapy should be considered as a possible application of MRT for brain tumor treatments due to reduced entrance doses. However, the realization brings several challenges, mainly related to the stability of the radiation field during rotation and to the prediction of radiobiological and clinical effects due to overlapping divergent microbeams.

12. Organ motion during MRT

12.1. Introduction

Physiological processes such as breathing, digestion, or the heartbeat cause internal motion of organs and tissue. For clinical radiotherapy, breathing poses a major challenge regarding intrafractional motion due to largest amplitudes. Countermeasures include breath holding, the application of an abdominal press, irradiations that are gated to a specific breathing phase, and real-time tracking of the tumor motion [223]. External motion can best be minimized for head and neck or brain tumor treatments by means of stereotactic immobilization.

Brain tumors are a potential target for first clinical trials with microbeam radiotherapy (MRT) due to promising preclinical studies [50, 53] and available, submillimeter-precise immobilization devices against external motion. Nevertheless, the cardiac pulsation of blood vessels in the human brain causes an internal motion with amplitudes of up to 200 µm [224], which is on the same length scale as the dose modulation of MRT. For this reason, the brain motion might distort the dose distribution and might thereby deteriorate the radiobiological benefits of MRT compared to conventional radiotherapy. For preclinical MRT studies, the pulsatile brain motion of mice or rats is of interest. In the carotid artery of mice, the maximum change in diameter was measured to be 45 µm [225]. Due to a lack of direct measurement data, the brain motion of mice can be estimated to amplitudes smaller than 45 µm based on the artery motion.

Some authors have published the maximum impact of the human brain motion on the microbeam dose distribution delivered to phantoms at third-generation synchrotron facilities [91, 92], which is summarized in section 12.2. This impact was investigated for MRT with compact sources in a strong collaboration with Suzana Spasova, who wrote her master's thesis on this topic. Section 12.3 shortly presents the main methods and results, which were partly published [226]. Based on this work, section 12.4 discusses the expectable effects of the breathing motion and the pulsation of blood vessels in the brain for future clinical MRT applications as well as possible mitigation measures.

12.2. MRT at synchrotrons

Duncan et al. [91] measured the distortion of an MRT dose distribution, which featured an original peak width of 50 µm, during the motion of a water-equivalent phantom at the biomedical beamline ID17 at the European Synchrotron Radiation Facility (ESRF, Grenoble, France) with a dose rate of 15 kGy/s and a mean photon energy of 100 keV.

The small height of the radiation field of 0.5 mm necessitated a vertical scanning of the phantom on the positioning stage through the beam with a velocity in the range of 5–20 mm/s along the peak direction (y-direction). The unidirectional motion in the direction of the peak-valley profile (x-direction) was modeled based on measurement data of the largest amplitude in human brain, which was 170 µm in the thalamus [227]. For the lowest vertical scan speed, dosimetry and Monte Carlo simulations revealed an increase of up to 100 % of the full width at half maximum (FWHM) of the peaks and a reduction of the peak-to-valley dose ratio (PVDR) down to 50 % of the PVDR without motion.

Manchado de Sola et al. [92] performed Monte Carlo simulations of a human head phantom irradiated with microbeams (peak width 25–50 µm) and minibeams (peak width 0.6–1.0 mm) from the beamline ID17 at the ESRF. The cardiosynchronous pulsation in the brain was artificially simulated with different displacement amplitudes up to 240 µm for the microbeams and up to 500 µm for the minibeams by modifying the photon fluence incident on the phantom. The simulated motion deteriorated the dose distribution, with stronger deterioration for microbeams than for minibeams. The FWHM of the microbeams matched approximately the displacement amplitude, and the PVDR decreased drastically with increasing displacement.

Serduc et al. [52] irradiated brain tumors in rats with the interlaced MRT geometry (confer chapters 9 and 10) at the beamline ID17 at the ESRF with similar beam characteristics as described by Duncan et al. [91]. By omitting a vertical scanning of the positioning stage, each of the four interlacing fields had a size of 0.5 mm × 2 mm. A homogeneous interlaced dose distribution was achieved within a small target volume of 7 mm^3 without accounting for brain motion. However, the authors admitted that the brain motion of humans is expected to deteriorate the interlaced microbeam dose distribution due to larger amplitudes.

These studies indicate that the cardiosynchronous brain motion does not severely affect preclinical MRT at synchrotrons with ultra-high dose rates of kGy/s if the target scanning is omitted. These irradiations without target scanning only allow the treatment of very small targets of an extent of less than 1 mm × 20 mm, though. In contrast, larger motion amplitudes in the human brain than in the brain of small rodents presumably affect the MRT dose distribution in clinical studies with larger target volumes, even at synchrotron beamlines.

12.3. Preclinical MRT at compact sources

The specific irradiation geometry with ultra-high dose rates and the need of a vertical scanning at synchrotron beamlines cannot be directly translated to MRT with compact sources that deliver larger fields at considerably lower dose rates. For this reason, the effect of brain motion on the microbeam dose distribution at two compact sources was investigated in this work.

The Monte Carlo simulations were performed in TOPAS [94] (version 3.6.1, based on Geant4 version 10.6.p03). The *G4EmPenelopePhysics* list was employed with default electromagnetic range limits (*EMRangeMin* = 100 eV, *EMRangeMax* = 500 MeV); default step sizes for electrons and positrons (step function parameters *dRoverRange* = 0.2, *finalRange* = 0.01 mm); and fluorescence electrons, Auger electrons, and particle-induced x-ray emission activated [95, 108]. A multislit collimator converted the homogeneous x-ray beam into a microbeam field with a size of $20 \times 20\,\mathrm{mm}^2$ ($x \times y$), a peak width of 50 µm, and a center-to-center distance of 400 µm (both in x-direction), measured at the rear side of the collimator, as described in chapter 4.2.1. The x-ray source with $2 \cdot 10^9$ primary particles had a divergence to fully cover the slits of the collimator. A phantom was placed contiguously behind the collimator with the phantom surface at a distance of 21 cm from the x-ray source in the z-direction. The dose-to-medium was scored in the phantom in a resolution of $10\,\mu\mathrm{m} \times 1\,\mathrm{mm} \times 1\,\mathrm{mm}$ ($x \times y \times z$). With the time feature in TOPAS, the phantom was moved by 200 µm forwards and backwards along the peak-valley profile in the x-direction with a constant velocity of 1 mm/s, which is the maximum velocity of the human brain motion [224]. The PVDR was defined as described in chapter 4.2 and the FWHM as the peak width that received at least 50 % of the maximum peak dose.

Two different compact x-ray sources were simulated. The first simulation represented a commercial small-animal irradiator (XenX by Xstrahl Ltd., Walsall, United Kingdom), which has been used in-house for preclinical MRT at low dose rates [73]. The elliptical focal spot had a size of $3.4\,\mathrm{mm} \times 3.4\,\mathrm{mm}$ ($x \times y$) and homogeneous intensity. The divergent x-rays had a 225 kVp spectrum from a tungsten target filtered by 0.8 mm beryllium and 0.15 mm copper. The dose was scored in a phantom made of polymethyl methacrylate (PMMA) with a size of $4 \times 4 \times 10\,\mathrm{cm}^3$ ($x \times y \times z$). The second x-ray source represented the preclinical prototype of the line-focus x-ray tube (LFxT) with a 300 kVp x-ray spectrum from a tungsten target filtered by 0.8 mm beryllium and 1 mm aluminum. The homogeneous focal spot of the LFxT had an elliptical size of $50\,\mu\mathrm{m} \times 30\,\mathrm{mm}$ ($x \times y$), and the dose was scored in a water phantom with a size of $3 \times 3 \times 4\,\mathrm{cm}^3$ ($x \times y \times z$). For both x-ray sources, the unfiltered spectra were obtained by scoring the phase space of produced photons from an electron beam hitting a tungsten target using Monte Carlo simulations in Geant4 [93] (version 10.4.p02), with the physics settings and geometry described in chapter 4.2.1, and the filtering was subsequently considered with energy-dependent mass attenuation coefficients from NIST [97].

The motion affected the microbeam dose distribution similarly for both x-ray sources. The PVDR decreased the most at the surface of the phantom from approximately 47 without motion to 14 with motion for both sources, which corresponded to a reduction by 70 % [226]. At the surface, the FWHM increased from 47 µm in the static phantom* to 196 µm in the moving phantom. The relative impact of the motion was smaller in larger depths in the phantom because the FWHM increased and the PVDR decreased with

*The FWHM was slightly smaller than in the simulations in chapter 4.3.1 due to different definition of the FWHM.

increasing depth, independent of the motion. The reasons of the motion-independent FWHM increase and the PVDR decrease were the divergent radiation fields, a higher amount of scattered radiation with depth, and, for the small-animal irradiator XenX, also a focal spot width that was markedly larger than the peak width (for details see chapter 4.3.1).

Film dosimetry confirmed the observations of the simulations for the small-animal irradiator. A realistic brain motion with the largest amplitude reported by Soellinger et al. [227], which was also used for investigating the effect of brain motion on MRT by Duncan et al. [91], was imitated during irradiations with the small-animal irradiator XenX. The experimental setup can be seen in figure 12.1a. A layered PMMA phantom with a total size of $4 \times 2 \times 5\,\mathrm{cm}^3$ ($x \times y \times z$) was placed at a distance of 7 mm behind the multislit collimator, this minimum distance was limited by the design of the collimator. The rear side of the multislit collimator had a distance of 212 mm from the focal spot. Gafchromic EBT-3 films (Ashland Advanced Materials, Bridgewater, USA) were placed at different depths in the phantom between the PMMA layers. The films were analyzed using a film scanner (ProScan10T, Reflecta GmbH, Eutingen im Gäu, Germany), the appertaining scan software CyberView X5, and Python (version 3.7.2). In this work, the reported brain motion was slightly modified to fulfill the technical constraints of the motorized translation stage (MTS50M-Z8, Thorlabs GmbH, Bergkirchen Germany) that was installed at the small-animal irradiator to imitate the one-dimensional brain motion in the x-direction. The modification was performed by a convolution of the motion positions with a normal distribution so that the filtered motion satisfied the maximum velocity of the stage of 2.4 mm/s and the maximum acceleration of $4.5\,\mathrm{mm/s}^2$ [228]. The filtered motion resulted in an amplitude of 160 µm, as shown in figure 12.1b.

The experiment was compared to additional Monte Carlo simulations using the setup of the experiment and the simulation settings described before. At the surface of the static phantom, the FWHM of the peaks was 88 µm according to the measurements and 63 µm according to the simulations. With motion, the FWHM at the surface increased to the motion amplitude of 160 µm according to both measurements and simulations. The motion decreased the PVDR at the surface from 32 to 20 according to the experiment, whereas from 44 to 21 according to the simulations. The discrepancy of the FWHM and PVDR values between the measurements and the simulations without motion presumably resulted from photon scattering at the rough inner surfaces of the collimator slits, which occurred in the experiment but was neglected in the simulations (details can be found in reference [73]).

Instead of time-dependent Monte Carlo simulations, the impact of motion on a dose distribution in a phantom can be obtained numerically in one step: The dose profile of a static phantom is thereby convolved with the probability density function (PDF) of the phantom positions during one motion period. The resolution of the PDF needs to match the resolution of the static dose profile, i.e., 10 µm in the x-direction in this work. The convolution method has been used to include breathing motion into three-dimensional dose calculation for radiotherapy in the upper abdomen [229]. In

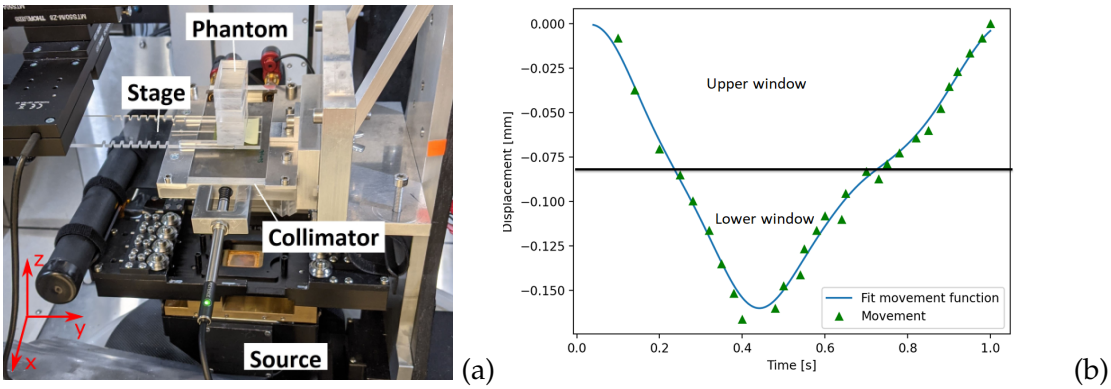

Figure 12.1.: (a) Setup of the experiment to measure the motion effect on the microbeam dose profile with a motorized stage integrated into the small-animal irradiator and film dosimetry. Gafchromic films were placed between the layers of the PMMA phantom. (b) The pattern of the cardiosynchronous brain motion (Movement) [227] was filtered (Fit movement function) to satisfy the limits of the motorized stage. The windows were used to analyze cardiac gating. The figures were created by Suzana Spasova.

this work, the validity of the convolution method for a microbeam dose distribution was confirmed by a comparison to full time-dependent Monte Carlo simulations. The discrete linear convolution of the static dose profile with the PDF of the motion positions was performed in Python. The convolved dose profile matched the dose profile of the moving phantom.

Subsequently, the convolution method was used to analyze the effect of cardiac gating for MRT at the small-animal irradiator XenX. Thereby, a gating window of 75 % referred to a beam-on time of 75 %, while the beam was blocked for 25 % of the cardiac cycle. The convolution was applied with two different motion profiles: a simple triangular motion profile with constant velocity, i.e., a rectangular PDF, and a realistic motion profile based on measurements [227] with two different gating window positions, as indicated in figure 12.1b. For the simple triangular motion with an amplitude of 200 µm, gating increased the PVDR at the phantom surface from 13 with full motion to 19 with a 75 % gating window and to 28 with a 50 % gating window, compared to 47 with a static phantom. As observed previously, the FWHM at the surface of a moving phantom corresponded to the motion amplitude, i.e., 47 µm for the static phantom, 95 µm with a 50 % gating window, 143 µm with a 75 % gating window, and 196 µm with the full motion [226]. With the realistic motion profile, the PVDR and FWHM values depended on the width and the positioning of the gating window. The FWHM at the phantom surface matched approximately the respective motion amplitude. The PVDR was 47 for

the static phantom, 32 and 29 for two different positions of the 50 % gating window, 23 for both positions of the 75 % gating window, and 18 for the full motion.

Concluding, human brain motion considerably distorted the dose distribution of MRT with compact sources in both simulations and phantom measurements. The strongest impact of the motion was discerned at the phantom surface because the divergence of the radiation field — and for the small-animal irradiator XenX also the large focal spot — decreased the PVDR and increased the FWHM with increasing depth. Brain motion of mice is presumably not relevant for preclinical MRT due to an amplitude smaller than the peak width. Breathing motion has not been specifically investigated for preclinical MRT but is assumed to distort the dose distribution due to larger amplitudes than those of the brain motion. Breath holding cannot be implemented for rodents. Preclinical MRT for thoracic targets therefore requires breath gating, the accuracy of which needs to be validated experimentally. The effect of human breathing motion on MRT is discussed in the next section.

12.4. Translation to clinical MRT

First clinical MRT trials will probably be approved at third-generation synchrotrons, where preparations have lasted for years, possibly for a brain tumor treatment [40, 46]. The size and location of the target volume will determine if the pulsatile brain motion should be considered in treatment planning. For very small target volumes of a few cubic millimeters, similar as in the preclinical study by Serduc et al. [52], vertical scanning of the patient through the beam can be omitted. Furthermore, dose rates of kGy/s allow irradiation times of a few milliseconds, which is notably shorter than the period of the resting heart rate. In this case, the cardiosynchronous brain motion is of minor importance. For larger target volumes, vertical scanning reduces the effective dose rate and increases the irradiation time so that the motion may distort the microbeam dose distribution. The clinical LFxT will have larger fields of a few square centimeters and a dose rate of approximately 100 Gy/s (see chapter 4.3.2), resulting in irradiation times of a few seconds for peak doses of a few hundred Gray. For these irradiation times that are longer than the period of the resting heart rate, the distortion of the dose distribution requires consideration and depends mainly on the amplitude, the direction, and the shape of the motion, but not on the velocity, independently of the x-ray source.

The motion amplitudes and resulting dose distortions presented in this chapter correspond to worst case scenarios with largest measured motion amplitudes. Different brain regions exhibit different motion amplitudes, profiles, and directions [224, 227]. For this reason, the motion pattern in the region of interest should ideally be measured before first clinical MRT trials by, e.g., spiral cine displacement-encoded stimulation echo (DENSE) magnetic resonance imaging [224, 227], to determine the necessity of motion mitigation. As the motion amplitudes differ for different directions, the peak-valley profile (x-direction) should be aligned to the direction of smallest amplitudes.

Cardiac gating appears promising for mitigation of the cardiosynchronous motion, as suggested previously [52, 92]: The brain returns to its original position with micrometer accuracy after a complete cardiac cycle [230], and the motion is linked to the R-wave of the electrocardiogram (ECG) [224, 231]. Cardiac gating employed with high or even ultra-high dose rates demands a very fast beam shut-off in the microsecond range, which is implemented at the ID17 at the ESRF [66] and achievable for the LFxT with the Pierce electrode (refer to chapter 7.1.3). With cardiac gating, position drifts over time and the amplitude of the gated motion will mainly determine the effect of the motion on the microbeam dose distribution.

MRT for thoracic and abdominal targets is more challenging than brain tumor treatments due to larger motion amplitudes and inferior motion mitigation possibilities. The breath hold technique seems feasible for irradiation times of several seconds, which would allow single-fraction treatments with third-generation synchrotrons and the clinical LFxT. However, breath holding is not always reliable, depending on the constitution of the patient [186] so that additional motion mitigation techniques are required and their precision needs to be tested for MRT.

In conclusion, organ or tissue motion can lead to a distortion of the microbeam dose distribution, occurring as a reduction in PVDR and an increase in peak width. The magnitude of the distortion mainly depends on the motion amplitude in the direction of the peak-valley dose profile but also on the course of the motion as well as on the irradiation geometry and dose rate. The impact of organ motion can be assessed most easily with a numeric convolution of a simulated static dose distribution with the PDF of the expected motion positions. For most sizes and locations of the target volume, the human organ motion needs to be considered and managed — even for brain tumor treatments at third-generation synchrotrons.

Part IV.

Summary and outlook

13. Summary

Microbeam radiotherapy (MRT) has shown promising results in preclinical experiments for the treatment of aggressive cancer types. Superior normal tissue sparing compared to conventional radiotherapy is achieved by a spatially fractionated dose distribution on the micrometer scale of high-dose peaks and low-dose valleys formed by x-rays in the orthovoltage range. A sharp peak-valley dose profile with steep penumbras, a high peak-to-valley dose ratio (PVDR), and high dose rates are essential for effective MRT. The development of MRT towards clinical application requires advancements in multiple research areas, such as a deeper understanding of the radiobiological effects, overcoming technical hurdles like developing a clinically applicable radiation source, and finding treatment cases where MRT can develop its full potential. Many of these aspects were covered in this work.

In part II, I presented the line-focus x-ray tube (LFxT) as an MRT source, proving the functionality of relevant technologies with numerical simulations to provide a basis for the construction of a prototype. The LFxT prototype serves as a proof of concept and enables preclinical MRT studies without the necessity of the scarcely available third-generation synchrotrons. The main advantage of the LFxT over these synchrotrons with parallel beams is the compact dimension, enabling an application in conventional radiotherapy rooms and thereby simplifying the accessibility to MRT. In part III, I extended microbeam treatment planning in order to enable realistic MRT plans on patient data and comparisons to clinical treatment plans, facilitating the finding of suitable treatment cases for first clinical trials.

In chapter 4, my Monte Carlo simulations validated the capability of the LFxT to produce a dose distribution and dose rates that are suitable for MRT. I optimized the divergent x-ray field with regard to the photon energy and focal spot size to achieve a sharp peak-valley dose profile with the highest PVDR. The width of the focal spot, where the electron beam hits the target and produces x-rays, was an essential parameter for a sharp peak-valley dose profile and should therefore be as narrow as the 50 µm-wide slits of the multislit collimator shaping the peaks. I obtained the highest PVDR of above 20 throughout a 100 mm-thick water phantom for 300–400 kVp x-ray spectra with a mean energy of 97–109 keV. In addition to the optimized x-ray field, I simulated the microbeam dose distribution for a realistic, non-uniform 300 keV electron beam of the LFxT prototype, which resulted in a mean x-ray energy of 76 keV and a PVDR above 15 throughout 100 mm of water. The obtained PVDR values were lower than for phantom measurements of parallel microbeams, however, in the same range as for successful preclinical MRT experiments, assessed at different third-generation synchrotrons.

A high dose rate requires a short distance of the sample to the focal spot of the LFxT due to the divergence of the microbeam field. The smallest possible distance of the multislit collimator to the focal spot of the preclinical LFxT was 20 cm because of construction limitations and a high heat load to the vacuum chamber housing due to scattering electrons (see chapter 6). With an electron energy of 300 keV and a current of 0.3 A, I simulated dose rates of approximately 10 Gy/s at a water depth of 15 mm, which was considerably higher than for currently available compact MRT sources, although not comparable to dose rates of kGy/s at third-generation synchrotrons.

Upscaling the LFxT for clinical MRT involves reaching deeper seated targets and therefore demands higher x-ray energies with less steep depth dose curves than used for preclinical MRT with the LFxT prototype. A 600 kVp spectrum with a mean energy of 131 keV resulted in a PVDR above 15 throughout 100 mm of water. With an electron beam current of 2.5 A, I simulated a dose rate of approximately 100 Gy/s at a water depth of 15 mm at a distance of 30 cm from the focal spot. The clinical LFxT therefore seems suitable for concurrent MRT and x-ray FLASH irradiations that require ultra-high dose rates, which possibly yield superior healthy tissue sparing compared to MRT with lower dose rates.

A main challenge of the LFxT development was a substantial heat load to the target at the focal spot arising from the high electron beam intensity, which was necessary to obtain high dose rates. In chapter 5, I investigated the temperature increase at the focal spot by using three-dimensional numerical simulations and demonstrated the potential of the LFxT technology: By operating in the heat capacity limit, the LFxT allows much higher electron beam power densities with a lower focal spot temperature than conventional x-ray tubes, which operate in the heat conduction limit. The transition to the heat capacity limit is determined by a narrow focal spot, a fast rotating target, and the electron penetration depth into the target. Beyond this transition, the focal spot temperature is independent of the spot width, which allows for a further reduction of the spot width without affecting the focal spot temperature. For the realistic, non-uniform electron beam of the LFxT prototype, the maximum temperature increase at the focal spot of less than 500 K was not critical, even if integrated into the heat management of the complete target, as long as active cooling was assumed. Although the clinical LFxT also operates in the heat capacity limit, my simulations resulted in a considerably higher temperature increase due to the higher electron beam power than for the preclinical LFxT, making a redesign of the target and the cooling system necessary.

Another challenge of the LFxT prototype development was the heat load to the vacuum chamber housing due to electrons that were scattered back from the target surface. In chapter 6, I assessed the thermal effects of the scattered electrons by using numerical simulations. I identified the locations of the highest heat load to the housing opposite the focal spot in the vicinity of the electron beamline and the x-ray exit window. An active cooling system was required to avoid damage to heat-sensitive components and to minimize hydrogen diffusion through the chamber walls, which would deteriorate the vacuum quality.

The construction of the LFxT prototype includes the same electric potential of the vacuum chamber housing and the target to avoid electrons being accelerated back onto the target, which could widen the focal spot. In contrast, my simulations in chapter 6 did not show a focal spot widening in the presence of electric fields in the vicinity of the focal spot. For this reason, the vacuum chamber housing may be on electric ground potential, which can simplify the electric insulation of the LFxT.

Chapter 7 subsumes three complementary aspects of the LFxT development. First, I assessed the development of the electron accelerator and beam optics for the LFxT prototype. Due to the high beam current of 0.3 A, main challenges were the emittance growth, which deteriorated the possibility of beam focusing, and space charge effects, which widened the cross section of the electron beam. A low emittance at the cathode hence enabled a focusing of the electron beam to an extremely eccentric focal spot with a size of 50 µm × 20–30 mm. I validated the usability of the electronic focal spot for MRT by implementing the phase space into the simulations of the radiation field in chapter 4 and into the simulations of the temperature increase at the focal spot in chapter 5. Second, I investigated a magnetic deflection system in the space between the electron beamline and the target surface to protect heat-sensitive components such as the electron beam focusing magnets and the x-ray exit window from scattering electrons. The concept seemed feasible to protect the heat-sensitive components, but the setup would complicate the electron beam optics, the construction of the vacuum chamber, and the cooling system. For these reasons, the magnetic deflection system will not be implemented into the LFxT prototype. Third, I defined the requirements of different x-ray exit windows of the LFxT prototype regarding a low x-ray absorption and a high thermomechanical stability. The window for MRT will consist of diamond due to a high thermal diffusivity, whereas two additional windows for imaging will be made of beryllium due to lower costs and lower heat-resistance requirements.

Although I described many components of the LFxT prototype in this work and others were developed by collaboration partners, there are still several steps required to bring the LFxT prototype into operation as an MRT source. In chapter 8, I delineated these steps as well as strategies to experimentally validate the LFxT technology. The construction of a clinical LFxT demands multiple redevelopments, whereof I presented concepts for the power supply, the electron accelerator (in chapter 7), and the rotating target. Besides the envisaged application of the LFxT for widely available MRT, the clinical LFxT appeared to be able to deliver ultra-high dose rates that are required for FLASH irradiations, a novel strategy in radiation oncology of high interest due to a widened therapeutic window compared to conventional radiotherapy. Additionally, the LFxT might be applicable as an imaging source for phase contrast x-ray imaging due to a high spatial coherence of the x-ray field in the short direction of the focal spot.

In chapter 10, I brought MRT an additional step further towards clinical application by facilitating microbeam treatment planning with multidirectional MRT on clinical patient data and comparisons to clinically applied radiotherapy plans. Multidirectional MRT enabled more realistic plans than with currently applied unidirectional MRT due

to a decreased entrance dose to healthy tissue. For that purpose, I extended the dose calculation algorithm hybridDC, which had been used for preclinical MRT experiments, and verified different multidirectional MRT geometries, such as the peak-on-peak, the interlaced, and the cross-firing geometry. To estimate the clinical effect, the strong dose modulation on the micrometer scale demanded a conversion to a biologically corresponding macroscopic dose, which I introduced as the equivalent uniform dose (EUD) into hybridDC. The EUD from MRT plans as well as the dose from clinical plans were converted into the equivalent dose in fractions of 2 Gy to enable a comparison of different temporal fractionation schemes. For five relevant treatment scenarios, the cross-firing MRT plans with kV photon beams, which were conformal to the planning target volume (PTV), were comparable to clinical plans with MV photons concerning the target coverage and the dose to organs at risk. To further improve the MRT plans, I identified the introduction of beam weighting and dose optimization as the most relevant approaches.

Steeper depth dose curves of kV photons of MRT than of MV photons of clinical radiotherapy require strategies to decrease the entrance dose while conserving the dose to a deep seated target volume. Besides multidirectional MRT, one of these strategies for MRT can be microbeam arc therapy, which I introduced in chapter 11. I simulated the dose distribution of a full-arc rotation of a divergent microbeam field in a simple head phantom. The target-to-entrance dose ratio drastically increased with microbeam arc therapy compared to unidirectional MRT. However, a partial overlap of divergent peaks led to a smeared out dose profile and EUD hotspots. In conclusion, microbeam arc therapy seemed to be a possible clinical application technique, while posing challenges on treatment planning and on a highly stable technical implementation to avoid distortion of the micrometer-scaled dose distribution during rotation.

The dose distribution of MRT can further be distorted by internal organ motion, which I investigated in chapter 12. The cardiosynchronous motion of blood vessels in the human brain can strongly decrease the PVDR and broadens the peak width up to the motion amplitude if the irradiation takes longer than one motion cycle. Clinical trials will therefore require cardiac gating, whereas the cardiosynchronous brain motion did not appear critical for preclinical MRT due to very small amplitudes. In contrast, breathing motion mitigation techniques are necessary for both preclinical and clinical MRT, especially for non-ultra-high dose rates.

14. Outlook

Based on work comprised in this thesis, the LFxT prototype is already under construction at the Technical University of Munich, while several steps are still necessary to bring the MRT source into operation, such as a software control as well as a monitoring and safety system for radiation protection and mechanical safety. Dosimetric, in-vivo, and in-vitro MRT experiments further require a sample stage, a multislit collimator, and an appropriate treatment planning system. After the prototype is brought into operation, an experimental proof of concept of the LFxT technology includes the validation of the heat capacity limit by measuring the focal spot temperature increase, which is anticipated to be independent of the spot width and considerably lower than predicted by the conventional heat conduction limit. To verify the suitability of the LFxT as an MRT source, radiochromic film dosimetry allows to determine the dose rate and the micrometer-scaled microbeam dose distribution, which is expected to form a sharp peak-valley profile with PVDR values similar to my simulations. Finally, in-vivo and in-vitro experiments should yield comparable results as previous MRT studies with different radiation sources.

The construction of a more powerful clinical LFxT involves new developments of the electron accelerator with the beam focusing optics; a target that withstands a very fast rotation and the high heat load; an efficient cooling system; and a high-voltage supply that facilitates ultra-high dose rates, enabling FLASH irradiations.

To prepare preclinical and clinical MRT irradiations with the LFxT, the microbeam dose calculation algorithm hybridDC needs to be adjusted to specifically model the radiation source. HybridDC should be extended to allow a more flexible beam shaping, beam weighting, and dose optimization to facilitate more sophisticated MRT plans and more realistic comparisons to clinical treatment plans than with the presented PTV-conformal beams of homogeneous intensity. Furthermore, the dose calculation in lung tissue should be revised, beam hardening effects introduced, and the EUD experimentally verified for MRT with high peak doses at single fractions for both normal tissues and tumors. Thereafter, a comprehensive MRT planning study with the variation of one treatment parameter at a time can identify suitable treatment scenarios for first clinical trials. A deeper understanding of the impact of the treatment parameters might finally allow for a generation of treatment plans specifically optimized for MRT outcome.

The application of the LFxT as an imaging source for, e.g., simultaneous phase contrast x-ray imaging of high- and low-density objects should be further investigated. The micrometer-wide, strongly eccentric focal spot satisfies the required high spatial coherence in one dimension only, which necessitates tomographic image acquisition besides a careful choice of the method of phase contrast imaging.

Part V.

Appendix

List of Figures

List of Tables

List of Abbreviations

BED	biological effective dose
CAD	computer aided design
CFRC	carbon fiber reinforced carbon
CT	computed tomography
DC	direct current
$D_{99.5\,\%}$	minimum dose to 99.5 % of a volume of interest
D_{max} / D_{mean}	maximum / mean dose to a volume of interest
DNA	deoxyribonucleic acid
CSDA	continuous slowing down approximation
DVH	dose-volume histogram
EQD2	equivalent dose in 2 Gy fractions
ESRF	European Synchrotron Radiation Facility (Grenoble, France)
EUD	equivalent uniform dose
FEM	finite element methods
FWHM	full width at half maximum
GTV	gross tumor volume
HV	high voltage
ICRU	International Commission on Radiation Units & Measurements
kV	kilovolt(age)
LFxT	line-focus x-ray tube
LQM	linear-quadratic model
MMC	modular multi-level converters
MRT	microbeam radiotherapy
MV	megavolt(age)
NIST	U.S. National Institute of Standards and Technology
OAR	organ(s) at risk
PCI	phase contrast imaging
PDF	probability density function
PMMA	polymethyl methacrylate
PTV	planning target volume
PVDR	peak-to-valley dose ratio
RBE	radiobiological effectiveness
rms	root mean square
SBRT	stereotactic body radiotherapy
TZM	titanium-zirconium-molybdenum
$V_{20\,\mathrm{Gy}}$	fractional or absolute volume that receives at least 20 Gy

Own publications

This work resulted in the publishing of the following articles in peer-reviewed journals and conference contributions. Moreover, I closely collaborated with two student projects.

Journal articles

J. Winter, M. Galek, C. Matejcek, J. J. Wilkens, K. Aulenbacher, S. E. Combs, S. Bartzsch. “Clinical microbeam radiation therapy with a compact source: specifications of the line-focus X-ray tube”. In: *Physics and Imaging in Radiation Oncology* 14 (2020), pp. 74–81. DOI: 10.1016/j.phro.2020.05.010.

K. M. Kraus*, J. Winter*, Y. Zhang, M. Ahmed, S. E. Combs, J. J. Wilkens, S. Bartzsch. “Treatment Planning Study for Microbeam Radiotherapy Using Clinical Patient Data”. In: *Cancers* 14.3 (2022), p. 685. DOI: 10.3390/cancers14030685. (*Shared first authorship.)

J. Winter*, A. Dimroth*, S. Roetzer, Y. Zhang, K.-L. Krämer, C. Petrich, C. Matejcek, K. Aulenbacher, M. Zimmermann, S. E. Combs, M. Galek, G. Natour, M. Butzek, J. J. Wilkens, S. Bartzsch. "Heat management of a compact x-ray source for microbeam radiotherapy and FLASH treatments". In: *Medical Physics* 49.5 (2022), pp. 3375–88. DOI: 10.1002/mp.15611. (*Shared first authorship.)
Featured on the issue cover and selected as Editor’s Choice.

C. Matejcek, J. Winter, K. Aulenbacher, A. Dimroth, G. Natour, S. Bartzsch. "A novel electron source for a compact x-ray tube for microbeam radiotherapy with very high dose rates". In: *Physica Medica: European Journal of Medical Physics* 106 (2023), p. 102532. DOI: 10.1016/j.ejmp.2023.102532

M. Ahmed*, S. Bicher*, J. Winter, S. Spasova, R. Lindner, J. J. Wilkens, T. E. Schmid, S. Bartzsch. "In-vivo microbeam radiation therapy at a small-animal irradiator". In preparation. (*Shared first authorship.)

Conference contributions

Oral presentations

Annual conference of the German Society of Medical Physics 2020 (51. Jahrestagung der Deutschen Gesellschaft für Medizinische Physik, DGMP).
J. Winter, M. Galek, C. Matejcek, J. J. Wilkens, K. Aulenbacher, S. E. Combs, S. Bartzsch. "(V71) Die Linienfokus-Röntgenröhre als kompakte Strahlenquelle für die klinische Mikrostrahltherapie". ISBN: 978-3-948023-10-2, p. 126.
Won the Young Investigator Award by the DGMP.

Annual conference of the European Society for Radiotherapy and Oncology (ESTRO) 2020.
J. Winter, J. J. Wilkens, S. E. Combs, S. Bartzsch. "(OC-0471) Optimization of a compact x-ray source for clinical microbeam radiation therapy". In: *Radiotherapy and Oncology* 152 Suppl. 1 (2020), p. S264. DOI: 10.1016/S0167-8140(21)00493-X.

Joint Conference of the Austrian, German and Swiss Societies of Medical Physics 2021 (Dreiländertagung der Medizinischen Physik der ÖGMP, DGMP, und SGSMP).
J. Winter, A. Dimroth, M. Butzek, S. E. Combs, J. J. Wilkens, S. Bartzsch. "(V53) Heat management of the line-focus x-ray tube for microbeam radiotherapy and FLASH treatments". ISBN: 978-3-948023-16-4, pp. 91–92.

FLASH Radiotherapy and Particle Therapy Conference (FRPT) 2021.
J. Winter, C. Matejcek, K. Aulenbacher, S. E. Combs, J. J. Wilkens, S. Bartzsch. "(O043) FLASH Modalities Track (Oral Presentations) A novel x-ray source for microbeam and FLASH radiotherapy: numerical simulations show the feasibility of the preclinical prototype". In: *Physica Medica: European Journal of Medical Physics* 94 Suppl. (2022), pp. S28–S29. DOI: 10.1016/S1120-1797(22)01494-6.

International Symposium on Medical Applications of X-Ray, Phase-Contrast, and Photon-Counting (IMXP) 2022.
J. Winter, N. Halat, L. Quénot, S. E. Combs, J. Herzen, J. J. Wilkens, E. Brun, S. Bartzsch. "Phase contrast imaging with a novel powerful source for orthovoltage x-rays."

4th European Congress of Medical Physics (ECMP) 2022.
J. Winter, K. M. Kraus, Y. Zhang, M. Ahmed, S. E. Combs, J. J. Wilkens, S. Bartzsch. "Comparison of microbeam radiotherapy to clinical treatment plans based on the equivalent uniform dose". In: *Physica Medica: European Journal of Medical Physics* 104 Suppl. 1 (2022), p. S53. DOI: 10.1016/S1120-1797(22)02238-4.

Poster presentations

Annual conference of the Radiation Research Society (RRS) 2020.
J. Winter, J. J. Wilkens, S. E. Combs, S. Bartzsch. "(PS11-10) The line-focus x-ray tube as a compact source for FLASH and microbeam radiation therapy".

Annual conference of the European Society for Radiotherapy and Oncology (ESTRO) 2021.
J. Winter, K. M. Kraus, M. Ahmed, S. E. Combs, J. J. Wilkens, S. Bartzsch. "(PD-0933) Microbeam radiotherapy planning for a clinical lung tumor case". In: *Radiotherapy and Oncology* 161 Suppl. 1 (2021), pp. S775–S776. DOI: 10.1016/S0167-8140(21)07212-1.

Contributions as co-author

Oral presentation at the DPG Spring Meeting of the German Society of Physics 2020 (Frühjahrstagung der Deutsche Physikalische Gesellschaft, DPG).
C. Matejcek, J. Winter, J. J. Wilkens, S. Bartzsch, K. Aulenbacher. "(AKBP 1.4) A novel X-ray source for microbeam radiation therapy".

Poster presentation at the annual conference of the German Society of Radiation Onocology 2020 (26. Jahrestagung der Deutschen Gesellschaft für Radioonkologie, DEGRO).
S. Bartzsch, J. Winter, C. Matejcek, J. J. Wilkens, K. Aulenbacher, S. E. Combs. "(P49-10-jD) Mikrostrahltherapie an einer kompakten Strahlenquelle". In: *Strahlentherapie und Onkologie* 196 Suppl. 1 (2020), p. S207. DOI: 10.1007/s00066-020-01620-0.

Oral presentation at Joint Conference of the Austrian, German and Swiss Societies of Medical Physics 2021 (Dreiländertagung der Medizinischen Physik der ÖGMP, DGMP, und SGSMP).
S. Spasova, J. Winter, S. E. Combs, J. J. Wilkens, S. Bartzsch. “(V82) Impact of pulse motion in the brain on the dose distribution of microbeam radiation therapy”. ISBN: 978-3-948023-16-4, pp. 193-–194.

Poster presentation at the FLASH Radiotherapy and Particle Therapy Conference (FRPT) 2021.
S. Bartzsch, A. Dimroth, J. Winter, C. Petrich, C. Matejcek, Y. Zhang, J. Rieser, S. Rötzer, K.-L. Krämer, M. Zimmermann, M. Galek, M. Butzek, K. Aulenbacher, J. Wilkens, S. Combs. "(EPD024) The line focus x-ray tube: an x-ray source for FLASH and spatially fractionated radiation therapy". In: *Physica Medica: European Journal of Medical Physics* 94 Suppl. (2022), pp. S71-S72. DOI: 10.1016/S1120-1797(22)01595-2.

Poster presentation at the FLASH Radiotherapy and Particle Therapy Conference (FRPT) 2021.
T. Schmid, M. Nguyen, A. Dombrowsky, S. Bicher, F. Treibel, J. Winter, M. Ahmed, S. Combs, S. Bartzsch. "(EPD052) Radiobiological mechanisms in microbeam radiation therapy (MRT)". In: *Physica Medica: European Journal of Medical Physics* 94 Suppl. (2022), p. S83. DOI: 10.1016/S1120-1797(22)01623-4.

Poster presentation at the annual conference of the German Society of Radiation Onocology 2022 (28. Kongress der Deutschen Gesellschaft für Radioonkologie, DEGRO).
K. M. Kraus, J. Winter, Y. Zhang, M. Ahmed, J. J. Wilkens, S. Bartzsch, S. E. Combs. "(P17-18) Mikrostrahltherapie (MRT) auf dem Weg in die Klinik — eine Therapieplanungsstudie". In: *Strahlentherapie und Onkologie* 198 Suppl. 1 (2022), pp. S176–S177. DOI: 10.1007/s00066-022-01932-3.

Oral presentation at the NordDesign conference 2022.
M. Ravichandran, J. Winter, S. Bartzsch, M. Zimmermann. "Material selection for extreme thermo-mechanical loads using design space projection: a concept study for an ultra-high power x-ray source". In: DS 118: *Proceedings of NordDesign* 2022. DOI: 10.35199/NORDDESIGN2022.33.

Oral presentation at the 4th European Congress of Medical Physics (ECMP) 2022.
C. Petrich, J. Winter, A. Dimroth, C. Matejcek, S. Rötzer, Y. Zhang, M. Ravichandran, M. Zimmermann, M. Butzek, K. Aulenbacher, J. J. Wilkens, S. Bartzsch. "Prototype of a line-focus x-ray tube (LFxT) as compact source for microbeam and FLASH radiotherapy". In: *Physica Medica: European Journal of Medical Physics* 104 Suppl. 1 (2022), pp. S61–S62. DOI: 10.1016/S1120-1797(22)02257-8.

Student projects

I strongly collaborated with two master students of the Physics Department at the Technical University of Munich, whereof one master project is still ongoing. Parts of the first master project are incorporated in chapter 12 and in the journal article by Ahmed et al., which is in preparation.

Bibliography

[1] F. Bray, M. Laversanne, E. Weiderpass, et al. "The ever-increasing importance of cancer as a leading cause of premature death worldwide". In: *Cancer* 127.16 (2021), pp. 3029–3030. DOI: 10.1002/cncr.33587.

[2] M. Joiner and A. van der Kogel. *Basic Clinical Radiobiology*. Ed. by M. Joiner and A. van der Kogel. 4th ed. CRC Press LLC, 2009, p. 350. ISBN: 978-0-340-92966-7.

[3] F. B. Furnari, T. Fenton, R. M. Bachoo, et al. "Malignant astrocytic glioma: genetics, biology, and paths to treatment". In: *Genes & Development* 21.21 (2007), pp. 2683–2710. DOI: 10.1101/gad.1596707.

[4] C. P. Karger. "Klinische Strahlenbiologie". In: *Medizinische Physik – Grundlagen – Bildgebung – Therapie – Technik*. Ed. by W. Schlegel, C. P. Karger, and O. Jäkel. Berlin, Heidelberg: Springer Berlin Heidelberg, 2018. Chap. IV 22, pp. 451–472. DOI: 10.1007/978-3-662-54801-1_22.

[5] J. F. Fowler. "The linear-quadratic formula and progress in fractionated radiotherapy". In: *British Journal of Radiology* 62.740 (1989), pp. 679–694. DOI: 10.1259/0007-1285-62-740-679.

[6] S. J. McMahon. "The linear quadratic model: usage, interpretation and challenges". In: *Physics in Medicine & Biology* 64.1 (2018), 01TR01. DOI: 10.1088/1361-6560/aaf26a.

[7] A. Köhler. "Röntgentiefentherapie mit Metallnetzschutz: Praktische Erfolge". In: *Strahlentherapie* 1 (1912), pp. 121–131.

[8] J. A. Laissue, H. Blattmann, and D. N. Slatkin. "Alban Köhler (1874-1947): Erfinder der Gittertherapie". In: *Zeitschrift für Medizinische Physik* 22.2 (2012), pp. 90–99. DOI: 10.1016/j.zemedi.2011.07.002.

[9] A. S. Meigooni, K. Dou, N. J. Meigooni, et al. "Dosimetric characteristics of a newly designed grid block for megavoltage photon radiation and its therapeutic advantage using a linear quadratic model". In: *Medical Physics* 33.9 (2006), pp. 3165–3173. DOI: 10.1118/1.2241998.

[10] P. Almendral, P. J. Mancha, and D. Roberto. "Feasibility of a simple method of hybrid collimation for megavoltage grid therapy". In: *Medical Physics* 40.5 (2013), p. 051712. DOI: 10.1118/1.4801902.

[11] E. Borzov, R. Bar-Deroma, and M. Lutsyk. "Physical aspects of a spatially fractionated radiotherapy technique for large soft tissue sarcomas". In: *Physics and Imaging in Radiation Oncology* 22 (2022), pp. 63–66. DOI: 10.1016/j.phro.2022.04.010.

[12] H. R. Withers, J. M. Taylor, and B. Maciejewski. “Treatment volume and tissue tolerance”. In: *International Journal of Radiation Oncology*Biology*Physics* 14.4 (1988), pp. 751–759. DOI: 10.1016/0360-3016(88)90098-3.

[13] W. Zeman, H. J. Curtis, E. L. Gebhard, et al. “Tolerance of Mouse-Brain Tissue to High-Energy Deuterons”. In: *Science* 130.3391 (1959), pp. 1760–1761. DOI: 10.1126/science.130.3391.1760.b.

[14] M. P. Grams, H. S. W. C. Tseung, S. Ito, et al. “A Dosimetric Comparison of Lattice, Brass, and Proton Grid Therapy Treatment Plans”. In: *Practical Radiation Oncology* 12.5 (2022), e442–e452. DOI: 10.1016/j.prro.2022.03.005.

[15] M. Mohiuddin, C. Lynch, M. Gao, et al. “Early clinical results of proton spatially fractionated GRID radiation therapy (SFGRT)”. In: *The British Journal of Radiology* 93.1107 (2020), p. 20190572. DOI: 10.1259/bjr.20190572.

[16] P. Deman, M. Vautrin, V. Stupar, et al. “Monochromatic minibeam radiotherapy: theoretical and experimental dosimetry for preclinical treatment plans”. In: *Physics in Medicine and Biology* 56.14 (2011), pp. 4465–4480. DOI: 10.1088/0031-9155/56/14/015.

[17] Y. Prezado, P. Deman, P. Varlet, et al. “Tolerance to Dose Escalation in Minibeam Radiation Therapy Applied to Normal Rat Brain: Long-Term Clinical, Radiological and Histopathological Analysis”. In: *Radiation Research* 184.3 (2015), pp. 314–321. DOI: 10.1667/RR14018.1.

[18] F. A. Dilmanian, J. G. Eley, and S. Krishnan. “Minibeam Therapy With Protons and Light Ions: Physical Feasibility and Potential to Reduce Radiation Side Effects and to Facilitate Hypofractionation”. In: *International Journal of Radiation Oncology*Biology*Physics* 92.2 (2015), pp. 469–474. DOI: 10.1016/j.ijrobp.2015.01.018.

[19] J. Meyer, J. Eley, T. E. Schmid, et al. “Spatially fractionated proton minibeams”. In: *The British Journal of Radiology* 92.1095 (2019), p. 20180466. DOI: 10.1259/bjr.20180466.

[20] D. N. Slatkin, P. Spanne, F. A. Dilmanian, et al. “Microbeam radiation therapy”. In: *Medical Physics* 19.6 (1992), pp. 1395–1400. DOI: 10.1118/1.596771.

[21] J. A. Laissue, N. Lyubimova, H.-P. Wagner, et al. “Microbeam radiation therapy”. In: *Proceedings of SPIE*. Ed. by H. B. Barber and H. Roehrig. Vol. 3770. Denver, Colorado: International Society for Optics and Photonics, 1999, p. 38. DOI: 10.1117/12.368185.

[22] S. H. Bartzsch, S. Corde, J. C. Crosbie, et al. “Technical advances in X-ray microbeam radiation therapy.” In: *Physics in Medicine and Biology* 65.2 (2020), 02TR01. DOI: 10.1088/1361-6560/ab5507.

[23] R. Serduc, A. Bouchet, E. Bräuer-Krisch, et al. “Synchrotron microbeam radiation therapy for rat brain tumor palliation - Influence of the microbeam width at constant valley dose”. In: *Physics in Medicine and Biology* 54.21 (2009), pp. 6711–6724. DOI: 10.1088/0031-9155/54/21/017.

[24] L. M. L. Smyth, J. F. Donoghue, J. A. Ventura, et al. “Comparative toxicity of synchrotron and conventional radiation therapy based on total and partial body irradiation in a murine model”. In: *Scientific Reports* 8.1 (2018), pp. 1–11. DOI: 10.1038/s41598-018-30543-1.

[25] E. Bräuer-Krisch, J.-F. Adam, E. Alagoz, et al. “Medical physics aspects of the synchrotron radiation therapies: Microbeam radiation therapy (MRT) and synchrotron stereotactic radiotherapy (SSRT)”. In: *Physica Medica* 31.6 (2015), pp. 568–583. DOI: 10.1016/J.EJMP.2015.04.016.

[26] C. Fernandez-Palomo, J. Fazzari, V. Trappetti, et al. “Animal Models in Microbeam Radiation Therapy: A Scoping Review”. In: *Cancers* 12.3 (2020), p. 527. DOI: 10.3390/cancers12030527.

[27] A. C. Dombrowsky, K. Burger, A.-K. Porth, et al. “A proof of principle experiment for microbeam radiation therapy at the Munich compact light source”. In: *Radiation and Environmental Biophysics* 59.1 (2020), pp. 111–120. DOI: 10.1007/s00411-019-00816-y.

[28] V. Trappetti, C. Fernandez-Palomo, L. Smyth, et al. “Synchrotron Microbeam Radiation Therapy for the Treatment of Lung Carcinoma: A Preclinical Study”. In: *International Journal of Radiation Oncology*Biology*Physics* 111.5 (2021), pp. 1276–1288. DOI: 10.1016/j.ijrobp.2021.07.1717.

[29] C. Fernandez-Palomo, V. Trappetti, M. Potez, et al. “Complete Remission of Mouse Melanoma after Temporally Fractionated Microbeam Radiotherapy”. In: *Cancers* 12.9 (2020), p. 2656. DOI: 10.3390/cancers12092656.

[30] E. Schültke, E. Bräuer-Krisch, H. Blattmann, et al. “Survival of rats bearing advanced intracerebral F 98 tumors after glutathione depletion and microbeam radiation therapy: conclusions from a pilot project”. In: *Radiation Oncology* 13.1 (2018), p. 89. DOI: 10.1186/s13014-018-1038-6.

[31] J. C. Crosbie, R. L. Anderson, K. Rothkamm, et al. “Tumor Cell Response to Synchrotron Microbeam Radiation Therapy Differs Markedly From Cells in Normal Tissues”. In: *International Journal of Radiation Oncology Biology Physics* 77.3 (2010), pp. 886–894. DOI: 10.1016/j.ijrobp.2010.01.035.

[32] Y. Yang, J. C. Crosbie, P. Paiva, et al. “In Vitro Study of Genes and Molecular Pathways Differentially Regulated by Synchrotron Microbeam Radiotherapy”. In: *Radiation Research* 182.6 (2014), p. 626. DOI: 10.1667/RR13778.1.

[33] L. M. L. Smyth, P. A. W. Rogers, J. C. Crosbie, et al. “Characterization of Diffuse Intrinsic Pontine Glioma Radiosensitivity using Synchrotron Microbeam Radiotherapy and Conventional Radiation Therapy In Vitro”. In: *Radiation Research* 189.2 (2017), p. 146. DOI: 10.1667/RR4633.1.

[34] H. Steel, S. C. Brüningk, C. Box, et al. “Quantification of Differential Response of Tumour and Normal Cells to Microbeam Radiation in the Absence of FLASH Effects”. In: *Cancers* 13.13 (2021), p. 3238. DOI: 10.3390/cancers13133238.

[35] A. Bouchet, E. Bräuer-Krisch, Y. Prezado, et al. “Better Efficacy of Synchrotron Spatially Microfractionated Radiation Therapy Than Uniform Radiation Therapy on Glioma”. In: *International Journal of Radiation Oncology Biology Physics* 95.5 (2016), pp. 1485–1494. DOI: 10.1016/j.ijrobp.2016.03.040.

[36] L. Eling, A. Bouchet, A. Ocadiz, et al. “Unexpected Benefits of Multiport Synchrotron Microbeam Radiation Therapy for Brain Tumors”. In: *Cancers* 13.5 (2021), p. 936. DOI: 10.3390/cancers13050936.

[37] E. Schültke, S. Bayat, S. Bartzsch, et al. “A Mouse Model for Microbeam Radiation Therapy of the Lung”. In: *International Journal of Radiation Oncology*Biology*Physics* 110.2 (2021), pp. 521–525. DOI: 10.1016/j.ijrobp.2020.12.030.

[38] E. A. Siegbahn, J. Stepanek, E. Bräuer-Krisch, et al. “Determination of dosimetrical quantities used in microbeam radiation therapy (MRT) with Monte Carlo simulations”. In: *Medical Physics* 33.9 (2006), pp. 3248–3259. DOI: 10.1118/1.2229422.

[39] J. C. Crosbie, I. Svalbe, S. Midgley, et al. “A method of dosimetry for synchrotron microbeam radiation therapy using radiochromic films of different sensitivity”. In: *Physics in Medicine and Biology* 53.23 (2008), pp. 6861–6877. DOI: 10.1088/0031-9155/53/23/014.

[40] I. Martínez-Rovira, J. Sempau, and Y. Prezado. “Development and commissioning of a Monte Carlo photon beam model for the forthcoming clinical trials in microbeam radiation therapy”. In: *Medical Physics* 39.1 (2011), pp. 119–131. DOI: 10.1118/1.3665768.

[41] J.-F. Adam, J. Balosso, S. Bayat, et al. “Toward Neuro-Oncologic Clinical Trials of High-Dose-Rate Synchrotron Microbeam Radiation Therapy: First Treatment of a Spontaneous Canine Brain Tumor”. In: *International Journal of Radiation Oncology*Biology*Physics* 113.5 (2022), pp. 967–973. DOI: 10.1016/j.ijrobp.2022.04.022.

[42] L. M. Smyth, L. R. Day, K. Woodford, et al. “Identifying optimal clinical scenarios for synchrotron microbeam radiation therapy: A treatment planning study”. In: *Physica Medica* 60 (2019), pp. 111–119. DOI: 10.1016/j.ejmp.2019.03.019.

[43] K. M. Kraus, J. Winter, Y. Zhang, et al. “Treatment Planning Study for Microbeam Radiotherapy Using Clinical Patient Data”. In: *Cancers* 14.3 (2022), p. 685. DOI: 10.3390/cancers14030685.

[44] L. M. L. Smyth, S. Senthi, J. C. Crosbie, et al. "The normal tissue effects of microbeam radiotherapy: What do we know, and what do we need to know to plan a human clinical trial?" In: *International Journal of Radiation Biology* 92.6 (2016), pp. 302–311. DOI: 10.3109/09553002.2016.1154217.

[45] M. J. Ibahim, J. C. Crosbie, Y. Yang, et al. "An Evaluation of Dose Equivalence between Synchrotron Microbeam Radiation Therapy and Conventional Broad-beam Radiation Using Clonogenic and Cell Impedance Assays". In: *PLoS ONE* 9.6 (2014). Ed. by G. C. Jagetia, e100547. DOI: 10.1371/journal.pone.0100547.

[46] M. Grotzer, E. Schültke, E. Bräuer-Krisch, et al. "Microbeam radiation therapy: Clinical perspectives". In: *Physica Medica* 31.6 (2015), pp. 564–567. DOI: 10.1016/j.ejmp.2015.02.011.

[47] M. Sammer, A. C. Dombrowsky, J. Schauer, et al. "Normal Tissue Response of Combined Temporal and Spatial Fractionation in Proton Minibeam Radiation Therapy". In: *International Journal of Radiation Oncology*Biology*Physics* 109.1 (2021), pp. 76–83. DOI: 10.1016/j.ijrobp.2020.08.027.

[48] M. D. Wright. "Microbeam radiosurgery: An industrial perspective". In: *Physica Medica* 31.6 (2015), pp. 601–606. DOI: 10.1016/j.ejmp.2015.04.003.

[49] S. Sabatasso, J. A. Laissue, R. Hlushchuk, et al. "Microbeam Radiation-Induced Tissue Damage Depends on the Stage of Vascular Maturation". In: *International Journal of Radiation Oncology*Biology*Physics* 80.5 (2011), pp. 1522–1532. DOI: 10.1016/j.ijrobp.2011.03.018.

[50] A. Bouchet, B. Lemasson, T. Christen, et al. "Synchrotron microbeam radiation therapy induces hypoxia in intracerebral gliosarcoma but not in the normal brain". In: *Radiotherapy and Oncology* 108.1 (2013), pp. 143–148. DOI: 10.1016/j.radonc.2013.05.013.

[51] A. Bouchet, N. Sakakini, M. El Atifi, et al. "Early Gene Expression Analysis in 9L Orthotopic Tumor-Bearing Rats Identifies Immune Modulation in Molecular Response to Synchrotron Microbeam Radiation Therapy". In: *PLoS ONE* 8.12 (2013). Ed. by F. Mattei, e81874. DOI: 10.1371/journal.pone.0081874.

[52] R. Serduc, E. Bräuer-Krisch, E. A. Siegbahn, et al. "High-precision radiosurgical dose delivery by interlaced microbeam arrays of high-flux low-energy synchrotron x-rays". In: *PLoS ONE* 5.2 (2010). DOI: 10.1371/journal.pone.0009028.

[53] A. Bouchet, B. Lemasson, G. Le Duc, et al. "Preferential Effect of Synchrotron Microbeam Radiation Therapy on Intracerebral 9L Gliosarcoma Vascular Networks". In: *International Journal of Radiation Oncology*Biology*Physics* 78.5 (2010), pp. 1503–1512. DOI: 10.1016/J.IJROBP.2010.06.021.

[54] V. Trappetti, M. Potez, C. Fernandez-Palomo, et al. “Microbeam Radiation Therapy Controls Local Growth of Radioresistant Melanoma and Treats Out-of-Field Locoregional Metastasis”. In: *International Journal of Radiation Oncology*Biology*Physics* 114.3 (2022), pp. 478–493. DOI: 10.1016/j.ijrobp.2022.06.090.

[55] K. M. Prise and J. M. O’Sullivan. “Radiation-induced bystander signalling in cancer therapy”. In: *Nature Reviews Cancer* 9.5 (2009), pp. 351–360. DOI: 10.1038/nrc2603.

[56] M. Tomita, M. Maeda, H. Maezawa, et al. “Bystander Cell Killing in Normal Human Fibroblasts is Induced by Synchrotron X-Ray Microbeams”. In: *Radiation Research* 173.3 (2010), pp. 380–385. DOI: 10.1667/RR1995.1.

[57] N. Autsavapromporn, M. Suzuki, T. Funayama, et al. “Gap Junction Communication and the Propagation of Bystander Effects Induced by Microbeam Irradiation in Human Fibroblast Cultures: The Impact of Radiation Quality”. In: *Radiation Research* 180.4 (2013), pp. 367–375. DOI: 10.1667/RR3111.1.

[58] R. S. Asur, S. Sharma, C.-W. Chang, et al. “Spatially Fractionated Radiation Induces Cytotoxicity and Changes in Gene Expression in Bystander and Radiation Adjacent Murine Carcinoma Cells”. In: *Radiation Research* 177.6 (2012), pp. 751–765. DOI: 10.1667/RR2780.1.

[59] S. Bartzsch, C. Cummings, S. Eismann, et al. “A preclinical microbeam facility with a conventional x-ray tube”. In: *Medical Physics* 43.12 (2016), pp. 6301–6308. DOI: 10.1118/1.4966032.

[60] S. Bazyar, C. R. Inscoe, T. Benefield, et al. “Neurocognitive sparing of desktop microbeam irradiation”. In: *Radiation Oncology* 12.1 (2017), p. 127. DOI: 10.1186/s13014-017-0864-2.

[61] E. Bräuer-Krisch, H. Requardt, T. Brochard, et al. “New technology enables high precision multislit collimators for microbeam radiation therapy”. In: *Review of Scientific Instruments* 80.7 (2009), p. 074301. DOI: 10.1063/1.3170035.

[62] M. Donzelli, E. Bräuer-Krisch, U. Oelfke, et al. “Hybrid dose calculation: a dose calculation algorithm for microbeam radiation therapy”. In: *Physics in Medicine & Biology* 63.4 (2018), p. 045013. DOI: 10.1088/1361-6560/aaa705.

[63] S. Bartzsch and U. Oelfke. “Line focus x-ray tubes—a new concept to produce high brilliance x-rays”. In: *Physics in Medicine & Biology* 62.22 (2017), pp. 8600–8615. DOI: 10.1088/1361-6560/aa910b.

[64] E. Bräuer-Krisch, H. Requardt, P. Régnard, et al. “New irradiation geometry for microbeam radiation therapy”. In: *Physics in Medicine and Biology* 50.13 (2005), pp. 3103–3111. DOI: 10.1088/0031-9155/50/13/009.

[65] European Synchrotron Radiation Facility. *ID17 Biomedical Beamline - Microbeam Radiation Therapy (MRT)*. 2022. URL: https://www.esrf.fr/home/UsersAndScience/Experiments/CBS/ID17/mrt-1.html (visited on 2022-07-19).

[66] M. Renier, T. Brochard, C. Nemoz, et al. “A white-beam fast-shutter for microbeam radiation therapy at the ESRF”. In: *Nuclear Instruments and Methods in Physics Research Section A: Accelerators, Spectrometers, Detectors and Associated Equipment* 479.2-3 (2002), pp. 656–660. DOI: 10.1016/S0168-9002(01)00905-6.

[67] M. Jacquet and P. Suortti. “Radiation therapy at compact Compton sources”. In: *Physica Medica* 31.6 (2015), pp. 596–600. DOI: 10.1016/j.ejmp.2015.02.010.

[68] E. Eggl, M. Dierolf, K. Achterhold, et al. “The Munich Compact Light Source: initial performance measures”. In: *Journal of Synchrotron Radiation* 23.5 (2016), pp. 1137–1142. DOI: 10.1107/S160057751600967X.

[69] K. Dupraz, M. Alkadi, M. Alves, et al. “The ThomX ICS source”. In: *Physics Open* 5 (2020), p. 100051. DOI: 10.1016/j.physo.2020.100051.

[70] E. C. Schreiber and S. X. Chang. “Monte Carlo simulation of a compact microbeam radiotherapy system based on carbon nanotube field emission technology”. In: *Medical Physics* 39.8 (2012), pp. 4669–4678. DOI: 10.1118/1.4728220.

[71] M. Hadsell, J. Zhang, P. Laganis, et al. “A first generation compact microbeam radiation therapy system based on carbon nanotube X-ray technology”. In: *Applied Physics Letters* 103.18 (2013), p. 183505. DOI: 10.1063/1.4826587.

[72] N. M. Esplen, L. Chergui, C. D. Johnstone, et al. “Monte Carlo optimization of a microbeam collimator design for use on the small animal radiation research platform (SARRP)”. In: *Physics in Medicine & Biology* 63.17 (2018), p. 175004. DOI: 10.1088/1361-6560/aad7e2.

[73] F. Treibel, M. Nguyen, M. Ahmed, et al. “Establishment of Microbeam Radiation Therapy at a Small-Animal Irradiator”. In: *International Journal of Radiation Oncology*Biology*Physics* 109.2 (2021), pp. 626–636. DOI: 10.1016/j.ijrobp.2020.09.039.

[74] R. F. de Paiva, M. Bisiaux, J. Lynch, et al. “High resolution x-ray tomography in an electron microprobe”. In: *Review of Scientific Instruments* 67.6 (1996), pp. 2251–2256. DOI: 10.1063/1.1147043.

[75] S. H. Heo, A. Ihsan, and S. O. Cho. “Transmission-type microfocus x-ray tube using carbon nanotube field emitters”. In: *Applied Physics Letters* 90.18 (2007), p. 183109. DOI: 10.1063/1.2735549.

[76] O. Hemberg, M. Otendal, and H. M. Hertz. “Liquid-metal-jet anode electron-impact x-ray source”. In: *Applied Physics Letters* 83.7 (2003), pp. 1483–1485. DOI: 10.1063/1.1602157.

[77] T. Tuohimaa, M. Otendal, and H. M. Hertz. “Phase-contrast x-ray imaging with a liquid-metal-jet-anode microfocus source”. In: *Applied Physics Letters* 91.7 (2007), p. 074104. DOI: 10.1063/1.2769760.

[78] M. Kachelrieß. “Computertomographie”. In: *Medizinische Physik – Grundlagen – Bildgebung – Therapie – Technik*. Ed. by W. Schlegel, C. P. Karger, and O. Jäkel. Berlin, Heidelberg: Springer Berlin Heidelberg, 2018. Chap. II 8, pp. 153–203. DOI: 10.1007/978-3-662-54801-1_8.

[79] M. Bangert and P. Ziegenhein. “Bestrahlungsplanung”. In: *Medizinische Physik – Grundlagen – Bildgebung – Therapie – Technik*. Ed. by W. Schlegel, C. P. Karger, and O. Jäkel. Berlin, Heidelberg: Springer Berlin Heidelberg, 2018. Chap. IV 24, pp. 485–514. DOI: 10.1007/978-3-662-54801-1_24.

[80] S. Keshmiri, S. Brocard, R. Serduc, et al. “A high-resolution dose calculation engine for X-ray microbeams radiation therapy”. In: *Medical Physics* 49.6 (2022), pp. 3999–4017. DOI: 10.1002/mp.15637.

[81] S. Bartzsch and U. Oelfke. “A new concept of pencil beam dose calculation for 40-200 keV photons using analytical dose kernels”. In: *Medical Physics* 40.11 (2013), p. 111714. DOI: 10.1118/1.4824150.

[82] C. Debus, U. Oelfke, and S. Bartzsch. “A point kernel algorithm for microbeam radiation therapy”. In: *Physics in Medicine & Biology* 62.21 (2017), pp. 8341–8359. DOI: 10.1088/1361-6560/aa8d63.

[83] J. A. Laissue, H. Blattmann, M. Di Michiel, et al. “Weanling piglet cerebellum: a surrogate for tolerance to MRT (microbeam radiation therapy) in pediatric neuro-oncology”. In: *Proceedings of SPIE*. Ed. by H. B. Barber, H. Roehrig, F. P. Doty, et al. Vol. 4508. International Society for Optics and Photonics, 2001, pp. 65–73. DOI: 10.1117/12.450774.

[84] A. Niemierko. “Reporting and analyzing dose distributions: A concept of equivalent uniform dose”. In: *Medical Physics* 24.1 (1997), pp. 103–110. DOI: 10.1118/1.598063.

[85] J. Meyer, R. D. Stewart, D. Smith, et al. “Biological and dosimetric characterisation of spatially fractionated proton minibeams”. In: *Physics in Medicine & Biology* 62.24 (2017), pp. 9260–9281. DOI: 10.1088/1361-6560/aa950c.

[86] Q. Wu, R. Mohan, A. Niemierko, et al. “Optimization of intensity-modulated radiotherapy plans based on the equivalent uniform dose”. In: *International Journal of Radiation Oncology*Biology*Physics* 52.1 (2002), pp. 224–235. DOI: 10.1016/S0360-3016(01)02585-8.

[87] J. Winter, M. Galek, C. Matejcek, et al. “Clinical microbeam radiation therapy with a compact source: specifications of the line-focus X-ray tube”. In: *Physics and Imaging in Radiation Oncology* 14 (2020), pp. 74–81. DOI: 10.1016/j.phro.2020.05.010.

[88] J. Winter, A. Dimroth, S. Roetzer, et al. “Heat management of a compact x-ray source for microbeam radiotherapy and FLASH treatments”. In: *Medical Physics* 49.5 (2022), pp. 3375–3388. DOI: 10.1002/mp.15611.

[89] W. Schlegel. “Physikalische Grundlagen der Röntgendiagnostik”. In: *Medizinische Physik 2 Medizinische Strahlenphysik*. Ed. by W. Schlegel and J. Bille. Berlin, Heidelberg: Springer Berlin Heidelberg, 2002. Chap. II 6, pp. 139–170. DOI: 10.1007/978-3-642-56259-4.

[90] R. Ringler. “Physikalisch-Technische Grundlagen der Röntgendiagnostik”. In: *Medizinische Physik – Grundlagen – Bildgebung – Therapie – Technik*. Ed. by W. Schlegel, C. P. Karger, and O. Jäkel. Berlin, Heidelberg: Springer Berlin Heidelberg, 2018. Chap. II 6, pp. 123–138. DOI: 10.1007/978-3-662-54801-1_6.

[91] M. Duncan, M. Donzelli, P. Pellicioli, et al. “First experimental measurement of the effect of cardio-synchronous brain motion on the dose distribution during microbeam radiation therapy”. In: *Medical Physics* 47.1 (2020), pp. 213–222. DOI: 10.1002/mp.13899.

[92] F. Manchado de Sola, M. Vilches, Y. Prezado, et al. “Impact of cardiosynchronous brain pulsations on Monte Carlo calculated doses for synchrotron micro- and minibeam radiation therapy”. In: *Medical Physics* 45.7 (2018), pp. 3379–3390. DOI: 10.1002/mp.12973.

[93] S. Agostinelli, J. Allison, K. Amako, et al. “Geant4 — a simulation toolkit”. In: *Nuclear Instruments and Methods in Physics Research Section A: Accelerators, Spectrometers, Detectors and Associated Equipment* 506.3 (2003), pp. 250–303. DOI: 10.1016/S0168-9002(03)01368-8.

[94] J. Perl, J. Shin, J. Schümann, et al. “TOPAS: An innovative proton Monte Carlo platform for research and clinical applications”. In: *Medical Physics* 39.11 (2012), pp. 6818–6837. DOI: 10.1118/1.4758060.

[95] Geant4 Collaboration. *Electromagnetic Interactions — Physics Reference Manual — Geant4 10.6v2*. 2020. URL: https://geant4-userdoc.web.cern.ch/UsersGuides/PhysicsReferenceManual/BackupVersions/V10.6c/html/electromagnetic/index.html (visited on 2022-07-19).

[96] Geant4 Collaboration. *Electromagnetic physics constructors — Physics List Guide — Geant4 10.4*. 2018. URL: https://geant4-userdoc.web.cern.ch/UsersGuides/PhysicsListGuide/BackupVersions/V10.4/html/electromagnetic/tables_by_constructor/pen.html (visited on 2022-07-19).

[97] J. H. Hubbell and S. M. Seltzer. *X-Ray Mass Attenuation Coefficients, NIST Standard Reference Database 126*. Tech. rep. National Institute of Standards and Technology (NIST), Physical Measurement Laboratory (PML), 2004. URL: https://www.nist.gov/pml/x-ray-mass-attenuation-coefficients.

[98] J. C. Crosbie, P. Fournier, S. Bartzsch, et al. “Energy spectra considerations for synchrotron radiotherapy trials on the ID17 bio-medical beamline at the European Synchrotron Radiation Facility”. In: *Journal of Synchrotron Radiation* 22.4 (2015), pp. 1035–1041. DOI: 10.1107/S1600577515008115.

[99] Geant4 Collaboration. *Electromagnetic physics constructors — Physics List Guide — Geant4 10.5*. 2019. URL: https://geant4-userdoc.web.cern.ch/UsersGuides/PhysicsListGuide/BackupVersions/V10.5-2.0/html/electromagnetic/tables_by_constructor/pen.html (visited on 2022-07-19).

[100] Ashland. *GAFCHROMIC EBT3 Dosimetry Film*. 2022. URL: http://gafchromic.com/documents/EBT3_Specifications.pdf (visited on 2022-07-19).

[101] J. Spiga, E. A. Siegbahn, E. Bräuer-Krisch, et al. "The GEANT4 toolkit for microdosimetry calculations: Application to microbeam radiation therapy (MRT)". In: *Medical Physics* 34.11 (2007), pp. 4322–4330. DOI: 10.1118/1.2794170.

[102] F. A. Dilmanian, T. M. Button, G. Le Duc, et al. "Response of rat intracranial 9L gliosarcoma to microbeam radiation therapy". In: *Neuro-Oncology* 4.1 (2002), pp. 26–38. DOI: 10.1093/neuonc/4.1.26.

[103] J. K. Molitoris, T. Diwanji, J. W. Snider III, et al. "Optimizing immobilization, margins, and imaging for lung stereotactic body radiation therapy". In: *Translational Lung Cancer Research* 8.1 (2018), pp. 24–31. DOI: 10.21037/tlcr.2018.09.25.

[104] A. Oppelt. *Imaging systems for medical diagnostics: fundamentals, technical solutions and applications for systems applying ionization radiation, nuclear magnetic resonance and ultrasound*. 2nd ed. Publicis, 2005, p. 996. ISBN: 978-3-89578-226-8.

[105] P. Schardt, J. Deuringer, J. Freudenberger, et al. "New x-ray tube performance in computed tomography by introducing the rotating envelope tube technology". In: *Medical Physics* 31.9 (2004), pp. 2699–2706. DOI: 10.1118/1.1783552.

[106] W. J. Oosterkamp. "The heat dissipation in the anode of an x-ray tube - I. Loads of short duration applied to stationary anodes". In: *Philips Research Reports* 3 (1948), pp. 49–59.

[107] W. J. Oosterkamp. "The heat dissipation in the anode of an x-ray tube - II. Loads of short duration applied to rotating anodes". In: *Philips Research Reports* 3 (1948), pp. 161–173.

[108] Geant4 Collaboration. *Electromagnetic physics constructors — Physics List Guide — Geant4 10.6v2*. 2020. URL: https://geant4-userdoc.web.cern.ch/UsersGuides/PhysicsListGuide/BackupVersions/V10.6c/html/electromagnetic/tables_by_constructor/pen.html (visited on 2022-07-19).

[109] COMSOL Multiphysics. *Version 5.5*. Stockholm, Sweden, 2020.

[110] Plansee SE. *Wolfram | Plansee*. 2021. URL: https://www.plansee.com/de/werkstoffe/wolfram.html (visited on 2022-07-19).

[111] F. Cardarelli. *Materials Handbook - A Concise Desktop Reference*. 2nd ed. London: Springer London, 2008. ISBN: 978-1-84628-668-1. DOI: 10.1007/978-1-84628-669-8.

[112] T. Tanabe, C. Eamchotchawalit, C. Busabok, et al. “Temperature dependence of thermal conductivity in W and W–Re alloys from 300 to 1000 K”. In: *Materials Letters* 57.19 (2003), pp. 2950–2953. DOI: 10.1016/S0167-577X(02)01403-9.

[113] T. Flohr and B. Ohnesorge. “Multi-slice CT technology”. In: *Multi-slice and Dual-source CT in Cardiac Imaging*. Ed. by B. M. Ohnesorge, T. G. Flohr, C. R. Becker, et al. 2nd ed. Berlin, Heidelberg: Springer Berlin Heidelberg, 2007, pp. 41–69. DOI: 10.1007/978-3-540-49546-8_3.

[114] E. S. M. Ali and D. W. O. Rogers. “Quantifying the effect of off-focal radiation on the output of kilovoltage x-ray systems”. In: *Medical Physics* 35.9 (2008), pp. 4149–4160. DOI: 10.1118/1.2966348.

[115] Diamond Materials GmbH. *CVD Diamond for Synchrotron Beamlines*. 2022. URL: https://www.diamond-materials.com/site/assets/files/1096/cvd_diamond_synchrotron_windows.pdf (visited on 2022-07-19).

[116] HeatWave Labs Inc. *Technical Bulletin TB-147*. 2004. URL: https://www.cathode.com/pdf/tb-147.pdf (visited on 2022-07-19).

[117] Stahlhandel Gröditz GmbH. *1.4404 Werkstoffdatenblatt*. 2022. URL: https://www.stahlportal.com/lagervorrat/14404-x2crnimo17-12-2-loesungsgeglueht-und-abgeschreckt/ (visited on 2022-07-19).

[118] F. Hinterberger. *Physik der Teilchenbeschleuniger und Ionenoptik*. 2nd ed. Berlin, Heidelberg: Springer Berlin Heidelberg, 2008. ISBN: 978-3-540-75281-3. DOI: 10.1007/978-3-540-75282-0.

[119] C. Matejcek. “Strahldynamik der Niederenergie-Strahlführung von MESA unter Berücksichtigung von Raumladung und Multipol-Beiträgen höherer Ordnung”. Dissertation. Johannes Gutenberg-Universität Mainz, 2020, p. 154. DOI: 10.25358/openscience-5654.

[120] I. V. Bazarov, B. M. Dunham, Y. Li, et al. “Thermal emittance and response time measurements of negative electron affinity photocathodes”. In: *Journal of Applied Physics* 103.5 (2008), p. 054901. DOI: 10.1063/1.2838209.

[121] K. Kittimanapun, C. Dhammatong, N. Juntong, et al. “Low Emittance Thermionic Electron Gun at SLRI”. In: *Proceedings, 9th International Particle Accelerator Conference (IPAC 2018): Vancouver, BC Canada, April 29-May 4, 2018*. 2018, THPMK088. DOI: 10.18429/JACoW-IPAC2018-THPMK088.

[122] HeatWave Labs Inc. *Standard Series Barium Tungsten Dispenser Cathodes TB-198*. 2002. URL: https://cathode.com/pdf/tb-198.pdf (visited on 2022-07-19).

[123] S. J. Humphries. *Charged Particle Beams*. John Wiley and Sons Ltd., 2002, p. 849. ISBN: 978-0-471-60014-5.

[124] T. Asaka, H. Ego, H. Hanaki, et al. “Low-emittance thermionic-gun-based injector for a compact free-electron laser”. In: *Phys. Rev. Accel. Beams* 20.8 (2017), p. 80702. DOI: 10.1103/PhysRevAccelBeams.20.080702.

[125] N. Sugiyama, T. Yokose, E. Iwamoto, et al. “A Line Cathode Electron Gun of the Pierce-Type Design”. In: *Japanese Journal of Applied Physics* 28 (1989), pp. 267–273. DOI: 10.1143/JJAP.28.267.

[126] E. Chu and D. M. Goebel. “High-Current Lanthanum Hexaboride Hollow Cathode for 10-to-50-kW Hall Thrusters”. In: *IEEE Transactions on Plasma Science* 40.9 (2012), pp. 2133–2144. DOI: 10.1109/TPS.2012.2206832.

[127] H. Wiedemann. *Particle Accelerator Physics*. 4th ed. Graduate Texts in Physics. Cham Heidelberg New York Dordrecht London: Springer International Publishing, 2015. ISBN: 978-3-319-18316-9. DOI: 10.1007/978-3-319-18317-6.

[128] A. Taran, D. Voronovich, S. Plankovskyy, et al. “Review of LaB_6, Re-W Dispenser, and BaHfO_3-W Cathode Development”. In: *IEEE Transactions on Electron Devices* 56.5 (2009), pp. 812–817. DOI: 10.1109/TED.2009.2015615.

[129] D. Hall, J. Perl, J. Shin, et al. *TOPAS Documentation*. 2022. URL: https://topas.readthedocs.io/ (visited on 2022-07-19).

[130] W. Wien. “Untersuchungen über die electrische Entladung in verdünnten Gasen”. In: *Annalen der Physik* 301.6 (1898), pp. 440–452. DOI: 10.1002/andp.18983010618.

[131] H. H. Rose. “Optics of high-performance electron microscopes”. In: *Science and Technology of Advanced Materials* 9.1 (2008), p. 014107. DOI: 10.1088/0031-8949/9/1/014107.

[132] N. Kovačević, J. Henderson, E. Chan, et al. “A Three-dimensional MRI Atlas of the Mouse Brain with Estimates of the Average and Variability”. In: *Cerebral Cortex* 15.5 (2005), pp. 639–645. DOI: 10.1093/cercor/bhh165.

[133] GTD Graphit Technologie GmbH. *Toyo Tanso Kohlenstoff-Graphit-Produkte*. 2022. URL: https://www.gtd-graphit.de/fileadmin/medien/pdf/2015_04_28_Heat_Treatement_en.pdf (visited on 2022-07-19).

[134] Diamond Materials GmbH. *Diamond Optical Vacuum Windows*. 2022. URL: https://diamond-materials.com/site/assets/files/1097/diamond_optical_windows.pdf (visited on 2022-07-19).

[135] Diamond Materials GmbH. *The CVD diamond booklet*. 2022. URL: https://diamond-materials.com/site/assets/files/1095/cvd_diamond_booklet.pdf (visited on 2022-07-19).

[136] C. A. Klein. “Diamond windows for high-power lasers: an initial assessment”. In: *Laser Induced Damage in Optical Materials*. Ed. by H. E. Bennett, L. L. Chase, A. H. Guenther, et al. Vol. 1624. Boulder, CO: US Department of Commerce, National Bureau of Standards, 1992, p. 475. DOI: 10.1117/12.60119.

[137] M. J. Berger, J. S. Coursey, M. A. Zucker, et al. *Stopping-Power & Range Tables for Electrons, Protons, and Helium Ions*. Tech. rep. National Institute of Standards and Technology (NIST), Physical Measurement Laboratory (PML), 2017. DOI: 10.18434/T4NC7P.

[138] Design Quantum GmbH. *DuraBeryllium® x-ray windows*. Darmstadt, 2022. URL: https://qd-europe.com/fileadmin/Mediapool/products/moxtek/_pdf/DuraBeryllium_x-ray_windows.pdf (visited on 2022-07-19).

[139] K. Burger, T. Urban, A. C. Dombrowsky, et al. "Technical and dosimetric realization of in vivo x-ray microbeam irradiations at the Munich Compact Light Source". In: *Medical Physics* 47.10 (2020), pp. 5183–5193. DOI: 10.1002/mp.14433.

[140] L. Zhang, H. Yuan, L. M. Burk, et al. "Image-guided microbeam irradiation to brain tumour bearing mice using a carbon nanotube x-ray source array". In: *Physics in Medicine and Biology* 59.5 (2014), pp. 1283–1303. DOI: 10.1088/0031-9155/59/5/1283.

[141] R. K. Sachs, P. Hahnfeld, and D. J. Brenner. "Review The link between low-LET dose-response relations and the underlying kinetics of damage production/repair/misrepair". In: *International Journal of Radiation Biology* 72.4 (1997), pp. 351–374. DOI: 10.1080/095530097143149.

[142] A. Lesnicar and R. Marquardt. "An innovative modular multilevel converter topology suitable for a wide power range". In: *2003 IEEE Bologna Power Tech Conference Proceedings*. Vol. 3. 2003, p. 6. DOI: 10.1109/PTC.2003.1304403.

[143] M. Galek. "M2C-Converter auf Basis von MOS-Transistoren für Niederspannungsnetze". Dissertation. Universität der Bundeswehr, München, 2016. ISBN: 978-3-8440-4870-4.

[144] Plansee SE. *Molybdän | Plansee*. 2021. URL: https://www.plansee.com/de/werkstoffe/molybdaen.html (visited on 2022-07-19).

[145] V. Favaudon, L. Caplier, V. Monceau, et al. "Ultrahigh dose-rate FLASH irradiation increases the differential response between normal and tumor tissue in mice". In: *Science Translational Medicine* 6.245 (2014), 245ra93. DOI: 10.1126/scitranslmed.3008973.

[146] N. Esplen, M. S. Mendonca, and M. Bazalova-Carter. "Physics and biology of ultrahigh dose-rate (FLASH) radiotherapy: a topical review". In: *Physics in Medicine & Biology* 65.23 (2020), 23TR03. DOI: 10.1088/1361-6560/abaa28.

[147] F. Gao, Y. Yang, H. Zhu, et al. "First demonstration of the FLASH effect with ultrahigh dose rate high-energy X-rays". In: *Radiotherapy and Oncology* 166 (2022), pp. 44–50. DOI: 10.1016/j.radonc.2021.11.004.

[148] E. Beyreuther, M. Brand, S. Hans, et al. "Feasibility of proton FLASH effect tested by zebrafish embryo irradiation". In: *Radiotherapy and Oncology* 139 (2019), pp. 46–50. DOI: 10.1016/j.radonc.2019.06.024.

[149] B. P. Venkatesulu, A. Sharma, J. M. Pollard-Larkin, et al. "Ultra high dose rate (35 Gy/sec) radiation does not spare the normal tissue in cardiac and splenic models of lymphopenia and gastrointestinal syndrome". In: *Scientific Reports* 9.1 (2019), p. 17180. DOI: 10.1038/s41598-019-53562-y.

[150] M.-C. Vozenin, P. De Fornel, K. Petersson, et al. “The Advantage of FLASH Radiotherapy Confirmed in Mini-pig and Cat-cancer Patients”. In: *Clinical Cancer Research* 25.1 (2019), pp. 35–42. DOI: 10.1158/1078-0432.CCR-17-3375.

[151] P. Montay-Gruel, A. Bouchet, M. Jaccard, et al. “X-rays can trigger the FLASH effect: Ultra-high dose-rate synchrotron light source prevents normal brain injury after whole brain irradiation in mice”. In: *Radiotherapy and Oncology* 129.3 (2018), pp. 582–588. DOI: 10.1016/j.radonc.2018.08.016.

[152] E. S. Diffenderfer, I. I. Verginadis, M. M. Kim, et al. “Design, Implementation, and in Vivo Validation of a Novel Proton FLASH Radiation Therapy System”. In: *International Journal of Radiation Oncology*Biology*Physics* 106.2 (2020), pp. 440–448. DOI: 10.1016/j.ijrobp.2019.10.049.

[153] W. Tinganelli, O. Sokol, M. Quartieri, et al. “Ultra-High Dose Rate (FLASH) Carbon Ion Irradiation: Dosimetry and First Cell Experiments”. In: *International Journal of Radiation Oncology*Biology*Physics* (2021). DOI: 10.1016/j.ijrobp.2021.11.020.

[154] U. A. Weber, E. Scifoni, and M. Durante. “FLASH radiotherapy with carbon ion beams”. In: *Medical Physics* (2021). DOI: 10.1002/mp.15135.

[155] T. Tessonnier, S. Mein, D. W. Walsh, et al. “FLASH Dose Rate Helium Ion Beams: First In Vitro Investigations”. In: *International Journal of Radiation Oncology*Biology*Physics* 111.4 (2021), pp. 1011–1022. DOI: 10.1016/j.ijrobp.2021.07.1703.

[156] P. Montay-Gruel, M. M. Acharya, K. Petersson, et al. “Long-term neurocognitive benefits of FLASH radiotherapy driven by reduced reactive oxygen species”. In: *Proceedings of the National Academy of Sciences* 116.22 (2019), pp. 10943–10951. DOI: 10.1073/pnas.1901777116.

[157] M.-C. Vozenin, J. Hendry, and C. Limoli. “Biological Benefits of Ultra-high Dose Rate FLASH Radiotherapy: Sleeping Beauty Awoken”. In: *Clinical Oncology* 31.7 (2019), pp. 407–415. DOI: 10.1016/j.clon.2019.04.001.

[158] J. Bourhis, W. J. Sozzi, P. G. Jorge, et al. “Treatment of a first patient with FLASH-radiotherapy”. In: *Radiotherapy and Oncology* 139 (2019), pp. 18–22. DOI: 10.1016/j.radonc.2019.06.019.

[159] M. Durante, E. Brauer-Krisch, and M. Hill. “Faster and safer? FLASH ultra-high dose rate in radiotherapy”. In: *The British Journal of Radiology* (2017), p. 20170628. DOI: 10.1259/bjr.20170628.

[160] D. Y. Breitkreutz, M. Shumail, K. K. Bush, et al. “Initial Steps Towards a Clinical FLASH Radiotherapy System: Pediatric Whole Brain Irradiation with 40 MeV Electrons at FLASH Dose Rates”. In: *Radiation Research* 194.6 (2020). DOI: 10.1667/RADE-20-00069.1.

[161] A. Sarti, P. De Maria, G. Battistoni, et al. “Deep Seated Tumour Treatments With Electrons of High Energy Delivered at FLASH Rates: The Example of Prostate Cancer”. In: *Frontiers in Oncology* 11 (2021). DOI: 10.3389/fonc.2021.777852.

[162] S. Wei, H. Lin, J. I. Choi, et al. “A Novel Proton Pencil Beam Scanning FLASH RT Delivery Method Enables Optimal OAR Sparing and Ultra-High Dose Rate Delivery: A Comprehensive Dosimetry Study for Lung Tumors”. In: *Cancers* 13.22 (2021), p. 5790. DOI: 10.3390/cancers13225790.

[163] P. van Marlen, M. Dahele, M. Folkerts, et al. “Ultra-High Dose Rate Transmission Beam Proton Therapy for Conventionally Fractionated Head and Neck Cancer: Treatment Planning and Dose Rate Distributions”. In: *Cancers* 13.8 (2021), p. 1859. DOI: 10.3390/cancers13081859.

[164] S. Wei, H. Lin, J. I. Choi, et al. “FLASH Radiotherapy Using Single-Energy Proton PBS Transmission Beams for Hypofractionation Liver Cancer: Dose and Dose Rate Quantification”. In: *Frontiers in Oncology* 11 (2022). DOI: 10.3389/fonc.2021.813063.

[165] E. Schüler, S. Trovati, G. King, et al. “Experimental Platform for Ultra-high Dose Rate FLASH Irradiation of Small Animals Using a Clinical Linear Accelerator”. In: *International Journal of Radiation Oncology*Biology*Physics* 97.1 (2017), pp. 195–203. DOI: 10.1016/j.ijrobp.2016.09.018.

[166] A. Patriarca, C. Fouillade, M. Auger, et al. “Experimental Set-up for FLASH Proton Irradiation of Small Animals Using a Clinical System”. In: *International Journal of Radiation Oncology*Biology*Physics* 102.3 (2018), pp. 619–626. DOI: 10.1016/j.ijrobp.2018.06.403.

[167] M. D. Wright, P. Romanelli, A. Bravin, et al. “Non-conventional Ultra-High Dose Rate (FLASH) Microbeam Radiotherapy Provides Superior Normal Tissue Sparing in Rat Lung Compared to Non-conventional Ultra-High Dose Rate (FLASH) Radiotherapy”. In: *Cureus* 13.11 (2021), e19317. DOI: 10.7759/cureus.19317.

[168] T. Schneider, C. Fernandez-Palomo, A. Bertho, et al. “Combining FLASH and spatially fractionated radiation therapy: The best of both worlds”. In: *Radiotherapy and Oncology* in press (2022). DOI: 10.1016/j.radonc.2022.08.004.

[169] P. G. Maxim, S. G. Tantawi, and B. W. Loo. “PHASER: A platform for clinical translation of FLASH cancer radiotherapy”. In: *Radiotherapy and Oncology* 139 (2019), pp. 28–33. DOI: 10.1016/j.radonc.2019.05.005.

[170] R. Longo, M. Tonutti, L. Rigon, et al. “Clinical study in phase-contrast mammography: image-quality analysis”. In: *Philosophical Transactions of the Royal Society A: Mathematical, Physical and Engineering Sciences* 372.2010 (2014), p. 20130025. DOI: 10.1098/rsta.2013.0025.

[171] J. Albers, S. Pacilé, M. A. Markus, et al. "X-ray-Based 3D Virtual Histology—Adding the Next Dimension to Histological Analysis". In: *Molecular Imaging and Biology* 20.5 (2018), pp. 732–741. DOI: 10.1007/s11307-018-1246-3.

[172] M. Elfarnawany, S. A. Rohani, S. Ghomashchi, et al. "Improved middle-ear soft-tissue visualization using synchrotron radiation phase-contrast imaging". In: *Hearing Research* 354 (2017), pp. 1–8. DOI: 10.1016/j.heares.2017.08.001.

[173] M. Romano, A. Bravin, A. Mittone, et al. "A Multi-Scale and Multi-Technique Approach for the Characterization of the Effects of Spatially Fractionated X-ray Radiation Therapies in a Preclinical Model". In: *Cancers* 13.19 (2021), p. 4953. DOI: 10.3390/cancers13194953.

[174] H. Yoshioka, Y. Kadono, Y. T. Kim, et al. "Imaging evaluation of the cartilage in rheumatoid arthritis patients with an x-ray phase imaging apparatus based on Talbot-Lau interferometry". In: *Scientific Reports* 10.1 (2020), p. 6561. DOI: 10.1038/s41598-020-63155-9.

[175] M. Stampanoni, Z. Wang, T. Thüring, et al. "The First Analysis and Clinical Evaluation of Native Breast Tissue Using Differential Phase-Contrast Mammography". In: *Investigative Radiology* 46.12 (2011), pp. 801–806. DOI: 10.1097/RLI.0b013e31822a585f.

[176] M. Saccomano, J. Albers, G. Tromba, et al. "Synchrotron inline phase contrast μCT enables detailed virtual histology of embedded soft-tissue samples with and without staining". In: *Journal of Synchrotron Radiation* 25.4 (2018), pp. 1153–1161. DOI: 10.1107/S1600577518005489.

[177] R. Deslattes, E. Kessler Jr., P. Indelicato, et al. *X-Ray Transition Energies Database, NIST Standard Reference Database 128*. Tech. rep. National Institute of Standards and Technology (NIST), Physical Measurement Laboratory, 2005. DOI: 10.18434/T4859Z.

[178] H. Wang, Y. Kashyap, and K. Sawhney. "From synchrotron radiation to lab source: Advanced speckle-based X-ray imaging using abrasive paper". In: *Scientific Reports* 6.1 (2016), p. 20476. DOI: 10.1038/srep20476.

[179] F. Pfeiffer, T. Weitkamp, O. Bunk, et al. "Phase retrieval and differential phase-contrast imaging with low-brilliance X-ray sources". In: *Nature Physics* 2.4 (2006), pp. 258–261. DOI: 10.1038/nphys265.

[180] M. Vassholz, B. Koberstein-Schwarz, A. Ruhlandt, et al. "New X-Ray Tomography Method Based on the 3D Radon Transform Compatible with Anisotropic Sources". In: *Physical Review Letters* 116.8 (2016), p. 088101. DOI: 10.1103/PhysRevLett.116.088101.

[181] J. A. Núñez, A. Goring, E. Hesse, et al. "Simultaneous visualisation of calcified bone microstructure and intracortical vasculature using synchrotron X-ray phase contrast-enhanced tomography". In: *Scientific Reports* 7.1 (2017), p. 13289. DOI: 10.1038/s41598-017-13632-5.

[182] C. L. Walsh, P. Tafforeau, W. L. Wagner, et al. “Imaging intact human organs with local resolution of cellular structures using hierarchical phase-contrast tomography”. In: *Nature Methods* 18.12 (2021), pp. 1532–1541. DOI: 10.1038/s41592-021-01317-x.

[183] F. A. Dilmanian, Z. Zhong, T. Bacarian, et al. “Interlaced x-ray microplanar beams: A radiosurgery approach with clinical potential”. In: *Proceedings of the National Academy of Sciences of the United States of America* 103.25 (2006), pp. 9709–9714. DOI: 10.1073/pnas.0603567103.

[184] F. M. Gagliardi, I. Cornelius, A. Blencowe, et al. “High resolution 3D imaging of synchrotron generated microbeams”. In: *Medical Physics* 42.12 (2015), pp. 6973–6986. DOI: 10.1118/1.4935410.

[185] R. Serduc, E. Bräuer-Krisch, A. Bouchet, et al. “First trial of spatial and temporal fractionations of the delivered dose using synchrotron microbeam radiation therapy”. In: *Journal of Synchrotron Radiation* 16.4 (2009), pp. 587–590. DOI: 10.1107/S0909049509012485.

[186] W. Schlegel, C. Thieke, O. Jäkel, et al. “Bestrahlungsverfahren”. In: *Medizinische Physik*. Ed. by W. Schlegel, C. P. Karger, and O. Jäkel. Berlin, Heidelberg: Springer Berlin Heidelberg, 2018. Chap. IV 26, pp. 525–577. DOI: 10.1007/978-3-662-54801-1_26.

[187] M. Donzelli, U. Oelfke, and E. Brauer-Krisch. “Introducing the concept of spiral microbeam radiation therapy (spiralMRT)”. In: *Physics in Medicine and Biology* 64.6 (2019). DOI: 10.1088/1361-6560/aaff23.

[188] J. Z. Wang and X. A. Li. “Evaluation of external beam radiotherapy and brachytherapy for localized prostate cancer using equivalent uniform dose”. In: *Medical Physics* 30.1 (2002), pp. 34–40. DOI: 10.1118/1.1527674.

[189] I. Martínez-Rovira, J. Sempau, J. M. Fernández-Varea, et al. “Monte Carlo dosimetry for forthcoming clinical trials in x-ray microbeam radiation therapy”. In: *Physics in Medicine and Biology* 55.15 (2010), pp. 4375–4388. DOI: 10.1088/0031-9155/55/15/012.

[190] M. Ahmed, J. J. Wilkens, S. Bartzsch, et al. “PO-1416: Dose calculation algorithm for a compact xray source in Microbeam Radiation Therapy”. In: *Radiotherapy and Oncology* 152.Supplement 1 (2020), S751–S752. DOI: 10.1016/S0167-8140(21)01434-1.

[191] L. R. J. Day, M. Donzelli, P. Pellicioli, et al. “A commercial treatment planning system with a hybrid dose calculation algorithm for synchrotron radiotherapy trials”. In: *Physics in Medicine & Biology* 66.5 (2021), p. 055016. DOI: 10.1088/1361-6560/abd737.

[192] *3D Slicer Image Computing Platform*. URL: https://slicer.org (visited on 2022-07-19).

[193] A. Fedorov, R. Beichel, J. Kalpathy-Cramer, et al. "3D Slicer as an image computing platform for the Quantitative Imaging Network." In: *Magnetic resonance imaging* 30.9 (2012), pp. 1323–41. DOI: 10.1016/j.mri.2012.05.001.

[194] C. Pinter, A. Lasso, A. Wang, et al. "SlicerRT: Radiation therapy research toolkit for 3D Slicer". In: *Medical Physics* 39.10 (2012), pp. 6332–6338. DOI: 10.1118/1.4754659.

[195] International Commission on Radiation Units & Measurements (ICRU). *ICRU Report 44, Tissue Substitutes in Radiation Dosimetry and Measurement*. Tech. rep. 1. Bethesda, MD, 1989. URL: https://physics.nist.gov/PhysRefData/XrayMassCoef/tab2.html (visited on 2022-07-19).

[196] G. Hanna, L. Murray, R. Patel, et al. "UK Consensus on Normal Tissue Dose Constraints for Stereotactic Radiotherapy". In: *Clinical Oncology* 30.1 (2018), pp. 5–14. DOI: 10.1016/j.clon.2017.09.007.

[197] C. M. van Leeuwen, A. L. Oei, J. Crezee, et al. "The alfa and beta of tumours: a review of parameters of the linear-quadratic model, derived from clinical radiotherapy studies". In: *Radiation Oncology* 13.1 (2018). DOI: 10.1186/s13014-018-1040-z.

[198] R. J. Klement, J.-J. Sonke, M. Allgäuer, et al. "Estimation of the α/β ratio of non-small cell lung cancer treated with stereotactic body radiotherapy". In: *Radiotherapy and Oncology* 142 (2020), pp. 210–216. DOI: 10.1016/j.radonc.2019.07.008.

[199] T. S. Kehwar. "Analytical approach to estimate normal tissue complication probability using best fit of normal tissue tolerance doses into the NTCP equation of the linear quadratic model." In: *Journal of Cancer Research and Therapeutics* 1.3 (2005), p. 168. DOI: 10.4103/0973-1482.19597.

[200] F. Tommasino, E. Scifoni, and M. Durante. "New Ions for Therapy". In: *International Journal of Particle Therapy* 2.3 (2015), pp. 428–438. DOI: 10.14338/IJPT-15-00027.1.

[201] L. B. Marks, E. D. Yorke, A. Jackson, et al. "Use of Normal Tissue Complication Probability Models in the Clinic". In: *International Journal of Radiation Oncology*Biology*Physics* 76.3 (2010), S10–S19. DOI: 10.1016/j.ijrobp.2009.07.1754.

[202] S. G. Gerhard, D. A. Palma, A. J. Arifin, et al. "Organ at Risk Dose Constraints in SABR: A Systematic Review of Active Clinical Trials". In: *Practical Radiation Oncology* 11.4 (2021), e355–e365. DOI: 10.1016/j.prro.2021.03.005.

[203] C. L. Rogers, M. Won, M. A. Vogelbaum, et al. "High-risk Meningioma: Initial Outcomes From NRG Oncology/RTOG 0539". In: *International Journal of Radiation Oncology*Biology*Physics* 106.4 (2020), pp. 790–799. DOI: 10.1016/j.ijrobp.2019.11.028.

[204] G.-P. Chen, F. Liu, J. White, et al. “A planning comparison of 7 irradiation options allowed in RTOG 1005 for early-stage breast cancer”. In: *Medical Dosimetry* 40.1 (2015), pp. 21–25. DOI: 10.1016/j.meddos.2014.06.007.

[205] M. Donzelli, E. Bräuer-Krisch, C. Nemoz, et al. “Conformal image-guided microbeam radiation therapy at the ESRF biomedical beamline ID17”. In: *Medical Physics* 43.6Part1 (2016), pp. 3157–3167. DOI: 10.1118/1.4950724.

[206] J. P. Kirkpatrick, D. J. Brenner, and C. G. Orton. “The linear-quadratic model is inappropriate to model high dose per fraction effects in radiosurgery”. In: *Medical Physics* 36.8 (2009), pp. 3381–3384. DOI: 10.1118/1.3157095.

[207] D. J. Brenner. “The Linear-Quadratic Model Is an Appropriate Methodology for Determining Isoeffective Doses at Large Doses Per Fraction”. In: *Seminars in Radiation Oncology* 18.4 (2008), pp. 234–239. DOI: 10.1016/j.semradonc.2008.04.004.

[208] H. H. Liu, P. Keall, and W. R. Hendee. “D_m rather than D_w should be used in Monte Carlo treatment planning”. In: *Medical Physics* 29.5 (2002), pp. 922–924. DOI: 10.1118/1.1473137.

[209] N. Dogan, J. V. Siebers, and P. J. Keall. “Clinical comparison of head and neck and prostate IMRT plans using absorbed dose to medium and absorbed dose to water”. In: *Physics in Medicine and Biology* 51.19 (2006), pp. 4967–4980. DOI: 10.1088/0031-9155/51/19/015.

[210] C.-M. Ma and J. Li. “Dose specification for radiation therapy: dose to water or dose to medium?” In: *Physics in Medicine and Biology* 56.10 (2011), pp. 3073–3089. DOI: 10.1088/0031-9155/56/10/012.

[211] N. Reynaert, F. Crop, E. Sterpin, et al. “On the conversion of dose to bone to dose to water in radiotherapy treatment planning systems”. In: *Physics and Imaging in Radiation Oncology* 5 (2018), pp. 26–30. DOI: 10.1016/j.phro.2018.01.004.

[212] J. V. Siebers, P. J. Keall, A. E. Nahum, et al. “Converting absorbed dose to medium to absorbed dose to water for Monte Carlo based photon beam dose calculations”. In: *Physics in Medicine and Biology* 45.4 (2000), pp. 983–995. DOI: 10.1088/0031-9155/45/4/313.

[213] L. H. Gray. “An ionization method for the absolute measurement of γ-ray energy”. In: *Proceedings of the Royal Society of London. Series A - Mathematical and Physical Sciences* 156.889 (1936), pp. 578–596. DOI: 10.1098/rspa.1936.0169.

[214] B. M. Koeppen and B. A. Stanton. *Berne and Levy Physiology*. 6th ed. Mosby, 2008. ISBN: 978-0-323-04582-7.

[215] J. E. Hall. *Guyton and Hall Textbook of Medical Physiology*. 12th ed. Saunders, 2010. ISBN: 978-1-4160-4574-8.

[216] G. Hombrink, J. J. Wilkens, S. E. Combs, et al. “Simulation and measurement of microbeam dose distribution in lung tissue”. In: *Physica Medica* 75 (2020), pp. 77–82. DOI: 10.1016/j.ejmp.2020.06.003.

[217] H. Okamoto, T. Kanai, Y. Kase, et al. “Relation between Lineal Energy Distribution and Relative Biological Effectiveness for Photon Beams according to the Microdosimetric Kinetic Model”. In: *Journal of Radiation Research* 52.1 (2011), pp. 75–81. DOI: 10.1269/jrr.10073.

[218] V. Paget, M. Ben Kacem, M. Dos Santos, et al. “Multiparametric radiobiological assays show that variation of X-ray energy strongly impacts relative biological effectiveness: comparison between 220 kV and 4 MV”. In: *Scientific Reports* 9.1 (2019), p. 14328. DOI: 10.1038/s41598-019-50908-4.

[219] J. Valentin. “ICRP Publication 92: Relative biological effectiveness (RBE), quality factor (Q), and radiation weighting factor (w_R)”. In: *Annals of the ICRP* 33.4 (2003), pp. 1–121. DOI: 10.1016/S0146-6453(03)00024-1.

[220] P. Cahoon, V. Giacometti, F. Casey, et al. “Investigating spatial fractionation and radiation induced bystander effects: a mathematical modelling approach”. In: *Physics in Medicine & Biology* 66.22 (2021), p. 225007. DOI: 10.1088/1361-6560/ac3119.

[221] L. C. Jones and P. W. Hoban. “Treatment plan comparison using equivalent uniform biologically effective dose (EUBED)”. In: *Physics in Medicine and Biology* 45.1 (2000), pp. 159–170. DOI: 10.1088/0031-9155/45/1/311.

[222] M. Krämer and M. Scholz. “Treatment planning for heavy-ion radiotherapy: Calculation and optimization of biologically effective dose”. In: *Physics in Medicine and Biology* 45.11 (2000), pp. 3319–3330. DOI: 10.1088/0031-9155/45/11/314.

[223] G. Echner. “Patientenlagerung und -positionierung”. In: *Medizinische Physik – Grundlagen – Bildgebung – Therapie – Technik*. Ed. by W. Schlegel, C. Karger, and O. Jäkel. Berlin, Heidelberg: Springer Berlin Heidelberg, 2018. Chap. IV 25, pp. 515–524. DOI: 10.1007/978-3-662-54801-1_25.

[224] X. Zhong, C. H. Meyer, D. J. Schlesinger, et al. “Tracking brain motion during the cardiac cycle using spiral cine-DENSE MRI”. In: *Medical Physics* 36.8 (2009), pp. 3413–3419. DOI: 10.1118/1.3157109.

[225] C. J. Hartley, A. K. Reddy, S. Madala, et al. “Doppler velocity measurements from large and small arteries of mice”. In: *American Journal of Physiology-Heart and Circulatory Physiology* 301.2 (2011), H269–H278. DOI: 10.1152/ajpheart.00320.2011.

[226] S. Spasova, J. Winter, S. E. Combs, et al. “V82 Impact of pulse motion in the brain on the dose distribution of microbeam radiation therapy”. In: *Joint Conference of the ÖGMP, DGMP and SGSMP*. Ed. by D. Georg and W. Birkfellner. 2021, p. 193. ISBN: 978-3-948023-16-4.

[227] M. Soellinger, A. K. Rutz, S. Kozerke, et al. "3D cine displacement-encoded MRI of pulsatile brain motion". In: *Magnetic Resonance in Medicine* 61.1 (2009), pp. 153–162. DOI: 10.1002/mrm.21802.

[228] Thorlabs GmbH. *MTS25-Z8 and MTS50-Z8 Brushed DC Motorized Translation Stages*. Bergkirchen, 2021. URL: https://www.thorlabs.com/thorProduct.cfm?partNumber=MTS50-Z8 (visited on 2022-07-19).

[229] A. E. Lujan, E. W. Larsen, J. M. Balter, et al. "A method for incorporating organ motion due to breathing into 3D dose calculations". In: *Medical Physics* 26.5 (1999), pp. 715–720. DOI: 10.1118/1.598577.

[230] D. R. Enzmann and N. J. Pelc. "Brain motion: measurement with phase-contrast MR imaging". In: *Radiology* 185.3 (1992), pp. 653–660. DOI: 10.1148/radiology.185.3.1438741.

[231] P. M. Pattany, I. H. Khamis, B. C. Bowen, et al. "Effects of Physiologic Human Brain Motion on Proton Spectroscopy: Quantitative Analysis and Correction with Cardiac Gating". In: *American Journal of Neuroradiology* 23.2 (2002), pp. 225–230. URL: http://www.ajnr.org/content/23/2/225.abstract.